

Evaluation of Powder Metallurgical Processing Routes for Multi- Component Niobium Silicide-Based High-Temperature Alloys

Zur Erlangung des akademischen Grades
Doktor der Ingenieurwissenschaften
der Fakultät für Maschinenbau des
Karlsruher Instituts für Technologie

genehmigte
Dissertation
von

Dipl.-Ing. Hans Christoph Maximilian Seemüller
aus Heppenheim (Bergstraße)

Tag der mündlichen Prüfung: 22.03.2016

Erstgutachter: Prof. Dr.-Ing. Martin Heilmaier

Zweitgutachter: Prof. Dr. John Perepezko

Zusammenfassung

Nickelbasis-Superlegierungen, wie sie z.B. in modernen Flugzeugturbinen eingesetzt werden, sind durch ihren Schmelzpunkt bei ca. 1400 °C in ihrer Anwendungstemperatur begrenzt. Niob-Silizium-basierte Komposite zeichnen sich in der Regel durch einen deutlich höheren Schmelzpunkt und eine geringere Dichte aus. Daher gelten sie als mögliche Kandidaten, Nickelbasis-Legierungen zu ersetzen. Neben der Legierungsentwicklung für die Eigenschaftsoptimierung sind auch geeignete Herstellungsprozesse zu entwickeln.

Das Ziel dieser Arbeit war, die Anwendbarkeit pulvermetallurgischer Prozesse zu prüfen, die in der Lage wären, endkonturnahe Turbinenbauteile im industriellen Maßstab herzustellen. Hierzu wurde die Modelllegierung Nb-20Si-23Ti-6Al-3Cr-4Hf (in at%) ausgewählt, angelehnt an die etablierte MASC-Legierung mit der Zusammensetzung Nb-16Si-25Ti-2Al-2Cr-8Hf (in at%) von Bewlay et al. [1]. Zwei Methoden zur Pulverherstellung wurden ausgewählt: das mechanische Legieren (engl. mechanical alloying, MA) von elementaren Pulvern und die tiegellose Inertgasverdüsung (engl. gas atomization, GA).

Mahlparameter wurden optimiert, um eine Balance aus Mahldauer, Verunreinigungsniveau und Pulverausbeute zu erreichen. Zwei Möglichkeiten wurden erarbeitet, um das Kaltverschweißen der duktilen Pulver mit der Mahlbehälterwand und den Mahlkugeln zu minimieren: Erniedrigung der Prozesstemperatur und der Einsatz von Mahlhilfsmitteln. Demnach wurden zwei Mahlchargen für die nachfolgende Kompaktierung hergestellt, eine bei kontinuierlicher Kühlung auf -15 °C (MA₁) und die zweite mit kontinuierlicher Kühlung auf Zimmertemperatur und 5 Gew.% Heptan als Mahlhilfsmittel (MA₂). Durch geeignete Wahl der Mahlparameter konnten Eisenverunreinigungen durch Abrieb von Mahlkugeln, Mahlbehälter und Rotor des verwendeten Attritors minimiert werden (≈ 1 At.%). Verunreinigung durch Interstitutionsatome, d.h. Kohlenstoff, Stickstoff und Sauerstoff, waren jedoch in beiden Fällen hoch. MA₁ wies hohe Gehalte an Sauerstoff und Stickstoff auf, verursacht durch den bei der Kühlung entstandenen Unterdruck im Mahlbehälter. MA₂ zeigte zwar einen vergleichsweise niedrigen Sauerstoffgehalt, durch das Aufbrechen des Heptans beim Mahlen jedoch einen hohen Kohlenstoffgehalt.

Das Pulver wurde durch Sieben in zwei Fraktionen getrennt. Pulverpartikel kleiner als 25 µm wurden mittels Pulverspritzgießen (engl. powder injection molding, PIM) und die grobe Fraktion durch heißisostatisches Pressen (HIP) kompaktiert.

Von dem gasverdüsteten Pulver wurden zwei Pulverfraktionen mittels HIP verdichtet, < 25 µm und (GA) 106-225 µm (CGA). Lediglich die feine Fraktion (< 25 µm) wurde mit PIM kompaktiert.

HIP von MA-Pulvern blieb erfolglos, da starke Rissbildung die Herstellung von quaderförmigen Proben mittels Drahterodieren verhinderte. Die geschlossene HIP-Kanne hat möglicherweise das Entweichen von Gasen beim Erhitzen verhindert und so zu starken Eigenspannungen geführt. Daher wurde diese Produktionsmethode früh verworfen. Die Kombinationen HIP GA, HIP CGA, PIM GA, PIM MA₁ und PIM MA₂ wurden weiter untersucht.

Mikrostruktur

Die Mikrostruktur der Kompaktproben wies hauptsächlich vier Phasen auf, den Niobmischkristall, zwei Modifikationen von Nb_5Si_3 , $\alpha\text{-Nb}_5\text{Si}_3$ und $\gamma\text{-Nb}_5\text{Si}_3$, und kleine Mengen an Hafniumoxid. Zusätzlich führten die Stickstoff- und Kohlenstoffverunreinigungen in MA1 bzw. MA2 zur Bildung von jeweils ca. 5 Vol.% Titanitrid bzw. Titankarbid. Durch die langsamere Abkühlgeschwindigkeit von CGA zeigte HIP CGA zudem größere, primär erstarrte Silizidkörner.

Um die thermische Stabilität des Phasengleichgewichts zu beurteilen und um die Mikrostruktur zu vergrößern, wurden Wärmebehandlungen bei 1300 und 1500 °C für 20 oder 100 h durchgeführt. Dabei blieb der Mischkristallgehalt bei 46 und 25 % konstant für GA- bzw. MA-basiertes Material. Die $\alpha\text{-Nb}_5\text{Si}_3$ - und $\gamma\text{-Nb}_5\text{Si}_3$ -Gehalte zeigten jedoch eine starke Abhängigkeit von der Wärmebehandlungstemperatur. Durch Erhöhung der Temperatur sank der Gehalt an $\alpha\text{-Nb}_5\text{Si}_3$ in GA-Proben von 36 auf 25 % und bei MA-Proben von 18 auf 0 %. Die Verunreinigungen durch Eisen, Stickstoff und Kohlenstoff stabilisieren das hexagonale $\gamma\text{-Nb}_5\text{Si}_3$. Im Vergleich zu $\alpha\text{-Nb}_5\text{Si}_3$ wird berichtet, dass $\gamma\text{-Nb}_5\text{Si}_3$ die Kriechfestigkeit verschlechtert [2, 3]. Außerdem führt die starke Anisotropie der Wärmeausdehnungskoeffizienten zu Rissbildung, was vor allem bei MA-Proben, die einen hohen $\gamma\text{-Nb}_5\text{Si}_3$ -Anteil aufweisen, beobachtet werden konnte. Obwohl es sich bei Kohlenstoff, Stickstoff und Sauerstoff um Zwischengitteratome handelt, beeinflussen sie stark die Zusammensetzung der einzelnen Phasen und führen zu dem unerwartet niedrigen Mischkristallanteil in MA-Proben. In GA-Proben wurde, ausgelöst durch inhomogene Sauerstoffverteilung, bei der Wärmebehandlungstemperatur von 1500 °C lokale Aufschmelzung beobachtet, was die Bildung von netzwerkartigen $\beta\text{-Nb}_5\text{Si}_3$ -Körnern zur Folge hatte. Dadurch wird das zur Verfügung stehende Temperaturintervall für Vergrößerungsglühungen eingeschränkt. Im Ausgangszustand wiesen HIP-Proben eine Korngröße von etwa 2 μm auf, PIM-Proben etwa 4 μm . Zwar glied sich die Korngröße nach 100 h bei 1500 °C zwischen den beiden Kompaktierungsverfahren an, sie blieb aber unter 10 μm .

Mechanische Eigenschaften

Bei Raumtemperatur konnten für alle Zustände sehr große Druckfestigkeiten erzielt werden (> 1700 MPa). MA-Proben zeigten aber kaum Plastizität, während GA-Proben ca. 3 % plastische Dehnung erreichten. Dies gilt für beide, den Herstellungs- (AC) und den wärmebehandelten (HT) Zustand. Bei hohen Temperaturen erlangte auch MA-Material plastische Verformbarkeit bei im Vergleich zu GA-Material 60 % höheren Festigkeiten. Dies kann der kontinuierlichen, intermetallischen Matrix zugeschrieben werden, führte aber auch zu starker Schädigung während der Verformung. Sehr starke Rissbildung und Abscheren der Probe unter einem Winkel von ca. 45° machen die mangelnde Anwendungseignung von MA-Material deutlich.

Druckkriechversuche an GA-Material zeigten, dass Korngrenzgleiten, ein Mechanismus bekannt von der Superplastizität, das Kriechverhalten bestimmt. Bei einem Spannungsexponenten von zwei konnte eine gleichachsige, texturfreie Mikrostruktur bis zu sehr hohen plastischen Dehnungen erhalten werden. Die Abhängigkeit der Verformungsgeschwindigkeit von der Korngröße war stärker als erwartet und lässt sich durch eine Kombination von Korngrenzgleiten und dem erhöhten Kriechwiderstand der wärmebehandelten Proben durch

die großen β - Nb_5Si_3 -Netzwerke erklären. Da Korngrenzengleiten gegenüber klassischer, versetzungsbasierter Verformung zu deutlich erhöhten Kriechraten führt, ist eine weitere Vergrößerung oder eine Stärkung der Korngrenzen unabdingbar, wenn eine Anwendung dieses pulvermetallurgischen Materials im Hochtemperaturbereich angestrebt wird. Die Korngröße durch Wärmebehandlung bei $1500\text{ }^\circ\text{C}$ in einen Bereich zu bringen, in dem Korngrenzengleiten unterdrückt wird ($\approx 20\text{ }\mu\text{m}$), würde ca. 1000 h benötigen. Eine Festigung der Korngrenzen durch feine Ausscheidungen könnte durch geeignetes Legieren möglich sein. Insgesamt liegt der Kriechwiderstand weit abgeschlagen hinter ähnlichen Legierungszusammensetzungen, die mittels klassischer Schmelzmetallurgie oder gerichteter Erstarrung hergestellt wurden (und ebenfalls hinter Nickelbasis-Superlegierungen).

Die Bruchzähigkeit bei Zimmertemperatur wurde durch Vierpunktbiegung von einseitig V-gekerbten Balken (SEVNB) an GA-Material ermittelt. Zwischen den verschiedenen Herstellungsrouten, HIP und PIM, und auch zwischen Herstellungszustand und wärmebehandeltem Zustand konnten keine signifikanten Unterschiede festgestellt werden, mit Bruchzähigkeitswerten im Bereich $7,7\text{--}8,7\text{ MPa}\cdot\text{m}^{0,5}$. Dies konnte auf die insgesamt ungenügende Duktilität der Mischkristallmatrix bei Zimmertemperatur zurückgeführt werden. Spaltbruch war dominant nicht nur bei den intermetallischen Phasen, sondern auch beim Mischkristall. Dies erklärt, warum Zähigkeitswerte von $15\text{--}20\text{ MPa}\cdot\text{m}^{0,5}$ ähnlicher Legierungen nicht erreicht werden konnten. Mit hoher Wahrscheinlichkeit ist der erhöhte Sauerstoffgehalt, selbst in GA-Proben, verantwortlich und führt zur Versprödung des Mischkristalls. Obwohl ein Großteil des Sauerstoffs mit Hafnium zu Hafniumoxid reagiert hat, bleibt seine Löslichkeit in Niob hoch.

Mittels Dreipunktbiegung wurde das Einsetzen der Duktilität mit steigender Temperatur untersucht. Die Größe zusammenhängender Silizidbereiche und die Porosität zeigten einen großen Einfluss auf die Spröd-Duktil-Übergangstemperatur (engl. ductile-to-brittle transition temperature, DBTT). Die großen Silizidkörner in HIP CGA AC (DBTT von $850\text{ }^\circ\text{C}$) im Vergleich zu dem ebenfalls porenfreien HIP GA AC (DBTT von $750\text{ }^\circ\text{C}$), führen zu einem Unterschied von $100\text{ }^\circ\text{C}$ in DBTT. Das Einsetzen lokaler Duktilität führt zu Spannungskonzentration und Bruch in den Silizidpartikeln und daraus folgend global sprödem Bruchverhalten. Gleiches gilt für Material hergestellt durch Lichtbogenschmelzen. Ebenfalls eine Erhöhung in DBTT ist durch Restporosität in PIM GA AC zu verzeichnen. Der letztgenannte Effekt kehrt sich nach einer Wärmebehandlung ($1500\text{ }^\circ\text{C}/100\text{ h}$) um, da bei HIP GA-Proben temperaturinduzierte Porosität (TIP, [4]) auftritt, während sich die Porosität in PIM GA verringert. Ein zusätzlicher HIP-Zyklus kann die TIP erneut schließen und bringt PIM GA und HIP GA auf ein gemeinsames Niveau bei $850\text{ }^\circ\text{C}$. PIM MA2 weist durch die kontinuierliche intermetallische Matrix eine DBTT von $1000\text{ }^\circ\text{C}$ auf.

Der Risspfad im Material ist stark temperaturabhängig. Bei Zimmertemperatur dominiert transkristalliner Spaltbruch in allen Phasen mit nur minimaler Duktilität im Niobmischkristall. Die ansteigende Duktilität des Mischkristalls mit der Temperatur führt zu Auftreten von Rissauffangverhalten und Rissablenkung entlang der Phasengrenzen. Steigt die Temperatur weiter, werden Phasengrenzen geschwächt und der Riss verläuft mehr und mehr entlang von Korn- und Phasengrenzen, insbesondere zwischen zwei intermetallischen Körnern. Bei Temperaturen über $1000\text{ }^\circ\text{C}$ verschwindet transkristalliner Spaltbruch (außer bei ungewöhnlich

großen Silizidbereichen, z.B. HIP CGA) zugunsten interkristallinen Bruchs der Silizide und duktilem Versagen der Mischkristallmatrix.

Insgesamt ist das Raumtemperaturverformungsverhalten durch die unzureichende Duktilität der Mischkristallphase gekennzeichnet, im Falle von MA auch durch zu geringe Phasenanteile ebendieser. Bei hohen Temperaturen führen die kleine Korngröße und die schwachen Korngrenzen zu niedriger Festigkeit.

Die Verwendung von pulvermetallurgischen Verfahren, die eine endkonturnahe Fertigung erlauben, wurde zwar erfolgreich auf eine mehrkomponentige NbSi-Legierung angewendet, einige Defizite müssen aber in der Zukunft noch verbessert werden. Das mechanische Legieren von Elementen, die eine starke Empfindlichkeit für Verunreinigungen aufweisen, insbesondere Niob und Titan, führt zu hohen Gehalten an Kohlenstoff, Stickstoff und Sauerstoff. Da sich dies stark auf das Phasengleichgewicht auswirkt und zur Versprödung führt, rät der Autor von der Verwendung des mechanischen Legierens für diese Materialklasse ab. Gasverdüsen zeigt zwar vertretbare Verunreinigungsniveaus, verlangt aber dennoch nach einer strikten Pulverhandhabung unter Schutzgasatmosphäre bei der kompletten Herstellungskette. Hauptproblem bleibt jedoch die geringe Korngröße, die die Hochtemperaturfestigkeit verringert.

Declaration

I hereby declare this work was produced by me with help of the stated aids and appliances only. To the best of my knowledge and belief, it contains no material previously published or written by another person, except for where due reference has been given. The rules for good scientific practice of the Karlsruhe Institute of Technology (KIT) have been respected.

Outside of the Department of Mechanical Engineering of the Karlsruhe Institute of Technology (KIT) no other doctoral procedures are pending or have been finalized unsuccessfully.

Ich erkläre hiermit, die vorliegende Arbeit selbstständig angefertigt und keine anderen als die angegebenen Quellen und Hilfsmittel benutzt zu haben. Wörtlich oder inhaltlich übernommene Stellen wurden als solche kenntlich gemacht. Die Satzung des Karlsruher Instituts für Technologie (KIT) zur Sicherung guter wissenschaftlicher Praxis wurde beachtet.

Hiermit erkläre ich, dass für mich Promotionsverfahren außerhalb der Fakultät für Maschinenbau des Karlsruher Instituts für Technologie (KIT) weder anhängig sind noch erfolglos abgeschlossen wurden.

Karlsruhe, den 22.10.2015

(Christoph Seemüller)

Acknowledgments

First and foremost, I want to thank Prof. Dr. Martin Heilmaier for the opportunity to carry out this work and his great scientific guidance. At all times, he gave me the freedom to pursue my own ideas and always challenged me to work scientifically.

I also want to thank Prof. Dr. John Perepezko for making himself available as the second examiner, several interesting discussions we had, and the insights he shared with me.

My gratitude goes to the European Union for funding my work within the HYSOP project (Framework Programme 7, grant no.: 266214) and to all project partners for the successful cooperation, especially Dr. Nicholas Adkins and Mick Wickins from the University of Birmingham, and Dr. Thomas Hartwig and Marco Mulser from Fraunhofer Institute for Manufacturing Technology and Advanced Materials for providing most of the sample material.

Furthermore, I thank my colleagues from IAM-WK, especially the members of the Physical Metallurgy group, but also my former coworkers at TU Darmstadt for providing an enjoyable working environment, support with experiments, and a great time together. When I got stuck, especially Florian Gang and Dr. Alexander Kauffmann, gave me new perspectives through many fruitful discussions.

Even though I would have to thank a great many from KIT and beyond, for their help and support, I will only name a few:

Dr. Alexander Kauffmann, Florian Gang, and Daniel Schliephake from IAM-WK for EBSD measurements, arc-melting, and mechanical testing, respectively;

Adelheid Ohl and Michaela Nagel from IAM-WK for their restless support in the metallography;

the members of our workshop, for manufacturing testing equipment and samples, and my student workers Bastian Baumann and Jonas Mülbauer, for helping with the metallographic preparation of the latter;

Dr. Günter Schell, Dr. Wolfgang Rheinheimer, and Thomas Hupfer from IAM-KWT for HIP, XRD, and ON-analysis, respectively;

Dr. Thomas Bergfeldt and Tatjana Kaiser from IAM-AWP for ONC-analysis;

Dr. Aaron Kobler and Dr. Di Wang from INT for help with TEM analysis;

Volker Zibat from LEM for SEM analysis;

Uta Gerhards from IMVT for WDX measurements.

Last but not least, I want to thank my parents, my sister, and my friend Tobias for their continued support through all ups and downs.

Table of Contents

Zusammenfassung	i
Mikrostruktur.....	ii
Mechanische Eigenschaften.....	ii
Declaration	v
Acknowledgments	vii
Table of Contents	ix
Abbreviations and Symbols	xiii
Abbreviations	xiii
Latin symbols	xv
Greek symbols.....	xvii
1 Introduction and Goal	1
2 Niobium-based Alloys	5
2.1 The Binary System Nb-Si.....	5
2.2 Alloying Additions.....	7
2.2.1 Titanium.....	8
2.2.2 Aluminum	9
2.2.3 Chromium	10
2.2.4 Hafnium.....	10
2.2.5 Others.....	11
2.2.6 Multi-Element NbSi-Alloys.....	11
3 Powder Metallurgy	15
3.1 Powder Production.....	15
3.1.1 Gas Atomization (GA)	16
3.1.2 Mechanical Alloying (MA).....	17
3.2 Compaction	20
3.2.1 Hot Pressing	21
3.2.2 Spark Plasma Sintering (SPS).....	21
3.2.3 Hot Isostatic Pressing (HIP).....	22
3.2.4 Powder Injection Molding (PIM)	23
3.2.5 Hot Extrusion.....	25
3.2.6 Direct Laser Fabrication (DLF)	25
4 Experimentals	27
4.1 Sample Production	27
4.1.1 Powder Production	27
4.1.2 Consolidation	28

4.1.3	Heat Treatments.....	29
4.1.4	Material Production by Arc-Melting	29
4.2	Microstructural Analysis	29
4.2.1	Metallographic Preparation	29
4.2.2	Scanning Electron Microscopy (SEM).....	30
4.2.3	Electron Backscatter Diffraction (EBSD).....	30
4.2.4	Transmission Electron Microscopy (TEM).....	31
4.2.5	Chemical Analysis	31
4.2.6	X-Ray Diffraction (XRD).....	32
4.2.7	Differential Scanning Calorimetry (DSC).....	32
4.2.8	Thermogravimetry with Mass Spectrometry	33
4.2.9	Density Measurement	33
4.2.10	Phase Diagram Calculations	33
4.3	Testing of Mechanical Properties	34
4.3.1	Quasi-Static Compression and Compression Creep.....	34
4.3.2	Fracture Toughness	35
4.3.3	Ductile-to-Brittle-Transition-Temperature (DBTT).....	36
4.3.4	Nano-Hardness	37
5	Production and Analysis of Powder	39
5.1	Mechanical Alloying (MA) of Elemental Powders	39
5.2	Phase Formations in MA ₁ Powder.....	44
5.3	Gas-Atomized Powder.....	47
6	Microstructural Analysis of Bulk Material.....	49
6.1	Qualitative Microstructural Analysis.....	50
6.1.1	As-Consolidated Condition.....	51
6.1.2	Heat-Treated at 1300 °C for 100 h and 1400 °C for 20 h	54
6.1.3	Heat-Treated at 1500 °C for 20 h and 100 h.....	57
6.2	Quantitative Microstructural Analysis	59
6.2.1	Threshold Analysis.....	60
6.2.2	Grid Counting Method	61
6.2.3	Electron Backscatter Diffraction (EBSD).....	63
6.2.4	Reference-Intensity-Ratio Method (RIR)	64
6.2.5	Lever Rule Calculations.....	68
6.2.6	Chemical Composition of Phases	72
6.2.7	Discussion of Microstructural Results	74
6.2.8	Grain Size Analysis.....	79
7	Compressive Tests.....	83
7.1	Quasi-Static Compressive Testing.....	84
7.1.1	Temperature Dependence	84

7.1.2	Strain Rate Dependence.....	87
7.2	Compressive Creep Testing	88
7.2.1	Stress Dependence.....	90
7.2.2	Temperature Dependence.....	96
7.2.3	Grain Size Dependence.....	97
7.2.4	Discussion of Creep Properties	99
8	Bending Tests.....	103
8.1	Fracture Toughness	103
8.1.1	Influence of Notch Root Diameter	104
8.1.2	Discussion of Fracture Toughness	105
8.2	Ductile-to-Brittle Transition Temperature (DBTT)	107
8.2.1	Fracture Strain.....	108
8.2.2	Yield / Cleavage Stress.....	111
8.2.3	Fracture Path.....	112
9	Final Discussion and Outlook	113
9.1	Ductility	113
9.2	Strength.....	115
9.3	Outlook	118
10	Summary	119
10.1	Microstructure.....	119
10.2	Mechanical Properties.....	120
11	References.....	123
12	List of Figures.....	137
13	List of Tables.....	145
14	Appendix.....	147
14.1	Figures.....	147
14.2	Tables.....	150
14.3	Reproducibility	153
15	Prior Publications on Parts of this Work	155

Abbreviations and Symbols

Abbreviations

abbreviation	description
AC	as-consolidated
bcc	body centered cubic
BHAM	University of Birmingham, Interdisciplinary Research Centre in Materials Processing, Birmingham, UK
BPR	ball-to-powder weight ratio
BSE	backscatter electron
CC	conventionally cast
CGA	coarse grained gas atomized powder
CIP	cold isostatic pressing
CTE	coefficient of thermal expansion
DBTT	ductile-to-brittle-transition-temperature
DLF	direct laser fabrication
DS	directionally solidified
DSC	differential scanning calorimetry
EBSD	electron backscatter diffraction
ECD	equivalent circle diameter
EDM	electro discharge machining
EDS	energy dispersive X-ray spectroscopy
EIGA	electrode induction-melting gas atomization
FAST	field assisted sintering technique (see also SPS)
fcc	face centered cubic
FIB	focused ion beam
GA	gas atomization
GE	General Electric Company
hcp	hexagonal close packing
HIP	hot isostatic pressing
HT	heat treatment
ICDD	International Centre for Diffraction Data
INT	Institute for Nano-Technology

abbreviation	description
ISM	induction skull melting
LIM	linear intersect method
MA	mechanical alloying
MASC	metal and silicide composite (Nb-16Si-25Ti-2Al-2Cr-8Hf)
MIM	metal injection molding (see also PIM)
MUD	multiples of uniform distribution
OM	optical microscopy
PBR	Pilling-Bedworth-ratio
PCA	process control agent
PIGA	plasma melting induction guiding gas atomization
PIM	powder injection molding
PIP	precision ion polishing
PM	powder metallurgy
PREP	plasma rotating electrode process
RIR	reference-intensity-ratio
RT	room temperature (25 °C)
SC	single crystalline
SE	secondary electron
SEM	scanning electron microscopy
SENB	single edge notched beam
SEPB	single edge pre-cracked beam
SEVNB	single edge V-notched beam
SPS	spark plasma sintering
SX	single crystalline
TBC	thermal barrier coating
TEM	transmission electron microscopy
DF-TEM	dark field transmission electron microscopy
STEM	scanning transmission electron microscopy
TGA-MS	thermo-gravimetric analysis with mass spectrometry
TIP	temperature induced porosity
TZM	titanium zirconium molybdenum (Mo-0.5Ti-0.08Zr-0.03C)
USAF	United States Air Force
VIGA	vacuum inert gas atomization

abbreviation	description
WDS	wavelength dispersive X-ray spectroscopy
XRD	X-ray diffraction
YSZ	yttria-stabilized zirconia

Latin symbols

symbol	description	unit
a	notch depth	m
a_0	diameter of ductile phase	m
$\vec{a}_j, \vec{b}_j, \vec{c}_j$	lattice vectors of phase j	–
A_{1-7}	material constants	–
A_r	molar mass	$\text{g}\cdot\text{mol}^{-1}$
b	Burgers vector	m
B	sample width	m
C_p	heat capacity	$\text{J}\cdot\text{K}^{-1}$
d_g	grain size	m
$d_{g,0}$	initial grain size	m
d_p	powder particle diameter	m
d_{hkl}	plane spacing with Miller indices hkl	m
D	diffusion coefficient	m^2s^{-1}
D_{gb}	diffusion coefficient for grain boundary diffusion	m^2s^{-1}
D_{sd}	diffusion coefficient for self-diffusion	m^2s^{-1}
e	electron charge	C
E	elastic modulus	GPa
E'	apparent stiffness of the system	GPa
E_d	elastic modulus of ductile phase	GPa
E_m	energy of milling	J
f	beam deflection	m
F	applied force	N
F_r	rupture force	N
G	shear modulus	GPa
h	Planck constant	$\text{J}\cdot\text{s}$
HM	Martens hardness	GPa
I_a, I_c	reflex intensities for analyte and corundum reference	–

symbol	description	unit
k	Hall-Petch constant	MPa·m ^{0.5}
k_B	Boltzmann constant	J·K ⁻¹
K	constant	–
K_{Ic}	fracture toughness	MPa·m ^{0.5}
$K_{Ic,c}$... of composite	MPa·m ^{0.5}
$K_{Ic,m}$... of matrix	MPa·m ^{0.5}
K_q	qualitative fracture toughness	MPa·m ^{0.5}
m	strain rate exponent	–
m_e	electron mass	kg
m_d	dry weight in air	kg
m_w	wet weight in water	kg
n	stress exponent	–
n_b	diffraction order	–
N_A	Avogadro constant	mol ⁻¹
p	grain size exponent	–
q	charge	C
Q	activation energy	kJ·mol ⁻¹
Q_c	... for creep	kJ·mol ⁻¹
Q_{gbd}	... for grain boundary diffusion	kJ·mol ⁻¹
Q_{sd}	... for bulk diffusion	kJ·mol ⁻¹
Q_{Ti}^{Nb}	... for diffusion of Ti in Nb	kJ·mol ⁻¹
r_1, r_2	radius of sinter neck	m
R	strength	MPa
R_{eS}	... yield strength	MPa
R_f	... fracture strength	MPa
R_m	... ultimate tensile strength	MPa
$R_{p0.2}$... 0.2 % offset yield strength	MPa
S	aspect ratio	–
S_1, S_2	outer and inner bearing distance	m
S_m	surface created during milling	m ²
t	annealing time	h
T	absolute temperature	K
T_m	absolute melting temperature	K

symbol	description	unit
U_a	acceleration voltage	V
V_f	volume fraction of ductile phase	–
$V_{uc,j}$	volume of the unit cell	m ³
w	width of grain boundary	m
W	sample thickness	m
Y	geometry factor	–
Z	number of atoms per unit cell	–

Greek symbols

symbol	description	unit
α	coefficient of thermal expansion	K ⁻¹
α_K	relative notch depth	–
β	constant	–
γ_s	surface energy	J·m ⁻²
$\vec{\delta}$	error vector	–
ε	strain	–
ε_{ef}	... extreme tensile fiber	–
ε_f	... fracture	–
ε_n	... total	–
ε_p	... plastic	–
ε_t	... true	–
ε_u	... uniform elongation	–
$\dot{\varepsilon}$	strain/creep rate	s ⁻¹
$\dot{\varepsilon}_C$... Coble	s ⁻¹
$\dot{\varepsilon}_{GBS}$... grain boundary sliding	s ⁻¹
$\dot{\varepsilon}_m$... minimum	s ⁻¹
$\dot{\varepsilon}_{NH}$... Nabarro-Herring	s ⁻¹
$\dot{\varepsilon}_s$... steady-state	s ⁻¹
η_{id}	ideal efficiency	–
θ	diffraction angle of positive interference	°
λ	wavelength	m
λ_e	... deBroglie of an electron	m
ρ	density	g·cm ⁻³

symbol	description	unit
ρ_{H_2O}	density of water	$\text{g}\cdot\text{cm}^{-3}$
σ	mechanical stress	MPa
σ_0	intrinsic yield strength	MPa
$\sigma_I, \sigma_{II}, \sigma_{III}$	principal stresses	MPa
σ_c	cleavage stress	MPa
σ_{ef}	extreme tensile fiber stress	MPa
σ_n	nominal stress	MPa
σ_S	sinter stress	MPa
σ_t	true stress	MPa
σ_{trans}	critical transition stress	MPa
σ_{ys}	yield strength	MPa
τ	shear stress	MPa
τ_{max}	maximum shear stress	MPa
τ_P	Peirls shear stress	MPa
τ_y	critical shear stress for yielding	MPa
$\vec{\phi}_p$	volume fraction of phases	–
$\vec{\chi}_0$	overall mole fraction of components	–
$\vec{\chi}_p$	mole fraction of phases	–
$\chi_{ij}/\underline{\chi}$	mole fraction of component i in phase j	–

1 Introduction and Goal

Today's world grows more and more interconnected. Globalization allows for goods produced in one country to be available all over the world. In many cases tourism and trade are no longer limited by national borders. The use of fossil fuel powered engines enabled this development. Beyond the economic driving force for innovation in engines, limited resources and ecological goals, such as lower greenhouse gas and noise emissions, have shifted into focus [5, 6]. A major carrier of transportation of goods and passengers are aircrafts. While first using piston engines with propellers, the invention of the jet engine allowed planes to leap forward in travelling speed, range, and comfort. Modern civil jet engines can be divided into four functional parts (Fig. 1-1), i.e fan, compressor, combustion chamber, and turbine.

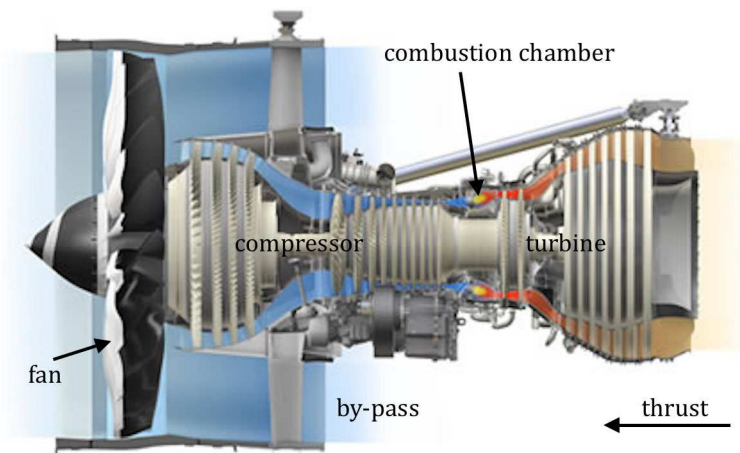


Fig. 1-1: schematic of modern aircraft engine General Electrics GENx-1B [7]; blue indicates cold air (before entering the combustion chamber), yellow the combustion chamber, and red air leaving the combustion chamber through the turbine

The fan – because of which they are also called turbo fan engines – sucks air into the engine. Part of the air (up to 90 %) is accelerated past the compressor intake, i.e. the core engine, as by-pass leading to the majority of thrust in modern turbo fans. The compressor comprises several stages of alternating rotating disks with blades, accelerating the air towards the combustion chamber, and static vanes providing optimized gas flow. Temperatures reach 300 – 500 °C at total compression ratios of 20 – 30; mostly titanium alloys are used in this part to minimize weight [8, pp. 141–143]. In the combustion chamber, fuel and air are burnt leading to the formation of hot gases. The hot gases expand through the turbine, which is similarly constructed as the compressor, accelerating the bladed discs to 10000 – 30000 rpm. Turbine and compressor are connected by a common shaft so that the turbine drives the compressor. The exiting gases behind the turbine produce additional thrust. The turbine inlet temperature, i.e. the temperature at the first turbine stage, surpasses 1400 °C, setting tremendous requirements on the materials used. Nickel-base superalloys are currently in service. To protect them from the hot gases reaching the alloys melting point, thermal barrier coatings (TBC) and complex air cooling systems are applied to reduce the temperature of the blade's core to values where the superalloy still shows sufficient strength (≈ 1100 °C). This cooling, however, leads to inefficiency losses from the ideal performance, as depicted in Fig. 1-2, since cooling air is extracted from the

compressor. Thus, gains in specific core power, i.e. power produced per kilogram weight, can be achieved by either using materials that do not necessitate cooling or that show a lower density.

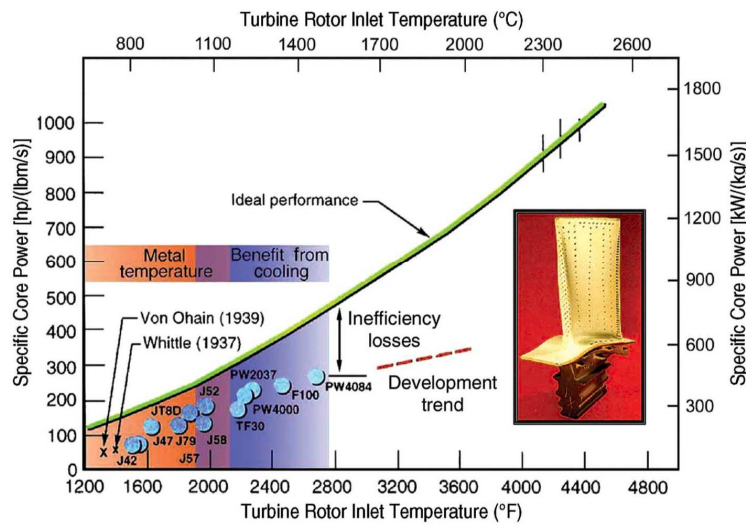


Fig. 1-2: core power versus turbine inlet temperature, blue points show specific engines; the inset shows a turbine blade coated with TBC, modified after [9]

The ideal efficiency η_{id} of a thermo-mechanical process is given by:

$$\eta_{id} = 1 - \frac{T_{low}}{T_{high}} \quad (1-1)$$

The outside temperature T_{low} is mainly dependent on the flying altitude. At cruising altitude, the outside temperature is typically 55 °C lower than at sea level [8, p. 1084]. Technological advances, however, have to be made concerning T_{high} , the turbine inlet temperature (Fig. 1-2). From the beginning of turbo jet engine development, nickel-base superalloys were found to provide the best balance of properties for the hot section of the turbine. In Fig. 1-3 creep strength, and hence operating temperature, is plotted over time for wrought, conventionally cast (CC), directionally solidified (DS), and single crystalline (SC or SX) nickel-base superalloys. DS and SC lead to, respectively, the reduction and elimination of transverse grain boundaries, which act as vacancy sources – necessary for creep deformation – and enable grain boundary sliding. For SC vacancies can only be generated at the components surface hereby increasing the length the of diffusion path. Every step in processing – with fast improvements and saturation over time – brought operating temperatures closer to the melting point at around 1400 °C. However, the really limiting factor is not the melting temperature, but the solvus temperature of the Ni_3Al intermetallic compound, which is the source of the high-temperature strength, at around 1300 °C. The volume fraction starts decreasing already from around 1150 °C, though, leading to reduced creep strength for temperatures above [10].

After the introduction of single crystalline blades at the beginning of the 1980's, improvements have been accomplished by alloying. Most notably, second generation SC alloys contained up to 3 wt% of rhenium, third generation up to 6 wt% rhenium and fourth generation also 2 – 4 wt% ruthenium [8, p. 1099, 11], leading to strong solid solution hardening of the nickel matrix.

Already operating at 85 % of their absolute melting point, requests for new material classes to take the next step towards more fuel-efficient aircraft engines were voiced.

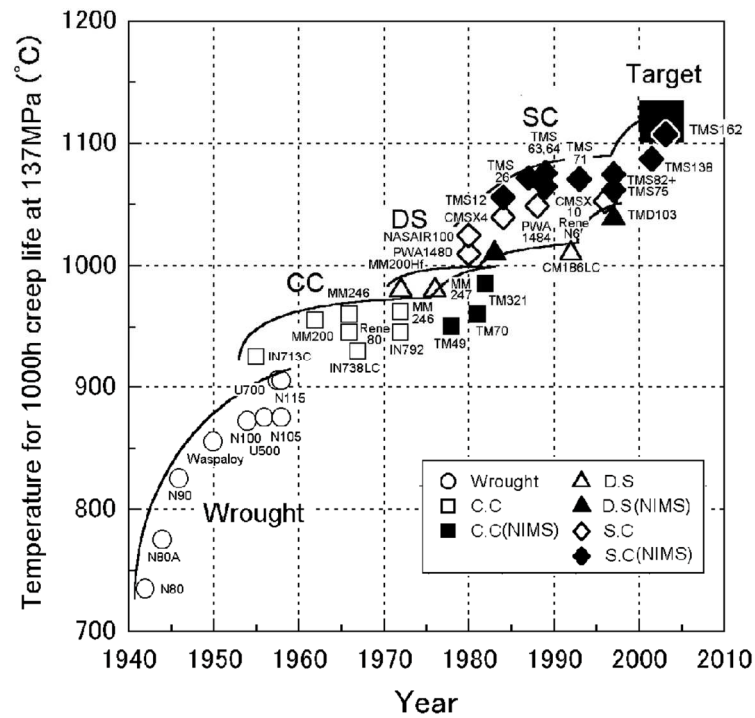


Fig. 1-3: development of creep strength and consequently operating temperature over time [12]

A high melting point that is at least 200 °C higher than for nickel-base alloys is necessary for sufficient high-temperature strength. Next to cobalt-based alloys [13–16], mainly refractory metal-based alloys (using niobium, tantalum, molybdenum, and tungsten) have been the focus of research, as the melting points of the pure elements are all higher than about 2400 °C (Table 1-1). In fact, in the 1950's and 1960's, strong efforts have been made to develop high-temperature alloys based on niobium and molybdenum, which were soon commercialized for aerospace applications [17]. For example, TZM (Mo-0.5Ti-0.08Zr-0.03C, wt%) is still widely used today for high-temperature structural applications in inert atmospheres or vacuum. A major shortcoming of those alloys is the limited oxidation resistance and their relatively high density (Table 1-1).

Table 1-1: refractory elements and their basic properties [17]

Property	Nb	Ta	Mo	W
melting point / °C	2470	2996	2610	3410
density / g·cm ⁻³	8.57	16.6	10.2	19.3
Young's modulus / GPa	110	186	290	358

The recent decades witnessed a renewed interest in niobium- and molybdenum-based materials alloyed with significant amounts of silicon to form intermetallic silicides. The combination of a ductile solid solution with a high-strength intermetallic compound promises a good balance of room temperature ductility or fracture toughness and high-temperature strength. This also improves oxidation resistance and positively reduces density to about $7 \text{ g}\cdot\text{cm}^{-3}$ and $9 \text{ g}\cdot\text{cm}^{-3}$ for niobium- and molybdenum-based alloys, respectively. Especially the low density and the ensuing weight reduction in engine design led to further research of niobium silicide alloys. While molybdenum silicides already provide good strength and adequate oxidation resistance in the ternary alloy with boron, the alloying approach for niobium silicides is more complex. Since the mid of the 1990's, research focused on alloying systems with six or more alloying elements. The most common approach is alloying the binary Nb-Si with titanium, aluminum, chromium, and hafnium to reach a balance of strength, ductility, and environmental resistance [1, 18–33].

To produce turbine components from those new alloys, processing known from nickel-base superalloys may be not directly transferable to the refractory-based composites. Possible elemental segregations [34] and high machining costs are two factors that are tackled by powder metallurgical processing. Very homogeneous microstructures and the ability of near net-shape components, even when castability is rather poor, are major advantages.

The HYSOP project funded by the European Union [35] was started in 2010 to investigate these issues. Next to the oxidation behavior and the development of oxidation resistant coatings [36], the research done within the framework of this project covers the majority of the current work.

Two powder production techniques (mechanical alloying and gas atomization) and two compaction techniques (hot isostatic pressing and powder injection molding) are evaluated in regard to their feasibility to produce the desired microstructures in multi-component niobium silicide alloys. Special attention was paid to the scalability of the processes and to net-shape capable compaction methods. That is the reason why an attritor was chosen to produce mechanically alloyed powders instead of a planetary ball mill, which are more commonly used at lab scale. The characterization of the powders produced, mechanically alloyed as well as gas atomized, is described in chapter 5.

Even though homogeneous microstructures are desirable, powder metallurgy usually also yields very fine grains. This may be detrimental to high-temperature properties. Accordingly, heat treatments are conducted to increase the grain size but also to investigate phase stability at different temperatures (chapter 6).

Mechanical properties essential for high-temperature structural materials such as strength and creep resistance are determined (chapter 7). Lower temperature properties like room temperature fracture toughness and ductile-to-brittle transition temperature, which are important for manageability of components and damage tolerance, are measured for as-consolidated and heat-treated material to be correlated to microstructural peculiarities of different processing routes (chapter 8).

2 Niobium-based Alloys

2.1 The Binary System Nb-Si

In equilibrium the niobium silicon system contains the niobium solid solution (Nb_{ss}) as well as four different intermetallic compounds, Nb_3Si , $\alpha\text{-Nb}_5\text{Si}_3$, $\beta\text{-Nb}_5\text{Si}_3$, and NbSi_2 , whereas the solubility of niobium in solid silicon is negligible (Fig. 2-1) [37]. Nb_3Si forms either through a peritectic reaction from $\beta\text{-Nb}_5\text{Si}_3$ and melt at 1975°C or by eutectic solidification together with Nb_{ss} at 1915°C . The Nb_3Si will decompose in a eutectoid reaction into $\alpha\text{-Nb}_5\text{Si}_3$ and Nb_{ss} , however, reaction kinetics are very slow, leading to retention of Nb_3Si at room temperature (RT) if not annealed for long times below the eutectoid reaction temperature of 1765°C . In zone refined binary Nb-17.5Si (all compositions throughout this work will be given in atomic percent unless specifically stated otherwise) no decomposition was observed even after annealing for 500 h at 1500°C [38]. Alloying additions like Zr [39], Ti [40], or others considerably accelerate the Nb_3Si decomposition. Nb_2Si forms two eutectic systems with silicon solid solution and Nb_5Si_3 at 1395 and 1895°C , respectively. To retain acceptable room temperature fracture toughness, for a structural material only composites containing Nb_{ss} are considered, since toughness of the intermetallic phases as well as of pure Si is very low ($\approx 3 \text{ MPa}\cdot\text{m}^{0.5}$ [41]).

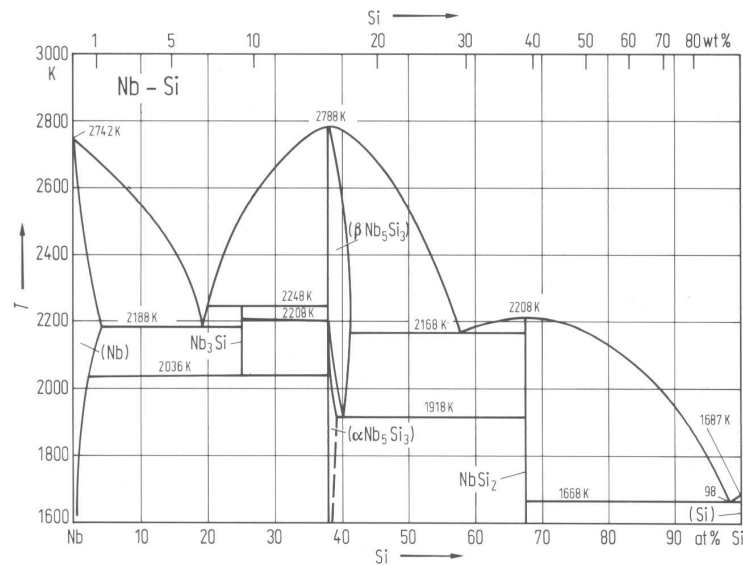
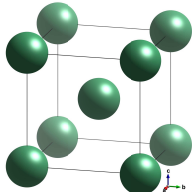
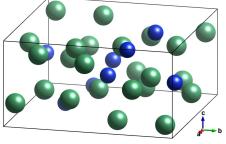
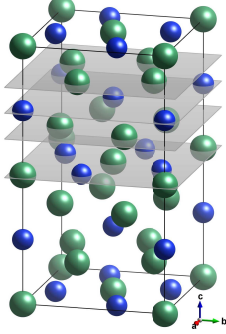
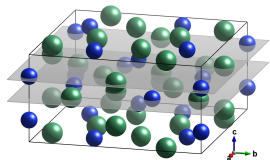
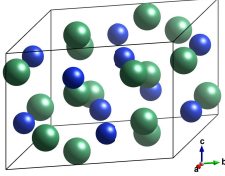


Fig. 2-1: binary phase diagram of the Nb-Si system [42]

High purity niobium shows very high ductility even at cryogenic temperatures [17, p. 34] and is used in radio frequency cavities for particle accelerators due to its superconducting properties. When containing silicon or impurities such as oxygen, nitrogen, hydrogen, or carbon, ductility decreases [43–45, 46, p. 20].

Table 2-1: properties of phases in the Nb-Si system, niobium atoms in green and silicon atoms in blue

	Nb	Nb ₃ Si	α-Nb ₅ Si ₃	β-Nb ₅ Si ₃	γ-Nb ₅ Si ₃
crystal structure (Strukturbericht designation) space group	bcc (A2) Im $\bar{3}$ m 	tetragonal (–) P4 ₂ /n 	tetragonal (D8 ₁) I4/mcm 	tetragonal (D8 _m) I4/mcm 	hexagonal (D8 ₈) P6 ₃ /mcm 
melting point / °C [37]	2467	1975	–	2515	–
Young's Modulus / GPa	105 [52]	–	188 [47] / 344 [49]	300 [49]	146–188 [47]
lattice constant a, c / nm [37]	0.3300	1.023, 0.518	0.6571, 1.1889	1.004, 0.5081	0.7461
density / g·cm ⁻³	8.57 [52]	7.46 [51]	7.11 [50]	7.15 [50]	7.06 [48]

Nb_5Si_3 shows two equilibrium modifications, the low-temperature $\alpha\text{-Nb}_5\text{Si}_3$ and the high-temperature $\beta\text{-Nb}_5\text{Si}_3$. While $\alpha\text{-Nb}_5\text{Si}_3$ is essentially a line compound, the stability range of $\beta\text{-Nb}_5\text{Si}_3$ is from 37.5 to 40.5 % Si. Stoichiometric $\beta\text{-Nb}_5\text{Si}_3$ will transform to $\alpha\text{-Nb}_5\text{Si}_3$ at 1935 °C. While both phases have the space group $I4/mcm$ (140), lattice constants vary strongly (Table 2-1). A third modification, the hexagonal $\gamma\text{-Nb}_5\text{Si}_3$, is meta-stable. It may be stabilized by alloying additions such as Hf [53] or Ti [54], which form a 5-3 silicide with the same crystal structure (Ti_5Si_3 and Hf_5Si_3), but also by interstitials such as carbon [55].

While the Nb_3Si phase has a lower high-temperature strength compared to Nb_5Si_3 [2], composites comprising Nb_{ss} and Nb_5Si_3 as well as Nb_3Si have been subject of considerable research. The binary system has already shown very good high-temperature strength properties combined with low density and sufficient fracture toughness [20, 56]. Unfortunately, the binary system does not reach the needed environmental resistance at elevated temperatures [57].

Refractory metals in general suffer from poor oxidation resistance at high temperatures [46, p. 34]. Especially at intermediate temperatures (above 800 °C), refractory metals suffer from “pesteing”, which is a term for very fast, catastrophic oxidation. For molybdenum and tungsten this is characterized by the formation of a volatile oxide (MoO_3 and WO_3 , respectively). In the case of niobium, fast oxygen diffusion along grain boundaries leads to oxidation and subsequent powderization of the grain structure. At high temperatures, molybdenum silicon composites containing Mo_{ss} and a silicide phase, especially when alloyed with boron, can form a borosilicate glass layer protecting the substrate [58]. This is based on (i) initial MoO_3 evaporation and (ii) subsequent formation of boron doped silicon oxide from the silicide, thus, leading to a closed borosilica layer protecting the substrate. The same effect is not available for the niobium silicon system, because the niobium oxide formed is not volatile. Going through several oxidation stages (NbO and NbO_2) niobium forms voluminous Nb_2O_5 [59, 60] with a Pilling-Bedworth-ratio (PBR) of 2.7 [61]. This means, that niobium by itself cannot form a protective coating and that even if a closed silica layer could be formed, an Nb_{ss} grain below would break the protective layer by the formation of an oxide, which is porous and 2.7 times larger than the metal. An ideal Pilling-Bedworth-ratio would be in the range of 1–2, which would result in slight compressive stresses in the oxide scale [62]. The best protective oxide coating known, Al_2O_3 (PBR = 1.28), lies well in that range. However, Cr_2O_3 (PBR = 2.05) and SiO_2 (PBR = 2.15)[63] also form protective coatings suggesting that this limit is not the only decisive factor. For a PBR below 1, tensile stresses occur in the scale and cracking is observed such as for MgO (PBR = 0.84). Hence, alloying efforts have focused on preventing the formation of niobium pentoxide in favor of an adhesive oxide.

2.2 Alloying Additions

Two main alloying efforts can be distinguished in literature. One of them is to further increase the melting point and improve the high-temperature strength. Along with that, the stronger 5-3 silicide is to be stabilized over Nb_3Si (in the following, intermetallic compounds will be represented by their binary NbSi-counterpart, independent of the actual amount of other components, e.g. Ti_5Si_3 will be designated $\gamma\text{-Nb}_5\text{Si}_3$ as both have the same crystal structure). Main alloying candidates for this first effort are other refractory metals such as molybdenum, tungsten, tantalum, or hafnium. Those elements are known as solid solution strengtheners [20] for the niobium phase. Mainly the groups around Hanada [55, 64–67] and Varma [68–71], but

also Chattopadhyay et al. [72] and Xiong et al. [73], use this alloying scheme. This results in higher strengths at elevated temperatures and increased room temperature fracture toughness to $10 \text{ MPa}\cdot\text{m}^{0.5}$ compared to $6 \text{ MPa}\cdot\text{m}^{0.5}$ typically reached for eutectic Nb-Si [74]. Since niobium shows the lowest density of the refractory metals, those additions unfortunately will also increase the composites density, which usually is a major advantage of niobium silicides.

Even though essentially every alloying element improves on the oxidation resistance of pure niobium or binary niobium silicon, the second alloying concept specifically aims towards oxidation resistance. Researchers agree that niobium silicides cannot be used without additional protective coating [20, 75, 76] just like current nickel-base superalloys. However, a higher oxidation resistance than provided by the aforementioned alloys is required, ideally with some self-healing capacity in case of spallation of the protective coating [77].

The main candidates for alloying have since been titanium, aluminum, and chromium. While titanium, in contrast to the two latter elements, will not form a passivating oxide layer, it slows down oxidation considerably [19, 20, 57, 78] and beneficially reduces the materials' density.

2.2.1 Titanium

Most research devoted today on niobium silicides is either done in the binary system or on materials highly alloyed with titanium (between 10–40 %). Titanium will substitute for niobium in the bcc A2 phase completely above the allotropic transformation temperature of titanium at $882 \text{ }^\circ\text{C}$ due to their similar atomic radii of 140 and 145 nm, respectively. Even at $570 \text{ }^\circ\text{C}$ about 50 % of titanium is still solvable in the A2 Nb phase.

Unlike Sekido et al. [40], Zelenitsas and Tsakiroopoulos [33] found no beneficial effect of titanium on the kinetically retarded decomposition of Nb_3Si leaving a two-phase $\text{Nb}_{ss}\text{-Nb}_3\text{Si}$ microstructure after a $1500 \text{ }^\circ\text{C}/100 \text{ h}$ heat treatment for Nb-18Si-24Ti. Sekido et al. also found a strongly retarded decomposition after zone refinement, which they attribute to reduced impurity levels – probably interstitials such as carbon, nitrogen and oxygen – after the directional solidification. Bewlay et al. [77] in contrast even suggest a stabilization of Nb_3Si by high titanium concentrations. This is backed by ternary phase diagram evaluations showing the presence of the $\text{Ti}_3\text{Si}/\text{Nb}_3\text{Si}$ phase below the eutectoid decomposition temperature of the binary system for titanium concentrations above 20 % (Fig. 2-2). In this evaluation the $\beta\text{-Nb}_5\text{Si}_3$ phase field is missing, which should be shown there at least for the binary niobium silicon side above $1935 \text{ }^\circ\text{C}$. At the 5-3 silicide concentration (37.5 % Si), $\alpha\text{-Nb}_5\text{Si}_3$ shows a transition into $\gamma\text{-Nb}_5\text{Si}_3$ at around 30 % of titanium (at $1100 \text{ }^\circ\text{C}$) as shown in Fig. 2-3.

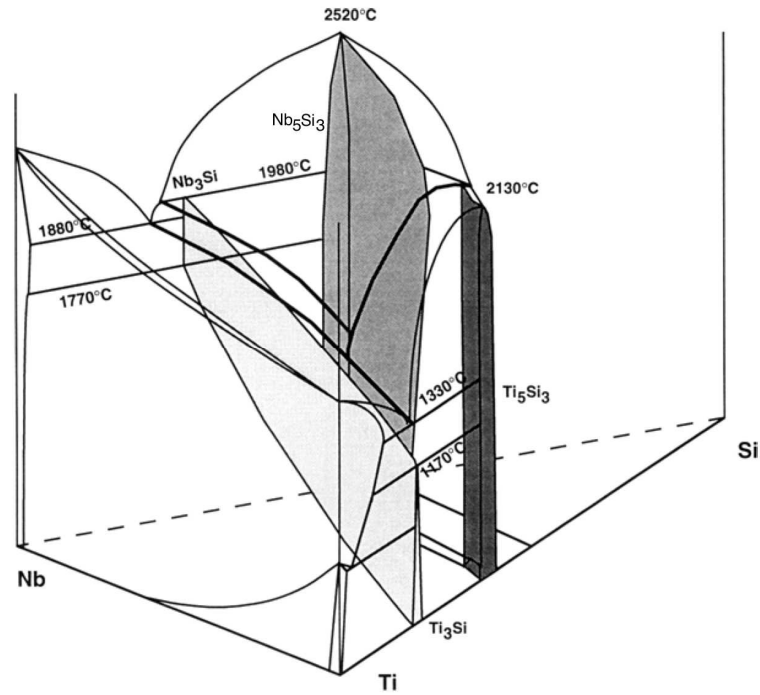


Fig. 2-2: proposed ternary phase diagram Nb-Si-Ti up to 37.5 % of silicon [54]

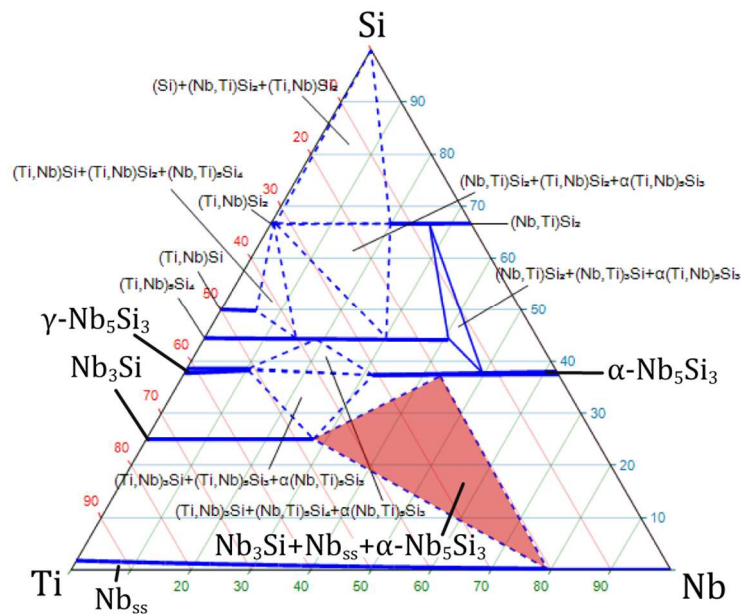


Fig. 2-3: isothermal section at 1000 °C of the ternary Nb-Si-Ti system modified after [79] with the three phase field typically researched highlighted in red

2.2.2 Aluminum

Aluminum is typically added for several reasons. It inhibits the formation of Nb_5Si_3 and will lead directly to a composite comprising Nb_{ss} and Nb_5Si_3 [33, 78]. Zhao et al. found it to stabilize $\beta\text{-Nb}_5\text{Si}_3$ down to temperatures as low as 1000 °C. Especially in non-equilibrium microstructures as produced by casting, $\beta\text{-Nb}_5\text{Si}_3$ is found at room temperature [80]. Also, it improves oxidation resistance significantly [3, 20, 78, 80] (Fig. 2-4). In typical niobium-based alloys, however, an

aluminum content below 10 % is far from sufficient to form a protective Al_2O_3 layer such as in NiAl or FeAl intermetallic compounds [81, 82]. Linear oxidation dominates after a few hours. In fact, even intermetallic Nb_3Al with 25 % of aluminum shows catastrophic oxidation [83].

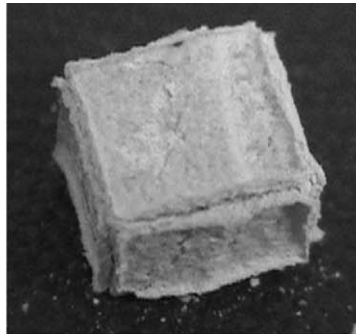


Fig. 2-4: sample of Nb-18Si-24Ti-5Al after oxidation at 800 °C for 100 h [78]

2.2.3 Chromium

Another element mainly added for oxidation resistance is chromium [1, 3, 78]. When added in small amounts it will – just like aluminum – destabilize the Nb_3Si phase [33] in favor of the stable Nb_5Si_3 and increase room temperature strength by solid solution hardening [84]. For amounts higher than 5 % the niobium-rich C_{14} Laves phase NbCr_2 will form [3, 33]. The oxidation resistance of this phase is significantly higher compared to the silicides or the solid solution, improving the composite's environmental resistance [3], but also its high-temperature strength; fracture toughness and ductility on the other hand are reduced [84, 85]. Both effects are mainly a result of the decreasing volume fraction of niobium solid solution as the Laves phase is formed. Recently, some research on the ternary system Nb-Si-Cr with high concentrations of chromium (more than 20 %) has been done [86–90].

2.2.4 Hafnium

Hafnium is usually added because it is a very effective solid solution strengthener [3] (compare section 2.2).

While arc-melted or directionally solidified material will typically end up with only minor contaminations by oxygen, in the particular case of using powder metallurgy, hafnium also acts as a very strong getter for the inevitably higher oxygen content. The oxygen solubility in niobium is very high (≈ 6 at% [60]) and leads to severe embrittlement [43, 46, p. 19]. Hence, it is of interest to add an element with a lower chemical potential than niobium to react with the oxygen. It is assumed, that small amounts of hafnium oxide are less detrimental to properties than solved oxygen in the solid solution.

Furthermore, together with aluminum and chromium, hafnium will destabilize the Nb_3Si and lead to a composite comprising Nb_{ss} and 5-3 silicides (Fig. 2-5). Just like titanium, hafnium forms the hP16 5-3 silicide as well [53, 91]. Consequently, it shows high solubility in the γ - Nb_5Si_3 phase [3].

The three roles as solid solution strengthener, oxygen getter, and 5-3 silicide stabilizer make hafnium an important element in alloy design – especially for powder metallurgically produced niobium silicides.

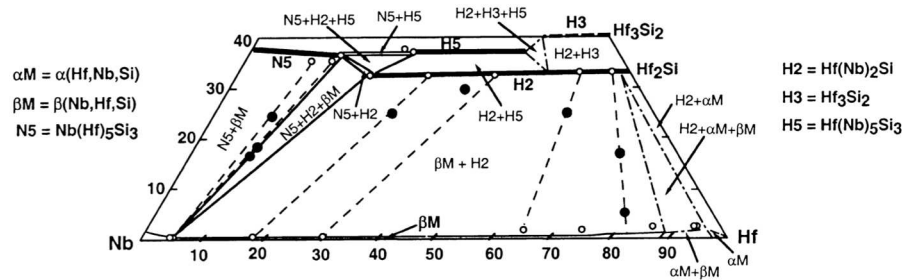


Fig. 2-5: isothermal section at 1500 °C of the ternary Nb-Si-Hf system [53]

2.2.5 Others

Other potential alloying elements include tin and germanium. Tin was reported to have a beneficial effect on the oxidation resistance, especially the pesting regime. Bewlay et al. [77] found that pesting is practically inhibited with relatively low additions of 1.5 % tin to a six-element alloy. Higher tin additions of up to 8 % were tested by Knittel et al. [92–94] (compare Fig. 2-7 and Fig. 2-8, showing an improvement of oxidation resistance mainly by the formation of an $A_{15}Nb_3Sn$ phase and the subsequent reduction in solid solution content. Additionally, tin was enriched at the oxide layer/substrate interface acting as a diffusion barrier for oxygen. This enrichment, however, leads to the formation of pure tin, which melted at oxidation temperatures. This effect was also observed by Bachmann [57]. Germanium was also added for improved oxidation behavior. Li and Tsakiroopoulos added up to 10 % of germanium to different base alloys [95–97].

2.2.6 Multi-Element NbSi-Alloys

Based on the mentioned advantages and disadvantages of possible alloying elements, Bewlay at General Electric (GE) developed the six-element alloy Nb-16Si-25Ti-2Al-2Cr-8Hf, also known as MASC (Metal And Silicide Composite). A typical microstructure of a similar, directionally solidified alloy can be seen in Fig. 2-6.

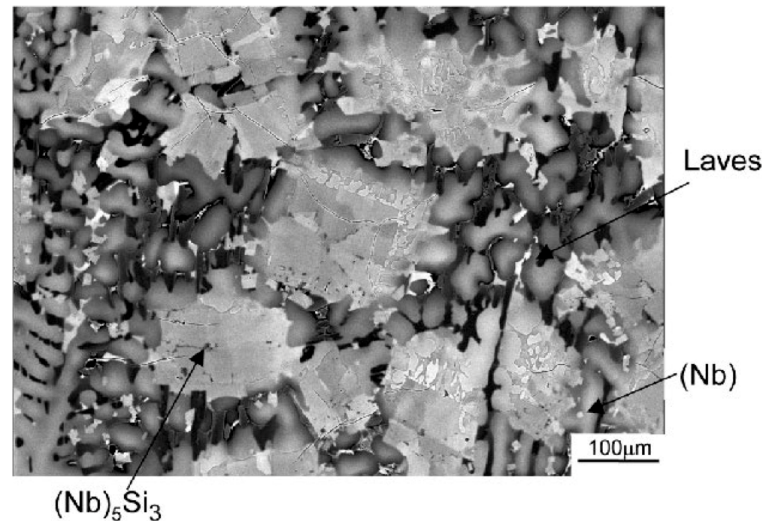


Fig. 2-6: typical microstructure of a directionally solidified multi-component alloy (Nb-16Si-19Ti-2Al-13Cr-4Hf-4B, transverse section) [77]

Besides the Bewlay group at GE Global Research, M.D. Mendiratta and D.M. Dimiduk from the United States Air Force (USAF) research lab have been the major driving forces of today's research on the topic. The reader is also advised to some review articles from this circle [3, 77, 98, 99].

Another substantial effort has been made by the group of P. Tsakirooulos from the University of Sheffield in conjunction with Rolls Royce, aiming at revealing the influences of each alloying element on the resulting microstructure, oxidation resistance (Fig. 2-7), and possible synergies between elements. Some recent works can be found here [95–97, 100–103].

Most of today's research on multi-element niobium silicides is based on variations of the MASC composition. Thus, also in the present work the elements composing the MASC alloy were maintained with some deviation. The silicon content was increased to 20 % to increase the silicide volume fraction and potentially also increase high-temperature strength. The amount of aluminum and chromium were increased to 6 and 3 %, respectively, to stabilize the tetragonal Nb_5Si_3 modifications and improve oxidation resistance. Hafnium partitions mostly to the γ - Nb_5Si_3 and will facilitate its formation at the cost of the more desirable α - Nb_5Si_3 . Its role as getter element for oxygen can be maintained at a lower content of 4 %.

In the following, some property data for typical niobium silicide-based composites from literature is presented. Fig. 2-7 (lower is better) shows isothermal oxidation data at 800 °C illustrating the beneficial effects of several alloying elements on oxidation behavior as mass gain over time is decreasing. Within the HYSOP project [35] oxidation behavior of the alloy composition used in the present work, Nb-20Si-23Ti-6Al-3Cr-4Hf, was determined in isothermal oxidation tests at 1100 °C for arc-melted as well as powder metallurgically (PM) produced material (hot isostatic pressing of gas-atomized powder). Fig. 2-8 compares the results to MASC alloy and a MASC alloy modified with 4% of tin. The fine microstructure of the PM alloy is beneficial to the oxidation resistance compared to arc-melted material.

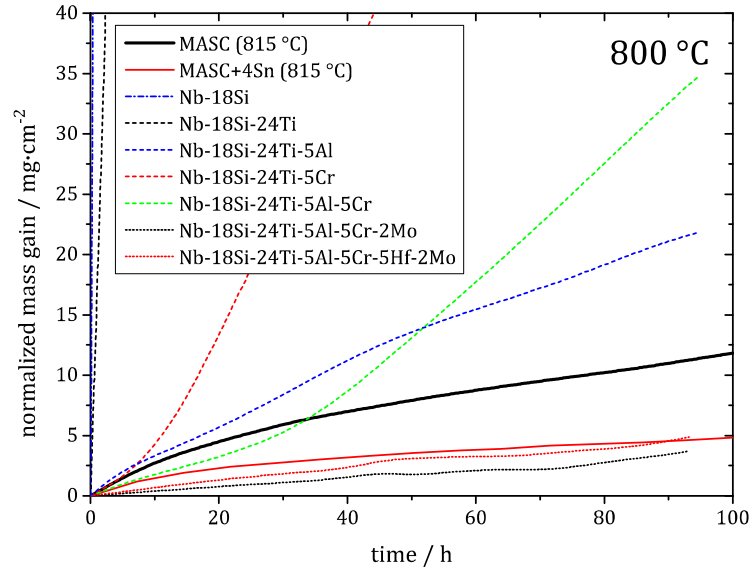


Fig. 2-7: data of normalized mass gain over isothermal oxidation time for different arc-melted niobium silicide-based composites at 800 °C; dash-dotted line: Bachmann [57], dashed lines: Zelenitsas and Tsakiroopoulos [78], dotted lines: Geng et al. [104], solid lines: Knittel et al. [92] (copper crucible induction melted)

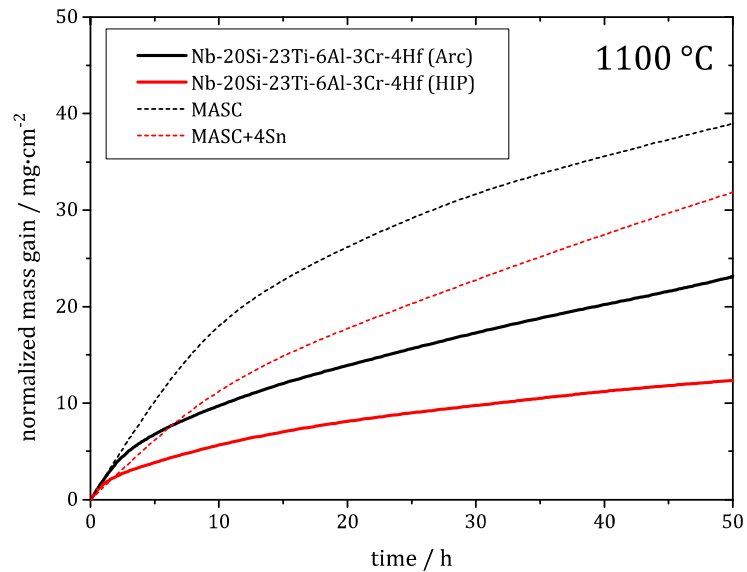


Fig. 2-8: data of normalized mass gain over isothermal oxidation time for different niobium silicide-based composites at 1200 °C; solid lines: data produced within the HYSOP project for arc-melted material and samples produced via hot isostatic pressing of gas-atomized powder, dashed lines: Knittel et al. [92] (copper crucible induction melted)

Creep resistance as part of high-temperature strength is presented as a minimum creep rate over stress plot in Fig. 2-9 (to the bottom right is better). At a testing temperature of 1200 °C the niobium silicide composites show their potential of surpassing nickel-base superalloys.

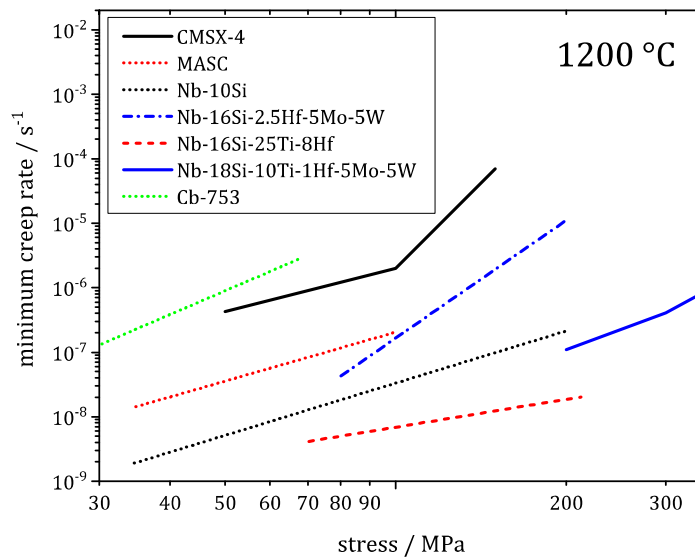


Fig. 2-9: creep data as minimum creep rate over applied constant stress for different niobium silicide-based composites as well as CMSX-4 (second generation single crystal nickel-base superalloy) and Cb-753 (commercial niobium-base alloy, Nb-5V-1.25Zr) at 1200 °C; solid lines: data produced during the ULTMAT project [105], dashed line: Bewlay et al. [1], dotted lines: Subramanian et al. [106], dash-dotted line: Fujikura et al. [107]

3 Powder Metallurgy

Today, turbine components are typically produced by investment casting and subsequent directional solidification of nickel-base superalloys. Oftentimes, sample material for new alloy development studies, such as silicide-based alloys, is produced by arc melting or plasma melting. Using this method, a button is produced from the pure elements and sufficiently often remelted (3 – 8 times) to ensure chemical homogeneity. Not considered in those cases (and rightfully so) is the sometimes high viscosity of the melt and its insufficient mold filling ability (Fig. 3-1), which would be necessary to produce actual parts by cast metallurgy and investment casting. Bewlay et al. found that casting defects like pores and cracks could not be removed by hot isostatic pressing treatments [98]. Hence, production routines from today's turbine materials may not be directly usable for next-generation materials such as niobium silicide alloys. Powder metallurgy could be a viable alternative and allows producing compacts from pre-alloyed powder by various means of shaping. Since powder metallurgy offers a manifold of processes to produce and treat powders and to compact them, this chapter will focus only on those processes that have been applied previously to niobium silicide-based alloys or are used in this work. For an extensive overview of powder metallurgy techniques the reader is referred to works by Schatt [108], German [109], or Upadhyaya [110].



Fig. 3-1: trial to drop cast Nb-20Si-23Ti-6Al-3Cr-4Hf into a cylindrical copper mould by arc-melting; only few drops reached the bottom of the mold; using the same technique, drop casting of molybdenum silicides with an even higher melting point was possible

3.1 Powder Production

Processes for powder production can be put into four different categories: (i) electrolytic deposition, (ii) chemical reaction/decomposition, (iii) atomization of molten metals, and (iv) mechanical processing of solids. Even though electrolytic deposition is possible for up to 60 metals, significant use is only reported for fused-salt electrolysis of tantalum and copper deposition from aqueous electrolytes [110].

Solid metal compounds can also be directly deoxidized with hydrogen or carbon, i.e. carbon monoxide, as a reducing agent. Using this technique, iron, nickel, or molybdenum ores can be transformed into a metal sponge that can easily be broken into powder. This method accounts for about half the iron powder produced [108]. Both methods produce pure elemental powders, which may, however, be used for the mechanical processing of solids, i.e., amongst others,

mechanical alloying in a ball mill. There are essentially two ways to produce pre-alloyed powder: atomization and mechanical processing, which are described in more detail as follows.

3.1.1 Gas Atomization (GA)

Next to – in some cases experimental – setups, where centrifugal forces are used to disperse the melt into small droplets, e.g. plasma rotating electrode process (PREP), the most common method is atomization of metal melt in a gas or water jet. Water and air can only be used for materials that are insensitive to oxygen contamination or where the oxide scale is easily removed afterwards. Water jet atomization is mainly used for iron and copper alloys, while air is used for production of zinc or aluminum powders [110]. For materials sensitive to oxidation, an inert gas such as argon is used instead of air. In all of these processes a melt stream is dropping through the opening of a high pressure (20–60 bar), high flow rate (10–40 m³·min⁻¹) ring nozzle. Since the refractory metals are very prone to oxygen pickup, only inert gas atomization is a viable option. Three different methods in producing the melt stream shall be introduced in the following (Fig. 3-2).

Vacuum inert gas atomization (VIGA) uses a ceramic crucible that is inductively heated to produce the entire melt volume to be atomized in one batch. Either by pouring the melt into a tundish via tilting or by simply removing a stopper rod from the bottom of the crucible, the whole melt volume will drop through the nozzle. This method is used for industrial production of batches of up to several tons. Small ceramic inclusions in the particles cannot be averted and melts that tend to react with ceramic crucibles (mostly alumina or yttria stabilized zirconia), such as titanium but also niobium alloys [111], cannot be produced by VIGA at all. In those cases, electrode induction-melting gas atomization (EIGA) is used instead.

For EIGA, a pre-alloyed rod of the desired material is continuously moved through an induction coil, while the outer layer of the conical tip is liquefied into a steady melt stream by the high frequency magnetic field. The atomization takes longer and thus uses higher amounts of argon. Also batch sizes are considerably smaller than for VIGA. However, since the material is melted in high vacuum with the melt having no contact to any surface, powders with very low contamination levels can be produced.

The third technique is called plasma-melting induction guiding gas atomization (PIGA). A plasma torch is used to melt the material in a cooled copper crucible until the bottom seal is removed to release the melt into the nozzle very much like for VIGA. This combines the ease of alloying in the atomization chamber known from VIGA with the low contamination of the EIGA process. However, due to the complexity of the setup and the corresponding high cost, this technique is not very common. [108, 110]

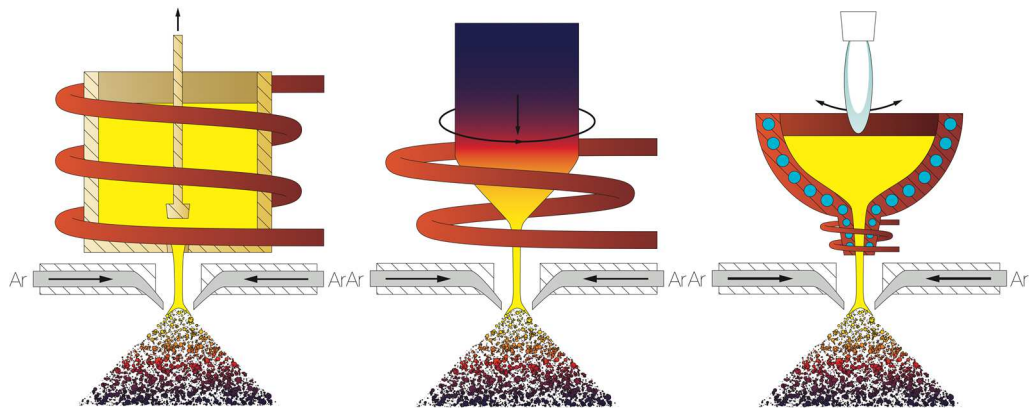


Fig. 3-2: schematic of the VIGA (left), EIGA (middle), and PIGA (right) processes

Gas atomization has rarely been used for production of niobium silicide based alloys. Bewlay et al. [98] atomized bulk material produced by induction skull melting (ISM) of the composition Nb-12.5Si-22.5Ti-2Al-6Cr-2Hf-3Fe-5Ge-1.2Sn by presumably EIGA and PREP. Even though the composition is clearly hypoeutectic, large silicide particles were present in both batches hinting at segregations in the original ingot. Only the PREP powder was consolidated by hot extrusion. As a starting powder for direct laser fabrication (section 3.2.6), Dicks et al. [21] atomized Nb-22Si-26Ti-2Al-6Cr-3Hf. Jéhanno et al. [23] used EIGA to produce Nb-20Si-24Ti-2Al-5Cr-3Hf powder from cold isostatically pressed (CIP) and sintered elemental powders. Subsequently, the GA powder was hot isostatically pressed (HIP) and hot extruded. This also demonstrates the expenditure needed to produce the electrodes for the EIGA process if the reactivity of the alloy does not allow use of the VIGA process.

3.1.2 Mechanical Alloying (MA)

Mechanical alloying (MA) is a non-equilibrium process in which elemental powders and milling balls are enclosed in a milling vial. Either by movement of the vial itself or by means of a rotor inside the vial, the balls perform a motion relative to the vial, leading to different kinds of collisions [112]:

- between balls and powder particles
- between balls, the powder particles, and the vial wall
- between powder particles

As a result of those events powder particles are deformed plastically. This can lead to different particles becoming cold welded together or particles being broken up (Fig. 3-3). At the beginning of milling, welding is the dominating process leading to an increase in mean particle size. With increasing milling duration dislocation hardening leads to a decrease in the tendency for welding and an increase in the tendency for breaking. The particle size is decreasing. At some point, for a given set of milling parameters, cold working reaches a saturation, and welding and breaking are in equilibrium. The particle size reaches a steady-state.

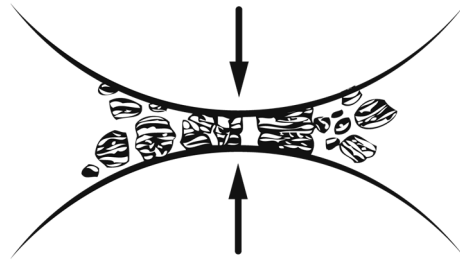


Fig. 3-3: schematic of ball-powder-ball collision early during MA showing layered structure of elements by cold-welding and breaking, after [113]

As for the microstructure of the particles, the welding leads to the formation of a layered structure, if ductile particles are milled. The layers become finer until they are no longer distinguishable by optical microscopy and a solid solution is formed. This is even possible for compositions outside of equilibrium solubility; hence super-saturated solid solutions can emerge [114].

If one of the components is of brittle nature the particles will break up and become enclosed in the ductile components. For sufficient milling times, this as well might lead to the formation of a solid solution. E.g. for mechanically alloyed oxide dispersion strengthened steels, the particle size of oxide particles may not only be reduced to the nanometer scale, but also the formation of nano-clusters was observed where a mixed oxide was produced by high-energy ball milling [115–117].

During the dissipation of kinetic energy of the balls, the process temperature increases. The high density in defects from the deformation together with short diffusion paths and elevated temperatures may lead to inter-diffusion through the fine lamellae and the formation of compounds such as intermetallics. The formation of amorphous powders is also possible. Whether amorphous particles, a super-saturated solid solution, or intermetallic compounds will form, strongly depends on the materials system as well as the processing parameters such as milling time, ball-to-powder weight ratio, and temperature [118, 119].

One advantage of this process is that even for material systems where during melt processing the formation of a continuous solid solution matrix is not possible, with this process a brittle phase can precipitate from the super-saturated solid solution.

Sometimes, very long milling durations are necessary to reach a homogeneous distribution of elements. This is not always practical, as other factors need to be taken into account. Most importantly, the longer the milling time the higher the amount of contamination. (i) The vial wall and especially the milling balls are subject to abrasion leading to increasing content of – in most cases – iron and, in case hard metal balls are used, tungsten carbide and cobalt. (ii) Powder particles have a very high surface to volume ratio. The formation of new surfaces during breaking of powder particles does not only make cold welding possible but also enables the reaction with gaseous impurities in the atmosphere of the vial. Even when working in protective atmosphere, small amounts of oxygen or nitrogen cannot be averted. (iii) With increasing milling time, the amount of powder sticking to the vial wall may increase leading to a reduced powder yield.

The use of milling agents or process control agents (PCA) helps the powder yield, but leads to even higher contamination. A PCA will reduce the tendency of freshly generated surface not only to cold weld to other particles, but also to balls and vial wall by wetting the particles surface after creation. Furthermore, it helps with the reduction of particle size. The Rehbinder effect correlates the amount of energy necessary to crush particles ΔE_m with the surface formed during that process ΔS_m .

$$\Delta E_m = \Delta S_m \cdot \gamma_s \quad (3-1)$$

The surface energy γ_s is reduced by the wetting, leading to reduced milling times at constant milling power for particle size reduction [108].

Typical milling agents would be stearic acid, ethanol, or heptane [119, 120]. However, during the high energy milling process the agent's molecules may be broken and incorporated into the powder particles leading to contamination with the components of the agent, i.e. carbon, hydrogen, and oxygen. Hydrogen normally would leave the component during compaction, but carbon and oxygen tend to form carbides and oxides, respectively. Hence, it is desirable to work without PCA if possible.

Different kinds of mills can be distinguished based on the amount of powder that is supposed to be produced. In general, the larger the vial and powder volume is, the slower the movement of the mill and the longer the milling time. SPEX® shaker mills/high energy ball mills are suitable for up to 10 g of powder and provide very short milling times by a three-dimensional, vibrational movement. Planetary ball mills consist of a rotating support disk with milling vials positioned on it, executing an opposite rotation, driven by a planetary gear. The superposition of centrifugal forces from disc and vial leads to milling balls rolling along the vial wall and then moving freely across the diameter to hit powder in a ball-powder-wall collision on the other side (Fig. 3-4). The milling intensity is lower than for the SPEX mill, but powder amounts up to several 100 g are possible. Most prominent manufacturers are the German companies Retsch GmbH and Fritsch GmbH.

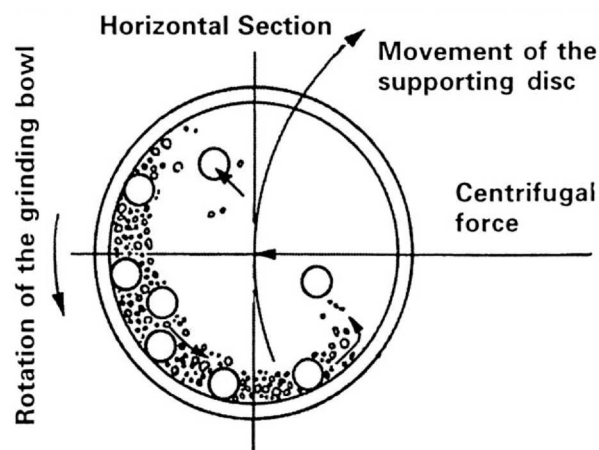


Fig. 3-4: schematic of ball motion in the vial of a planetary ball mill [119]

Attrition mills traditionally feature a vertical drum with an impeller to accelerate the balls to perform collisions with the powder. Newer designs, e.g. by Zoz GmbH (compare Fig. 4-1),

implement a horizontal drum together with double walled cooling for heat dissipation and sealings for milling under inert atmosphere. Attritors can mill up to several tens of kilograms of powder per batch, and range from laboratory size to commercial production units.

Standard commercial ball mills operate by rotation of a large (> 1 m) horizontal drum just below the speed, where the milling balls would be pinned to the wall by centrifugal forces. Gravity will lead to collision when the balls drop on the powder. Batch sizes of several tons are possible [113, 119].

Milling balls and vials are usually made from unalloyed steel (100Cr6), tool steel, or stainless Cr-Ni-steels, but – depending on the application – may also be made from hard metal (WC-Co), yttria-stabilized zirconia (YSZ), silicon nitride, agate, or other specifically chosen alloys or ceramics.

Several authors have previously reported on mechanical alloying of niobium silicides. In most cases a SPEX shaker mill or planetary ball mill were used which resulted in limited powder volumes. The alloys investigated are mostly limited to the binary system and oftentimes, to the intermetallic compound compositions specifically, i.e. Nb_3Si , Nb_5Si_3 , and NbSi_2 . In these cases, intermetallic compound formation was often observed prior to heating during consolidation. This was reported by Liu et al. [72] and Morris and Morris [73] in the Nb-Si system, who found the formation of NbSi_2 in an Nb-66.6Si mixture to take place for milling times of only 3 h, depending on the ball-to-powder weight ratio. For longer milling times, the dissolution of the compound and amorphization of the powder were reported. Perdigão et al. [121, 122] produced amorphous powder by high-energy ball milling of Nb-16Si, which, after compaction, yielded a desirable microstructure of homogeneously distributed Nb_5Si_3 particles in a continuous niobium solid solution matrix. Kajuch et al. [74] and Kumar and Mannan [75] looked into the Nb_5Si_3 compound formation in Nb-37.5Si and found that specifically the intervallic milling with intermediate cooling to room temperature led to the formation of Nb_5Si_3 precipitates from the super-saturated solid solution. Kumar and Mannan were also successful in forming Nb_5Si_3 directly by milling of Nb-14Si without the subsequent heat treatment that was necessary by Perdigão. However, milling of Nb-10Si led to amorphization without compound formation showing the sensitivity of the process to subtle changes. Several other researchers [120, 123–128] have milled binary Nb-16Si and Nb-18Si in planetary ball mills without observing the formation of intermetallic compounds. Yu et al. [129–132] produced mechanically alloyed powder of binary Nb-Si modified with 2 % of iron and silicon contents between 3 and 16 %. Unfortunately, details on the process and the properties of the powder are omitted. Gang et al. [133] produced vanadium-modified Nb_5Si_3 powder. Beyond that, more promising, highly alloyed niobium silicides with 6–10 alloying elements have not been produced by mechanical alloying, yet.

3.2 Compaction

To produce compact materials from powders, a combination of shaping and sintering is necessary. Traditionally, shaping is done by cold pressing, producing a green part of loosely connected powder, followed by sintering under vacuum or inert atmosphere. Newer methods combine both steps such as hot pressing, hot isostatic pressing, or spark plasma sintering. All processes have the connection of powder particles and removal of porosity by sintering in common. In an ideal system, neck formation between particles in contact is driven by the

difference in excess surface energy between powders and a pore-free compact. This consideration leads to the Laplace equation:

$$\sigma_s = \gamma_s \left(\frac{1}{r_1} + \frac{1}{r_2} \right) \quad (3-2)$$

The equation attributes a stress σ_s to curved surfaces with the principal radii r_1 and r_2 and the surface energy γ_s . For concave and convex surfaces this stress will be tensile and compressive, respectively. Material flow from convex to concave surfaces ensues. The redistribution of material along the surface will not reduce the porosity, though. Grain boundaries play a decisive role as vacancy sinks and the resulting convergence of particle centers. Material flux is determined by diffusion through the volume or along the surface; in some cases also evaporation/condensation, and viscous or plastic flow. In real systems, especially e.g. in case of reactive sintering, the compositional gradient may pose a much more dominant driving force than the surface energy. Normally elevated temperatures are necessary, often in conjunction with external pressure (see 3.2.1) [134, p. 2628].

3.2.1 Hot Pressing

Hot pressing refers to the application of uniaxial pressure on a powder volume in a heated die. The pressure leads to yielding of the powder particles at the contacts resulting in an acceleration of the sintering process especially in the early stages. The mechanisms at hand are comparable to power-law creep and diffusional creep (sections 7.2 and 7.2.3) depending on the stress in the contact area of the particles [134, p. 2646].

The die and punches are made from high-temperature materials such as TZM (titanium-zirconium-molybdenum), ceramics, or carbon. Because most of those materials are sensitive to oxidation at high temperatures (including the powders) hot pressing is performed in vacuum or under protective atmosphere [135, p. 646]. Typical pressures are 50 MPa. Heating is done conductively, inductively, or by radiation. Because of long cycle times, cold pressing in combination with pressureless sintering will be favored, whenever possible [108, p. 135]. For materials that will not sinter to full density or in laboratory environments, hot pressing is a quite common method for powder compaction. Several researchers have employed it for niobium silicide alloys. Yu et al. [129–132] and Ma et al. [125] consolidated binary alloys with silicon contents of 3 – 16 % by reactive hot pressing. Yu et al. substituted niobium with 2 % of iron, though. Wang et al. [120, 123, 124] and Kimura et al. [128] consolidated mechanically alloyed binary Nb-16Si and Nb-18Si, respectively.

3.2.2 Spark Plasma Sintering (SPS)

Spark plasma sintering, also known as field assisted sintering technique (FAST), is a rather novel technique with very short processing times. Essentially, SPS is a variant of the hot pressing process, where the heating is applied by a pulsed electrical current (millisecond regime) through the powder sample and a graphite die (Fig. 3-5). The technique, however, can also be used for materials systems that are not properly compactable via hot pressing [136]. While holding times for hot pressing are in the range of hours, they are in the range of minutes for SPS. The electrical current running through the die and through the powder allows for very high heating rates of more than 150 K/min. In the powder, the current passes through the

contact points causing localized heating and fast development of sintering necks. Due to the brevity of the pulses, very high temperature gradients on the length scale of the particle size occur, which can even lead to partial melting or evaporation at the powder contacts. Compaction is usually performed in vacuum.

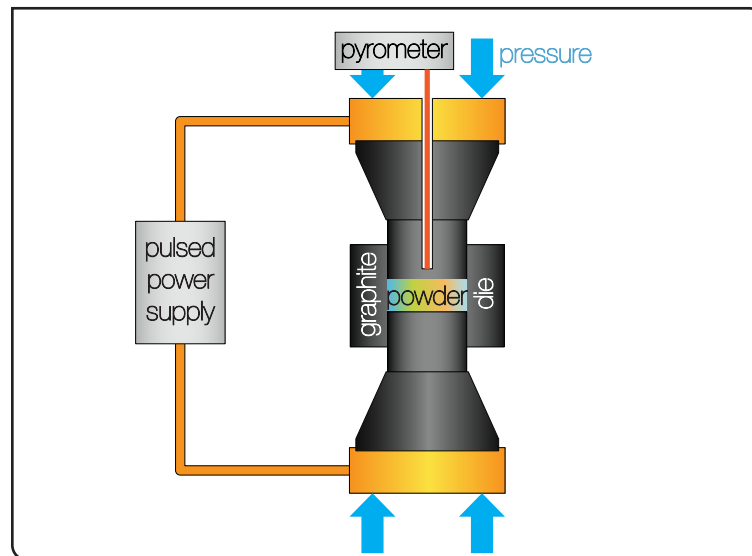


Fig. 3-5: schematic of the spark plasma sintering process, a modification of hot pressing

Today, SPS is mostly used for simple shapes as cylinders or cuboids. However, there are efforts to use this technique to produce near net-shape components [137, 138]. Very recently, Voisin et al. [139] produced a part resembling a turbine blade from a γ -TiAl alloy powder using a multiple-punch system on an SPS machine.

SPS is regularly used for refractory-based alloys such as niobium silicides but also molybdenum silicides [140–142]. In the niobium system, mostly binary alloys with compositions close to the eutectic point (16–20 at%) have been consolidated [73, 126–128, 143, 144] with good success, achieving $\text{Nb}_{ss}/\text{Nb}_5\text{Si}_3$ microstructures. Elemental powders were either milled prior to compaction or only mixed using reactive SPS. Gang et al. [133] produced a vanadium-modified monolithic Nb_5Si_3 alloy and Xiong et al. [73] partially substituted niobium for molybdenum or tungsten in a Nb-20Si powder mixture.

3.2.3 Hot Isostatic Pressing (HIP)

HIP is a well-established process nowadays, using a combination of a pressure tank and heating. A pressurized medium, usually argon, is used at pressures up to around 300 MPa while the chamber is heated to up to 1500 °C, sometimes even 2000 °C [108, p. 137]. In order to convert loose powder into a compact using HIP, it has to be filled into a can made of glass or a soft metal, e.g. low alloy steel, molybdenum, or tantalum, that is subsequently evacuated and sealed. The isostatic gas pressure at sintering temperature will produce very homogeneously compacted solids. Those cans usually come in simple shapes, such as cylinders etc. Of particular interest, however, is the use of near net-shape cans, opening this technique to directly produce components with minimal need for post-processing. These cans can be made by welding [145], galvanic technique, plasma spraying [108], or selective laser melting (SLM). Others have

successfully shown net-shape production capabilities by complex assembled cans with undeformable cores for shape accuracy [146, 147].

If the powder was previously compacted by other means to closed porosity, HIP often is used to remove the remaining porosity and improve tensile properties, which are very sensitive to defects. In these cases, a can is not necessary.

Previously, only Jéhanno et al. [23] used HIP for the compaction of niobium silicide material using gas-atomized powder of a complex niobium silicide alloy (Nb-20Si-24Ti-2Al-5Cr-3Hf) that was subsequently hot-extruded.

In the course of the HYSOP project, turbine blades and vanes have been produced from gas-atomized niobium silicide powder (Nb-20Si-23Ti-6Al-3Cr-4Hf) by means of an SLM produced HIP can (Fig. 3-6).



Fig. 3-6: double vane segment (left) and turbine blade geometries (middle and right) produced by HIPing of a gas-atomized Nb-20Si-23Ti-6Al-3Cr-4Hf powder, HIP can was produced by SLM, courtesy of The University of Birmingham, Interdisciplinary Research Centre in Materials Processing, Birmingham, UK

3.2.4 Powder Injection Molding (PIM)

Powder injection molding (PIM) also called metal injection molding (MIM) is a process adapted from polymer technology. The production of very high quantities of complexly shaped components at a relatively low cost is also very appealing to metallurgy. PIM parts can typically be produced with high accuracy from a variety of materials. The steps involved are depicted in Fig. 3-7. The metal powder is mixed with a binder and pelletized. High shear strains are desirable to ensure proper mixing of the components. The feedstock is fed into an injection molding machine. A screw plasticizes the feedstock and produces a melt reservoir that is pushed into the mold cavity by a lateral movement of the screw. The mold is opened and the green part ejected. Subsequently, the binder is removed by a solvent and/or thermally before the brown part is sintered.

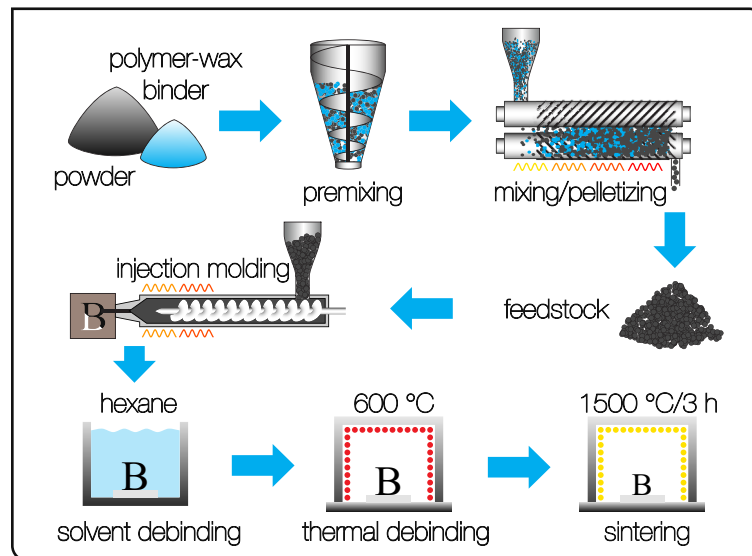


Fig. 3-7: schematic of powder injection molding process

To achieve sufficient flowability of the feedstock, very fine powders have to be used, typically smaller than $30\ \mu\text{m}$. Also, spherical powders such as those produced by gas atomization are favored. This will also keep the abrasion on the tooling to a minimum. This combination leads to a large portion of GA powder not being usable, hence increasing cost [108, p. 146].

The green part is produced by low pressures compared to cold or hot pressing, which means that the powder will not deform plastically; adhesion of the powder is very weak as soon as the binder is removed. Therefore, binder mixtures are used. The primary component will ensure flowability and will be removed in a low-temperature debinding step, mostly in conjunction with a solvent. The second component is retained as a backbone until the thermal debinding provides sufficient powder adhesion for the component not to deform due to gravity. The sintering takes place in the same furnace in order not to break the fragile brown parts. Some commercial binder systems are available, but many PIM manufacturers, however, develop their own feedstock, keeping the composition secret as intellectual property [110, p. 137].

PIM was another process used during the HYSOP project to produce net-shape turbine components. Fig. 3-8 shows a turbine seal segment produced from gas-atomized powder.

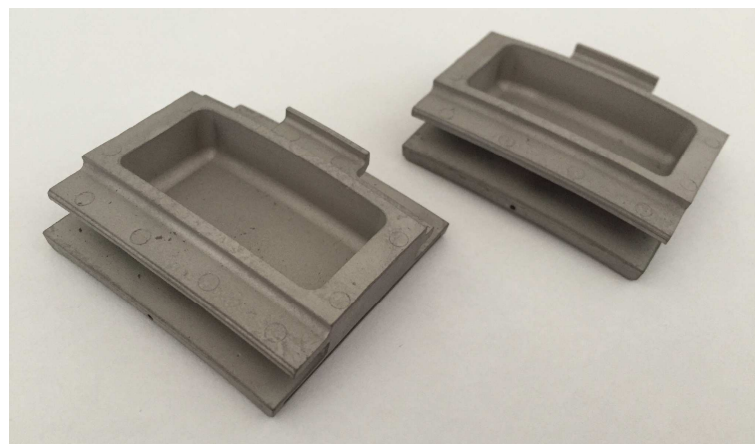


Fig. 3-8: seal segment of a turbine produced via PIM from gas-atomized Nb-20Si-23Ti-6Al-3Cr-4Hf powder

3.2.5 Hot Extrusion

During hot extrusion a rod is pushed through an opening of smaller diameter to change the geometry and induce shear forces. It can be used to reach full density in pre-sintered blanks or as a one-step compaction method. Compact material can be extruded as is, while loose powder needs to be put in a can of a soft and highly deformable metal, e.g. molybdenum or tantalum. The shear forces help breaking up particle boundaries or oxide scales on the particles surface that would otherwise prevent achieving the necessary properties [109].

Both principles, direct compaction of loose powder [98] and forming of pre-compacted material [23, 132] are reported in literature for niobium silicides.

3.2.6 Direct Laser Fabrication (DLF)

Recently, a multicomponent niobium silicide composite (Nb-22Si-26Ti-2Al-6Cr-3Hf) was successfully produced by direct laser fabrication of gas-atomized powder [21], yielding dense homogeneous microstructures. The process is based on the powder being sprayed into a focused laser beam (Fig. 3-9). The powder will melt and deposit on the substrate. A movable stage enables the layered net-shape production of complex geometries, making DLF a rapid prototyping technique.

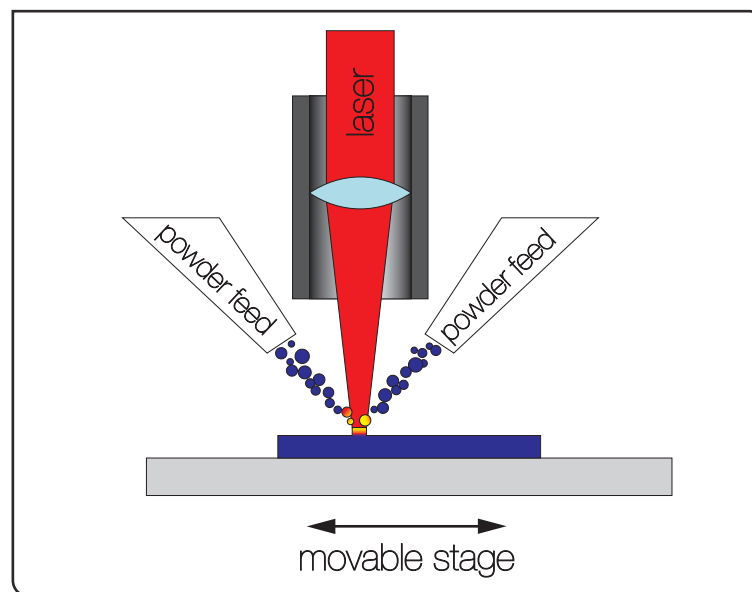


Fig. 3-9: schematic of the direct laser fabrication process

4 Experimentals

4.1 Sample Production

Most samples were produced by powder metallurgy (PM). For comparison, additional specimens were produced by traditional arc melting (section 4.1.4) for bending and compression testing.

4.1.1 Powder Production

Two kinds of powders were used. For the gas-atomized (GA) powder, pieces of pure elements were weighed to achieve the nominal composition, Nb-20Si-23Ti-3Cr-6Al-4Hf (all compositions throughout this work will be given in atomic percent unless specifically stated otherwise), and subsequently plasma melted into rods at BHAM¹. The rods were gas atomized at TLS² facilities by the electrode induction-melting gas atomization (EIGA) process. The resulting powder was separated by sieving into different size classes, of which the fraction with particle sizes < 25 μm and 106-225 μm were comparatively used. As PIM requires fine powders, only the < 25 μm powder was used. HIP does not have any requirements on particle size. Both fractions were compacted via HIP.

The other powder was produced by mechanical alloying in a Zoz CM01 type lab sized attritor (Fig. 4-1). Elemental powders of the same nominal composition as the GA powder were milled with hardened steel or hard metal (WC-Co) balls at 1200 rpm (≈ 7.3 m/s rotor tip speed) under argon atmosphere in batches of 200 g. The ball-to-powder weight ratio (BPR) was 10:1. The mechanical alloying is described in further detail in section 5.1. The powder was separated into two size classes by sieving (< 25 μm and > 25 μm). The fine fraction (< 25 μm) was used for consolidation via PIM, the coarse fraction was used for HIP.

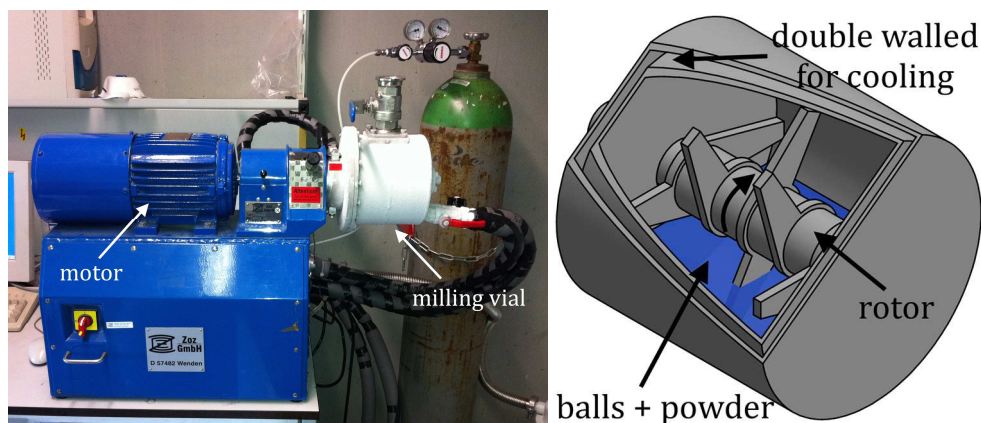


Fig. 4-1: picture of attritor setup (left), schematic section of the double walled design

¹ The University of Birmingham, Interdisciplinary Research Centre in Materials Processing, Birmingham, UK

² TLS Technik GmbH & Co. Spezialpulver KG, PC-Strasse, 06749 Bitterfeld, Germany

4.1.2 Consolidation

Both kinds of powders were either consolidated by conventional hot isostatic pressing (HIP) or by powder injection molding (PIM). For HIPing the powder was filled in an iron can on a vibrating table and, subsequently, the can was evacuated overnight and sealed by mechanical crimping and welding. HIPing was performed at 1230 °C and 150 MPa for 4 h in an EPSI³ HIP furnace at BHAM (Fig. 4-2).

A second HIP treatment of bulk material was undertaken at IAM-KWT⁴ with the same parameter set in a carbon crucible.

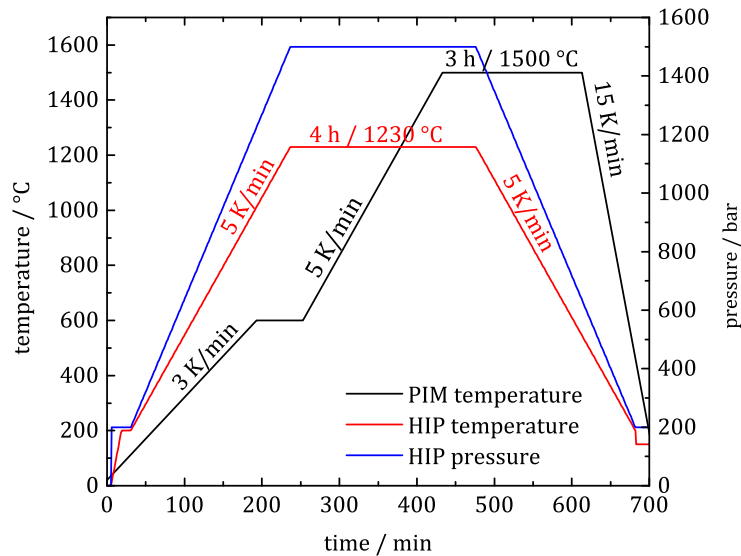


Fig. 4-2: temperature profile of thermal debinding and sintering for the PIM process and pressure and temperature profile for the HIP cycle

PIM processing was done at IFAM⁵. The powder was mixed in a double-sigma mixer with a polymer-wax based binder (70 % paraffin wax, 25 % low density polyethylene, and 5 % stearic acid) at powder loads of 70 vol% and 52 vol% for GA and MA powder, respectively. After pelletizing and injection molding, at least 95 % of the binder was extracted with heptane at room temperature followed by a 1 hour thermal debinding step at 600 °C. Subsequent sintering was done under vacuum ($1 \cdot 10^{-4}$ mbar) at 1500 °C for 3 h (see Fig. 4-2 for temperature profile).

In the following the compacted conditions will be described by the consolidation process followed by the powder used as HIP GA, PIM GA, and PIM MA, respectively. If the HIP sample is based on the coarse-grained GA powder (106 – 225 μm), its denotation is HIP CGA. The as-consolidated samples carry the token AC.

³ EPSI, Inc., Haverhill, Massachusetts, USA

⁴ Institute of Applied Materials – Ceramic Materials and Technologies, Karlsruhe Institute of Technology, Karlsruhe, Germany

⁵ Fraunhofer Institute for Manufacturing Technology and Advanced Materials, Bremen, Germany

4.1.3 Heat Treatments

Consolidated samples were placed in a boat made from YSZ and heat treated (HT) under argon atmosphere in a Gero tube furnace type HTRH 70-600/18 at 1300, 1400, and 1500 °C for 20 or 100 hours and will be designated by HT followed by the temperature in centigrade and the duration in hours, e.g. HIP GA HT₁₃₀₀₋₁₀₀. The furnace was surveyed to have an actual temperature of 1302 ± 1 , 1400 ± 1 , and 1499 ± 1 °C, respectively, in the hot zone of the samples. To prevent residual oxygen in flowing argon gas from contaminating the samples, they were placed in a powder bed of GA powder of the same composition leading to the samples having no contact to the boat and being completely covered by the powder. Because sintering of the powder at 1500 °C is too strong to remove the sample from the powder bed after heat treatment, for HT₁₅₀₀₋₁₀₀, the samples had to be placed directly in the boat and another boat with NbSi powder was placed in front of the samples to remove some oxygen from the gas flow.

4.1.4 Material Production by Arc-Melting

Blanks for the manufacturing of bending and compression samples of the alloy composition Nb-20Si-23Ti-6Al-3Cr-4Hf were produced at ORNL⁶. Element pieces were weighed and put together to yield the nominal composition. They were melted by conductively heating the material in a copper crucible with a high current electric arc. To insure homogeneity the so-formed buttons were turned and remelted ten times. The weight loss was below 1 wt% showing a deviation from the nominal composition to be negligible. Their designation will be ARC.

To validate if the intermetallic phases in the composite take part in the deformation process, monolithic α -Nb₅Si₃ and γ -Nb₅Si₃ were produced in the composition determined from the composite's phases by energy dispersive X-ray spectroscopy (section 4.2.5), i.e. Nb-36.5Si-13Ti-1Al-4Hf and Nb-36Si-23.5Ti-2.5Al-0.5Cr-7.5Hf, respectively. This was done using an Edmund Bühler AM_{0,5} arc melting furnace in the same way as described in the previous paragraph.

4.2 Microstructural Analysis

4.2.1 Metallographic Preparation

Metallographic cross-sections were prepared by grinding with SiC paper twice for 15 min at each step on P₁₀₀₀, P₂₅₀₀, and P₄₀₀₀ grit. Subsequently, samples were polished with pH-neutral Sommer OPS suspension FS₁ (particle size below 0.05 μm).

In this work, in micrographs showing deformed samples the direction of the applied mechanical stress is parallel to the vertical edge of the figure unless stated otherwise.

Because phase contrast is very low in the scanning electron microscope, quantitative, microstructural analysis was performed either via EBSD (section 4.2.3) or by optical microscopy (OM) of etched samples. An etching solution for niobium-based alloys from Petzow [148], Cr m₁₁ – i.e. 50 ml H₂O, 50 ml HNO₃ (65 %), and 50 ml HF (40 %) – was used for 5 – 10 seconds. This led to minor areal etching on Nb_{ss}, massive etching on γ -Nb₅Si₃, and minor phase boundary etching on α -Nb₅Si₃, making the three phases distinguishable by OM.

⁶ Oak Ridge National Laboratory, Oak Ridge, Tennessee, USA

4.2.2 Scanning Electron Microscopy (SEM)

Due to the lower wavelength of electrons when accelerated by several kV compared to visible light, the theoretical resolution of an SEM is much higher than for OM, making it possible to discriminate finer microstructural features. The smaller aperture results in higher depth of field, making it also suitable for non-flat samples such as fracture surfaces. For observation of topography, usually secondary electrons (SE) are used for imaging. A backscatter electron detector (BSE) provides compositional contrast, because the backscatter efficiency correlates strongly with the elemental mass. The addition of an energy dispersive X-ray spectroscopy (EDS) silicon drift detector allows for spatially resolved chemical analysis. SEM micrographs in this work were created by a Zeiss Evo 50 (IAM-WK⁷) or a Zeiss Leo 1530 (LEM[®]).

4.2.3 Electron Backscatter Diffraction (EBSD)

Another expansion of the SEM can be an EBSD unit. This allows for space-resolved analysis of the crystal structure, i.e. phase and orientation. It can, however, only distinguish between a limited number of phases, which makes the phase analysis via XRD (section 4.2.6) a necessary prerequisite prior to an EBSD analysis.

The wavelength of the primary electrons in the SEM is generally assumed to be the de Broglie wavelength [149]:

$$\lambda_e = \frac{h}{\sqrt{2m_e \cdot U_a \cdot e}} \quad (4-1)$$

λ_e : de Broglie wavelength of an electron

h : Planck constant

m_e : electron mass

U_a : acceleration voltage

e : electron charge

For the used acceleration voltage of 20 kV, this results in a wavelength of $\lambda_e = 8.673$ pm. Since this is considerably smaller than for Cu-K α radiation ($\lambda \approx 154$ pm), the Kossel-cones are obtuse-angled and will form lines when intersecting the fluorescent screen used to record the diffraction pattern (Fig. 4-3).

By analyzing the diffraction bands' widths, which are inversely proportional to d_{hkl} , their position, and angle to each other, the software can decide on one of the pre-selected phases and its orientation in relation to the sample axes.

A Zeiss Auriga SEM with field emission gun that was available at INT⁹ was used for EBSD measurements.

⁷ Institute for Applied Materials – Materials Science and Engineering, Karlsruhe Institute of Technology, Karlsruhe, Germany

[®] Laboratory for Electron Microscopy, Karlsruhe Institute of Technology, Karlsruhe, Germany

⁹ Institute for Nano-Technology, Karlsruhe Institute of Technology, Karlsruhe, Germany

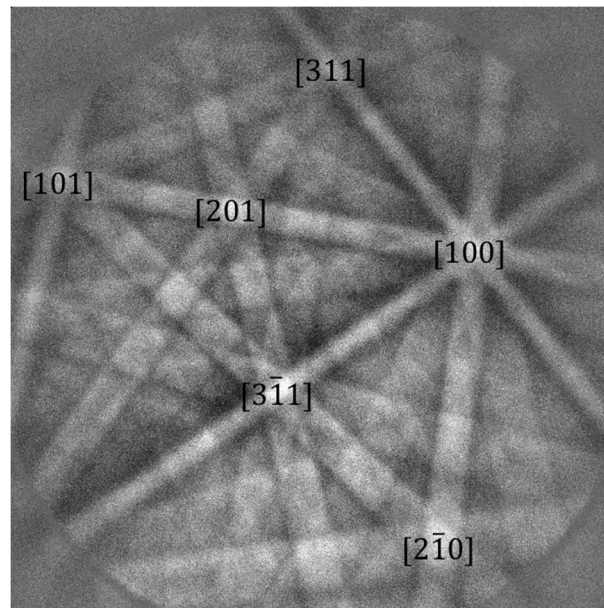


Fig. 4-3: indexed EBSD diffraction pattern for a bcc-metal

4.2.4 Transmission Electron Microscopy (TEM)

Dislocations and dislocation networks, as formed by plastic deformation, can be used to determine which phase in a composite is responsible for the deformation. Also, the creep behavior suggests defect formation very early during deformation, which cannot be observed by the methods described above, but is accessible through TEM.

Because the mean free path of electrons in solids is very small (< 100 nm) TEM samples have to be prepared very thin. This can be achieved in a modern SEM with an additional focused ion beam (FIB) to prepare specific microstructural features for TEM analysis. This was not necessary in this case and the traditional method for TEM foil preparation was used. After plane parallel grinding of a sample platelet to a thickness < 100 μm and punching out a 3 mm diameter disk, a dimple grinder was used to polish a recess into both surfaces with 3 μm and 1 μm diamond polishing paste. Subsequently, the foil was thinned by precision ion polishing (PIP) until a hole formed in the middle of the sample. The area just around the rim of said hole is thin enough to allow electron transmission.

For TEM analysis an FEI Titan at INT was used at 300 kV acceleration voltage. Scanning TEM (STEM) as well as imaging and dark field TEM (DF-TEM) micrographs were taken. Phase identification was carried out using a combination of EDS and diffraction analysis.

4.2.5 Chemical Analysis

Due to the high surface-to-volume ratio of powders, chemical analysis of impurities that may be picked up during processing is very important. Gaseous impurities (oxygen and nitrogen) were determined by hot carrier gas extraction with a Leco TC500 at IAM-KWT or a Leco TC600 at

IAM-AWP¹⁰. Carbon uptake from milling balls, milling vial, milling agent, or PIM binder was determined by combustion analysis via a Leco CS600 at IAM-AWP.

Wavelength dispersive X-ray spectroscopy (WDS) was performed on the solid solution phase of PIM samples from different powders with a standard calibrated JEOL JXA-8530F electron probe micro analyzer at IMVT¹¹.

All other elemental analysis was done by means of the EDS detector in the SEM.

4.2.6 X-Ray Diffraction (XRD)

X-ray diffraction can be used to identify the phases present in crystalline samples. Regularly spaced atoms in a crystal will, according to Bragg's law (Eq. (4-2)), result in positive interference at specific angles.

$$n_b \cdot \lambda = 2d_{hkl} \cdot \sin(\theta) \quad (4-2)$$

n_b : diffraction order

λ : wavelength of incident radiation

d_{hkl} : lattice spacing of diffracting plane with Miller indices hkl

θ : diffraction angle of positive interference

The combination of crystal structure and lattice parameters leads to a specific diffraction pattern. Some knowledge of the chemistry and possible phases enables not only the identification of the phases present in a given sample, but also to refine lattice parameters and derive phase fractions.

Interference patterns in this work were recorded with a Bruker D2 Phaser diffractometer with Cu-K α radiation ($\lambda = 0.15406$ nm) and an attached Lynxeye line detector at room temperature. The X-ray tube was operated at 30 kV and 10 mA. A Ni-filter in the secondary beam path was used to filter Cu-K β radiation. To increase grain statistics the ϕ -circle rotated at 60 rpm, i.e. the sample normal axis, while the integration time per step was set to 2 s.

Lattice constants were determined by full pattern analysis with Maud¹² [150] software. Structure data for all present phases was refined using the Rietveld [151] method.

4.2.7 Differential Scanning Calorimetry (DSC)

For evaluation of phase formation, MA powder was measured in a Netzsch DSC 404 Pegasus calorimeter up to 1300 °C at a heating and cooling rate of 10 K/min under argon atmosphere. To correlate DSC peaks with phases formed, MA powder was held at specific temperatures for 1 hour for subsequent XRD analysis. The argon gas used as flow gas was of grade 5.0, i.e. a purity

¹⁰ Institute for Applied Materials – Applied Materials Physics, Karlsruhe Institute of Technology, Karlsruhe, Germany

¹¹ Institute for Micro Process Engineering, Karlsruhe Institute of Technology, Karlsruhe, Germany

¹² Maud is an open-source software developed for all kinds of diffraction analysis available at: <http://maud.radiographema.com> (as of 02.09.2015)

of 99.999 %, which only leaves 5 ppm of oxygen. However, since most of the metals milled are very sensitive to oxygen exposure, especially at elevated temperatures, and to ensure no oxidation effects were being observed during DSC, an oxygen getter capsule by AirLiquide and an yttrium getter ring in the heat zone of the furnace were used.

In accordance with DIN 51007 [152] three DSC curves $\Phi(T)$ consisting of isothermal sections at 80 °C and 1300 °C enveloping the dynamic heating or cooling sections were recorded: baseline Φ_b (empty crucible), reference Φ_{sap} (bulk sapphire disk), and sample Φ_s . With the known specific heat capacity of sapphire $c_{p,sap}(T)$ the specific heat capacity of the sample $c_{p,s}(T)$ was determined using the following equation.

$$c_{p,s}(T) = \frac{m_{sap}}{m_s} \cdot \frac{[\Phi_s(T) - \Phi_{s,0}(T)] - [\Phi_b(T) - \Phi_{b,0}(T)]}{[\Phi_{sap}(T) - \Phi_{sap,0}(T)] - [\Phi_b(T) - \Phi_{b,0}(T)]} \cdot c_{p,sap}(T) \quad (4-3)$$

m_s, m_{sap} : mass of sample and sapphire reference,
respectively

$\Phi_{b,0}, \Phi_{sap,0}, \Phi_{s,0}$: respective linearly interpolated baseline
between the isothermal sections

4.2.8 Thermogravimetry with Mass Spectrometry

MA powder was also analyzed by thermogravimetry (TGA) with a Netzsch STA 449 F1 Jupiter and attached mass spectrometer (MS) type Netzsch QMS 403D Aëolos. While heating in an argon atmosphere at 10 K/min to 1200 °C, mass change and gaseous species leaving the sample material were analyzed for a mass to charge ratio between 1 and 100.

4.2.9 Density Measurement

Density and, thus indirectly, porosity were measured by the Archimedes principle. Samples (typically 0.5 – 1 g) were weighed five times in air and 5 times while submerged in water. Using the equation

$$\rho = \frac{m_d \cdot \rho_{H_2O}}{m_d - m_w} \quad (4-4)$$

ρ : density

m_d : dry weight in air

m_w : wet weight in water

ρ_{H_2O} : density of water

the density including closed porosity was calculated. Porosity was estimated by using a theoretical full density of 6.85 g·cm⁻³.

4.2.10 Phase Diagram Calculations

For the niobium system with most common alloying elements, as they are used in this work, CompuTherm LLC, Madison, Wisconsin, USA provides a database (PanNb) for thermodynamic phase calculations together with the software PANDAT. Isoleth sections in this work were calculated with database version PanNb8.

4.3 Testing of Mechanical Properties

4.3.1 Quasi-Static Compression and Compression Creep

The thrust faces of compression samples with circular or rectangular cross-section were ground coplanar to a grit of P2500. To reduce friction with the punches, a thin layer of hexagonal boron nitride was applied.

At elevated temperatures, a universal electro-mechanical testing machine Zwick Z100 with attached molybdenum vacuum radiation furnace by Maytec was used to load the samples (Fig. 4-4).

For room temperature compression testing, a Zwick Zmart.Pro electromechanical testing machine was used. The punches were made from hard metal (WC-Co).

Quasi-static compression was conducted with a constant initial strain rate of $10^{-2} - 10^{-4} \text{ s}^{-1}$.

For creep testing, samples were loaded within 50 s with constant true stresses of 50 – 300 MPa at elevated temperatures of 900 – 1300 °C.

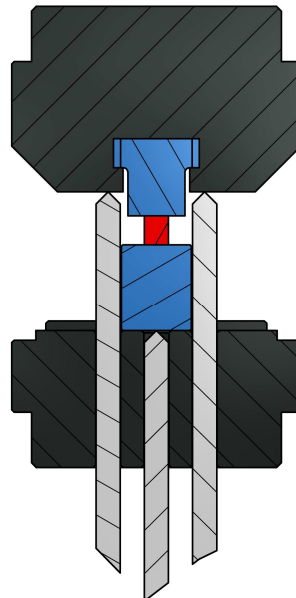


Fig. 4-4: schematic of strain measurement in compression; sample in red, SiC compression punches in blue, TZM load discs in black, and Al_2O_3 strain gage rods in grey

The elastic modulus is only accessible, if the strain gauge is directly attached to the sample. Due to the sample size and the setup used (Fig. 4-4), strain measurements include the elastic deformation of the SiC-punches and the upper load disc.

Hence, only plastic strain will be shown, where for each data point the elastic deformation of the load assembly was subtracted via:

$$\varepsilon_p = \varepsilon_n - \frac{\sigma_n}{E'} \quad (4-5)$$

ε_p : plastic strain

ε_n : total strain

σ_n : nominal stress

E' is the apparent stiffness of the system, i.e. the linear elastic slope during compression.

4.3.2 Fracture Toughness

DIN CEN/TS 14425 is a pre-standard describing methods to determine fracture toughness in technical ceramics. This standard is used here since the fracture toughness of intermetallic NbSi-alloys ($\approx 10 \text{ MPa}\cdot\text{m}^{0.5}$) is generally closer to ceramics than metals. Of the methods introduced in said standard, the single edge V-notched beam method was chosen with several points in mind: indentation toughness is generally not recommended and hardness indentations did not result in clearly visible cracks, limited amount of sample material, and manufacturability of the sample geometry with available equipment.

Seven beams were fixed to a holding plate with hot glue and a pre-notch was introduced by electro discharge machining (EDM). Using the oscillating movement of a razor blade covered with $3 \mu\text{m}$ and subsequently $1 \mu\text{m}$ diamond polishing paste on the bottom of the pre-notch produced a sharp V-notch. The notch root radius was documented for all samples to fall below the allowance of the standard. For comparison the HIP GA AC condition was also tested without introduction of a V-notch and only the EDM notch instead. Example micrographs of corresponding notches are found in Fig. 14-1 in the Appendix.

Subsequently, the samples were loaded at room temperature in 4-point bending mode (Fig. 4-5) with a cross-head displacement rate of 0.5 mm/min so that the notched surface was loaded under tension.

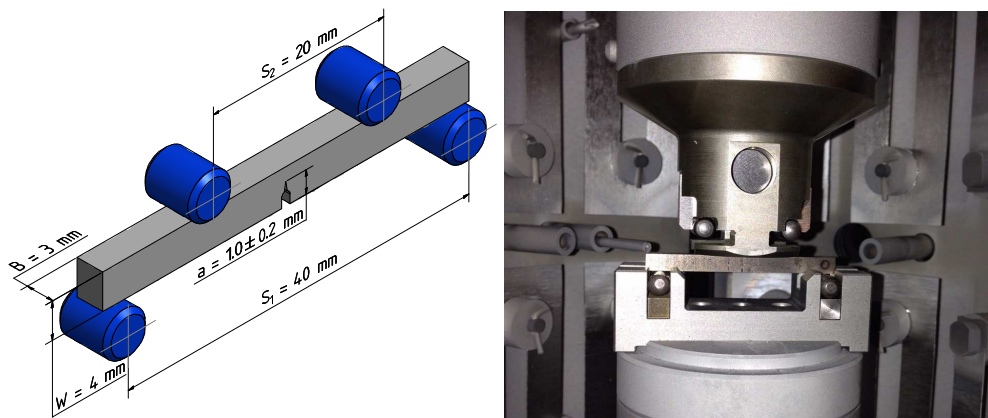


Fig. 4-5: schematic (left) and photograph (right) of 4-point-bending of V-notched samples.

After testing, the notch depth a was determined by optical microscopy as the average of three measurements on the fracture surface. The mode I fracture toughness K_{Ic} was calculated using the following equation:

$$K_{Ic} = \frac{F_r}{B\sqrt{W}} \cdot \frac{S_1 - S_2}{W} \cdot \frac{3\sqrt{\alpha_K}}{2(1 - \alpha)^{1.5}} \cdot Y \quad (4-6)$$

F_r : force at rupture

B : width of sample

W : thickness of sample

S_1 : outer bearing distance

S_2 : inner bearing distance

$\alpha_K = \frac{a}{W}$: relative notch depth

with

$$Y = 1.9887 - 1.326\alpha_K - \frac{(3.49 - 0.68\alpha_K + 1.35\alpha_K^2)\alpha(1 - \alpha_K)}{(1 + \alpha_K)^2} \quad (4-7)$$

4.3.3 Ductile-to-Brittle-Transition-Temperature (DBTT)

The determination of the ductile-to-brittle transition temperature is based on the onset of plastic deformation under tensile loading. This can be done by tensile testing [23] or by bending tests, where the surface on the outer bearings is subjected to the highest tensile load. In this work three-point bending was chosen (Fig. 4-6, left) giving the distribution of bending moment M_b seen in Fig. 4-6, right).

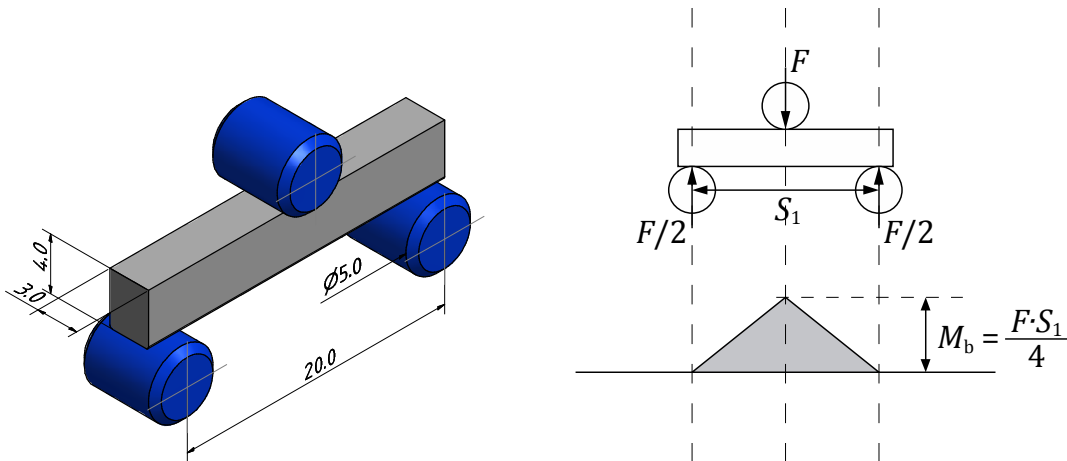


Fig. 4-6: sample and loading geometry for DBTT testing (left), distribution of the bending torque along the bottom edge (right)

The bottom side enduring the highest tensile load is called the extreme (tensile) fiber and the highest stress below the middle bearing disregarding any plastic deformation can be derived from elastic beam theory [153].

$$\sigma_{ef} = \frac{3 \cdot F \cdot S_1}{2 \cdot B \cdot W^2} \quad (4-8)$$

σ_{ef} : extreme tensile fiber stress

F : applied load

Accordingly, the tensile strain of the extreme fiber is given by:

$$\varepsilon_{ef} = \frac{6 \cdot f \cdot W}{S_1^2} \quad (4-9)$$

ε_{ef} : extreme tensile fiber strain

f : measured deflection

The compression surface was ground to P1000 grit. All other faces were ground down to P4000 grit parallel to the longest edge. The two tensile edges were filleted with P4000 grit to a typical radius of 50 – 70 μm and all three faces were subsequently polished with pH-neutral Sommer OPS FS1.

Testing was done on the Zwick Z100 universal testing machine introduced in 4.3.1 at temperatures ranging from 700 °C to 1000 °C. The crosshead displacement rate was chosen (according to Eq. (4-9)) to result in initial extreme fiber strain rates of 10^{-3} s^{-1} or 10^{-5} s^{-1} .

4.3.4 Nano-Hardness

Nano-hardness of individual grains was determined with a Fischer Fischerscope micro hardness tester. Loading and unloading to the maximum load P of 10 mN was done in 20 s, each. A holding time was omitted. The indenter type used was a Vickers pyramid. Martens hardness HM was determined according to the DIN EN ISO 14577-1 standard [154] as

$$HM = \frac{P}{26.43 \cdot h^2} \quad (4-10)$$

h : indentation depth at maximum load P

5 Production and Analysis of Powder

5.1 Mechanical Alloying (MA) of Elemental Powders

Preliminary alloying trials of niobium silicides in a planetary ball mill have shown a strong tendency to adhesion of powder to the vial walls. This effect could be reduced by lowering the milling temperature by submersion of the vial into liquid nitrogen prior to milling. The attritor used for this work has the possibility to cool its vial continuously by means of a double walled design (Fig. 4-1, right, p. 27). Using a cryostat with a water and anti-freeze mixture a constant temperature of $-15\text{ }^{\circ}\text{C}$ could be realized. To allow for the heat produced by the milling to dissipate properly, milling cycles of 2 minutes were repeated containing 1 min of milling and 1 min of milling break (Table 5-1).

As with the planetary ball mill, milling trials in the attritor with pre-alloyed powder of the nominal composition Nb-20Si-23Ti-6Al-3Cr-4Hf showed a strong dependency of powder yield and powder particle size on the temperature (Fig. 5-1). While after five hours of milling at $+18\text{ }^{\circ}\text{C}$, only 6 % of the initial powder could be extracted from the attritor, at $-15\text{ }^{\circ}\text{C}$, powder yield was 75 %. This is sufficient for attrition milling to be an economically feasible option. Hence, all subsequent milling batches were carried out at $-15\text{ }^{\circ}\text{C}$.

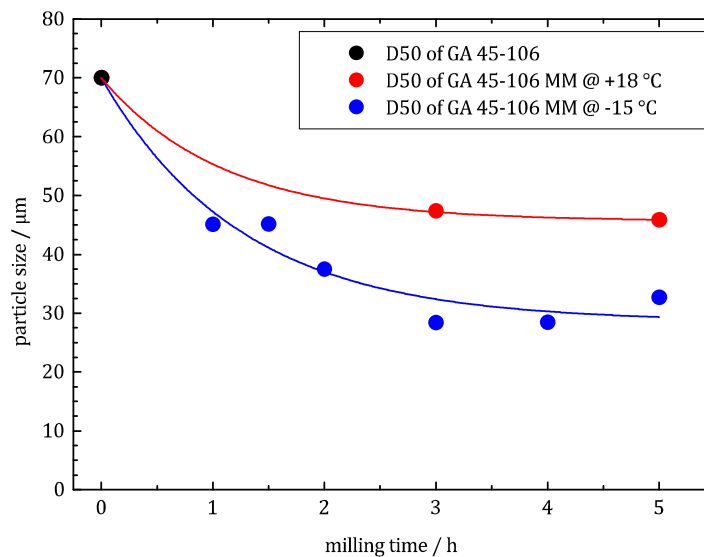


Fig. 5-1: powder particle size in relation to milling time and vial temperature

Several milling parameters were tested to optimize powder yield, contamination level, and microstructural development. The cycles of one minute net milling time were repeated to reach the desired milling duration (Table 5-1).

Table 5-1: investigated milling parameters, each cycle comprising 1 min net milling time (top), powder yield and contamination level after given net milling time (bottom).

	process 1	process 2	process 3
1	1300 rpm / 45 s	1200 rpm / 30 s	800 rpm / 30 s
2	900 rpm / 15 s	0 rpm / 30 s	0 rpm / 30 s
3	0 rpm / 60 s	1200 rpm / 30 s	800 rpm / 30 s
4	—	0 rpm / 30 s	0 rpm / 30 s
milling time / h	8	10	20
powder yield / %	95	90	50
Fe / at%	6	1.3	8

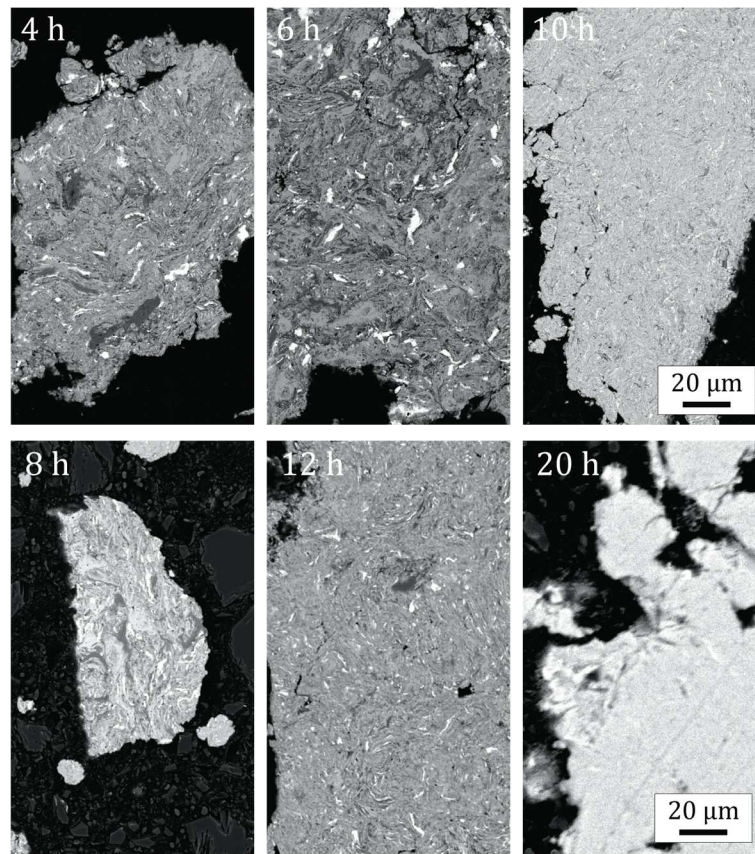


Fig. 5-2: backscatter electron micrographs of milled powder for process 2 (top) and process 3 (bottom); all with same magnification, net milling time as indicated

Process 1 already shows too high contamination by abrasion from balls and rotor after 8 hours. A slight decrease of the maximum rotor speed to 1200 rpm reduces the iron content almost

below the detection limit of EDS. For process 3, the milling time considered had to be increased to 20 h to reach similar milling progress as for process 2 (Fig. 5-2). This led not only to increasing iron abrasion but also to reduced powder yield. Hence, process 2 was chosen for all following milling trials as it was found to be superior.

It is visible from the micrographs of milled powder (Fig. 5-2) that, as typical for the milling of ductile powders, the elements form lamellae as refinement increases with the milling time. However, even after the longest milling times of 10 and 20 hours for process 2 and 3, respectively, some white regions corresponding to hafnium are still visible. This may be due to the miscibility gap in the Nb-Hf-system (Fig. 5-3). Hafnium shows a hexagonal structure up to 1775 °C that has no solubility at RT in the bcc-Nb solid solution. Titanium forms a similar phase diagram with niobium (Fig. 5-4), but transforms into bcc at a much lower temperature of 882 °C. This still leaves almost no solubility at RT. However, phase diagrams depict the thermodynamically stable state. Since mechanical milling is a non-equilibrium process, higher solubilities than suggested in phase diagrams can be possible [155], but the miscibility gap at higher temperatures in case of hafnium might be the reason why titanium solutes and hafnium does not. Unfortunately, the solution of titanium in niobium cannot be evaluated by XRD since all peaks overlap and peak shift is also caused by the other alloying elements.

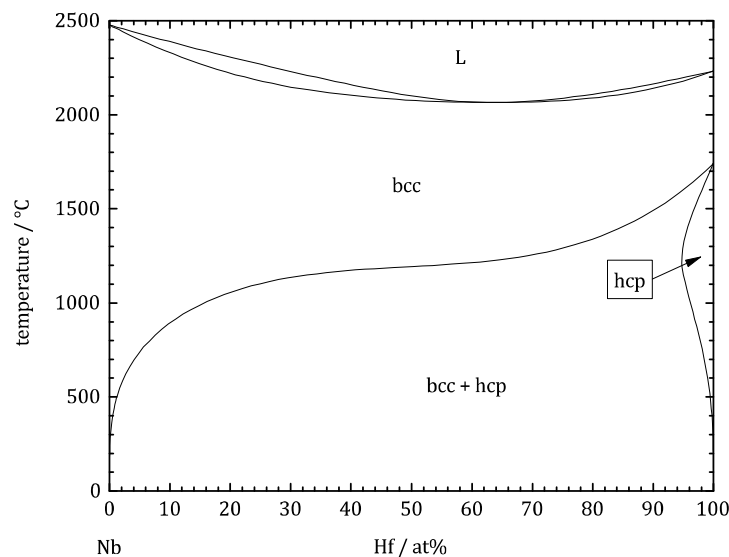


Fig. 5-3: calculated phase diagram of Nb-Hf by PANDAT

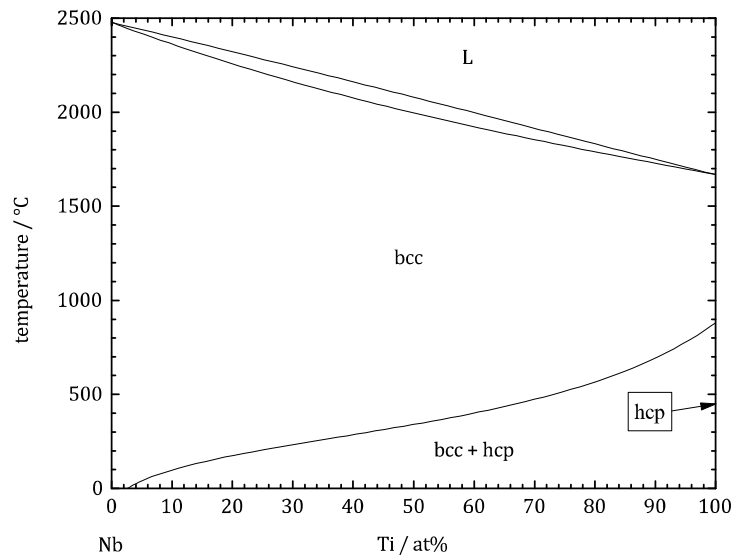


Fig. 5-4: calculated phase diagram of Nb-Ti by PANDAT

During compaction it turned out, that samples produced from mechanically alloyed powder in the described manner (from hereafter referred to as MA₁) have a relatively high content of oxygen and nitrogen (Table 5-2). While the oxygen content of the starting powders is already in the range of 2000 – 8000 ppm, the nitrogen content of the elemental powders is typically very low. Due to the decrease of pressure by 130 mbar in the milling vial during initial cool down from room temperature to -15 °C, air is entering the vial from the environment, probably through the dynamic sealing at the rotor shaft. While most of the oxygen is intentionally gettered by hafnium, the nitrogen may lead to the formation of nitrides as shown later (section 6.1).

Table 5-2: typical contents of gaseous impurities in milled and elemental powders; * is taken from the certificate of analysis from the supplier Alfa Aesar

	oxygen / wt%	nitrogen / wt%
process 2	0.85	0.77
Nb	0.39	0.03
Si	0.30	< 0.01
Ti	0.43	< 0.01
Al	0.40	< 0.01
Cr	0.85	0.02
Hf	0.38*	0.04*

Since room temperature milling leads to insufficient powder yield and temperature reduction leads to high nitrogen and oxygen contamination, milling trials with an added process control

agent (PCA) were undertaken to suppress cold welding of powder to the vial walls at room temperature. Heptane was chosen due to its lack of oxygen in the compound compared to other milling agents such as ethanol or stearic acid. Active cooling cannot be omitted due to heat-up during milling, but was instead set to room temperature to prevent underpressure in the vial. In three successive milling batches, powder yields were above 96 % and mean particle sizes were lower than for PCA-free milling at $-15\text{ }^{\circ}\text{C}$ (hereafter this powder will be designated MA2). Oxygen and nitrogen contents were $0.57 \pm 0.03\text{ wt}\%$ and $0.007 \pm 0.002\text{ wt}\%$. Milling at room temperature with PCA leads to essentially no further nitrogen contamination. Oxygen content is only slightly above the calculated minimum oxygen content from starting powders of $0.40\text{ wt}\%$. However, to clean the milled powder off the heptane a subsequent heat treatment may be necessary to remove it before compaction.

A TGA-MS measurement scanning for mass (m) to charge (q) ratios $1 < m/q < 100\text{ u/e}$ (the highest possible mass of an intact heptane molecule, C_6H_{14} , charged only once) a heating cycle from RT to $1200\text{ }^{\circ}\text{C}$ shows a mass loss of the powder between 450 and $750\text{ }^{\circ}\text{C}$, closely correlated with a peak in hydrogen (Fig. 5-5). Small peaks in $m/q = 17$ and 18 u/e correspond to adsorbed water and $m/q = 44\text{ u/e}$ to adsorbed carbon dioxide, which desorb from the surface before $400\text{ }^{\circ}\text{C}$.

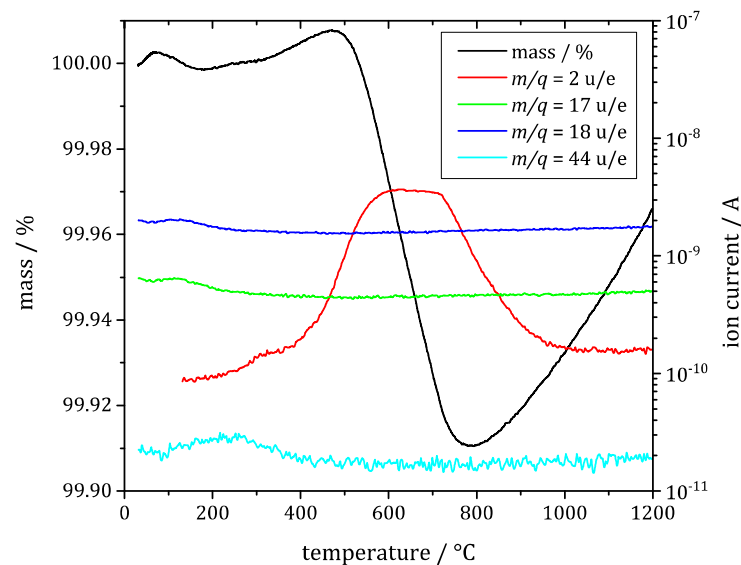


Fig. 5-5: TGA-MS measurement of MA powder with heptane addititon

All other ratios m/q show no change during the cycle. Since, no other hydrogen source besides the heptane was present and heptane-free powder does not show this peak, this means (i) adsorbed heptane is no longer present at the powder surface prior to the TGA-MS measurement since no mass spectrometer peak corresponding to heptane could be detected (compare to Fig. 14-2 in the Appendix). (ii) Heptane either dissociates into hydrogen and carbon during high energy milling or cannot leave the powder during heating and dissociates thermally so that hydrogen leaves the powder while carbon or carbon compounds remain. (iii) The hydrogen leaving the powder corresponds to $0.1\text{ }\%$ in mass change. Because of the stoichiometry of heptane, this means a minimum of $0.53\text{ wt}\%$ of carbon remains in the powder. This corresponds to $3.1\text{ at}\%$ for the nominal powder composition Nb-20Si-23Ti-6Al-3Cr-4Hf. In fact, carbon

content in the milled powder was measured by combustion analysis to be 1.01 wt% (6.9 at%). This leads to the formation of carbides in the compacted samples (section 6.1).

5.2 Phase Formations in MA₁ Powder

The resulting curve of the specific heat capacity c_p from the DSC measurement of MA₁ is shown in Fig. 5-6.

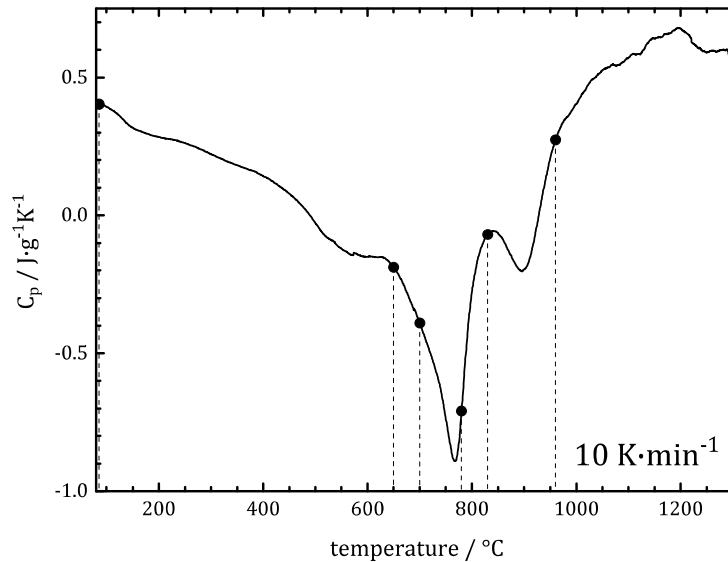


Fig. 5-6: c_p -measurement of MA₁ powder; dashed lines indicate holding temperatures for subsequent XRD measurements

The measurement is dominated by exothermic heat. Starting from 80 °C the exothermic slope indicates recovery from the high amount of deformation implemented by the milling process. This effect is superimposed by several peaks between 650 and 960 °C. To identify the reactions taking place at each peak, small amounts of powder were heated to the temperatures indicated by the dashed lines in Fig. 5-6, i.e. 650, 700, 780, 830, 960, and 1300 °C and held there for 1 hour before cool down. Subsequent XRD revealed the phases present (Fig. 5-7). It is apparent, that up to 650 °C no intermetallic compounds were forming. Next to a small peak at 36.81° corresponding to elemental hafnium, the main peak with a maximum at 38.58° belongs to a bcc solid solution phase, i.e. Nb_{ss}. Upon further heating, this peak shifts to higher angles (39.09° for 1300 °C) while previously solved elements form intermetallic phases. The calculated lattice constants are found in Table 5-3. The lattice constant after milling is actually very close to the database value of pure niobium of 0.3301 nm (atomic radius 145 pm) [156, PDF 01-1183]. Due to decomposition the lattice constant drops upon heating by about 1.2 %, the trend in lattice constant corresponds very well with the decreasing amount of Nb_{ss} (Fig. 5-8). In all cases the niobium lattice is strongly distorted by solute atoms. In the as milled condition, the influence of larger and smaller atoms seems to cancel out. The solid solution in the AC sample still is macro alloyed, with a composition of Nb-0.4Si-19.1Ti-7.5Al-5.2Cr-0.7Hf-1.7Fe (as determined by EDS). There is no change in lattice constant between 1300 °C and the AC condition (1500 °C) suggesting, that the decomposition of the solid solution phase is finalized already at 1300 °C.

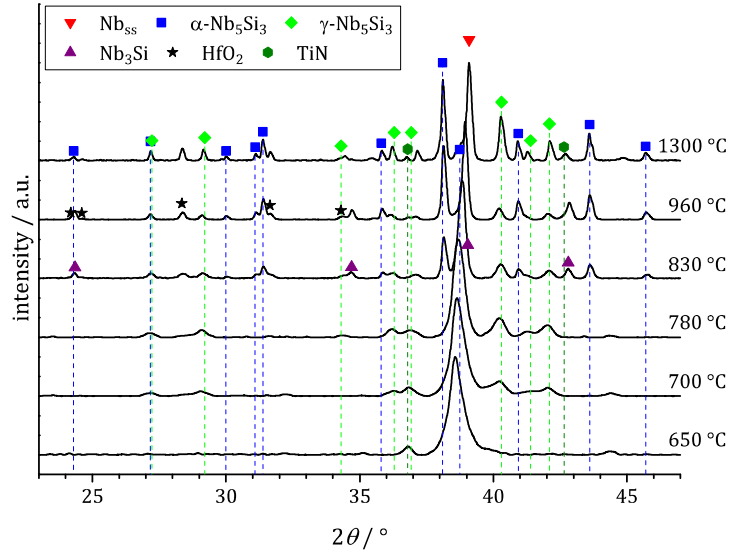


Fig. 5-7: XRD-patterns for differently heat-treated MA₁ powders

If the lattice constant of pure niobium is normalized by the chemical composition and the atomic radii of the individual atomic species, lattice constants of 0.3135 (mean atomic radius of 137.7 pm) and 0.3236 nm (mean atomic radius of 142.1 pm) can be estimated for the milled and AC condition, respectively. In the milled condition, the measured lattice constant is larger than expected. This can be attributed to interstitial elements oxygen and nitrogen widening the lattice. The value for the AC condition corresponds well with the measured one. Most of the interstitials are gettered by hafnium and titanium to form hafnium oxide and titanium nitride, respectively, minimizing their influence.

Table 5-3: calculated lattice constants for niobium solid solution in milled and heat-treated MA₁ and AC

heat treatment temperature / °C	Nb _{ss} lattice constant / nm
650	0.3298 ± 0.0001
700	0.3293 ± 0.0001
780	0.3289 ± 0.0000
830	0.3282 ± 0.0001
960	0.3272 ± 0.0001
1300	0.3258 ± 0.0000
1500 (AC)	0.3258 ± 0.0003

γ -Nb₅Si₃ is the first phase to be formed at 700 °C. Peaks are very wide, meaning that only small colonies of γ -Nb₅Si₃ have formed at that point. At 780 °C just after the minimum of the largest

peak (765 °C), still only Nb_{ss} and γ -Nb₅Si₃ can be found. Starting with 830 °C, additionally Nb₃Si and α -Nb₅Si₃ appear. The Nb₃Si seems not to be the tetragonal equilibrium modification (Table 2-1 on p. 6), but the cubic A15 variant instead. 830 °C seems to be past the second peaks onset, so the holding time leads to significant formation of α -Nb₅Si₃ as is the case for the temperature past the peak (960 °C). Even though there seems to be an exothermic peak just below 650 °C, no phase transformation takes place there.

The reference-intensity-ratio method described in section 6.2.4 cannot be used for determining phase fractions in the powder, as calibration of the phase fractions is necessary for a system's state. The chemistry of the phases, however, changes significantly during heating, making this approach unfeasible. Therefore, merely the raw intensity ratios are plotted in Fig. 5-8 as they develop at different heat treatment temperatures. This can only be seen as a qualitative illustration of the phases forming and disappearing during heating. The peaks used and their approximate positions – as they are changing during heating – are given in Table 6-5 on p. 66.

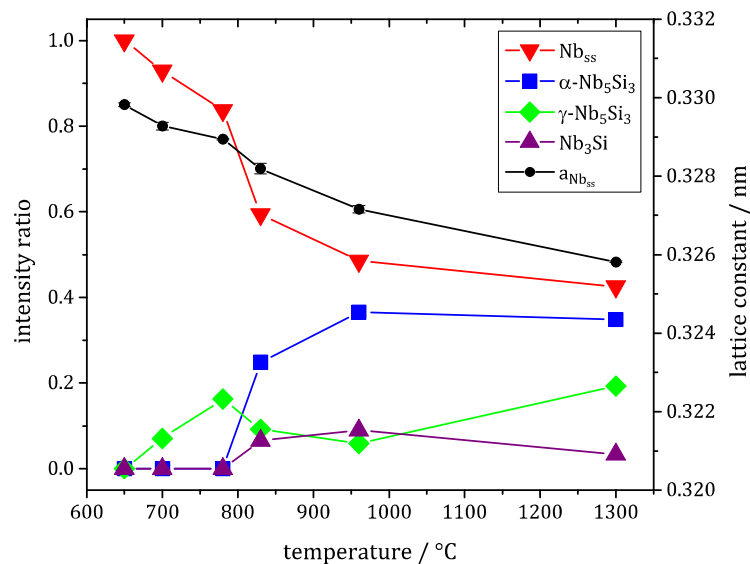


Fig. 5-8: intensity ratios of niobium solid solution and silicide phases in differently heat-treated MA₁ powders; calculated lattice constant of niobium solid solution $a_{\text{Nb}_{ss}}$ shown in black

Others have previously made similar observations on mechanically alloyed Nb-Si powders, albeit only on the binary system, i.e. Ma et al. on Nb-16Si and Kajuch et al. on Nb-37.5Si. Both found three exothermic reactions taking place at similar temperatures as in this study. Seeing some temperature shift happening is not surprising, considering the very different compositions and heating rates. While Kajuch et al. just assume the peak at 780 °C to correlate to Nb₅Si₃ formation and do not discuss the two other peaks, Ma et al. use XRD measurements to verify phase formations in the milled powder. They found the first peak to correlate to the formation of Nb₃Si, as in this work, the meta-stable A15 modification, and the second peak to α -Nb₅Si₃. The third peak is presumed to stem from recrystallization of highly deformed niobium solid solution. Also, Savitskiy et al. [157] and Srinivasan et al. [158] found recrystallization temperatures for cold rolled niobium and its alloys to be above 940 °C. Suryanarayana et al. [159] produced small volume fractions of A15 Nb₃Si by annealing amorphous, rapidly solidified Nb-19Si, which disappeared again in favor of the equilibrium phases upon further heating. The

annealing was done at 600 °C for 48 h, which correlates well with the findings of Ma et al. The rapidly solidified, amorphous material is comparable to the MA, since both microstructures are supersaturated with silicon and far away from equilibrium. This behavior is similar to the one observed in this work, though the first unpronounced peak at 600 °C could not be associated with any intermetallic formation, Nb₃Si was only detected for the third peak, at temperatures of about 250 °C higher. However, recrystallization is not unlikely in highly deformed MA powder and may be superimposed on the formation of Nb₃Si and α -Nb₅Si₃.

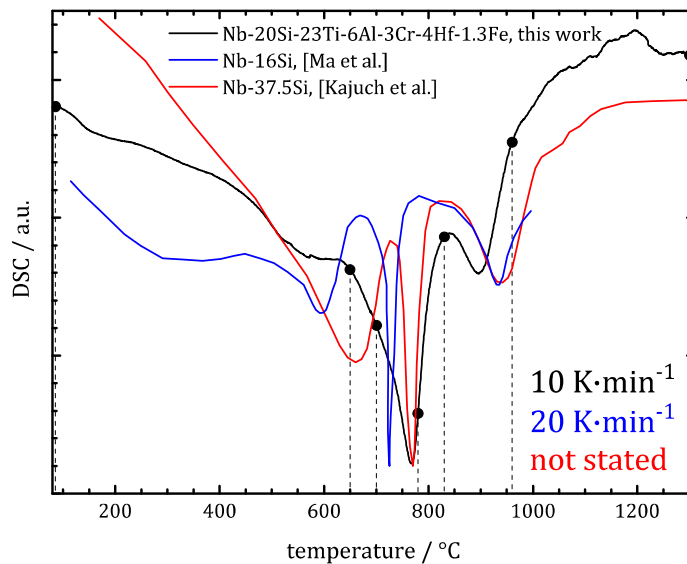


Fig. 5-9: DSC/DTA measurement of MA1 powder compared to literature data by Ma et al. [125] and Kajuch et al. [160]

5.3 Gas-Atomized Powder

Three batches of gas-atomized powder were produced from pre-alloyed plasma melted rods. Subsequently the powder was fractionated into five size classes, i.e. < 25, 25 – 45, 45 – 106, 106 – 225, > 225 μm . The weight distribution of powders can be seen in Fig. 5-10 on the left. -25 and 25 – 45 μm powder was trialed with PIM, -25 and 106 – 225 μm powder was used for HIP, and 45 – 106 μm powder was mechanically milled to reduce particle sizes for subsequent PIM. In this work, results for PIM are limited to the compaction of -25 μm GA powder.

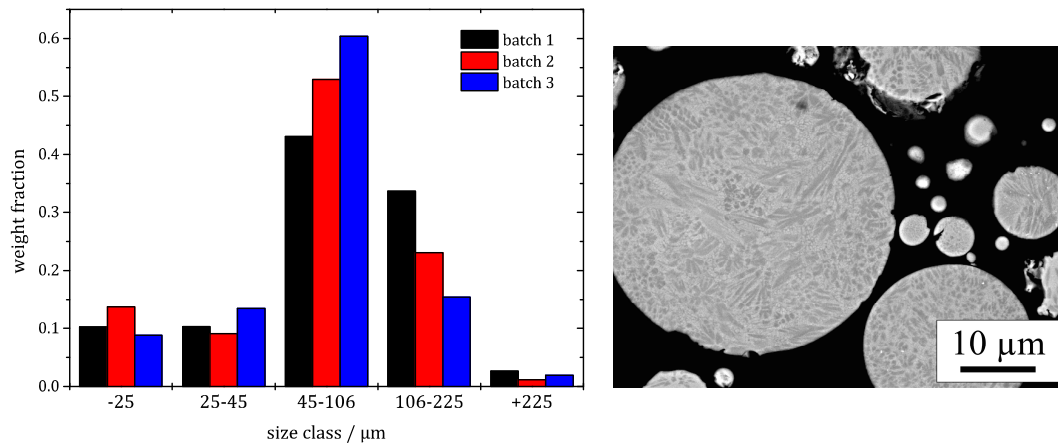


Fig. 5-10: left: weight distribution in the size classes of gas-atomized powder for the three batches produced; right: backscatter electron micrograph of < 25 μm gas-atomized powder; silicides in dark gray and solid solution in bright grey

Fig. 5-11 reveals the presence of three phases in the spherical GA powder, i.e. Nb_{ss} , $\beta-Nb_5Si_3$, and $\gamma-Nb_5Si_3$. The silicides are shown as dark gray in the backscatter electron micrograph due to their high silicon content (Fig. 5-10, right), Nb_{ss} is the bright gray phase. Hafnium oxide appearing white is only rarely visible.

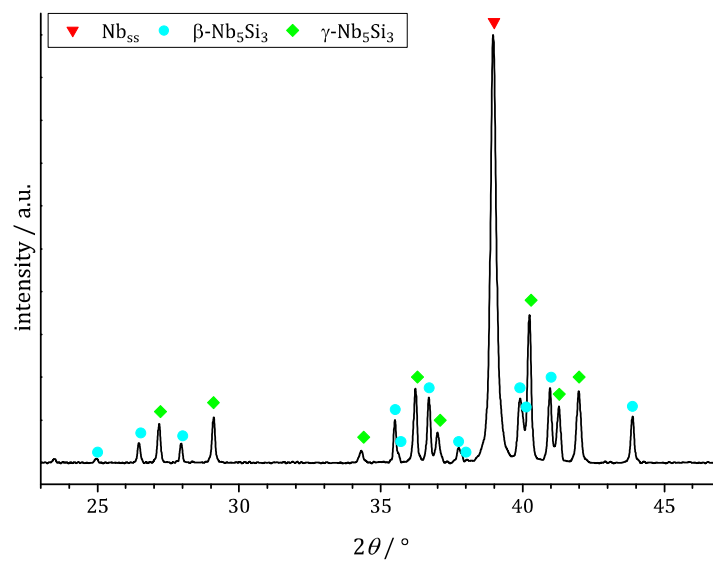


Fig. 5-11: XRD pattern of gas-atomized powder showing the presence of Nb_{ss} , $\beta-Nb_5Si_3$ and $\gamma-Nb_5Si_3$

6 Microstructural Analysis of Bulk Material

The combination of the various powder batches with two compaction processes, HIP and PIM, resulted in seven different conditions of as-consolidated material, because PIM requires particle sizes below 30 μm and thus could not be used with the coarse-grained GA powder, CGA (Table 6-1).

Table 6-1: processing routes for compact material explored in this work

powder	HIP	PIM
GA ($< 25 \mu\text{m}$)	HIP GA successful	PIM GA successful
CGA ($106 - 225 \mu\text{m}$)	HIP CGA successful	<i>PIM requires < 30 μm</i>
MA ₁ (milled at $-15 \text{ }^\circ\text{C}$)	<i>HIP MA₁ cracking</i>	PIM MA ₁ successful
MA ₂ (milled with heptane)	<i>HIP MA₂ cracking</i>	PIM MA ₂ successful

MA₁ and MA₂ powders compacted via HIP seemed to have very high internal stresses. All sample production (GA and MA powders) from HIP cylinders (as well as bending bar preparation from PIM material) was successfully done via EDM. HIP MA material showed low machinability via EDM leading to repeated rupture of the EDM wire. Additionally, extensive cracking was observed during cutting (Fig. 6-1). Preparation of samples with defined geometry (cuboids) was not possible. Probable cause is that the pressure sintering in a closed can inhibited gaseous impurities from leaving the powder, leading to high internal stresses, which are released through cracking during EDM. Hence, HIP MA material was not investigated any further. This leaves five processing routes for analysis: HIP GA, HIP CGA, PIM GA, PIM MA₁, and PIM MA₂.



Fig. 6-1: photographs of cracked HIP MA material after EDM trials; partially still encased by the iron HIP can; can diameter 30 mm

Fig. 6-2 shows the calculated isopleth phase diagram of Nb-xSi-23Ti-6Al-3Cr-4Hf ($0 < x < 30$). Accordingly, heat treatment temperatures were chosen to be below the expected solidus at 1534 °C. Depending on the phase formation kinetics, heat treatments above 1352 °C are expected to yield two phase Nb_{ss}-α-Nb₅Si₃ composites or at least a stabilization of the α-Nb₅Si₃ at higher temperatures.

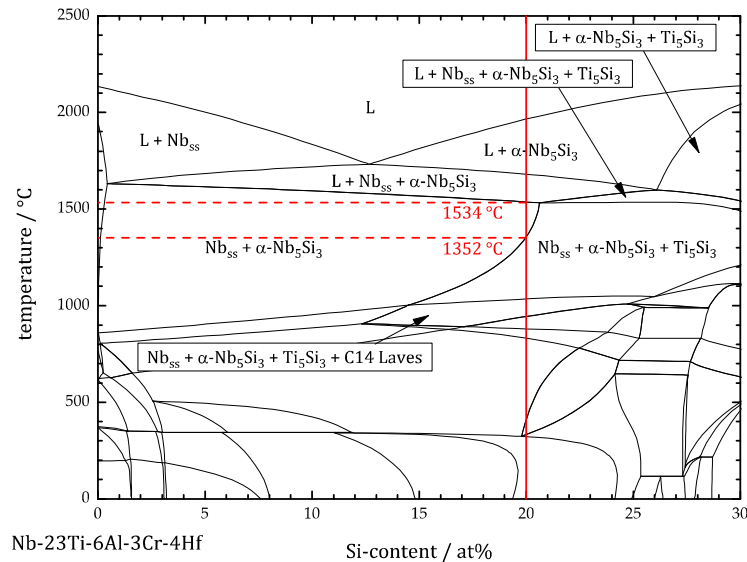


Fig. 6-2: phase diagram calculation using PANDAT of the Nb-xSi-23Ti-6Al-3Cr-4Hf ($0 < x < 30$) isopleth, solid red line indicates the nominal composition used, dashed lines indicate Nb_{ss} and α-Nb₅Si₃ two-phase field boundary temperatures

6.1 Qualitative Microstructural Analysis

Besides the as-consolidated (AC) state four different heat treatments (Table 6-2) were applied to the four AC conditions HIP GA, HIP CGA, PIM GA, and PIM MA₁ to analyze stability ranges of the present phases and to coarsen the microstructure. PIM MA₂ was only heat treated at 1500 °C for 100 h.

Table 6-2: heat treatments investigated

designation	temperature / °C	duration / h
HT1300-100	1300	100
HT1400-20	1400	20
HT1500-20	1500	20
HT1500-100	1500	100

It should be noted that the heat input into the samples after powder production was an additional four hours at 1230 °C for HIP and three hours at 1500 °C for PIM compacted samples.

6.1.1 As-Consolidated Condition

In general four phases could be identified in as-consolidated GA samples using XRD, i.e. Nb_{ss} , $\alpha-Nb_5Si_3$, $\gamma-Nb_5Si_3$, and HfO_2 (Fig. 6-3). In backscatter electron micrographs they appear light grey, dark grey, medium grey, and white, respectively. The $\beta-Nb_5Si_3$ phase that was still present in the gas-atomized powder (section 5.3) transformed into the $\alpha-Nb_5Si_3$, which was absent in the powder.

Samples produced from mechanically alloyed powder (MA1 and MA2) have essentially no $\alpha-Nb_5Si_3$ peaks present. Additionally, PIM MA1 AC comprises some $\beta-Nb_5Si_3$ and titanium nitride, formed due to nitrogen contamination. Hafnium oxide reflexes are much more pronounced in MA samples hinting at a higher oxygen contamination than in GA samples. Instead of titanium nitride PIM MA2 shows the presence of titanium carbide, a result of the carbon contamination from the PCA.

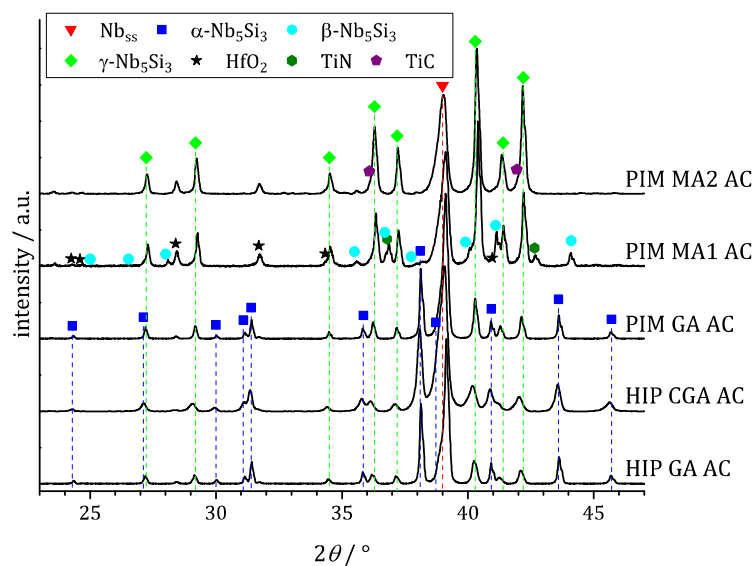


Fig. 6-3: XRD pattern of as-consolidated samples

The heat input during the HIP cycle is lower than for PIM. This leads to very limited coarsening of the microstructure in as-HIP samples. Dendritic structures from the primary solidification of the high-melting Nb_5Si_3 -phase remain visible (dark gray) (Fig. 6-4 and Fig. 6-5). Hafnium oxide is visible as small white particles. Especially in HIP GA, hafnium oxide seems to line the surface of former powder particles indicating a contamination of the powder surface with oxygen prior to consolidation (Fig. 6-5). Since the surface of the loose powder does not show any hafnium oxide (compare section 5.3) the atomization process itself is not responsible. Exposure to oxygen rather happened during powder handling or filling of the HIP can.

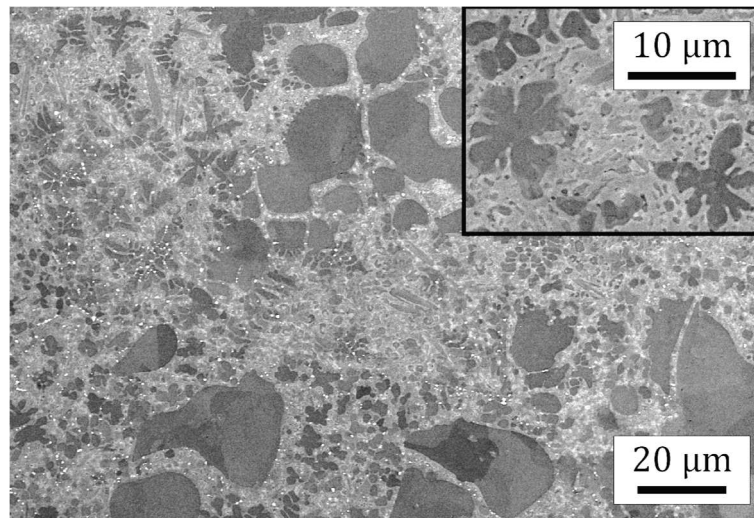


Fig. 6-4: backscatter electron micrograph of HIP CGA AC; inset with higher magnification showing dendritic structures of the solidification; Nb_{ss}, α-Nb₅Si₃, γ-Nb₅Si₃, and HfO₂ in light grey, dark grey, medium grey, and white, respectively

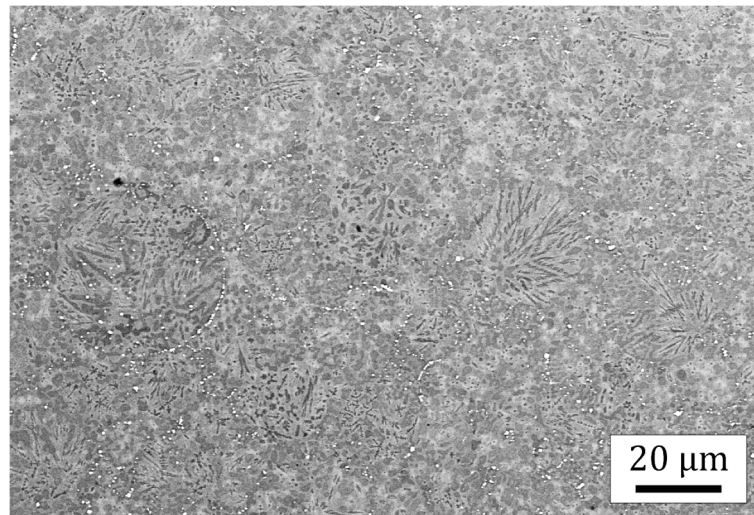


Fig. 6-5: backscatter electron micrograph of HIP GA AC showing HfO₂ lining of the former powder particles; Nb_{ss}, α-Nb₅Si₃, γ-Nb₅Si₃, and HfO₂ in light grey, dark grey, medium grey, and white, respectively

A simple estimation assuming the arithmetic mean of the maximum and minimum size values of 12.5 μm for -25 μm powder fraction and 165.5 μm for the 106-225 μm powder fraction shows a 13 times higher surface area in the -25 μm powder. Hence, it makes sense that lining of the former particles' surface would be more pronounced in the finer powder.

HIP CGA AC shows larger regions of α-Nb₅Si₃ (Fig. 6-4). Macro-segregations in the EIGA electrode are unlikely to be the reason for this, since overall composition as determined by EDS is the same for both samples and both fine and coarse powders are produced simultaneously from the same rod. It is rather a result of a difference in cooling rate. Larger melt droplets take longer to solidify during the gas atomization process and, hence, larger primary Nb₅Si₃ crystals can form [109, p. 97]. This can also be seen in arc-melted material where large primary Nb₅Si₃-dendrites are forming with sizes of the order of 100 μm (Fig. 6-6).

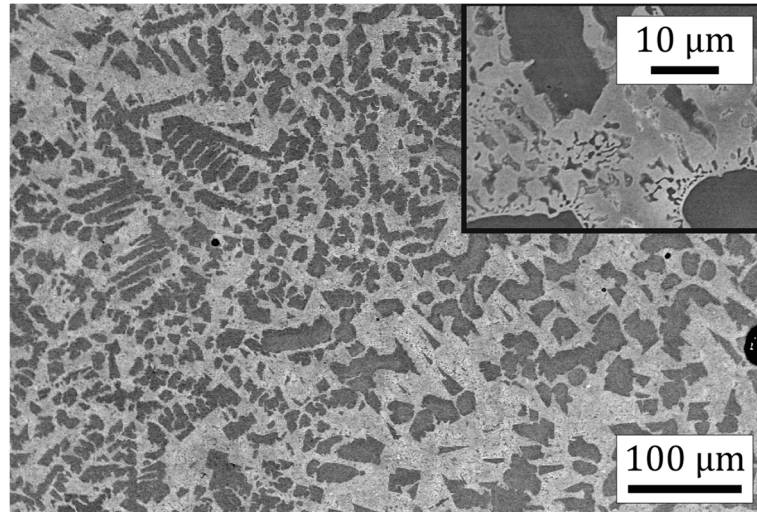


Fig. 6-6: backscatter electron micrograph of ARC showing large blocky primary silicide dendrites; inset with higher magnification showing interdendritic eutectic microstructure; Nb_{ss}, α-Nb₅Si₃, γ-Nb₅Si₃, and HfO₂ in light grey, dark grey, medium grey, and white, respectively

PIM GA AC samples (Fig. 6-7) show that at the sintering temperature of 1500 °C significant coarsening takes place. Solidification dendrites disappeared and equiaxed grains form the microstructure. All GA samples as well as ARC provide a seemingly continuous solid solution matrix with α-Nb₅Si₃ and γ-Nb₅Si₃ grains in-between.

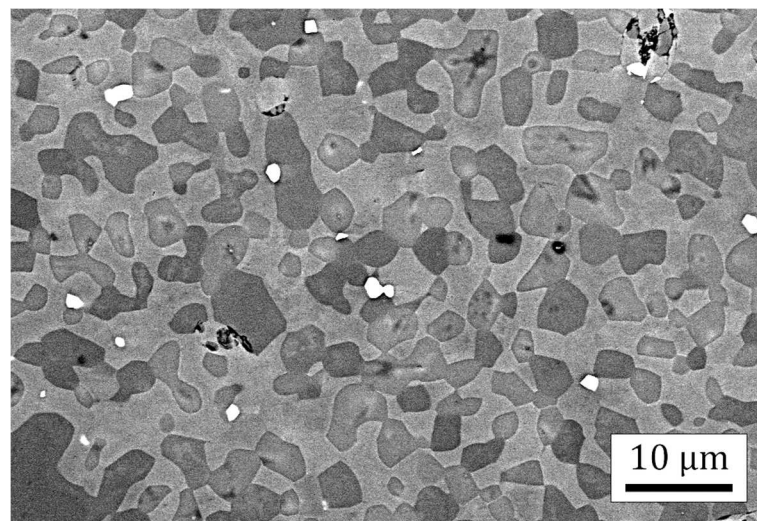


Fig. 6-7: backscatter electron micrograph of PIM GA AC showing an equiaxed microstructure after sintering at 1500 °C for 3 h; Nb_{ss}, α-Nb₅Si₃, γ-Nb₅Si₃, and HfO₂ in light grey, dark grey, medium grey, and white, respectively

The structure is quite different for PIM compacted MA₁ powder (Fig. 6-8). In XRD (Fig. 6-3), the α-Nb₅Si₃ is hardly showing, instead, β-Nb₅Si₃ seems to be stabilized by interstitial contaminations next to the γ-Nb₅Si₃. Still, only the γ-Nb₅Si₃ phase is visible in backscatter electron micrographs. The hafnium oxide content seems to be considerably higher than for GA and a phase containing high titanium contents was identified as TiN. This is a result of the very high content of oxygen and nitrogen, which is gettered by hafnium and titanium, respectively,

during consolidation. Phase distribution is not as homogeneous as for PIM GA. Despite having the same composition, PIM MA₁ AC seems to have a continuous silicide matrix.

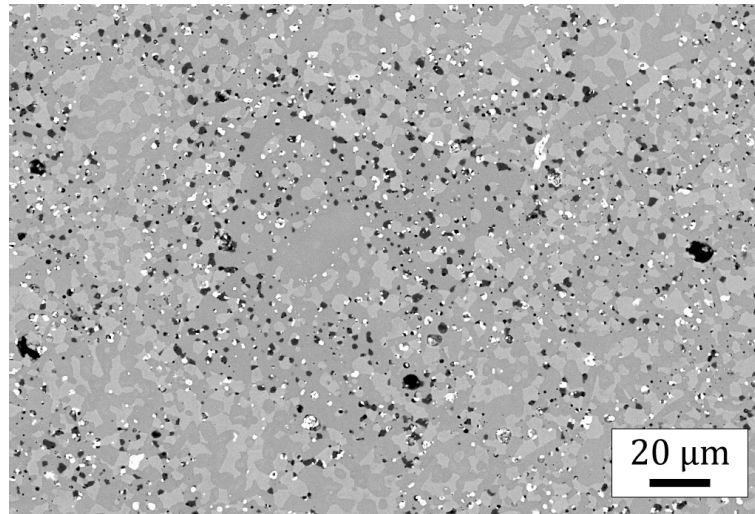


Fig. 6-8: backscatter electron micrograph of PIM MA₁ AC; Nb_{ss}, γ -Nb₅Si₃, HfO₂, and titanium nitride in light grey, dark grey, white, and black, respectively

PIM MA₂ also shows only one silicide, i.e. γ -Nb₅Si₃, in XRD and BSE (Fig. 6-9). Carbon contamination takes the place of nitrogen, leading to the presence of titanium carbide. This can be interpreted as carbon stabilizing γ -Nb₅Si₃ [55] while nitrogen would stabilize γ -Nb₅Si₃ and β -Nb₅Si₃.

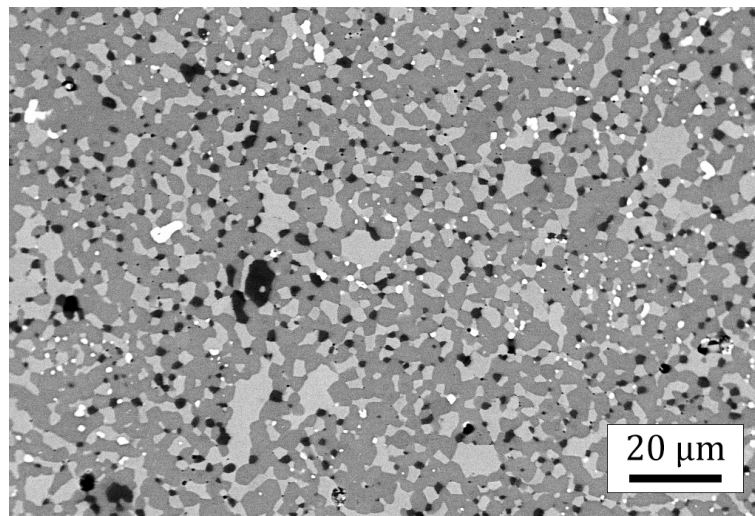


Fig. 6-9: backscatter electron micrograph of PIM MA₂ AC; Nb_{ss}, γ -Nb₅Si₃, HfO₂, and titanium carbide in light grey, dark grey, white, and black, respectively

6.1.2 Heat-Treated at 1300 °C for 100 h and 1400 °C for 20 h

Material from GA powders contains the same phases as the AC condition after heat treatments at 1300 and 1400 °C (Fig. 6-10 for HIP GA, PIM GA is found in the Appendix Fig. 14-3, p. 148). Next to some coarsening of the microstructure, it appears that for HT1300-100 also the phase contrast changes. γ -Nb₅Si₃ has a higher solubility for hafnium making it appear brighter than the solid solution. XRD on PIM MA₁ (Fig. 6-11) suggests a considerable amount of α -Nb₅Si₃

being present after both heat treatments; however, those are not distinguishable from γ - Nb_5Si_3 in SEM. Backscatter electron micrographs for all performed heat treatments are shown in Fig. 6-12.

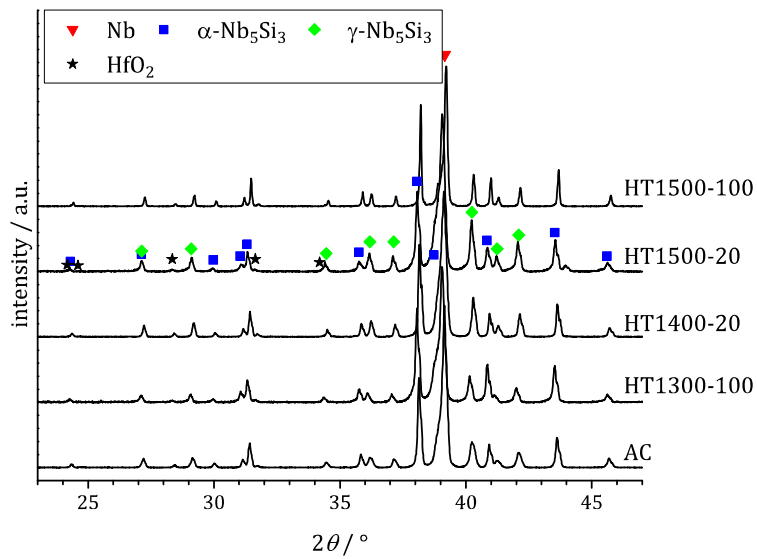


Fig. 6-10: XRD pattern for HIP GA AC and heat-treated conditions

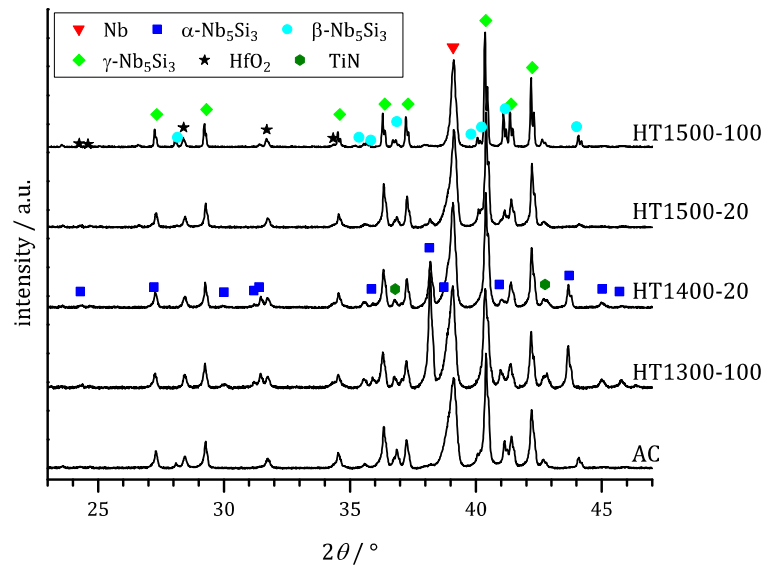


Fig. 6-11: XRD pattern for PIM MA1 AC and heat-treated conditions

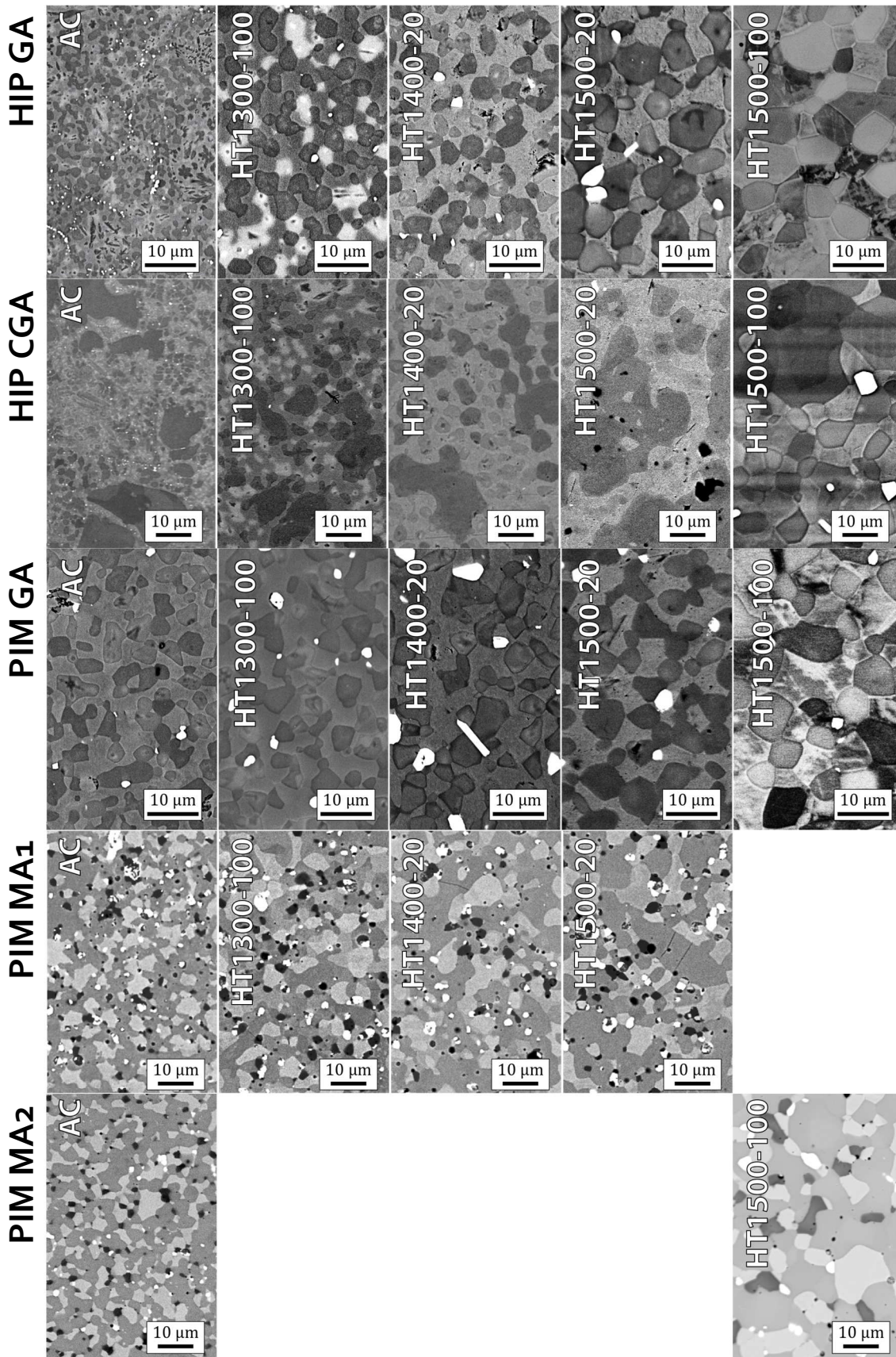


Fig. 6-12: backscatter electron micrographs of AC and heat-treated conditions for HIP GA, HIP CGA, PIM GA, PIM MA₁, PIM MA₂; Nb_{ss} in light grey, α-Nb₅Si₃ in dark grey, γ-Nb₅Si₃ in medium grey, HfO₂ in white, and titanium nitride and titanium carbide in black for PIM MA₁ and PIM MA₂, respectively; for HT₁₃₀₀₋₁₀₀ of GA material, γ-Nb₅Si₃ is brighter than Nb_{ss}

6.1.3 Heat-Treated at 1500 °C for 20 h and 100 h

XRD measurements on GA samples still show the same phases after heat treatments at 1500 °C as for AC and the lower temperature heat treatments (Fig. 6-10). In the SEM, samples heat-treated at 1500 °C show regions of increased hafnium oxide content surrounded by networks of a dark gray phase (Fig. 6-16, left), which, judging from its composition, seems to be $\alpha\text{-Nb}_5\text{Si}_3$. However, it only comes to light with the help of EBSD local structure analysis that actually diffraction patterns from the center of this network do not belong to the $\alpha\text{-Nb}_5\text{Si}_3$, but a different tetragonal phase instead. Both Nb_3Si and $\beta\text{-Nb}_5\text{Si}_3$ are tetragonal with similar lattice constants (see Table 2-1 on p. 6) and fit the diffraction pattern (Fig. 6-13). However, of the two measured diffraction bands marked in red in Fig. 6-13, only one should be present in Nb_3Si . $\beta\text{-Nb}_5\text{Si}_3$ on the other hand possesses both bands, showing that the networks consist of $\beta\text{-Nb}_5\text{Si}_3$.

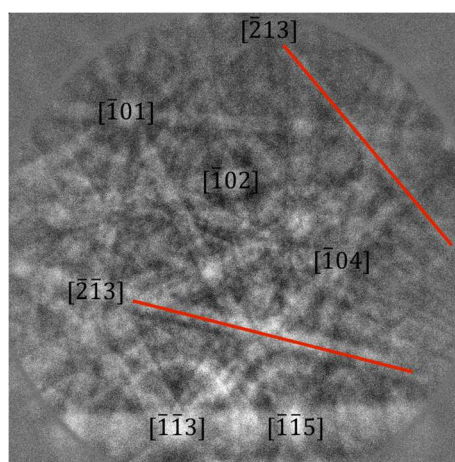


Fig. 6-13: indexed electron backscatter diffraction pattern of $\beta\text{-Nb}_5\text{Si}_3$ with the relevant bands marked in red

This is supported by the EDS analysis giving a concentration of Si+Al of 34.9 %, which is in the expected range for a 5-3 silicide. This $\beta\text{-Nb}_5\text{Si}_3$ is engulfed by an $\alpha\text{-Nb}_5\text{Si}_3$ seam (Fig. 6-14). Because of the network structure of $\beta\text{-Nb}_5\text{Si}_3$, where each network represents a single crystallographic orientation, the chance for it to fulfill the Bragg condition during XRD is very low and, thus, this phase did not show up in XRD measurements. Fig. 6-15, left, shows only three $\beta\text{-Nb}_5\text{Si}_3$ grains are present in the analyzed section. The solid solution does not show any preferential orientation Fig. 6-15, middle. Two aspects are noteworthy here: the localization of $\beta\text{-Nb}_5\text{Si}_3$ formation and the fact that each network seems to represent a single grain. In a homogeneous material, if $\beta\text{-Nb}_5\text{Si}_3$ forms, it should not be confined to spots of 300 μm in diameter. The localization is explained by the higher amount of hafnium oxide in the vicinity of $\beta\text{-Nb}_5\text{Si}_3$ grains. An inhomogeneous distribution of oxygen throughout the sample is most likely responsible. This is confirmed by the fact that if the sample is lying directly on the boat during heat treatment, oxygen leaving the boat increases the oxygen content on that side of the sample, leading to increased hafnium oxide formation and subsequently to $\beta\text{-Nb}_5\text{Si}_3$. Over and above the penetration depth of this extrinsic oxygen increase, only very locally some spots show the formation of $\beta\text{-Nb}_5\text{Si}_3$ (Fig. 6-16). This suggests oxygen content is indeed inhomogeneously distributed throughout the sample or at least it agglomerates during heat treatment and is the reason for $\beta\text{-Nb}_5\text{Si}_3$ formation.

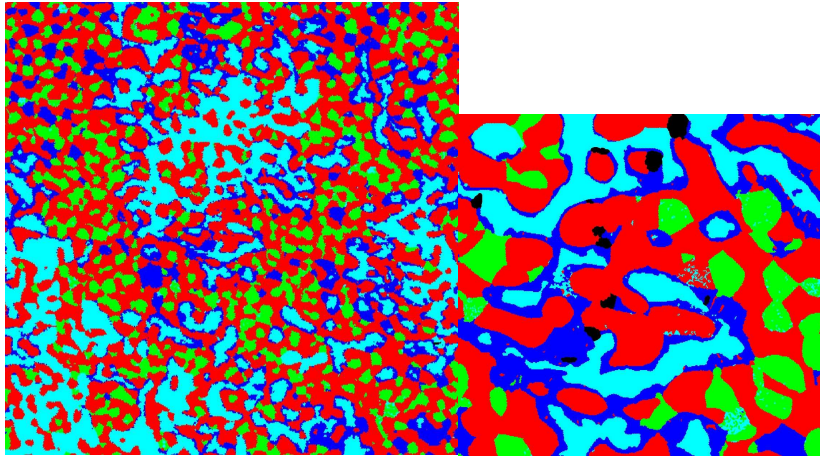


Fig. 6-14: left: EBSD phase map of HIP GA HT₁₅₀₀₋₁₀₀, Nb_{ss} in red, α -Nb₅Si₃ in blue, β -Nb₅Si₃ in light blue, γ -Nb₅Si₃ in green, image width 320 μ m; right: detail of left, HfO₂ (not indexed) manually recolored in black from image quality data, image width 80 μ m

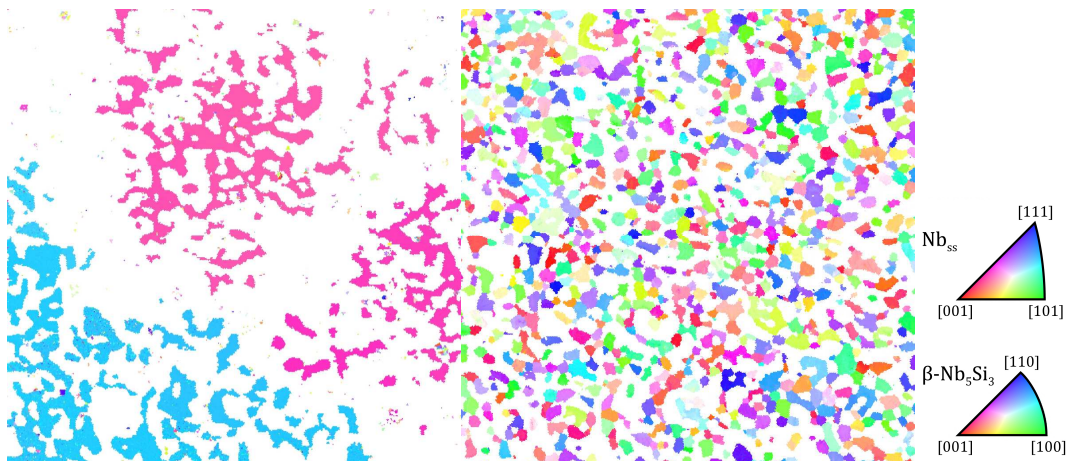


Fig. 6-15: EBSD orientation map of β -Nb₅Si₃ (left) and Nb_{ss} (middle), same field of view as the left part of Fig. 6-14, with IPF coloring legend (right)

Each β -Nb₅Si₃ network forming a single grain can only be explained by going through the liquid phase. Local melt – due to compositional differences – solidifies during furnace cooling (250 K/h) as one single grain. The melting seems mainly confined to the silicide phases as no preferential orientation of the solid solution can be detected (Fig. 6-15, right).

There is no data on the influence of oxygen on the melting temperature of Nb₅Si₃ or any silicide available, except for the iron silicides, which show a decrease in melting temperature with the addition of oxygen [161]. Also, the binary Nb-O phase diagram indicates a steep decrease of solidus temperature with increasing amount of solute oxygen [162]. A similar behavior is assumed for the mixture of silicides in this case, with oxygen reducing the melting temperature below 1500 °C, while the melting temperature of the solid solution is still above 1500 °C. The furnace was calibrated to have an actual temperature of 1499 ± 1 °C in the hot zone. Even though the cooling rate is much lower after heat treatment than during gas atomization, β -Nb₅Si₃ is still present at room temperature. As β -Nb₅Si₃ transforms to α -Nb₅Si₃ for the powder, also for the bulk material an additional heat treatment at lower temperature should result in the

disappearance of $\beta\text{-Nb}_5\text{Si}_3$, as it is in fact the case for material HIPed again after heat treatment (Fig. 14-4 in the Appendix).

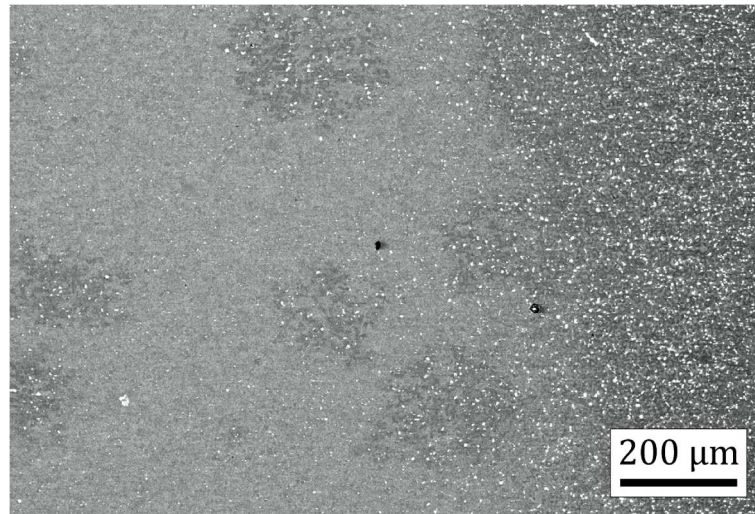


Fig. 6-16: backscatter electron micrograph of PIM GA HT1500 showing high hafnium oxide content close to the surface lying on the boat with resulting $\beta\text{-Nb}_5\text{Si}_3$ formation (right) and only select spots of $\beta\text{-Nb}_5\text{Si}_3$ in the bulk (left)

PIM MA₁ HT1500 goes back to the phase constituents of the AC condition with $\alpha\text{-Nb}_5\text{Si}_3$ disappearing and $\beta\text{-Nb}_5\text{Si}_3$ coming back (Fig. 6-11). In this case, it is not clear, if liquid is forming during heat treatment. But no network-like structures as in the GA material were visible and the significantly different chemistry (compare next chapter) may lead to $\beta\text{-Nb}_5\text{Si}_3$ without liquid phase formation.

6.2 Quantitative Microstructural Analysis

Phase diagrams describe the equilibrium state of a system. Heating and cooling rates during real-life heat treatments generally do not comply with that assumption. An extreme example would be the quenching of age-hardenable alloys after solution annealing, where solute atoms remain in the matrix, contrary to the equilibrium state. Also, kinetically retarded reactions may not take place, even if temperature is held for a long time, e.g. decomposition of Nb_3Si into Nb_{ss} and $\alpha\text{-Nb}_5\text{Si}_3$ [38]. Hence, depending on the heat treatment temperature – and cooling rate thereafter –, samples may not end up in the same microstructural configuration. Quantitative phase analysis is, thus, a prerequisite to connecting microstructure with mechanical properties. In the following chapter, different methods for determining the phase fractions in differently produced and heat-treated Nb-20Si-23Ti-6Al-3Cr-4Hf will be introduced and discussed regarding their suitability for the system. Analyses are usually done on two-dimensional cross-sections of the samples. It is accepted that phase fractions determined by areal analysis (6.2.1 Threshold Analysis, 6.2.3 Electron Backscatter Diffraction (EBSD), and 6.2.4 Reference-Intensity-Ratio Method (RIR)) or point counting (6.2.2 Grid Counting Method) on representative cross-sections will yield the volume fraction of the analyzed phases [163, p. 427].

As the studied alloy is very sensitive to the surrounding atmosphere and phase fractions may be influenced by oxygen absorption, only samples that were heat-treated in a powder bed will be discussed in this section, i.e. AC, HT1300-100, HT1400-20, and HT1500-20.

6.2.1 Threshold Analysis

The easiest way to determine the phase fractions would be to evaluate several micrographs of a cross-section in which each phase shows a distinct brightness. By using image analysis software such as ImageJ¹, the number of pixels in a brightness range specific to each phase can be determined compared to the overall number of pixels. Typically, backscatter electron imaging of an SEM shows feasible phase contrast, as the mean atomic numbers are usually quite different. The three main phases in GA produced material are Nb_{ss}, α-Nb₅Si₃, and γ-Nb₅Si₃ with mean atomic numbers of about 29, 33, and 33, respectively. The similarity of the mean atomic numbers together with inevitable noise leads to insufficient contrast to separate these phases (Fig. 6-17, left). Only hafnium oxide due to the high atomic mass of hafnium is separable, as it appears white. PIM MA₁ and PIM MA₂ on the other hand show four distinct peaks in the brightness histogram (Fig. 6-17, right). The overlap of the silicide peak with the solid solution peak is not separable by a simple threshold value, but can be evaluated by fitting with a double peak function. This makes PIM MA₁ and PIM MA₂ accessible to phase fraction analysis based on backscatter electron micrographs. The hafnium oxide content determined by the brightness threshold is given in Table 6-3.

Optical micrographs show insufficient contrast for all samples.

Table 6-3: area fraction of HfO₂ as determined from backscatter electron micrographs in %

	HIP GA	PIM GA	PIM MA ₁	PIM MA ₂
AC	0.8 ± 0.1	0.8 ± 0.1	3.4 ± 0.3	1.5 ± 0.1
HT1300-100	0.7 ± 0.1	0.8 ± 0.0	3.3 ± 0.4	—
HT1400-20	0.7 ± 0.1	0.7 ± 0.1	2.9 ± 0.4	—
HT1500-20	0.8 ± 0.3	0.9 ± 0.2	3.3 ± 0.4	—

The overall hafnium oxide content stays constant throughout all heat treatments suggesting most of the oxygen was gettered already during manufacturing. The slightly higher standard deviation for GA HT1500-20 material is a result of some BSE micrographs containing localized β-Nb₅Si₃ regions with subsequently increased hafnium oxide content as discussed in section 6.1.3. The allocation of the brightness threshold includes a subjective error, as the phase boundary is not infinitely sharp. To minimize this issue, all micrographs evaluated for each sample were taken without changing the brightness settings of the SEM and the threshold value stayed constant. This means that the standard deviation given in Table 6-3 represents only the statistical variation in hafnium oxide content throughout the micrographs while the choice of threshold value per sample condition would add an additional error of about 0.1 %.

¹ ImageJ is a Java based image analysis software developed by Wayne Rasband from the National Institutes of Health, USA, and is free to use without a license. Available at: <http://imagej.nih.gov/ij/> (as of June 2015)

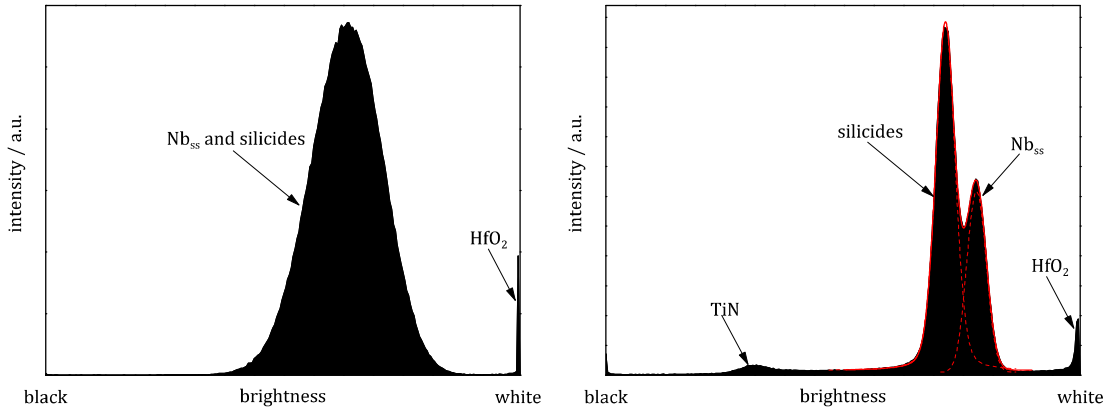


Fig. 6-17: brightness histogram for PIM GA AC (left) showing insufficient separation of the brightness ranges of the three main phases, hafnium oxide to the right is separable; brightness histogram for PIM MA₁ AC (right) shows four separable phases with acceptable overlap of the brightness ranges of Nb_{ss} and silicides

The whole phase results for PIM MA₁ can be seen in Fig. 6-18. Different silicides could not be distinguished from micrographs. The total silicide content shows a slight decrease from 65 to 62 % for HT1500-20, which may be due to higher solubility of silicon in Nb_{ss}. The volume fractions of solid solution, silicide, titanium carbide, and hafnium oxide in PIM MA₂ AC are 25.0 ± 2.0 , 66.8 ± 1.5 , 6.8 ± 0.7 , and 1.5 ± 0.1 %, respectively. This is very similar to PIM MA₁ AC. In both cases, the titanium-rich phase (TiN and TiC) and hafnium oxide add up to 8.3 %, with niobium solid solution contents being only about 26.2 and 25.0 % for the MA₁ and MA₂, respectively.

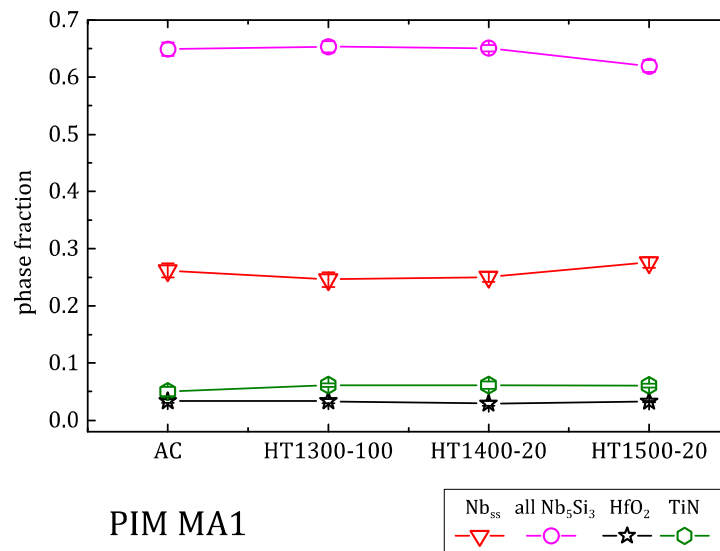


Fig. 6-18: phase fractions determined by brightness threshold on BSE micrographs for PIM MA₁.

6.2.2 Grid Counting Method

Even though the contrast on a polished cross-section is insufficient in electron and optical microscopy, etching can remedy that, if the attack is different on each phase. The recipe Cr m11 by Petzow [148] does not enable automatic phase detection, but makes it possible to manually

discriminate phases (Fig. 6-19). The grid spacing was chosen to be in the range of the phase size. A minimum of 1800 points were counted for each condition of heat-treated PIM GA samples. The resulting phase volume fractions are plotted in Fig. 6-20.

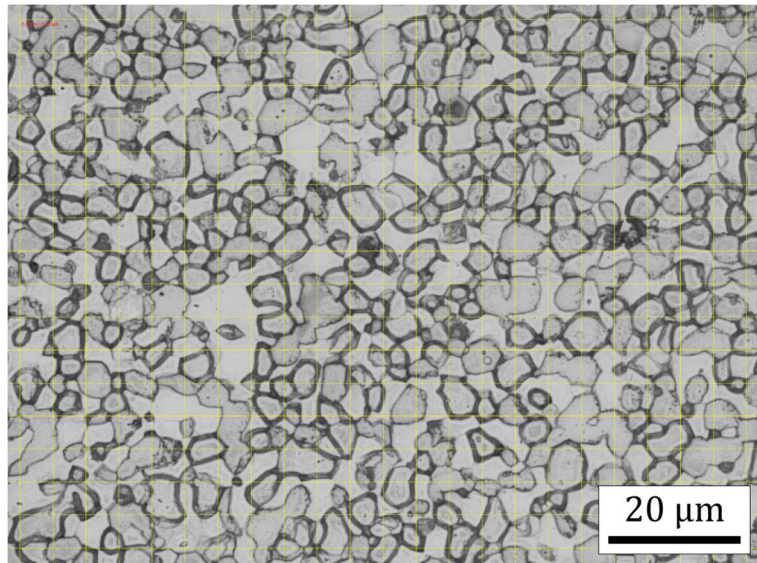


Fig. 6-19: optical micrograph of PIM GA HT₁₄₀₀₋₂₀ after polishing and etching. A typical grid used for counting is overlaid

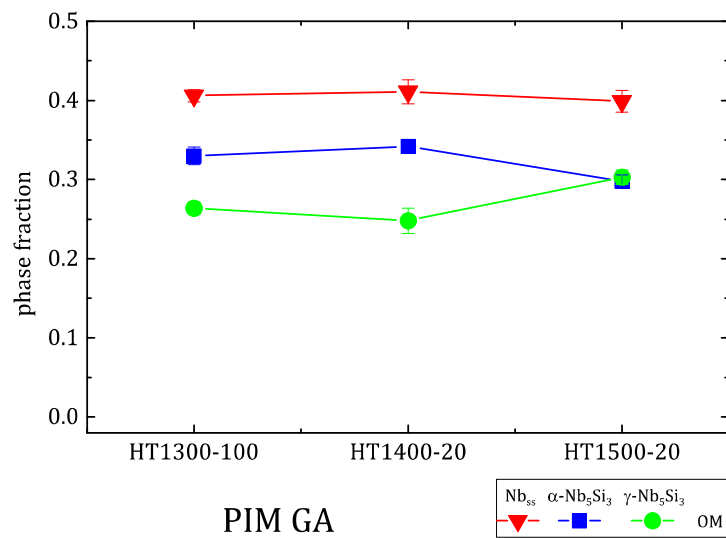


Fig. 6-20: phase fractions determined by grid counting for PIM GA

The error bars shown give the standard deviation from several micrographs analyzed. The absolute error made in regard to the number of points is its inverse, in this case < 0.06 %, and, hence, negligible. However, other errors play a more important role. Hafnium oxide cannot be distinguished from γ -Nb₅Si₃, but takes up only about 0.8 % for the GA samples. Also, due to the very different hardness of the phases, a pronounced topography after polishing cannot be completely suppressed. The subsequent etching leads to marked phase boundaries with a certain thickness, which makes attribution to the correct phase difficult.

6.2.3 Electron Backscatter Diffraction (EBSD)

EBSD is a very versatile tool, which can give – by determining the crystallographic orientation in each raster point – information about the deformation state, the type of grain boundaries, grain sizes, or even residual stresses and dislocation structures. This is done by correlation of the diffraction pattern recorded to a crystallographic orientation. Thus, the crystallographic structure needs to be known, or at least only a small number of possible phases with sufficiently different crystallography has to be preselected. The method is quite similar to the point counting method with a much higher number of points and an automated “counting” algorithm. Still, some orientations of different crystals may look similar in the diffraction pattern. Examples of indexed patterns for Nb_{ss} , $\alpha-Nb_5Si_3$, $\beta-Nb_5Si_3$, and $\gamma-Nb_5Si_3$ are given in Fig. 6-22. Hafnium oxide is not properly distinguishable from $\gamma-Nb_5Si_3$ and will therefore be allocated to the latter. The software calculates the likelihood for either phase to be the right choice, but may choose the wrong one. This would lead to singular meter points in a grain to show a different phase (Fig. 6-21, left). Especially $\gamma-Nb_5Si_3$ oftentimes is falsely detected as $\alpha-Nb_5Si_3$. Cleanup procedures can help reducing the wrongly indexed points, but they have to be applied carefully, because this could also change correctly indexed points or even “eat up” whole grains (Fig. 6-21, middle). Manual control of the effect of each cleanup step led to a grain dilation correction giving the best compromise between removing wrongly indexed points and keeping the original morphology of the grains (Fig. 6-21, right).

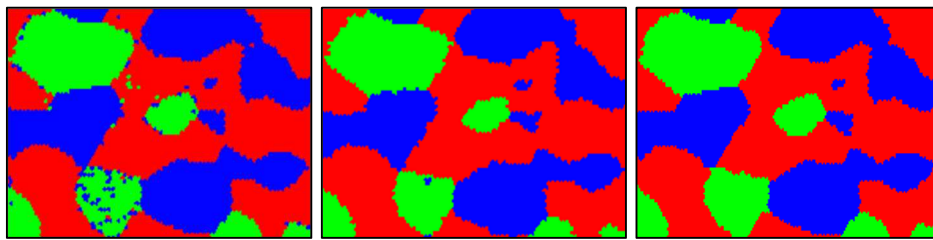


Fig. 6-21: partial of a phase map of HIP GA HT₁₃₀₀₋₁₀₀ (Nb_{ss} : red, $\alpha-Nb_5Si_3$: blue, $\gamma-Nb_5Si_3$: green) showing obviously wrong phase identifications mainly in the $\gamma-Nb_5Si_3$ phase and influences from cleanups: raw (left), standard cleanup procedure consisting of three steps: grain dilation, neighbor CI correlation, and neighbor phase correlation (middle), one-step cleanup with grain dilation only (right); image width is 15 μm , each

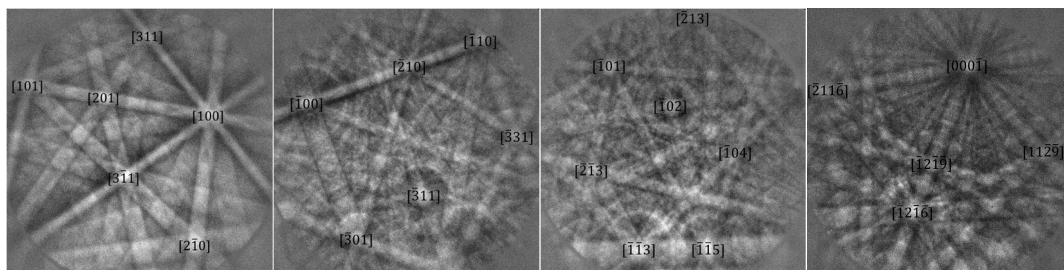


Fig. 6-22: indexed EBSD pattern of Nb_{ss} , $\alpha-Nb_5Si_3$, $\beta-Nb_5Si_3$, and $\gamma-Nb_5Si_3$ (from left to right)

The analyzed area divided by the squared step size (resolution) yields the number of points indexed (duration of the measurement). Hence, to keep the duration acceptable, a compromise between morphological resolution and analyzed area has to be found. Phase fraction analysis

was done on the HT₁₃₀₀₋₁₀₀ condition of HIP and PIM as a comparison to the other methods for $80 \times 80 \mu\text{m}^2$ with $0.2 \mu\text{m}$ step size and $320 \times 320 \mu\text{m}^2$ with $0.8 \mu\text{m}$ step size, each. The result is given in Table 6-4. The errors estimated represent the standard deviation of the sampling error done when determining the phase fractions on the 16 individual $80 \times 80 \mu\text{m}^2$ tiles of the $320 \times 320 \mu\text{m}^2$ map. This error, as a result of choice of analyzed area, is in all cases below 3 vol%. The high-resolution measurements on $80 \times 80 \mu\text{m}^2$ areas yield phase fractions comparable to the large area scans within the sampling error.

Table 6-4: phase fractions of HIP and PIM after HT₁₃₀₀₋₁₀₀ determined by EBSD

phase	HIP GA HT ₁₃₀₀₋₁₀₀ 80 × 80	HIP GA HT ₁₃₀₀₋₁₀₀ 320 × 320	PIM GA HT ₁₃₀₀₋₁₀₀ 80 × 80	PIM GA HT ₁₃₀₀₋₁₀₀ 320 × 320
Nb _{ss}	0.466	0.467 ± 0.013	0.451	0.458 ± 0.008
α-Nb ₅ Si ₃	0.368	0.357 ± 0.015	0.333	0.337 ± 0.020
γ-Nb ₅ Si ₃	0.167	0.177 ± 0.008	0.216	0.206 ± 0.025

6.2.4 Reference-Intensity-Ratio Method (RIR)

Getting quantitative phase analysis information from XRD measurements generally involves doing a full pattern fit e.g. by the Rietveld method [151]. This method is based on the description of a diffraction pattern by analytical functions. Using the least squares method several functional parameters are fitted simultaneously to achieve a good agreement between the actual measurement and the analytical description. For all present phases a structure model is needed for the method to be applicable. This is why the applicability for the system analyzed in this work is not given. While the binary phases of the niobium silicide system are well described, i.e. Nb_{ss}, α-Nb₅Si₃, β-Nb₅Si₃, γ-Nb₅Si₃, and Nb₃Si, the atomic positions within the unit cell for the other alloying elements, i.e. Ti, Al, Cr, and Hf, are not clear. For example, aluminum is known to occupy silicon atomic sites in the intermetallic compounds [164]. However, α-Nb₅Si₃ and β-Nb₅Si₃ have two silicon sites for which the partitioning of aluminum may be different. The same holds true for titanium on niobium sites and so on. The diffracted intensity I_{hkl} over the incident intensity I_0 of a lattice plane hkl is generally given by [149]:

$$\frac{I_{hkl}}{I_0} = K \cdot G_f(\theta) \cdot L(\theta) \cdot P(\theta) \cdot A \cdot E \cdot H \cdot |F(hkl)|^2 \quad (6-1)$$

K : constant factors

G_f : angle dependent factors

L : Lorentz factor

P : polarization factor

A : absorption factor

E : extinction factor

H : multiplicity of equivalent planes

$F(hkl)$: structure factor

The factor influencing the intensity the most with respect to the composition is the structure factor $F(hkl)$, which comprises of the form factor – diffraction contribution of the element species – and the position of each species in the unit cell.

Hence, in the six-component system Nb-20Si-23Ti-6Al-3Cr-4Hf the atomic structure that has a significant influence on the relative intensities of the diffraction peaks is unclear. To conclusively shed light on this, a lot of work in the ternary and quaternary systems, Nb-Si-X and Nb-Si-X-Y, would be necessary, which is outside of the scope of this work.

Nevertheless, attempts were made to describe a diffraction pattern of Nb-20Si-23Ti-6Al-3Cr-4Hf analytically with the Rietveld method. The relative intensities of each phase could not be properly fitted, making it impossible to extract reliable quantitative phase data.

To still be able to extract quantitative phase information from XRD analysis, the RIR-method as proposed by the International Centre for Diffraction Data (ICDD) was used. This method compares the measured peak intensity to a common standard, i.e. corundum. The scaling factor can be obtained by dividing the highest peak's integral intensity of the analyte I_a by the highest peak's integral intensity of corundum I_c in a 50/50-% mixture of analyte and corundum. Knowing this ratio for different materials makes it possible to estimate quantitative phase data also from mixtures not containing corundum by comparing the highest peaks. The I_a/I_c ratio is provided for many phases in the ICDD database of powder diffraction data [156]. Of course, this is as inaccurate as the Rietveld refinement due to the presence of the alloying elements changing the intensities in comparison to the binary phases from the database. But the RIR method can be "tuned" to the system analyzed, by adjusting the I_a/I_c ratios using phase fraction measurements by other means. The limitation on this is obviously that this calibration would hold true only if the composition of the analyzed phase is the same as the one used for calibration. If that would actually be the case, phase fractions could not change. Hence, depending on the amount of changes in the composition in each phase during heat treatment, some errors are expected. However, as will be described in chapter 6.2.6, changes between heat treatment conditions are rather minor compared to the total amount of alloying elements present in each phase. The peaks used for the phase fraction analysis of XRD data are given in Table 6-5.

Table 6-5: diffraction plane of highest intensity, diffraction angle of this peak in the database and as determined in this work, and corresponding PDF entry from the ICDD database

phase	main peak	2 θ (database) / °	2 θ (this work) / °	PDF [156]
Nb _{ss}	{110}	38.610	39.10	01-1183
α -Nb ₅ Si ₃	{213}	38.101	38.15	30-0874
β -Nb ₅ Si ₃	{411}	41.128	40.98	30-0875
γ -Nb ₅ Si ₃	{21 $\bar{3}$ 1}	40.340	40.334	08-0422
Nb ₃ Si	{211}	42.941	42.843	89-5321

Crystallite size and preferred crystallite orientation, i.e. texture, will influence diffraction statistics and hence the relative intensities. This could lead to the effect of mismatch in relative intensities, which inhibited the use of the Rietveld method. The isotropic cooling of the droplets during GA, the lack of preferential orientation of spherical powder particles, and the isotropic heat input in the PIM and HIP processes and during heat treatment suggest the absence of any crystallographic texture. Even though not spherical in shape, also MA powder is expected to not have any texture present. Texture information is also a result of the EBSD measurement from the previous section and proves this assumption for the two samples HIP GA HT₁₃₀₀₋₁₀₀ and PIM GA HT₁₃₀₀₋₁₀₀ (Table 6-6). Since the analyzed area is relatively small, some minor texture as a result of grain statistics is visible with the multiples of the uniform distribution (MUD) not surpassing values of 2 for γ -Nb₅Si₃ (< 20 vol%). The phase with the highest volume fraction, Nb_{ss} (\approx 45 vol%) does not even reach 1.15. Hence, this minor texture does not imply overall preferential grain orientation.

Phase fractions for HIP GA and PIM GA obtained by the RIR method show relatively good agreement (Fig. 6-23 and Fig. 6-24). The intensity ratios I_a/I_c were fitted on the actual volume fractions obtained by EBSD for the HT₁₃₀₀₋₁₀₀ condition. Both HIP and PIM show the same tendency of decreasing α -Nb₅Si₃ and increasing γ -Nb₅Si₃ content as heat treatment temperature rises from 1300 °C to 1500 °C. Meanwhile Nb_{ss} content stays constant. Also absolute values show good agreement. For the GA powder, I_a/I_c of the β -Nb₅Si₃ phase was adjusted, so that Nb_{ss} content would attain the mean value of all other conditions. Since the GA powder after quenching from the melt is far from equilibrium and phase compositions may be significantly different from those in compacted samples, those data points have a rather qualitative character to illustrate the presence of β -Nb₅Si₃ in the powder and its transformation into α -Nb₅Si₃ already after compaction.

In case of PIM MA₁ (Fig. 6-25), which was calibrated on HT₁₃₀₀₋₁₀₀ from the threshold analysis data, the same tendency of higher heat treatment temperatures stabilizing γ -Nb₅Si₃ and a constant Nb_{ss} volume fraction is apparent, although at different absolute volume fractions. Peak intensities of α -Nb₅Si₃ after being heated to 1500 °C, i.e. AC and HT₁₅₀₀₋₂₀, are minimal and are only partially replaced by β -Nb₅Si₃. γ -Nb₅Si₃ is the main silicide phase present in all cases.

Table 6-6: inverse pole figures for the three main phases of HIP GA HT₁₃₀₀₋₁₀₀ (left) and PIM GA HT₁₃₀₀₋₁₀₀ (right); colors indicate multiples of the uniform distribution (MUD)

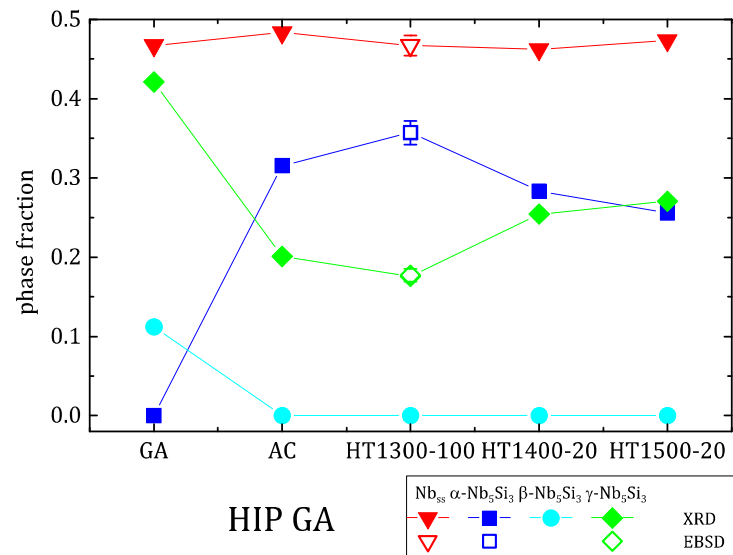
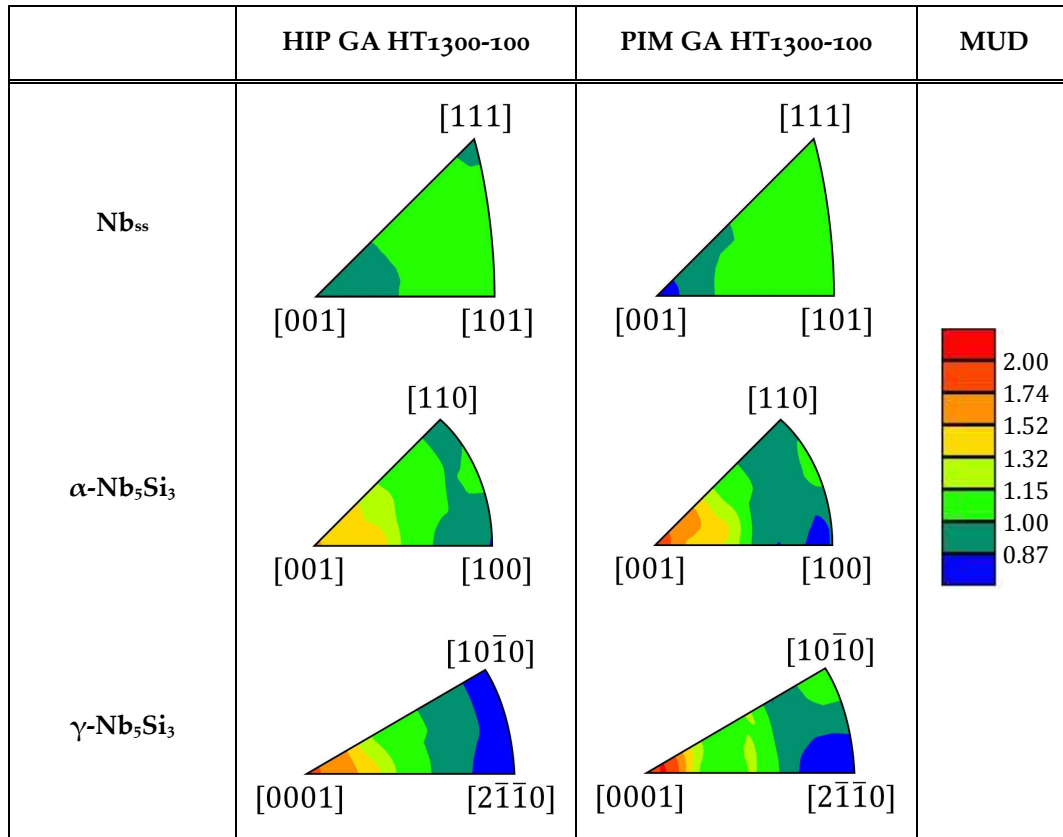


Fig. 6-23: phase fractions obtained by the RIR method for HIP GA; I_a/I_c ratios were calibrated on the EBSD measurement of the heat treatment HT₁₃₀₀₋₁₀₀.

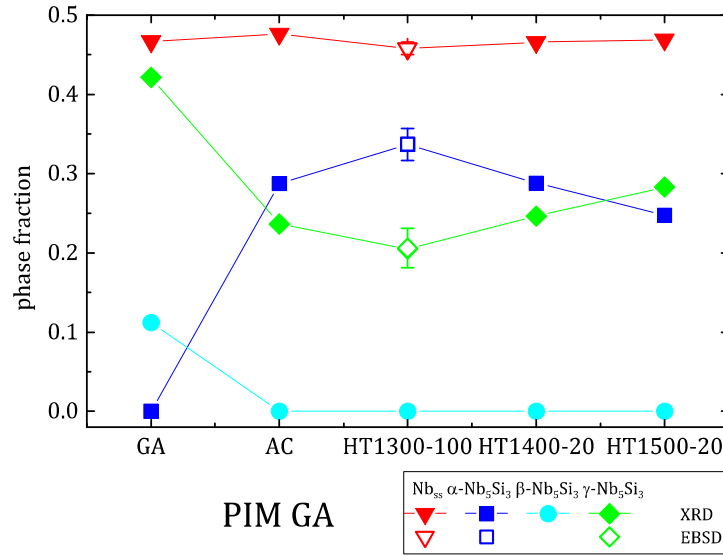


Fig. 6-24: phase fractions obtained by the RIR method for PIM GA; I_a/I_c ratios were calibrated on the EBSD measurement of the heat treatment HT1300-100.

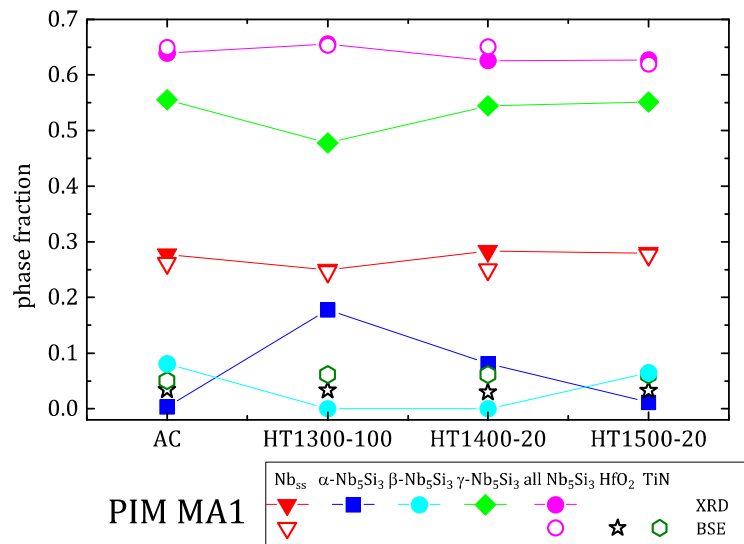


Fig. 6-25: phase fractions obtained by the RIR method for PIM MA1; I_a/I_c ratios were calibrated on the threshold analysis fractions for heat treatment HT1300-100.

6.2.5 Lever Rule Calculations

If the chemical composition of each phase in the composite as well as the overall one is known, the following linear system of equations can be set up (Eq. (6-2)), which could be seen as the expansion of the lever rule to multiple components and phases. This is based on a matrix (χ_{ij} or $\underline{\chi}$) containing the mole fractions of each constituent i in each phase j , the vector of the mole fractions $\vec{\chi}_p$ of the phases, and the vector of the overall composition $\vec{\chi}_0$.

$$\underline{\chi} \cdot \vec{\chi}_p = \vec{\chi}_0 \quad (6-2)$$

For the analyzed system of this work, containing Nb_{ss} (ss), α-Nb₅Si₃ (α), γ-Nb₅Si₃ (γ), and HfO₂, the resulting equation system looks like this.

$$\begin{pmatrix} \chi_{Nb}^{ss} & \chi_{Nb}^{\alpha} & \chi_{Nb}^{\gamma} & \chi_{Nb}^{HfO_2} \\ \chi_{Si}^{ss} & \chi_{Si}^{\alpha} & \chi_{Si}^{\gamma} & \chi_{Si}^{HfO_2} \\ \chi_{Ti}^{ss} & \chi_{Ti}^{\alpha} & \chi_{Ti}^{\gamma} & \chi_{Ti}^{HfO_2} \\ \chi_{Al}^{ss} & \chi_{Al}^{\alpha} & \chi_{Al}^{\gamma} & \chi_{Al}^{HfO_2} \\ \chi_{Cr}^{ss} & \chi_{Cr}^{\alpha} & \chi_{Cr}^{\gamma} & \chi_{Cr}^{HfO_2} \\ \chi_{Hf}^{ss} & \chi_{Hf}^{\alpha} & \chi_{Hf}^{\gamma} & \chi_{Hf}^{HfO_2} \end{pmatrix} \cdot \begin{pmatrix} \chi_p^{ss} \\ \chi_p^{\alpha} \\ \chi_p^{\gamma} \\ \chi_p^{HfO_2} \end{pmatrix} = \begin{pmatrix} \chi_{Nb}^0 \\ \chi_{Si}^0 \\ \chi_{Ti}^0 \\ \chi_{Al}^0 \\ \chi_{Cr}^0 \\ \chi_{Hf}^0 \end{pmatrix} \quad (6-3)$$

Since only the four components of $\vec{\chi}_p$ are unknown in a system of six equations the system is over-determined and not solvable analytically. It should be noted that in an ideal system two equations should be canceled out, but due to inherent deviations in the determination of the mole fractions and scatter in the composition of individual grains, this system cannot be solved. Hence, an additional error element $\vec{\delta}$ is introduced for each constituent to account for those deviations.

$$\begin{pmatrix} \chi_{Nb}^{ss} & \chi_{Nb}^{\alpha} & \chi_{Nb}^{\gamma} & \chi_{Nb}^{HfO_2} \\ \chi_{Si}^{ss} & \chi_{Si}^{\alpha} & \chi_{Si}^{\gamma} & \chi_{Si}^{HfO_2} \\ \chi_{Ti}^{ss} & \chi_{Ti}^{\alpha} & \chi_{Ti}^{\gamma} & \chi_{Ti}^{HfO_2} \\ \chi_{Al}^{ss} & \chi_{Al}^{\alpha} & \chi_{Al}^{\gamma} & \chi_{Al}^{HfO_2} \\ \chi_{Cr}^{ss} & \chi_{Cr}^{\alpha} & \chi_{Cr}^{\gamma} & \chi_{Cr}^{HfO_2} \\ \chi_{Hf}^{ss} & \chi_{Hf}^{\alpha} & \chi_{Hf}^{\gamma} & \chi_{Hf}^{HfO_2} \end{pmatrix} \cdot \begin{pmatrix} \chi_p^{ss} \\ \chi_p^{\alpha} \\ \chi_p^{\gamma} \\ \chi_p^{HfO_2} \end{pmatrix} = \begin{pmatrix} \chi_{Nb}^0 \\ \chi_{Si}^0 \\ \chi_{Ti}^0 \\ \chi_{Al}^0 \\ \chi_{Cr}^0 \\ \chi_{Hf}^0 \end{pmatrix} + \begin{pmatrix} \delta_{Nb} \\ \delta_{Si} \\ \delta_{Ti} \\ \delta_{Al} \\ \delta_{Cr} \\ \delta_{Hf} \end{pmatrix} \quad (6-4)$$

Even if not solvable analytically, the problem can be numerically approximated for $|\vec{\delta}_i|$ to be minimal with the mathematical tool MATLAB². This is essentially a least squares optimization of $\vec{\chi}_p$.

$$\min_{\vec{\chi}_p} \underline{\chi} \cdot \vec{\chi}_p - \vec{\chi}_0 = \vec{\delta} \quad (6-5)$$

Following boundaries have to be considered:

$$\sum_j \chi_{p,j} = 1 ; \chi_{p,j} \geq 0 \quad (6-6)$$

SEM/EDS was used to determine the chemical composition of the individual phases, as spatial resolution and phase identification is necessary as well. At least five grains were measured per phase. Overall composition was determined on three different areas of about 1 mm², each. HfO₂ particles are too small to be accurately measured by EDS, but are assumed to be stoichiometric with negligible solubility of the other constituents. This leads to – since oxygen is not

² MATLAB is a commercial numerical computing environment developed by MathWorks used in version R2015a.

considered in this calculation – the fourth matrix column containing all zeroes except for the hafnium content being unity.

$\vec{\chi}_p$ was calculated for all conditions except HIP GA AC, as phase sizes are too small so that EDS information would also stem from neighboring phases. $\vec{\chi}_0$ shows only small deviation from the nominal composition Nb-20Si-23Ti-6Al-3Cr-4Hf. This may be in part due to minor compositional changes during plasma remelting and gas atomization. Rather more likely, this may be caused by matrix effects of the alloy for EDS measurements as the heavy niobium is overestimated while the lighter elements are underestimated. This error, however, is the same for all phases and conditions. Reproducibility is very good with the standard deviation within a phase and condition typically being below 0.2 %. The influence of this was evaluated by increasing and decreasing each element in $\underline{\chi}$ by its standard deviation and subsequent optimization of $\vec{\chi}_p$. From these 36 iterations the maximum and minimum values for each phase were taken to estimate the error of the calculation resulting from the EDS measurement uncertainty itself. The error vector $\vec{\delta}$ – which determines the quality of the optimization – gives values much smaller than the certainty of the EDS measurement with all elements being below 0.1 at%. Hence, it will be neglected. All mean compositions with standard deviations can be found in the Appendix Table 14-1 – Table 14-3.

The mole fraction of phases $\vec{\chi}_p$ can be converted into a volume fraction of phases $\vec{\phi}_p$. This requires the mean relative atomic mass $\vec{A}_{r,0}$ and the density $\vec{\rho}$ of each phase. $\vec{A}_{r,0}$ can be easily calculated as

$$A_{r,0,j} = \sum_i A_{r,i} \cdot \chi_{ij} \quad (6-7)$$

For the density of the phases, literature values as presented in chapter 2.1 are not suitable since they are not available for the exact phase composition. Hence, the crystallographic density will be used:

$$\rho_j = \frac{Z_j \cdot A_{r,0,j}}{V_{uc,j} \cdot N_A} \quad (6-8)$$

$$V_{uc,j} = |(\vec{a}_j \times \vec{b}_j) \cdot \vec{c}_j| \quad (6-9)$$

Z_j : number of atoms per unit cell

$V_{uc,j}$: volume of the unit cell

N_A : Avogadro constant

$\vec{a}_j, \vec{b}_j, \vec{c}_j$: lattice vectors

With that, the volume fraction can be given as

$$\phi_{p,j} = \frac{\frac{\chi_{p,j} \cdot A_{r,0,j}}{\rho_j}}{\sum_j \frac{\chi_{p,j} \cdot A_{r,0,j}}{\rho_j}} \quad (6-10)$$

Fig. 6-26 to Fig. 6-28 show the phase fractions calculated from EDS measurements for HIP GA, PIM GA, and PIM MA₁, respectively. Based on the different solubilities of the components in

the phases for different heat treatment temperatures, phase fractions vary, as during cool down the system is not kept in equilibrium. The GA material generally shows a significantly decreasing content of $\alpha\text{-Nb}_5\text{Si}_3$ with increasing heat treatment temperature. The content of Nb_{ss} does not change significantly. Compared to phase fraction assessment from SEM micrographs, the content of hafnium oxide is mostly well estimated at around 0.7 vol%.

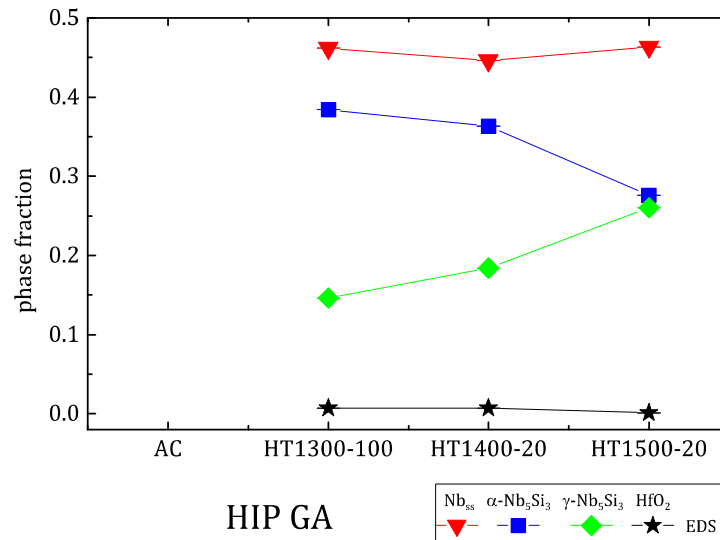


Fig. 6-26: phase fractions calculated by the expanded lever rule for HIP GA for the AC and different heat treatment conditions

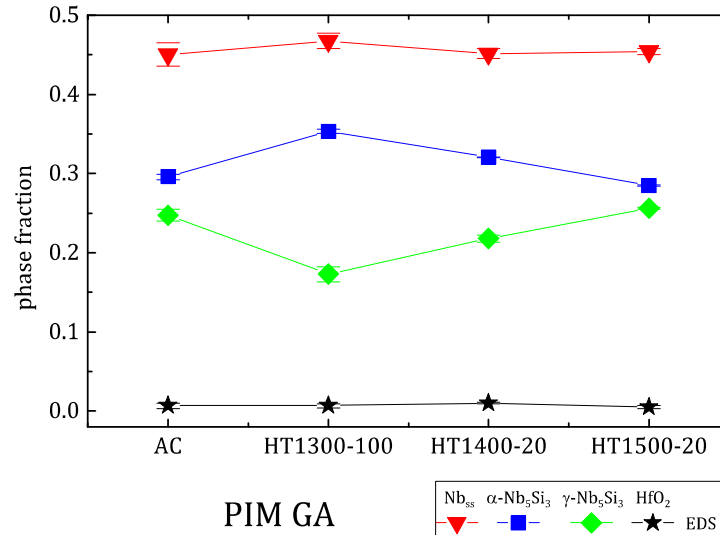


Fig. 6-27: phase fractions calculated by the expanded lever rule for PIM GA for different heat treatment conditions

In BSE imaging only one silicide phase, i.e. $\gamma\text{-Nb}_5\text{Si}_3$, could be distinguished in PIM MA1, even though XRD analysis suggested the presence of $\alpha\text{-Nb}_5\text{Si}_3$ or $\beta\text{-Nb}_5\text{Si}_3$ as well. Thus, EDS measurements could only be done on $\gamma\text{-Nb}_5\text{Si}_3$, which was also used for the lever rule calculations. The result shows the same stable behavior of constant silicide phase fraction as the threshold analysis. This is somewhat surprising as only the composition of $\gamma\text{-Nb}_5\text{Si}_3$ could be used for calculating phase fractions. But, as silicon content is strongly different in Nb_{ss} and

silicide, silicide phase fractions will be dominated by the silicon contents while the other elements play a minor role.

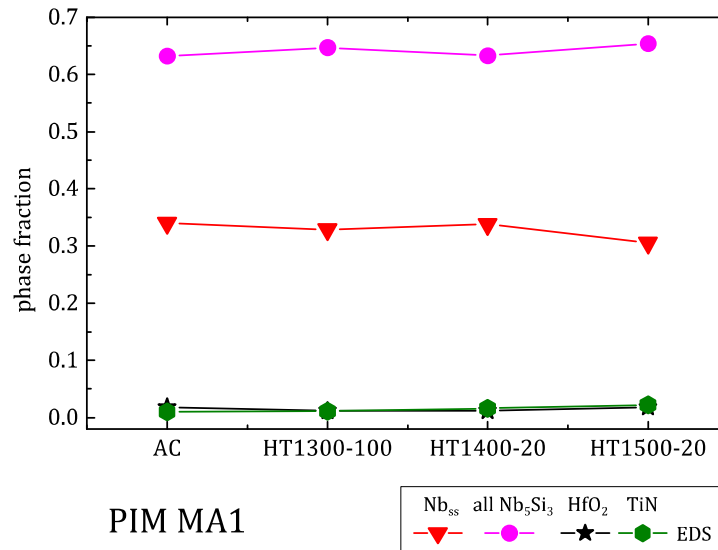


Fig. 6-28: phase fractions calculated by the expanded lever rule for PIM MA₁ for the AC and different heat treatment conditions

6.2.6 Chemical Composition of Phases

Comparing the overall compositions measured by EDS with the nominal one shows good agreement within the measurement uncertainty of EDS. PIM MA₁ is also very close to the nominal composition, but seems to have lost a little niobium and titanium compared to GA, a likely result of the two ductile elements preferentially sticking to milling vial and balls.

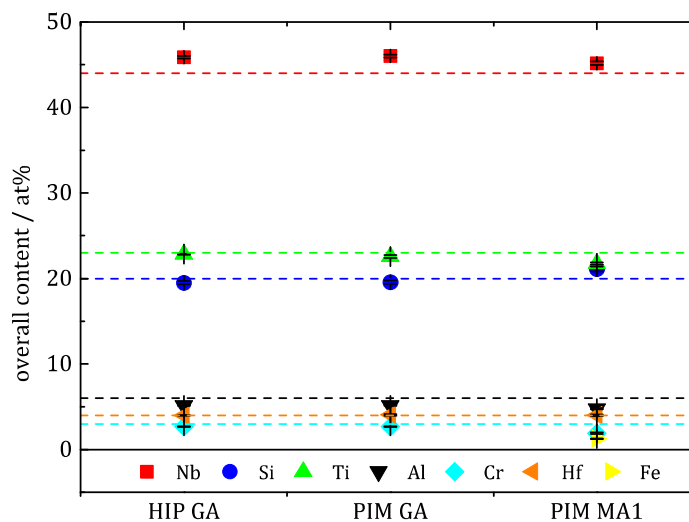


Fig. 6-29: overall chemical composition of HIP GA, PIM GA, and PIM MA₁ as determined by EDS in the AC condition; dashed lines indicate nominal composition

The main change in phase composition (in Fig. 6-30 – Fig. 6-32) that could be made responsible for changes in phase distribution over heat treatment temperature is the γ -Nb₅Si₃ phase. Niobium content increases with higher temperatures while titanium and hafnium decreases. The other two phases Nb_{ss} and α -Nb₅Si₃ do not show significant change in composition. This is in line with the results for the phase fractions. Hafnium and titanium are known γ -Nb₅Si₃ stabilizers. Both show a decreasing solubility in γ -Nb₅Si₃ with increasing temperature. With lower temperature the rest of the system becomes leaner in those two elements and, hence, α -Nb₅Si₃ is preferentially formed. While HIP GA and PIM GA are generally in very good agreement, PIM MA1 shows different absolute phase compositions: in Nb_{ss}, the titanium solubility is much lower, resulting in higher niobium contents. In γ -Nb₅Si₃, where titanium and hafnium solubilities are typically rather high, these values and also the silicon content are significantly lower than for GA material. This could also be a consequence of the higher amount of hafnium oxide and titanium nitride making the residual alloy leaner in both elements.

The dashed lines in Fig. 6-30 – Fig. 6-32 show the compositions calculated by PANDAT. Best agreement between calculation and measurement was achieved for α -Nb₅Si₃. Main deviations in this case are the underestimated niobium content and the overestimated silicon content. The latter is a result of aluminum, which can substitute silicon [99, 164], but is assumed unsolvable in α -Nb₅Si₃ by the database. Still the actual aluminum content in α -Nb₅Si₃ is much lower than the 8 % found by Zhao et al. [164]. For the solid solution, niobium is highly underestimated due to lower than expected solubility of aluminum and hafnium. More importantly than the absolute contents, the tendency of slightly decreasing titanium and slightly increasing niobium content with temperature is not properly modeled. The calculations for γ -Nb₅Si₃ are not shown, since the calculated stability range ends at 1350 °C.

For PIM MA1 a comparison with calculations is not feasible due to the overall high amounts of contamination. While iron is included in the thermodynamic database of PANDAT, oxygen and nitrogen are not. The significant amounts of HfO₂ and TiN cannot be accounted for.

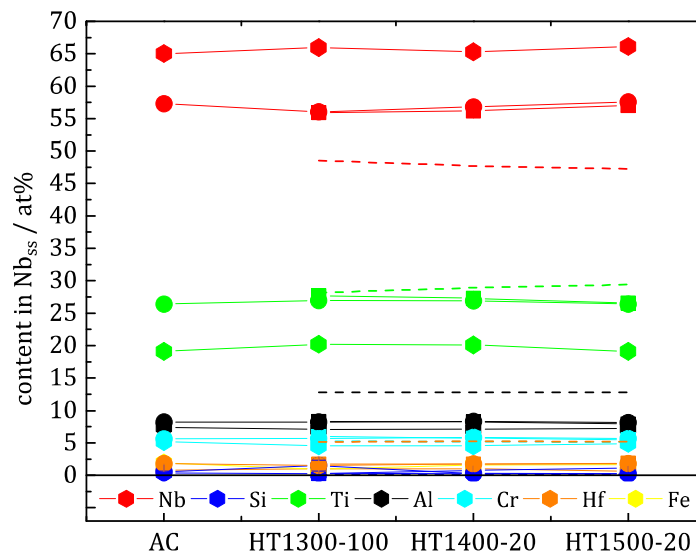


Fig. 6-30: chemical composition of Nb_{ss} in HIP GA (squares), PIM GA (circles), and PIM MA1 (hexagons) as determined by EDS over heat treatment; dashed lines indicate PANDAT calculations

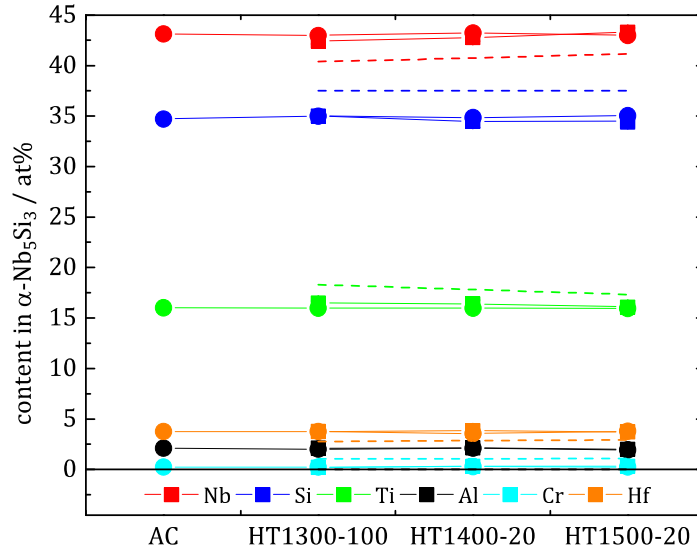


Fig. 6-31: chemical composition of $\alpha\text{-Nb}_5\text{Si}_3$ in HIP GA (squares) and PIM GA (circles) over heat treatment; dashed lines indicate PANDAT calculations

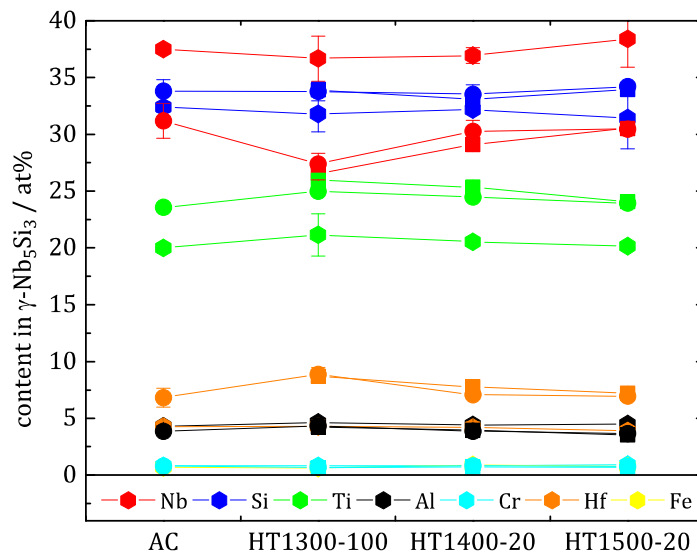


Fig. 6-32: chemical composition of $\gamma\text{-Nb}_5\text{Si}_3$ in HIP GA (squares), PIM GA (circles), and PIM MA1 (hexagons) over heat treatment

6.2.7 Discussion of Microstructural Results

To compare the phase fraction results obtained by the different methods (sections 6.2.1 – 6.2.5), they are summarized in Fig. 6-33 – Fig. 6-35 per manufacturing process. For HIP GA (Fig. 6-33), the amount of Nb_{ss} for all conditions is in very good agreement between all methods at an average of 46 vol%. The tendency of falling $\alpha\text{-Nb}_5\text{Si}_3$ content down from ≈ 37 vol% at HT1300-100 with increasing heat treatment temperature is well depicted even though in the XRD measurements the drop at 1400 °C is found to be stronger than for lever-rule calculations from EDS. An additional EBSD phase analysis of HIP GA HT1500-100 confirms the low volume fraction of $\alpha\text{-Nb}_5\text{Si}_3$ (≈ 28 vol%) and also affirms that thermodynamic equilibrium is reached

after HT₁₅₀₀₋₂₀ and an increase in the heat treatment duration will only promote grain coarsening but no change in phase relation.

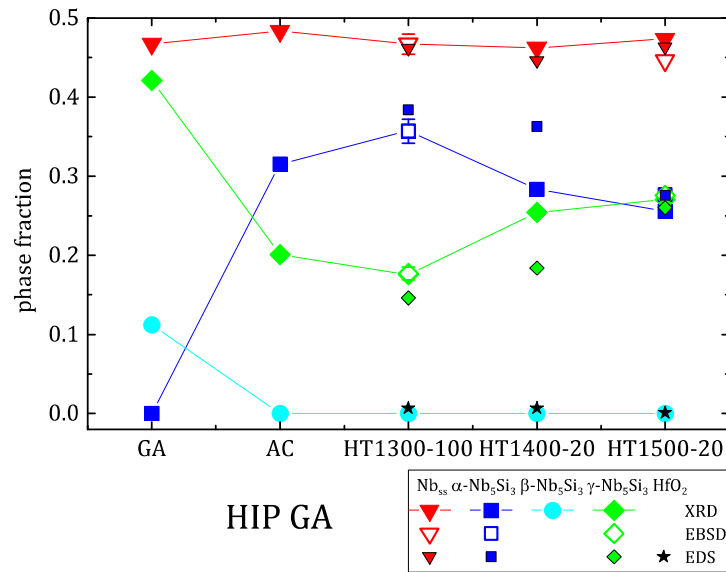


Fig. 6-33: phase fractions determined by all introduced methods for HIP GA; additionally, the EBSD data was extended by a HT₁₅₀₀₋₁₀₀ measurement, which was put in at HT₁₅₀₀₋₂₀

For PIM GA (Fig. 6-34) the situation is very similar for phase fractions obtained by XRD, EBSD, and EDS measurements, even though as for HIP, lever-rule calculations (EDS) slightly overrate $\alpha-Nb_5Si_3$ and underrate $\gamma-Nb_5Si_3$ contents compared to the RIR (XRD) and EBSD methods. Again, EBSD on PIM GA HT₁₅₀₀₋₁₀₀ gives perfect agreement with XRD results on PIM GA HT₁₅₀₀₋₂₀ after calibration on the HT₁₃₀₀₋₁₀₀ condition. Nb_{ss} is constant at ≈ 46 vol% as well and $\alpha-Nb_5Si_3$ content is about 3 vol% lower for PIM GA than for HIP GA in the HT₁₃₀₀₋₁₀₀ condition, but drops to similar values at 1500 °C. The $\beta-Nb_5Si_3$ phase in those measurements was not taken into account as it appears only clustered locally and shows almost the same chemical composition as $\alpha-Nb_5Si_3$. For EDS, phase compositions of Nb_{ss} , $\alpha-Nb_5Si_3$, and $\gamma-Nb_5Si_3$ were taken from regions without the presence of $\beta-Nb_5Si_3$. In EBSD maps $\beta-Nb_5Si_3$ appeared only in the area analyzed for HIP GA HT₁₅₀₀₋₁₀₀ and for the sake of this diagram, it was attributed to the very similar and also tetragonal $\alpha-Nb_5Si_3$. On the EBSD cross-section of PIM GA HT₁₅₀₀₋₁₀₀ no $\beta-Nb_5Si_3$ was detected, underlining the statement of it being a result of localized inhomogeneous oxygen distribution. At etched cross-sections of PIM GA also the grid counting method was applied. This technique, in the current case, seems to systematically underrate Nb_{ss} content and also does not show the clear trend in silicide phase balance established by all other means.

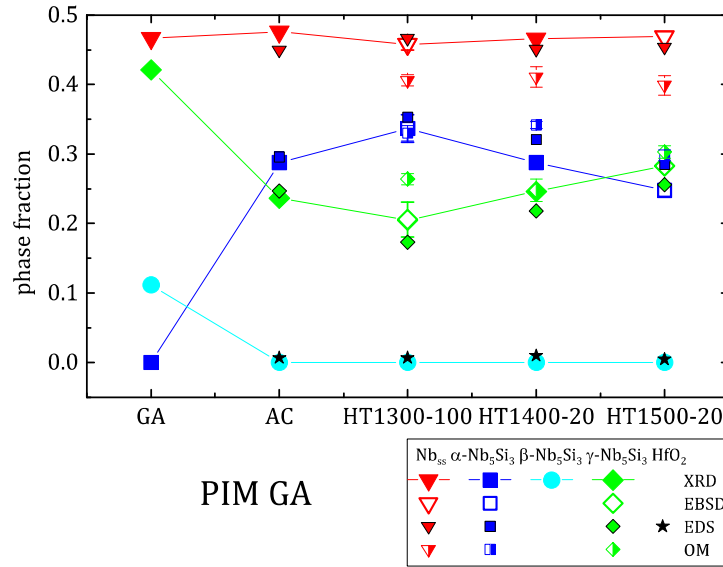


Fig. 6-34: phase fractions determined by all introduced methods for PIM GA; additionally the EBSD data was extended by a HT1500-100 measurement, which was put in at HT1500-20

The presence of two silicides was only measurable by XRD for PIM MA1. That makes the calibration of the XRD results less reliable than for the GA samples, as the sum of $\alpha-Nb_5Si_3$, $\beta-Nb_5Si_3$, and $\gamma-Nb_5Si_3$ fractions from XRD was fitted to the overall silicide fraction from the threshold method (Fig. 6-35). Lever rule calculations seem to fit well regarding the silicide content, but Nb_{ss} content is higher than for other methods, while TiN content is too low. The reason for that could be that XRD shows the presence of $\alpha-Nb_5Si_3$ (HT1300-100 and HT1400-20) and $\beta-Nb_5Si_3$ (AC and HT1500-20), which was not distinguishable in the SEM and, hence, could not be integrated into the lever rule calculations.

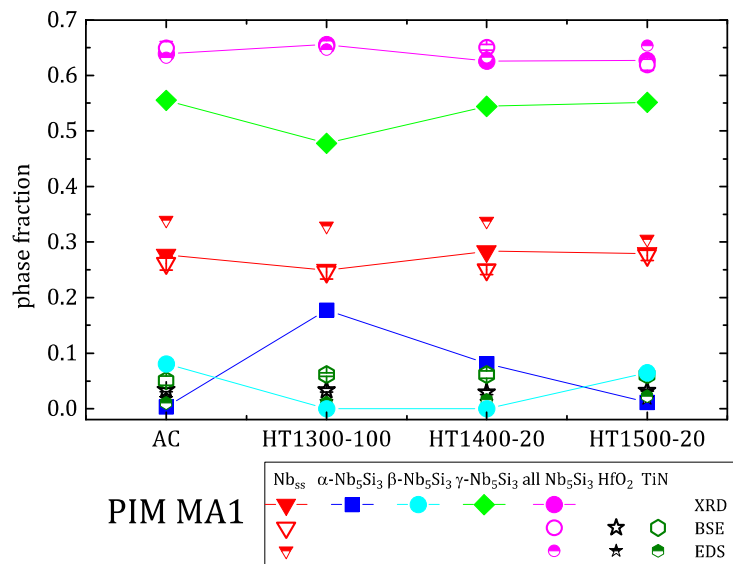


Fig. 6-35: phase fractions determined by all introduced methods for PIM MA1

The threshold method – as far as it is applicable – and EBSD measurements should give the most reliable results for phase fraction determination, as both are direct methods to determine area fraction on a cross-section. The lever-rule calculation is an indirect method, but yields absolute phase fractions. It is in good agreement with the direct methods for GA samples, where chemical compositions could be determined for all phases. The RIR method can be used to obtain absolute values if the database composition is used, in this case binary niobium silicides. For the complex composition of the given alloy, a calibration of the relative intensity ratio for each phase has to be carried out with at least one method that yields absolute phase fractions. In combination, the easily workable RIR method on all conditions with only one high effort EBSD measurement per sample class is a very viable option to obtain reliable phase analyses, especially for the three main phases.

The hafnium oxide content is generally very small – below 1 vol% – which makes an accurate determination difficult by any means. That the overall hafnium oxide content from threshold analysis does not change significantly with heat treatment suggests, that solute oxygen is in equilibrium with hafnium oxide formation already after compaction or even that all oxygen was gettered by hafnium. Using the overall oxygen content in the sample as determined by hot carrier gas extraction, the phase fractions of the other phases, and equation (6-10), the maximum amount of hafnium oxide that would form in the latter case can be calculated (Table 6-7).

Table 6-7: oxygen, nitrogen, and carbon contents determined by hot carrier gas extraction and resulting, calculated amounts of hafnium oxide, titanium nitride, and titanium carbide, respectively; measured contents from threshold analysis presented previously (section 6.2.1) in paranthesis

	HIP GA	PIM GA	PIM MA ₁	PIM MA ₂
Oxygen / wt%	0.209 ± 0.002	0.269 ± 0.004	0.850 ± 0.004	0.571 ± 0.026
HfO₂ / vol%	1.2 (0.8)	1.5 (0.8)	4.2 (3.4)	2.8 (1.5)
Nitrogen / wt%	< 0.01	0.037 ± 0.002	0.766 ± 0.004	< 0.01
TiN / vol%	—	—	5.3 (6.1)	—
Carbon / wt%	—	0.061 ± 0.002	0.212 ± 0.016	1.01 ± 0.02
TiC / vol%	—	—	—	7.9 (6.8)

The comparison of this estimation with the threshold method results (Table 6-3) yields only small variations of 0.4 – 0.8 vol%. Considering the low hafnium oxide content in general this is a good agreement and most oxygen is indeed gettered by hafnium, though some seems to remain in solution in the other phases. Oxygen solubility is up to 6.3 % in niobium [162]. Lever-rule calculations on the other hand throughout underestimate the amount of hafnium oxide. The same estimation can be done for titanium nitride in PIM MA₁ and titanium carbide in PIM MA₂. In this case, estimation from hot carrier gas extraction is around 0.8 – 1.1 vol% lower than the average content from the threshold method for TiN, which is also an acceptable

conformance, considering that pores with a dark contrast may have been falsely identified as TiN. As a comparison, a Nb-Si-Mo-Hf alloy could be produced with contents as low as 0.003, 0.006, and 0.005 wt% of carbon, nitrogen, and oxygen, respectively, by arc melting [55]. Others have found similar contents [66, 67, 107], which may prove above said.

For PIM MA1 one may conclude, that 2.2 at% of hafnium and 4.4 at% of titanium (for PIM MA2 1.4 and 6.4 %, respectively) will be bound in hafnium oxide and titanium nitride, respectively. Since both are γ -Nb₅Si₃ stabilizers, this would lead to a reduced γ -Nb₅Si₃ content compared to GA material. The opposite is the case. This can be explained by the presence of iron contamination which is demonstrated in phase diagram calculations to also be a strong γ -Nb₅Si₃ stabilizer (Fig. 6-36). As for all other phase diagram calculations with that number of components, the phase fields may be shifted, but the stabilizing effect is reasonable as iron also forms the hexagonal hP16 5-3 silicide (prototype Mn₅Si₃), i.e. γ -Nb₅Si₃. Carbon is also known to stabilize γ -Nb₅Si₃ [55]. Beyond that, one may speculate that nitrogen or oxygen also have that effect, even though not reported, yet.

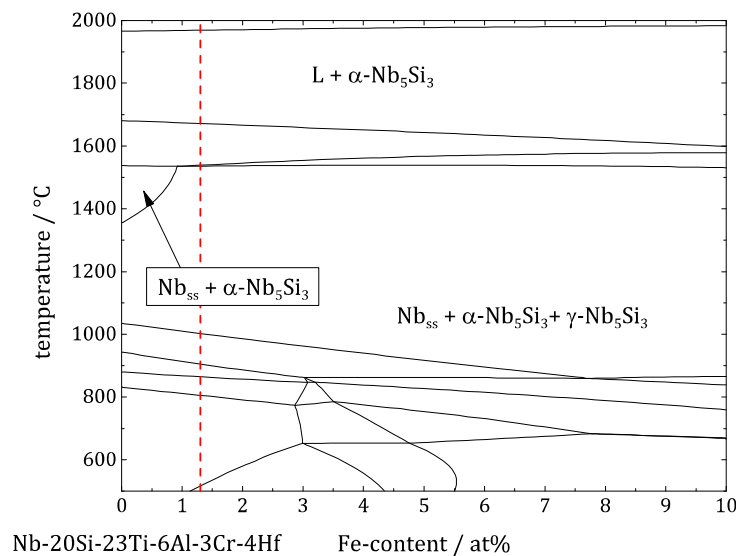


Fig. 6-36: calculated phase diagram of Nb-20Si-23Ti-6Al-3Cr-4Hf for increasing iron content; the red dashed line indicates the iron content determined by EDS

Bewlay et al. reported [2, 3] that γ -Nb₅Si₃ is detrimental to creep properties.

Also, this phase shows a strong anisotropy in the coefficient of thermal expansion (CTE) α , which may lead to cracking due to thermal misfit. Schneibel and Rawn [165], and Nakashima and Umakoshi [166] both measured an anisotropy of α_c/α_a of $16.6 \cdot 10^{-6} \text{ K}^{-1}/6.1 \cdot 10^{-6} \text{ K}^{-1} = 2.7$. Zhang and Wu even found a value of $\alpha_c/\alpha_a = 22.2 \cdot 10^{-6} \text{ K}^{-1}/5.1 \cdot 10^{-6} \text{ K}^{-1} = 4.7$ in the binary Ti₅Si₃ phase [47]. On the other hand α -Nb₅Si₃ was measured to have an anisotropy of only $\alpha_c/\alpha_a = 12.4 \cdot 10^{-6} \text{ K}^{-1}/8.6 \cdot 10^{-6} \text{ K}^{-1} = 1.4$. The CTEs will change with solute components, but Schneibel and Rawn could not achieve a reduction of the anisotropy below 1.9 for Ti₅Si₃ alloyed with other transition metals. Niobium even increased the ratio to $\alpha_c/\alpha_a = 2.9$. The CTE for pure niobium at room temperature is $7.3 \cdot 10^{-6} \text{ K}^{-1}$ [52], which is also subject to change with alloying additions. Hence, the presence of higher α -Nb₅Si₃ contents is preferred over γ -Nb₅Si₃.

PIM MA₁ especially, having high amounts of γ -Nb₅Si₃, but also GA material shows some cracking of the silicide already after heat treatment (Fig. 6-12 on p. 56) as a result of thermal stresses.

A significant influence on the mechanical properties is expected from the amount of solid solution present in the composite. While higher amounts of silicide will increase the hardness and strength [125], fracture toughness is known to decrease at the same time [3, 74, 85], as is the case for other silicide-based composites [112, 167], where the solid solution is much tougher than the intermetallic. For GA material the solid solution phase fraction lies consistently at 46 vol% and provides a continuous matrix. The samples from mechanically alloyed powder show a significantly lower volume fraction of solid solution (25 – 28 %). In part this is a result of the high contamination contents of oxygen, nitrogen, and carbon forming hafnium oxide and titanium nitride/carbide, respectively, and hence capturing elements that would otherwise form the solid solution. Additionally, Si+Al contents in the silicides are a little lower than for GA. Overall silicide contents in GA is in the range of 52 – 55 %, while in MA samples silicide content is 62 – 65 %. The calculation leading to this result, based on the phases' compositions, is done in section 6.2.5. To make it understandable, one may take a look at the Si+Al contents in the silicides, the solid solution, and the alloy as a whole. While overall Si+Al content is slightly higher in e.g. PIM MA₁ than PIM GA (25.9 and 24.7 %, respectively), the amounts of the two elements in each phase are lower (7.6 and 8.9, and 36.4 and 37.4 %, for solid solution and silicides, respectively). This leads to considerably higher amounts of silicide phases forming and the solid solution being embedded in a silicide matrix for MA material instead of a continuous solid solution matrix as has been found in GA material.

6.2.8 Grain Size Analysis

Another quantitative aspect of the microstructure that has significant impact on mechanical properties is the grain size. At low temperatures the Hall-Petch effect [168, 169] describes the influence of grain size on the yield strength σ_{ys} :

$$\sigma_{ys} = \sigma_0 + \frac{k}{\sqrt{d_g}} \quad (6-11)$$

σ_0 : intrinsic yield stress

k : Hall-Petch constant

d_g : grain size

At high temperatures, creep (and for ultra-fine grained material also at room temperature [170]) by a mechanism called grain boundary sliding may become more prevalent, where grain size has a strong influence on the creep rate $\dot{\epsilon}$ (see also section 7.2.3).

$$\dot{\epsilon}(d_g) \sim \frac{1}{d_g^p} \quad (6-12)$$

p : grain size exponent, typically 1 – 3

Since the etching does not reveal grain boundaries, but only distinguishes the three main phases Nb_{ss}, α -Nb₅Si₃, and γ -Nb₅Si₃, Table 6-8 gives the mean phase sizes as determined by the linear

intersect method (LIM). Three micrographs were analyzed horizontally and vertically for each condition resulting in six measurements and a total of at least 2500 line segments analyzed, each. The standard deviation between those six measurements of $< 0.1 \mu\text{m}$, shows very good agreement between different frames and sample directions. In comparison, EBSD offers actual grain sizes determined from areas of same crystallographic orientation and, hence, also distinguishes phases. The grain size given is the mean equivalent circle diameter (ECD) weighted by the area fraction of each grain. LIM on the other hand yields the mean length of phase sections, which are typically smaller, as grains are mostly not cut at the widest point.

Table 6-8: phase and grain sizes of undeformed HIP GA and PIM GA for different heat treatment conditions on a cross-section determined by the linear intersect method (top) and EBSD (bottom)

	HIP GA		PIM GA		
	HT1300-100	HT1500-100	HT1300-100	HT1500-20	HT1500-100
phase size / μm	—	—	4.0 ± 2.5	5.0 ± 3.1	7.3 ± 4.4
Nb _{ss} grain size / μm	3.9 ± 1.5	8.9 ± 2.9	4.9 ± 1.9	—	9.2 ± 3.1
α -Nb ₅ Si ₃ grain size / μm	3.5 ± 1.2	9.6 ± 6.6	4.6 ± 1.5	—	8.9 ± 3.4
γ -Nb ₅ Si ₃ grain size / μm	3.1 ± 1.0	8.1 ± 2.4	4.2 ± 1.5	—	8.3 ± 2.6
mean grain size / μm	3.6 ± 1.4	8.8 ± 3.9	4.7 ± 1.7	(6.0)	8.9 ± 3.0

The linear extrapolation of the phase size against mean grain size for PIM GA should intersect in the origin, which is satisfied reasonably well for the amount of available data (Fig. 6-37). Hence, an expected mean grain size for PIM GA HT1500-20 can be interpolated to be around $6.0 \mu\text{m}$. HT1400-20 was not evaluated as mechanical properties are not determined for this condition, however, grain sizes seem to be in the same range as for HT1300-100.

HIP GA shows slightly lower grain sizes for HT1300-100. As coarsening rate is very slow at $1300 \text{ }^\circ\text{C}$, the heat input during compaction still plays a significant role ($1230 \text{ }^\circ\text{C} / 4 \text{ h}$ for HIP, $1500 \text{ }^\circ\text{C} / 3 \text{ h}$ for PIM). This difference is negligible after HT1500-100 and the mean grain size is comparable for PIM and HIP.

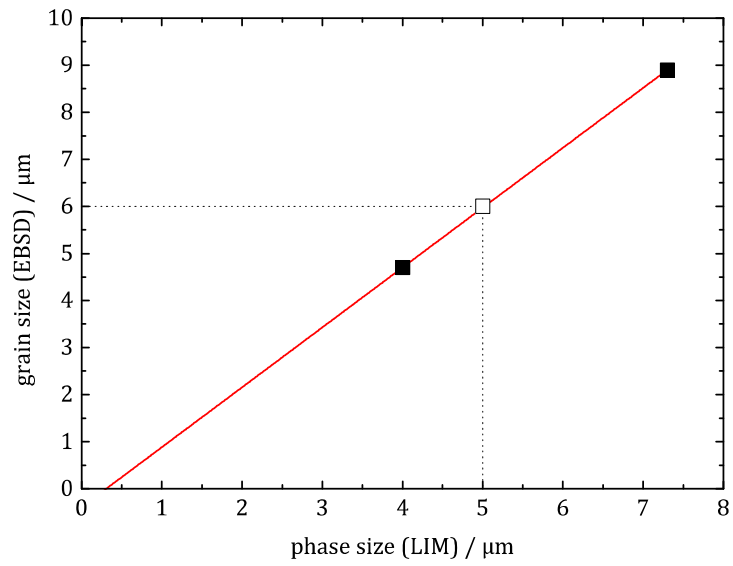


Fig. 6-37: plot of the EBSD grain size over the phase size from the linear intersect method (LIM), solid symbols are data points, the open symbol is an interpolation

7 Compressive Tests

The shear stress necessary for yielding τ_y in bcc metals is strongly temperature dependent as shown in Fig. 7-1, left. For uniaxial loading ($\sigma_2 = \sigma_3 = 0$), which is the condition for most materials testing setups, the maximum available shear stress $\tau_{\max} = \sigma_1/2$ (Fig. 7-1, right). If for low temperatures, the applied stress σ_1 surpasses the temperature-independent cleavage stress σ_c before $\tau_{\max} > \tau_y$, deformation behavior transitions from ductile to a brittle manner and a ductile-to-brittle transition temperature (DBTT) can be observed (Fig. 7-1, left, see section 8.2). Pure niobium shows such a DBTT at around $-200\text{ }^\circ\text{C}$ [17, 171]. This thermal activation of plastic flow is based on non-planar cores of $\langle 111 \rangle/2$ screw dislocations which lead to a high Peierls stress compared to fcc metals (see nickel in Fig. 7-1, left). The Peierls barrier is overcome by the thermally activated formation of kink pairs on the designated slip plane, i.e. $\{110\}$ or $\{112\}$ [172, 173]. This in turn also leads to a pronounced strain rate sensitivity for low temperatures. For sufficiently high temperatures the flow stress stays rather constant – as mobility of edge dislocations catches up – and depends only on temperature due to the rather weak temperature dependence of the elastic modulus [174].

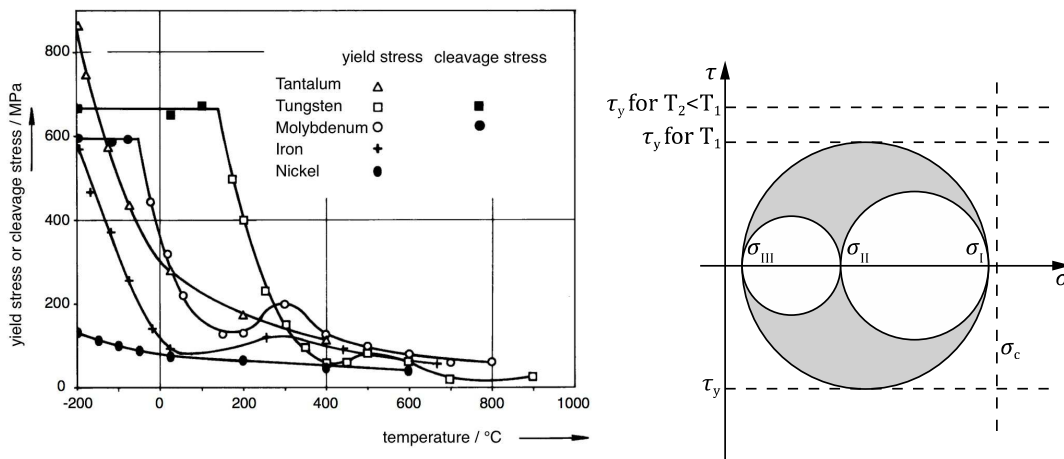


Fig. 7-1: left: yield stress and cleavage stress in case of brittle fracture for some bcc metals and nickel, modified after [175, p. 230]; right: Mohr circle for a three-dimensional stress state, including the temperature dependent shear stress for yielding τ_y and the temperature independent cleavage stress σ_c , based on [176, p. 196]

At temperatures above 40 % of the absolute melting temperature T_m , diffusion becomes fast enough for climb of edge dislocations – i.e. change of slip plane by diffusion – to play a significant role for the flow stress. This also leads to the diffusion-based phenomenon called creep, which describes the time-dependent deformation of a material under constant stress, even below the yield stress (section 7.2). Once again, the thermal activation of diffusion results in a strong strain rate sensitivity. This behavior is summarized in Fig. 7-2, showing strong strain rate dependence for low temperatures (below $0.15 T/T_m$, based on the high Peierls barrier) and high temperatures (above $0.4 T/T_m$, based on diffusion) and the very low strain rate sensitivity in-between. Strong alloying, as done in the present case, may elevate the DBTT to higher temperatures [17, 134, p. 2281] and, hence, yield a smooth transition from Peierls-controlled to diffusion-controlled temperature/strain rate dependence of yielding (compare section 7.1.1).

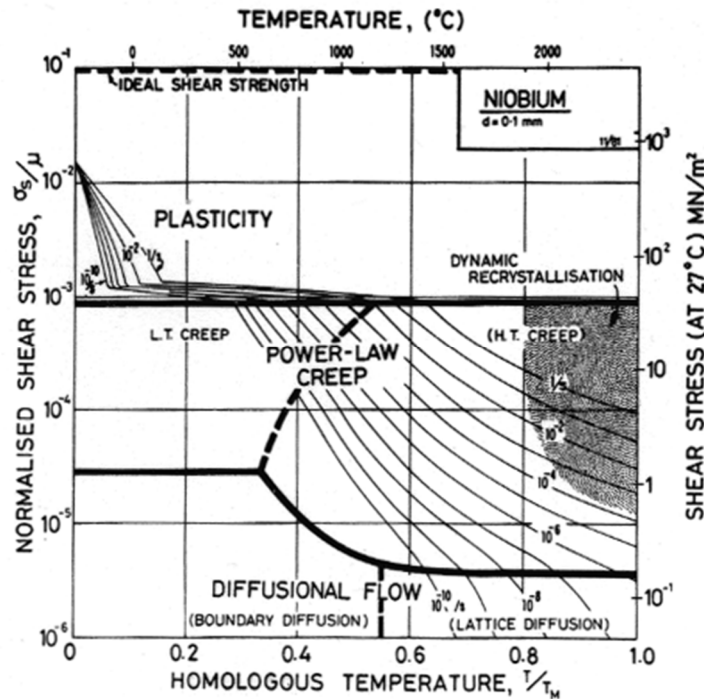


Fig. 7-2: deformation mechanism map for pure niobium (grain size 100 μm) showing lines of constant strain rate over normalized shear stress and homologous temperature; heavy lines separate regimes of different dominant deformation mechanisms [177]

Due to constraints in sample amount available, compression tests were done instead of (preferred) tensile tests. Even though fewer material properties are available in compression, for an isotropic material as is the case for a polycrystal, the yield strength R_{eS} will be the same in tension and compression. In compression, yield strength may be obtained even if it is higher than the tensile fracture stress [175].

7.1 Quasi-Static Compressive Testing

7.1.1 Temperature Dependence

Fig. 7-3 shows the stress-strain curves (in compression) for compact material at room temperature. All samples fracture at high stresses above 1700 MPa leading to the material disintegrating into small pieces as the elastically stored energy is released. Samples from gas-atomized powder, HIP as well as PIM, in the AC condition show some plasticity, as fracture strains of about 2.5 % are reached with a stress plateau at around 2760 and 2010 MPa, respectively. This difference can be attributed to grain boundary strengthening. Grain size varies greatly (see 6.1.1) with HIP having considerably smaller grains than PIM, resulting in a higher strength for the former. After the heat treatment HT1500-100 the maximum stress level is about the same for HIP and PIM (2200 MPa) with fracture strains of about 2 %. The MA AC material however does not even show 0.2 % of plastic deformation. This is hardly exceeded after heat treatment. PIM GA HT1500-100 left an analyzable sample piece after fracture. Extensive cracking parallel to the loading direction could be found in the silicides (Fig. 7-5, left). Neither shearing nor plastic flow of the solid solution but tensile forces normal to the compression direction can be made responsible at those low plastic strains.

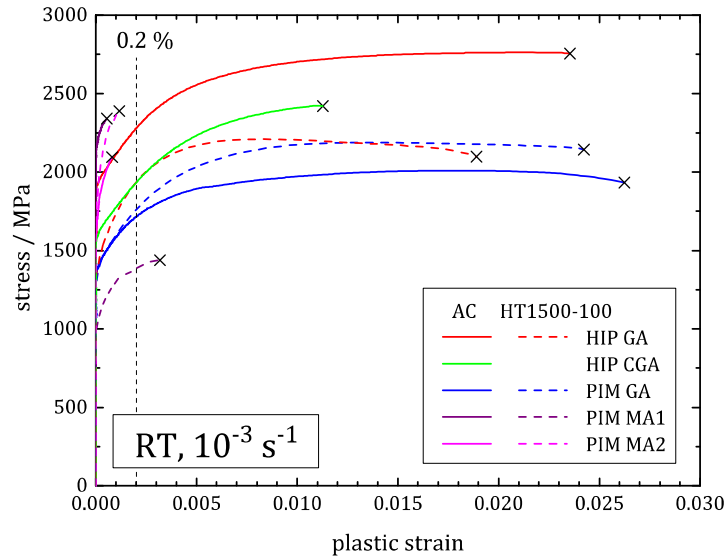


Fig. 7-3: stress-strain curves for consolidated material at room temperature (RT) with a strain rate of 10^{-3} s^{-1}

At $1000 \text{ }^\circ\text{C}$ for GA AC samples (Fig. 7-4) almost ideal plastic flow is observed at a stress level of 450 MPa . Yielding seems to start at very low stresses, though. The reason for this is that at $1000 \text{ }^\circ\text{C}$ ($0.46 T_m$) the material already shows creep at stresses below the yield point with creep rates rivaling the deformation rate (see chapter 7.2). After reaching the maximum, the stress stays almost at the same level until the test is stopped at up to 20 %. PIM still shows slightly lower strength than HIP.

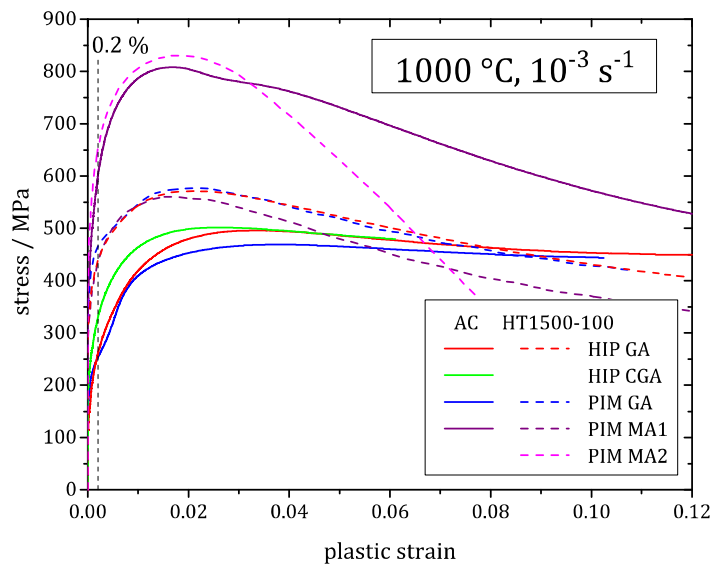


Fig. 7-4: stress-strain curves for consolidated material at $1000 \text{ }^\circ\text{C}$ with a strain rate of 10^{-3} s^{-1}

Material from mechanically alloyed powder shows a maximum strength of 800 MPa but reaches the strength of HIP and PIM after about 18 % of plastic deformation, even faster for the heat-treated material. This strong decay in PIM MA is induced by developing of transgranular cracking of the intermetallic matrix phase. This also leads to some intermetallic particles falling out during cross-section preparation (Fig. 7-5, right). Those cracks connect at roughly 45° to the

loading axis and lead to shearing of the upper and lower part of the sample. PIM GA on the other hand shows no macroscopic cracking but only small phase boundary cracks for the coarse grained, heat-treated state (Fig. 7-5, middle). The intergranular cracks also explain, why in the heat-treated condition GA material shows a stress decay after about 2 % of plastic strain, while the fine grained AC material rather shows a plateau (no noticeable cracking). Reproducibility of plastic deformation behavior and strength can be seen in section 14.3 in the Appendix.

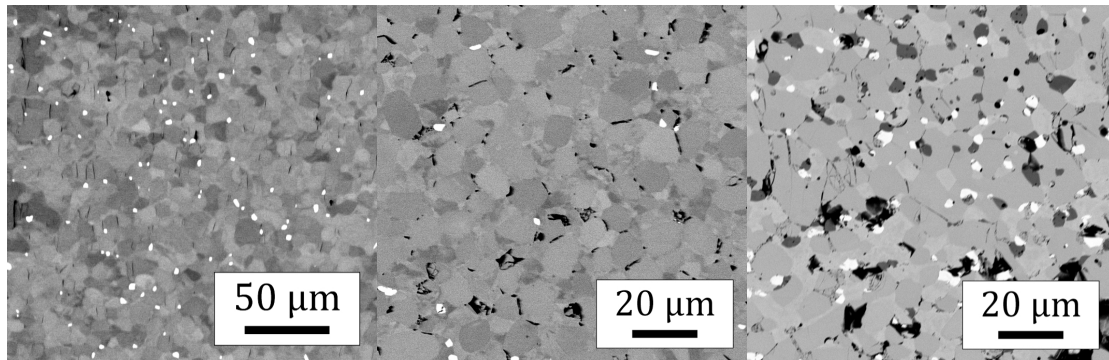


Fig. 7-5: backscatter electron micrographs of PIM GA HT₁₅₀₀₋₁₀₀ after deformation at room temperature until fracture (left) after deformation at 1000 °C to 20 % true plastic strain (middle) and PIM MA₁ HT₁₅₀₀₋₁₀₀ after deformation at 1000 °C to 20 % true plastic strain; strain rate of 10^{-3} s^{-1} ; loading direction parallel to vertical edge

Maximum strength is shown in Fig. 7-6 as a function of temperature (values are provided in Table 7-1 including 0.2 % offset yield strength). Only slight reduction in strength is noticed by increasing the testing temperature to 600 °C due to the decrease in elastic modulus with temperature. With further rising temperature, the strength is almost divided by four at 1000 °C. The decay in strength leads for PIM MA₁ to R_{eS} falling below the cleavage strength σ_c and hence the onset of plasticity. Also plotted in Fig. 7-6 are values for CMSX-4, a typical second generation single-crystal nickel-base superalloy, and for MASC and MASC-type niobium silicide composites, giving similar strengths of around 500 MPa at 1000 °C. A very similar composition (Nb-20Si-24Ti-2Al-5Cr-3Hf), produced by HIP of GA powder by Jéhanno et al. [23], however, showed much lower strength, albeit under tension.

Compression tests on molybdenum- and tungsten-modified (up to 25 at% in total) Nb-16Si showed retention of this strength level up to 1500 – 1600 °C depending on composition [178]. As mentioned in section 2.2, however, oxidation properties are insufficient with those alloys.

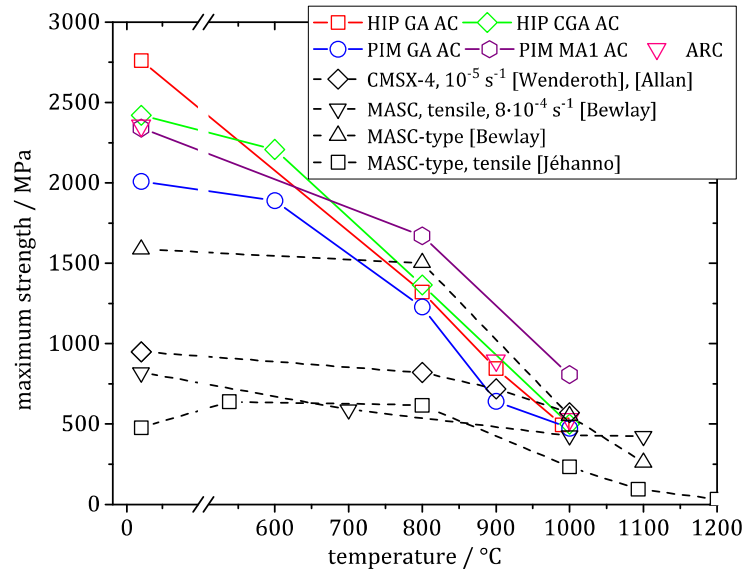


Fig. 7-6: maximum strength over temperature for a strain rate of 10^{-3} s^{-1} ; literature data by Wenderoth et al. [179], Allan [180], Bewlay et al. [1, 98], and Jéhanno et al. [23]

Table 7-1: strength values obtained for bulk material in the AC condition, 0.2 % offset yield strength and maximum stress in parentheses, both in MPa

temperature / °C	HIP GA	PIM GA	PIM MA ₁	PIM MA ₂
25	2404 (2760)	1763 (2009)	— (2340)	— (2094)
600	—	1357 (1890)	—	—
800	1061 (1321)	953 (1227)	1380 (1670)	—
900	539 (846)	514 (641)	—	—
1000	303 (496)	254 (474)	590 (808)	650 (830) HT1500-100

7.1.2 Strain Rate Dependence

The ideal plastic flow behavior shown for 1000 °C, i.e. the absence of strain hardening beyond 2 % of plastic deformation, points at diffusion-based recovery processes being active. As diffusion is a time-dependent process, strain rate sensitivity is implied as described at the beginning of this chapter. Exemplarily, strain rate $\dot{\epsilon}$ was varied between 10^{-2} s^{-1} and 10^{-4} s^{-1} at 1000 °C. The result is shown in Fig. 7-7. Strain rate sensitivity of the yield stress is generally given by a power law [175, p. 279, 181]:

$$R_{eS} \sim \dot{\epsilon}^m \quad (7-1)$$

For PIM GA AC a strain rate sensitivity of about $m = 0.18$ can be derived. This is typical for dislocation-based deformation at higher temperatures. HIP GA AC, however, shows a kink.

While the stresses determined for 10^{-3} s^{-1} and 10^{-2} s^{-1} are in good accordance with those of PIM GA AC, at 10^{-4} s^{-1} , the yield stress is much lower than anticipated. This can be explained by a change in deformation mode, where m would be much higher (≈ 0.5).

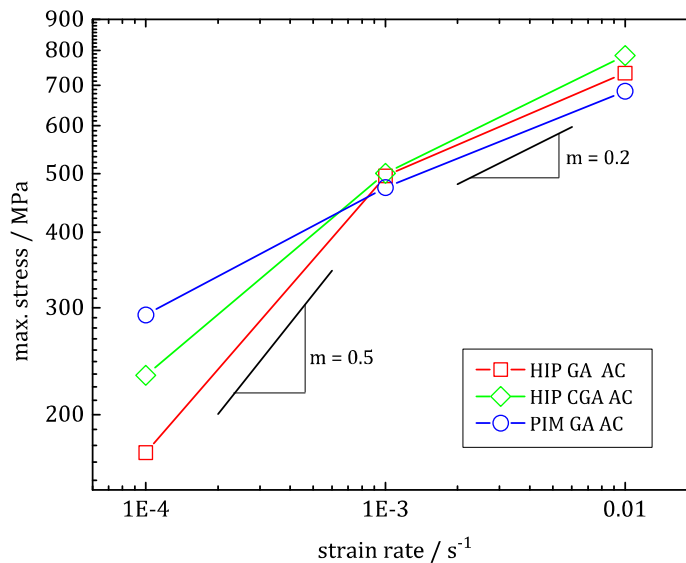


Fig. 7-7: maximum strength over strain rate for a testing temperature of $1000 \text{ }^\circ\text{C}$

A possible mechanism is already known from superplasticity, i.e. grain boundary sliding. For a detailed analysis of this phenomenon, the tests would have to be extended to even lower strain rates. Since at $1000 \text{ }^\circ\text{C}$ the stress strain curves show almost ideal plastic flow with no strain hardening after about 2 % this test can also be reinterpreted as a creep test at constant stress. Hence, the high-temperature compression tests will be complemented by the creep tests of the next section.

7.2 Compressive Creep Testing

Components under mechanical loading (below the yield stress) at high temperatures, i.e. $T > 0.4 T_m$, show a time-dependent deformation phenomenon called creep. This is one of the main limiting factors for the lifetime of turbine blades. This introduction will focus on dislocation-based creep as the technologically most relevant variant. Diffusional creep is described in more detail in section 7.2.3.

Creep deformation can usually be separated into three different regimes. The primary creep regime is dominated by strain hardening and the formation of sub-grain structures. The initially very high strain rate decreases, as dislocation reactions, i.e. formation and annihilation, in the sub-grain boundaries become rate-controlling. In the secondary regime, a constant strain rate is observed. Recovery processes are in equilibrium with strain hardening. Accordingly, the resulting constant strain rate is called steady-state strain rate. In the tertiary part, defect formation takes place. Pores and cracks will form mostly at grain boundary triple junctions, reducing the materials strength until failure, i.e. in tensile loading.

Typically, the steady-state creep rate $\dot{\epsilon}_s$ is described as a function of applied stress σ and temperature T :

$$\dot{\epsilon}_s(\sigma, T) = A_1 \cdot \sigma^n \cdot \exp\left(\frac{-Q_c}{RT}\right) \quad (7-2)$$

A_1 : material constant

n : stress exponent

Q_c : activation energy for creep

R : gas constant

T : absolute temperature

The stress dependence of strain rate is commonly called Norton power law [182]. Often values of 3 – 5 are obtained for the stress exponent n , when dislocation slip and climb are dominating deformation mechanisms. In contrast to low temperatures, at high temperatures, diffusion controlled processes play a more and more important role. By means of vacancy diffusion, dislocations can climb. This describes a movement of edge dislocations perpendicular to their slip plane. Accumulation of vacancies along the dislocation line of the core will lead to a change in slip plane. This could mean that in the new slip plane movement is no longer inhibited leading to plastic deformation or annihilation with another dislocation, i.e. recovery. Consequently, the temperature dependence of strain rate is usually governed by an Arrhenius type law (Eq. (7-2)) [182].

Smaller values of 1 – 2 hint at diffusional creep (see section 7.2.3), but also values up to 8 have been measured [182, 183]. If values beyond 8 are determined, power-law breakdown is probable. To take into account this mechanism change for high stresses to an exponential dependency (power-law breakdown), the approach by Barrett and Nix [184], however, seems more feasible to describe the entire stress regime [185]:

$$\dot{\epsilon}_s(\sigma, T) = A_2 \cdot \sigma^{n-1} \cdot \sinh(\beta\sigma) \cdot \exp\left(\frac{-Q_c}{RT}\right) \quad (7-3)$$

A_2 : material constant

β : constant

The concept of the steady-state strain rate only holds true, if the microstructure remains unchanged during the whole creep experiment. A true steady-state regime can be assumed, if the strain rate stays constant for several percent of deformation [186, p. 391]. For multiphase and particle strengthened alloys this is often not the case. Nickel-base superalloys, for example, show microstructural weakening very early during deformation due to so called “rafting”. This leads to the tertiary creep regime starting, before a steady state can be reached. The superposition of primary and tertiary creep results in a minimum strain rate $\dot{\epsilon}_m$ rather than a constant, steady-state strain rate $\dot{\epsilon}_s$ [186].

Similar behavior is observed for the powder metallurgical material in this work. A typical creep curve for constant true stress loading in compression can be seen in Fig. 7-8. After a normal primary creep transient with sharply dropping creep rate up to 1.5 % of plastic strain, strain rate increases continuously with no constant strain rate over a marked amount of strain.

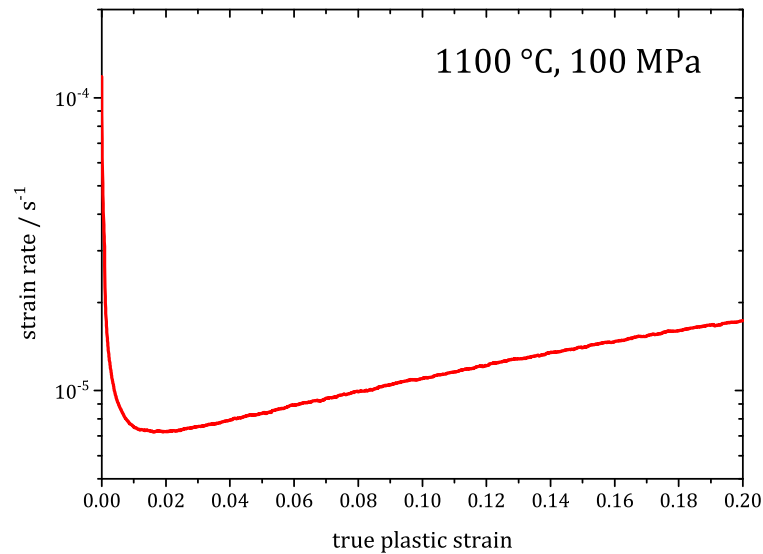


Fig. 7-8: typical creep curve of the analyzed material, in this case HIP GA HT1500-100 tested at 1100 °C and 100 MPa

This could hint at microstructural changes during deformation. As will be shown later, this is not the case. Another possibility would be the onset of damaging very early on during plastic deformation due to weak phase boundaries. This is proven exemplarily for the sample condition from Fig. 7-8, as significant cracking along the phase boundaries could be observed after 15 % of true plastic deformation (Fig. 7-9). Fine cracks originating from ruptured phase boundaries propagate along phase boundaries and through adjacent grains. In compression, still large amounts of deformation are achievable. However, when under tension these cracks will open and lead to premature failure of the sample.

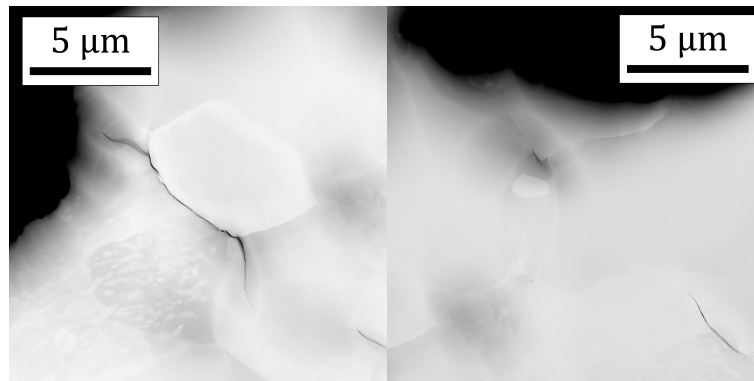


Fig. 7-9: TEM micrographs of HIP GA HT1500-100 after plastic deformation of 15 % showing the presence of phase boundary cracks

7.2.1 Stress Dependence

The “Norton plot” is a very typical way to display isothermal creep results as steady-state creep rate $\dot{\epsilon}_s$ is plotted over the true stress σ_t in a double logarithmic coordinate system. “Steady-state” would imply a constant true strain rate for at least 2 % of plastic strain [186, p. 391]. Due to the damage, this value cannot be obtained and the minimum creep rate will be used instead. In Fig. 7-10 and Fig. 7-11, creep results for compressive creep testing at 1000 °C and 1100 °C, respectively, are shown for the AC as well as different heat-treated conditions.

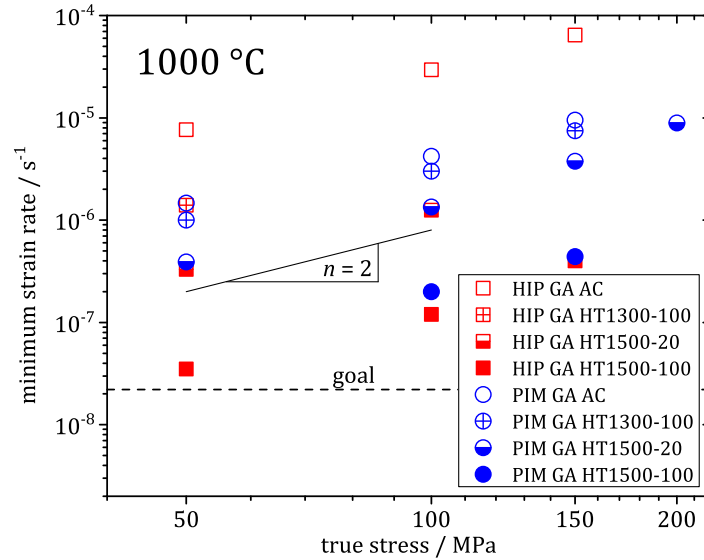


Fig. 7-10: plot of minimum strain rate over applied true stress at testing temperature of 1000 °C for material produced by HIP or PIM from gas-atomized powders in the AC and heat treated conditions; the dashed line indicates the creep goal for 1200 °C and stresses of 150 MPa

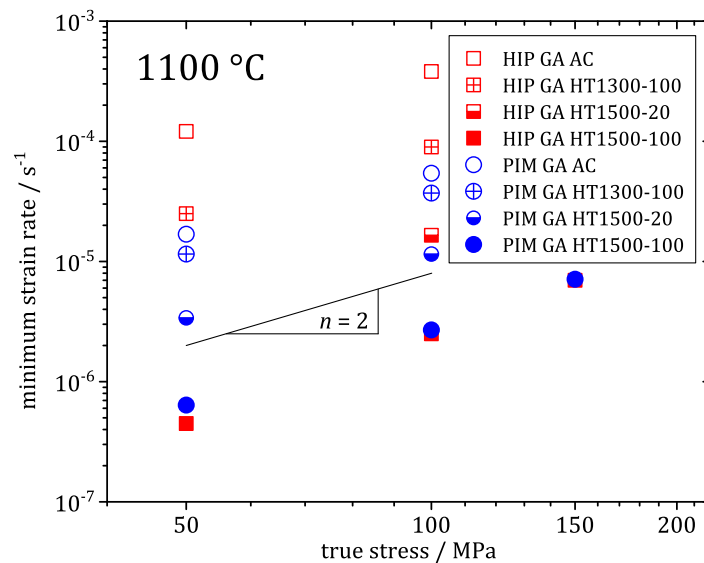


Fig. 7-11: plot of minimum strain rate over applied true stress at testing temperature of 1100 °C for material produced by HIP or PIM from gas-atomized powders in the AC and heat treated conditions

In Fig. 7-10, also the aspired steady-state creep rate is added (corresponding to < 1% deformation in 100 – 125 h) according to researchers familiar with requirements for aircraft turbines [19, 77, 98, 106]. This is the goal for temperatures higher than operating temperatures of today's nickel-base superalloys (≥ 1200 °C) and stresses of the order of 150 MPa. This goal is not reached by the investigated alloy in this work, even at a mere temperature of 1000 °C and a stress of 50 MPa. Another prerequisite that is not met is a small amount of primary creep strain (< 0.5 %) [77]. Together with the non-steady state creep deformation, the goal for this kind of creep behavior would be even lower.

It is apparent, that for all conditions tested, the stress exponent n for this material is about 2. This value is in the range often observed for grain boundary sliding to be operative and has been found for very fine-grained ($< 10 \mu\text{m}$) multiphase alloys [186, p. 411]. This means, that grain boundaries can easily move past another, inducing high stresses in grain triple junctions. Hence, triple junctions either rupture or the misfit is accommodated by material flow. Usually, the latter happens until this process cannot keep up with deformation and the former takes place. To prove that grain boundary sliding is indeed the dominant deformation mechanism, a heat-treated sample (PIM GA HT1300-100) was deformed to a (large) true strain of $\epsilon_t = 1$ (1100 °C, 50 MPa, corresponding to a height reduction by 63 %). If dislocation creep played a minor role as compared to grain boundary sliding, no significant shape change of grains is expected. Hence, on the cross-section of the sample, phase sizes parallel and normal to the loading axis were analyzed by the linear intersect method and compared to the values of an undeformed sample (Table 7-2). The aspect ratio S is in this case defined as the phase size perpendicular to the loading direction divided by the phase size parallel to it (Eq. (7-4)).

Table 7-2: phase sizes of deformed and undeformed PIM GA HT1300-100 on a cross-section determined by the linear intersect method

phase size / μm	$\epsilon_t = 0$	$\epsilon_t = 1$
to loading axis	4.01 ± 0.13	3.59 ± 0.16
⊥ to loading axis	3.94 ± 0.05	4.39 ± 0.33
aspect ratio S	1.00 ± 0.03	1.23 ± 0.15

The increase to 1.23 in the aspect ratio S is hardly significant with respect to the standard deviation but rather minor considering the overall plastic strain. This is rationalized as follows: for the limiting case of purely dislocation-based grain shape deformation an aspect ratio S can be estimated according to the following derivation (Eq. (7-7)). Constant volume (Eq. (7-5)), deformation parallel to edge a (Eq. (7-6)) and an initially cubic grain shape (Fig. 7-12) are assumed.

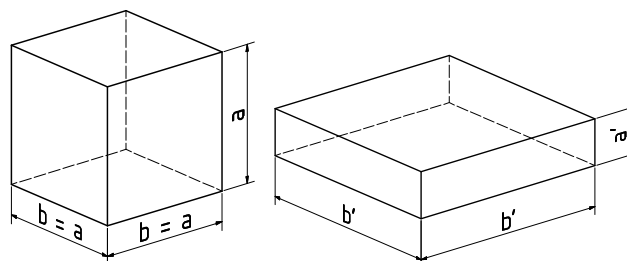


Fig. 7-12: schematic of deformation for an originally cubic grain with edge length a (left) to a uniaxially compressed cuboid grain of the same volume (right)

$$S = \frac{a'}{b'} \quad (7-4)$$

$$a \cdot b^2 = a' \cdot b'^2 \quad (7-5)$$

$$\varepsilon_t = \ln\left(\frac{a' - a}{a} + 1\right) \quad (7-6)$$

$$S = \exp\left(-\frac{3}{2}\varepsilon_t\right) \quad (7-7)$$

For the true strain $\varepsilon_t = 1$, an aspect ratio of $S = 4.48$ is expected. Hence, changes in grain shape (either by dislocation or diffusional creep) to induce strain can only play a minor role. Besides the change in grain shape, also a crystallographic texture should evolve during dislocation-based deformation. Slip systems will be activated according to the highest available Schmid-factor for either slip system. In bcc structures, this is mostly the $\{110\}\langle 111 \rangle$ system, but at elevated temperatures, also $\{112\}\langle 111 \rangle$ and $\{123\}\langle 111 \rangle$ may be activated. The following will describe the evolution of texture in a single crystal. The initial compression direction is arbitrarily situated in the standard triangle (Fig. 7-13). As deformation takes place in compression, the normal vector of the active slip plane will rotate towards the compression direction as indicated by the heavy arrows. As the symmetry lines $[001]/[111]$ or $[001]/[101]$ are reached, double slip is activated leading to the $[111]$ or $[001]$ direction, respectively, rotating towards the compression direction.

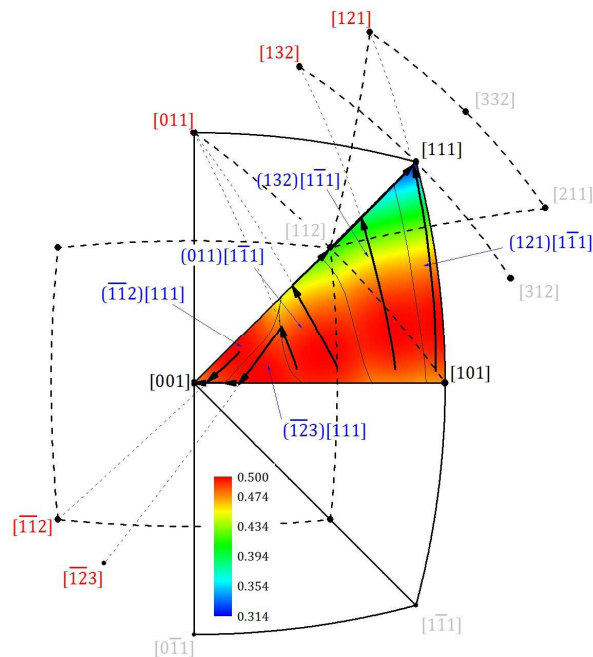


Fig. 7-13: standard triangle of a cubic crystal, colored according to the maximum Schmid-factor available in any of the bcc slip systems (blue); dotted lines connect an arbitrary crystal orientation with the respective active slip plane normal (red); heavy arrows indicate rotation of the compression direction towards symmetry lines, $\langle 111 \rangle$, or $\langle 100 \rangle$, depending on the initial orientation; dashed lines connect slip plane normals under multiple slip condition

In polycrystals, the initial orientation of each grain will determine if the $\langle 111 \rangle$ or $\langle 001 \rangle$ direction will rotate towards the compression direction. Also strain and stress compatibility with the neighboring grains have to be fulfilled. In the present multiphase material, the silicide phases would impose additional constraints, as they are not taking part in the deformation. For very high plastic strains in a polycrystal, this will lead to a very pronounced $\langle 111 \rangle / \langle 001 \rangle$ fiber texture [187, p. 192].

An EBSD mapping of the deformed cross-section shows no obvious texture (Fig. 7-14). The inverse pole figures (Table 7-3) exhibit no increase in texture from the heat-treated to the deformed condition. To the contrary, texture of intermetallic phases is reduced. Like the aspect ratio, this texture should be much more pronounced, if dislocation movement was responsible for the major amount of plastic deformation [188]. Some research was done on the texture formation during rolling of niobium and its alloys [189–191], which typically resulted in very pronounced fiber textures with the $\langle 001 \rangle$ or $\langle 111 \rangle$ directions being parallel to the normal direction. Vishwanadh et al. [189] found the anisotropy in the IPF to show a $MUD > 3$ for 60 % thickness reduction. The 100 % of true plastic strain achieved during uniaxial creep in the present work correspond to a thickness reduction of 63 % and resulted in a $\langle 111 \rangle$ fiber of intensity less than 1.3 (Table 7-3).

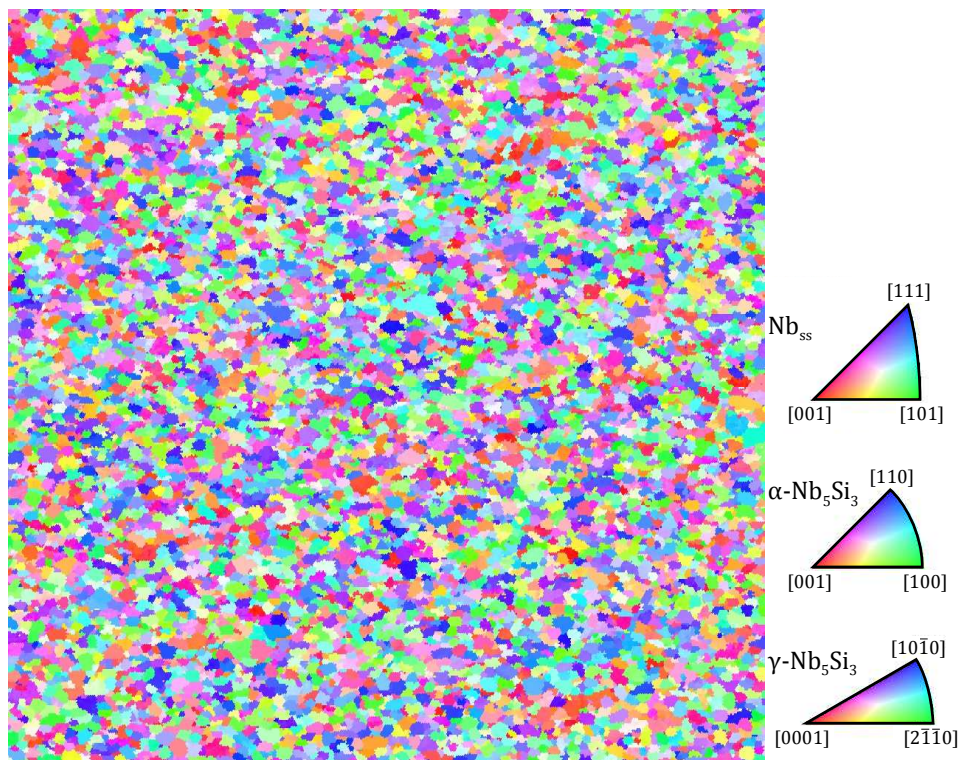
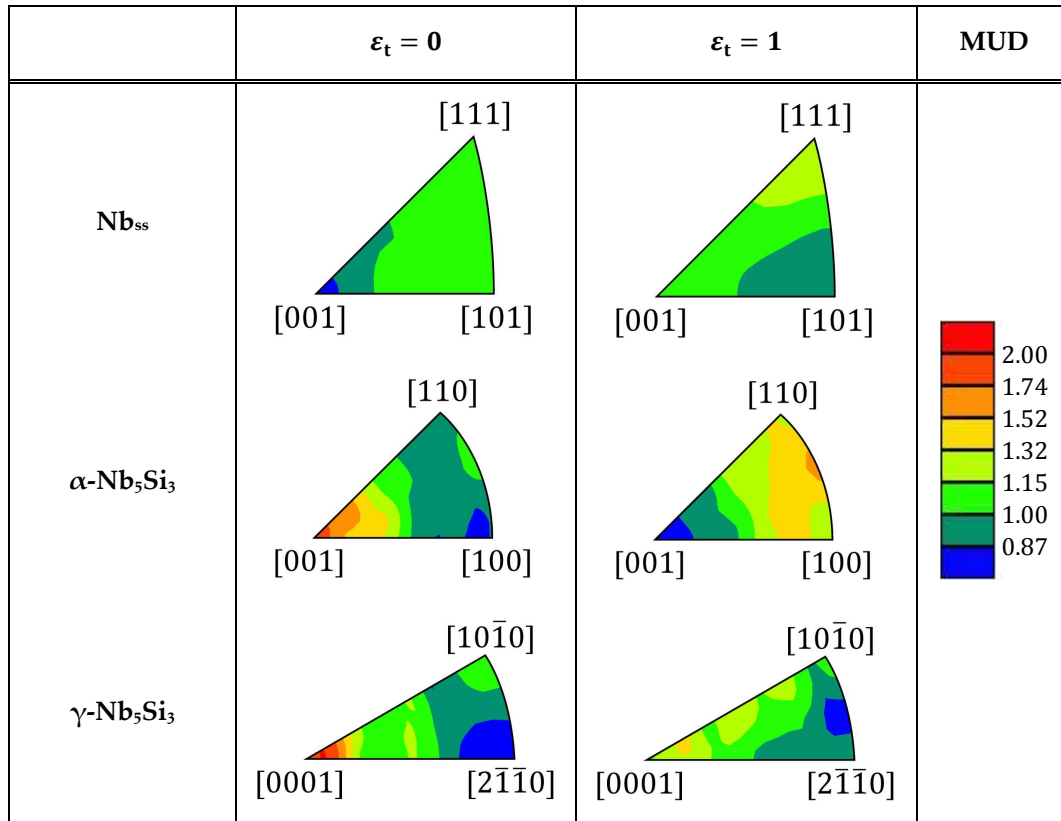


Fig. 7-14: EBSD mapping of the cross-section of the deformed PIM GA HT₁₃₀₀₋₁₀₀, the coloring indicates the crystallographic orientation of the lattice parallel to the deformation direction, i.e. parallel to the vertical figure edge; image width is 320 μm

Table 7-3: inverse pole figures for the three main phases of undeformed and deformed PIM GA HT₁₃₀₀₋₁₀₀; colors indicate multiples of the uniform distribution (MUD)



To conclude, the major amount of the deformation is carried out by grain boundary sliding, while dislocation slip and diffusional creep may act as accommodation mechanisms. Finally, TEM investigations yield a low density of dislocations in the niobium solid solution grains (Fig. 7-15), indicating that accommodation by dislocation slip is at least in parts active.

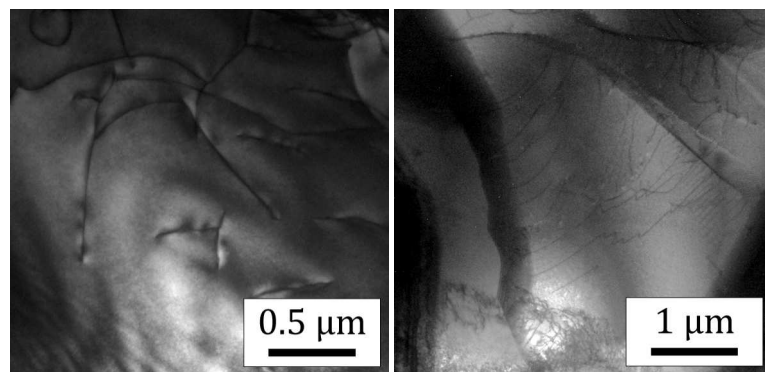


Fig. 7-15: TEM micrographs of solid solution grains in HIP GA HT₁₅₀₀₋₁₀₀ after plastic deformation of 15 % showing dislocations

And closing the circle, a high activity in grain boundary sliding may also lead to grain boundary cracks (Fig. 7-9), if accommodation processes cannot keep up with the rate of deformation [63], which in turn leads to a short-termed minimum strain rate instead of a steady-state.

7.2.2 Temperature Dependence

The temperature dependence of creep rate is usually characterized by the activation energy for creep, i.e. the numerator in the exponential term in Eq. (7-2). For several heat treatment conditions, the activation energy for creep could be determined by temperature jump tests between 900 and 1100 °C (example given in Fig. 7-16).

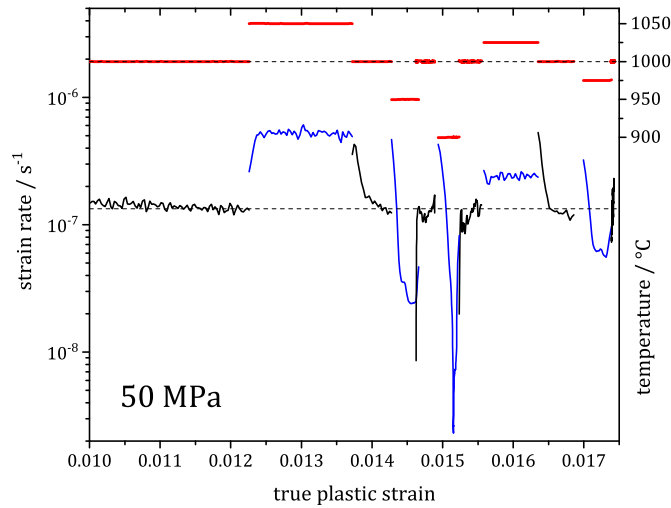


Fig. 7-16: strain rate of HIP GA HT1500-100 during temperature jump test; temperature in red, reference strain rate at 1000 °C in black (also dashed lines), strain rate for deviating temperatures in blue

The activation energy Q_c can then be determined as the slope of an $\ln(\dot{\epsilon}_m)$ over $1/RT$ plot at constant stress (Fig. 7-17).

$$\ln(\dot{\epsilon}_m) = \ln(A_3) - Q_c \cdot \frac{1}{RT} \tag{7-8}$$

A_3 : constant

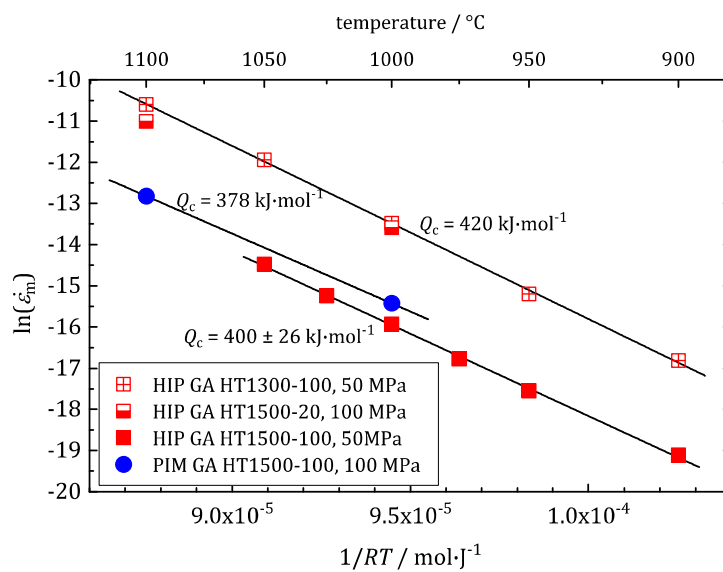


Fig. 7-17: temperature dependence of strain rate for select sample conditions to determine activation energy for creep

The energies that could be determined lie well in the range of about $400 \text{ kJ}\cdot\text{mol}^{-1}$. This is reasonably low scatter, considering that the minimum strain rate is only constant in a very small strain regime and some data points may lie before or after the minimum. To control that effect, temperature was changed back to the starting temperature after each measuring temperature for HIP GA HT1500-100 (Fig. 7-16). The control strain rate was constant with a relative standard deviation of 6.4 %, which results in a standard deviation of $26 \text{ kJ}\cdot\text{mol}^{-1}$ for the activation energy. Hence, all determined activation energies for creep in the composite show no significant deviation from $400 \text{ kJ}\cdot\text{mol}^{-1}$.

7.2.3 Grain Size Dependence

For pure dislocation creep no change in creep rate is expected for different grain sizes as long as the latter exceeds the size of the sub-grains formed during deformation. If formed, sub-grain boundaries limit the mean free path of dislocations rather than large-angle grain boundaries. And even for small grains, dislocation interaction (formation and annihilation) is assumed to take place mainly in the three-dimensional dislocation network inside the grains. Increasing creep rates for small grains are a result of grain boundary sliding becoming not negligible anymore compared to the dislocation creep portion [185].

Diffusional creep on the other hand is governed by vacancy diffusion from regions under tension to regions under compression. Grain boundaries are assumed to act as ideal sinks and sources for vacancies. Nabarro [192] and Herring [193] derived a strain rate that showed a grain size dependence to the power of two, based on bulk diffusion.

$$\dot{\epsilon}_{\text{NH}} = A_4 \cdot \frac{D_{\text{sd}}\sigma}{d_g^2} \quad (7-9)$$

$\dot{\epsilon}_{\text{NH}}$: Nabarro-Herring creep rate

A_4 : constant

D_{sd} : diffusion coefficient for self-diffusion

b : Burgers vector

d_g : grain size

Coble [194] extended this model by implying that grain boundary diffusion was the dominant diffusion path for lower temperatures. Hence, the cross-section of the diffusion path is introduced as well.

$$\dot{\epsilon}_{\text{C}} = A_5 \cdot \frac{D_{\text{gb}}\sigma \cdot w}{d_g^3} \quad (7-10)$$

$\dot{\epsilon}_{\text{C}}$: Coble creep rate

A_5 : constant

D_{gb} : diffusion coefficient for grain boundary diffusion

w : width of grain boundary

Noteworthy is also the stress exponent of 1, which is smaller than that measured. When grain boundary sliding is dominant, dislocation creep and diffusional creep are mainly accommodation processes to insure material integrity. In this case, depending on main

accommodation process, second order stress dependence with grain size dependence up to the third order is measured [195]:

$$\dot{\epsilon}_{\text{GBS}} = A_6 \cdot \frac{D_{\text{sd}} \sigma^2}{d_g^2} \quad (7-11)$$

$\dot{\epsilon}_{\text{GBS}}$: grain boundary sliding creep rate

A_6 : constant

$$\dot{\epsilon}_{\text{GBS}} = A_7 \cdot \frac{D_{\text{gb}} \sigma^2}{d_g^3} \quad (7-12)$$

A_7 : constant

However, in a few cases, also grain size exponents of unity are reported, mainly for slip accommodated grain boundary sliding [63, 195].

Hence, it is even more surprising that in this work an average exponent of 4.4 could be determined for PIM GA (Fig. 7-18). The grain sizes used for this calculation are the ones determined by EBSD on undeformed samples (see chapter 6.2.8, Table 6-8 on p. 80).

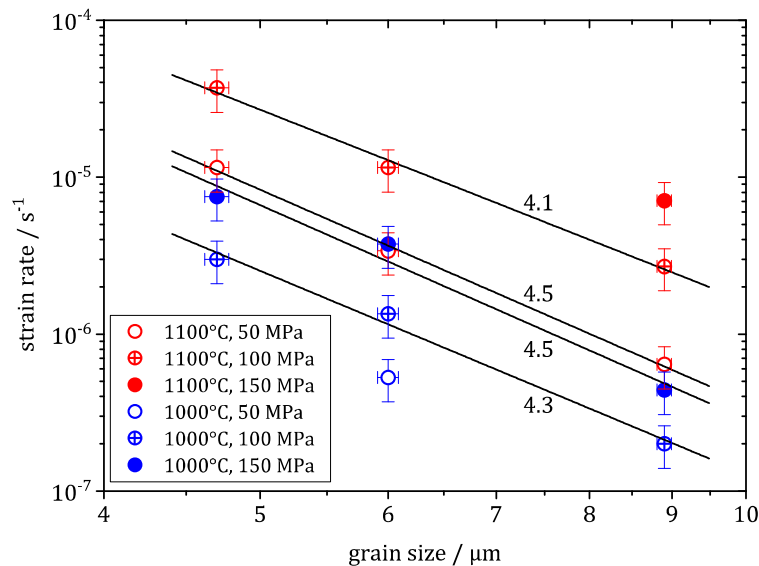


Fig. 7-18: double logarithmic plot of creep rate over grain size for PIM GA; grain sizes of 4.7, 6.0, and 8.9 μm correspond to the heat treatments HT1300-100, HT1500-20, and HT1500-100, respectively

Since there is no basis for grain size exponents larger than three in the literature, it is suggested that a second mechanism besides the grain size itself is superimposed. The three mean grain sizes 4.7, 6.0, and 8.9 μm correspond to the heat treatments HT1300-100, HT1500-20, and HT1500-100, respectively. It was shown in section 6.1.3 that for heat treatments at 1500 $^{\circ}\text{C}$ the previously present silicides $\alpha\text{-Nb}_5\text{Si}_3$ and $\gamma\text{-Nb}_5\text{Si}_3$ transform locally into the $\beta\text{-Nb}_5\text{Si}_3$ modification due to inhomogeneous oxygen distribution. Each localized $\beta\text{-Nb}_5\text{Si}_3$ network corresponds to one single grain. In those regions grain boundary sliding is not readily active, increasing the local resistance to creep. This could explain why HT1500-20 and HT1500-100 show lower minimum creep rates than expected from the mean grain size. After large creep

strains ($\varepsilon_t = 1.23$), EBSD shows localized bands of very fine grains (Fig. 7-19) presumably forming during the transformation from β -Nb₅Si₃ back to α -Nb₅Si₃.

To reduce porosity forming during heat treatment, HIP GA was subjected to a second HIP cycle (for details see section 8.2.1). After those additional four hours at 1230 °C, β -Nb₅Si₃ disappeared completely (see Fig. 14-4 in the Appendix), while coarsening is negligible. The resulting creep rates at 1100 °C are by a factor of 2 larger than for the β -Nb₅Si₃ containing samples. This is hardly significant, but would, however, reduce the grain size exponent to a mere 3.1, getting it into an explainable range.

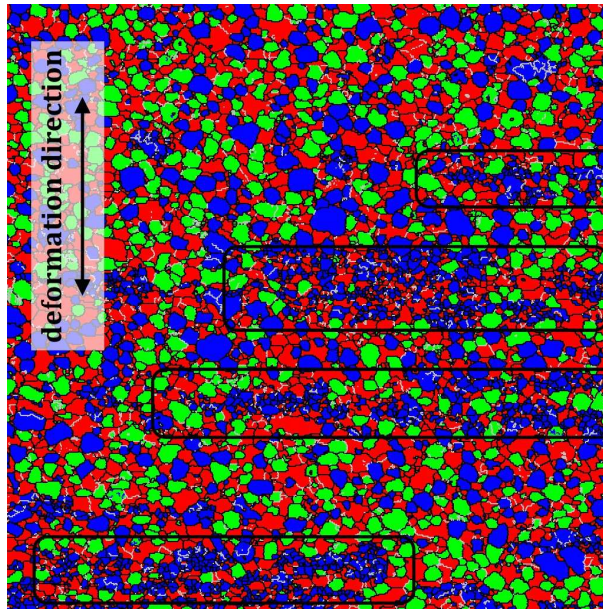


Fig. 7-19: EBSD phase mapping of the cross-section of the deformed HIP GA HT1500-100, Nb_{ss} in red, α -Nb₅Si₃ in blue, γ -Nb₅Si₃ in green, high angle grain boundaries in black, low angle grain boundaries in grey; black boxes highlight fine grained α -Nb₅Si₃ regions after deformation; image width 320 μ m

7.2.4 Discussion of Creep Properties

Creep in composites is determined by combined creep in the silicide and solid solution phase [3]. Finite element simulations have shown that due to the lower creep resistance and accordingly higher strain of the solid solution, stress transfer to the silicide takes place [196] during slip-controlled creep. This suggests a significant influence of phase ratios but also of the creep resistance of the individual phases.

Arc-melted material – with compositions close to the ones measured by EDS (Nb-36.5Si-13Ti-1Al-4Hf and Nb-36Si-23.5Ti-2.5Al-0.5Cr-7.5Hf for α -Nb₅Si₃ and γ -Nb₅Si₃, respectively) – formed monolithic intermetallic compounds (see Fig. 14-5 in the Appendix). The two silicide phases, α -Nb₅Si₃ and γ -Nb₅Si₃, show minimum creep rates more than three orders of magnitude lower than for the composite. At 1100 °C, creep rates are lower than the limit of determination, i.e. below $1 \cdot 10^{-9} \text{ s}^{-1}$. For γ -Nb₅Si₃, minimum creep rates were also determined at 1200 and 1300 °C and a stress of 200 MPa (see Table 7-4), showing good accordance with data from Subramanian et al. [197] who tested binary Nb₅Si₃. They found a stress exponent of unity with activation

energy close to that for niobium diffusion in Nb_5Si_3 , $234 \text{ kJ}\cdot\text{mol}^{-1}$, which points to Nabarro-Herring-type diffusional creep. Similar results were obtained by Bewlay et al. [2, 198] for binary Nb_5Si_3 . However, for multicomponent monolithic silicides, strain rates about one order of magnitude higher were determined, with $\gamma\text{-Nb}_5\text{Si}_3$ alloys showing the lowest strength of all Nb_5Si_3 modifications. This is conclusive with data for binary Ti_5Si_3 [199] giving significantly higher strain rates of about $1\cdot 10^{-6} \text{ s}^{-1}$ at $1200 \text{ }^\circ\text{C}$ and only 100 MPa . It has to be assumed, though, that highly alloying with niobium, which has a higher melting point, will be beneficial for creep resistance of Ti_5Si_3 .

In the 1960's some single-phase niobium solid solution high-temperature alloys were developed for commercial use. Those were typically highly alloyed with other refractory metals such as tungsten and/or tantalum to achieve sufficient high-temperature strength. Oxidation resistance was expectably limited and protective coatings were necessary [17]. For the creep goal of 1% strain in 100 hours, stresses in the range of 20 to 60 MPa could be endured at $1200 \text{ }^\circ\text{C}$ [111]. In contrast, Nb-1Si and a more complex $\text{Nb-0.9Si-27Ti-2Al-2Cr-5Hf}$, which is close to the solid solution composition in this work, could only bear 20 and 10 MPa , respectively [200].

Table 7-4: minimum creep rates obtained for monolithic silicides $\alpha\text{-Nb}_5\text{Si}_3$ and $\gamma\text{-Nb}_5\text{Si}_3$ at 200 MPa in s^{-1}

temperature / $^\circ\text{C}$	$\alpha\text{-Nb}_5\text{Si}_3$	$\gamma\text{-Nb}_5\text{Si}_3$
1100	$< 1\cdot 10^{-9}$	$< 1\cdot 10^{-9}$
1200	—	$2.3\cdot 10^{-9}$
1300	—	$1.4\cdot 10^{-8}$

Bewlay et al. investigated the influence of silicon content and, thus, of solid solution phase fraction on creep resistance of Nb-xSi-25Ti-8Hf (with $12 \leq x \leq 22$). Both, very low and very high volume fractions of silicide phases are detrimental to creep resistance. For low contents, the creep behavior of the solid solution dominates creep, whereas at high volume fractions, cracking of the silicide phases deteriorates creep resistance. In the range of $16 - 20 \%$ silicon the strain rate was minimal and the creep goal could be met [200]. It has to be considered, that the compositions tested – since aluminum and chromium are not present – contain Nb_3Si as the main silicon-containing phase and, thus, silicide fractions are higher than for Nb_5Si_3 -containing composites of the same silicon content, reaching $62 \text{ vol}\%$ at $18 \text{ at}\%$ of silicon. Hence, the $53 \text{ vol}\%$ of silicide phases in the present work should be below the crack controlled creep regime.

Composite materials of MASC-type compositions have been claimed to reach the intended creep goal. Exact compositions of the directionally solidified alloys were not given, though [98]. Also, titanium-free composites, alloyed with 5% of other refractory metals, surveyed during the ULTMAT project [105] undercut the $2\cdot 10^{-8} \text{ s}^{-1}$ threshold. Compositions with $4 - 5$ components come close, such as Nb-16Si with $21 - 25 \%$ titanium and around 8% hafnium [201] or the $\text{Nb-16Si-5Hf-5Mo-15W}$ [107].

The present alloy should have a high potential to reach sufficient creep resistance due to the high volume fraction of intermetallics (over 50%), which also possess a very high creep

resistance. But despite that, the composites creep strength is even lower than that of single phase niobium solid solution alloys. The small grain size and the subsequent activation of grain boundary sliding as the dominant creep mechanism prevent the high-temperature strength of the silicide to be utilized.

The activation energy for creep is $400 \pm 26 \text{ kJ}\cdot\text{mol}^{-1}$. This range shows good agreement with the activation energy for self-diffusion of niobium, which has been determined by several sources to be 349 [202], 398 [203], 402 [204], or 440 $\text{kJ}\cdot\text{mol}^{-1}$ [205], and also for titanium in niobium, the second most abundant element in the solid solution ($Q_{Ti}^{Nb} = 364 \text{ kJ}\cdot\text{mol}^{-1}$ [206]). On the other hand, activation energies for diffusion of Si and Nb in Nb_5Si_3 have been measured to be much smaller with $Q_{Nb/Si}^{Nb_5Si_3} = 271 \text{ kJ}\cdot\text{mol}^{-1}$ [207], $Q_{Nb/Si}^{Nb_5Si_3} = 263 \text{ kJ}\cdot\text{mol}^{-1}$ [208], and $Q_{Si}^{Nb_5Si_3} = 201 \text{ kJ}\cdot\text{mol}^{-1}$ [209]. This finding further points at creep of the silicide phase itself not being a significant contributor to creep. The activation energy for grain boundary diffusion Q_{gbd} is typically around half that for bulk diffusion Q_{sd} ($Q_{\text{gbd}} = 0.5Q_{\text{sd}}$) [210, p. 623], and hence about $200 \text{ kJ}\cdot\text{mol}^{-1}$ for niobium. Even if grain boundary sliding is the dominating mechanism, misfits in triple junctions have to be accommodated by other processes, i.e. dislocation or diffusional creep, that contribute a non-negligible part to the total deformation (minimum of 20 – 30 % [211, p. 419, 212]). The accommodation processes are considered rate controlling [213]. Hence, the activation energy for the accommodation processes corresponds to the activation energy for creep. Based on the presence of dislocations in the solid solution of deformed and their absence in undeformed samples, and the obvious activation energy for creep, dislocation accommodated creep seems prevalent. However, the other processes likely take place simultaneously. Typically, activation energy for grain boundary sliding is close to that for grain boundary diffusion, which would be half of what was measured.

Similar behavior was observed for molybdenum-based silicide composites [214, 215] starting with a sub-micron grain size that was coarsened by annealing to $6.6 \mu\text{m}$ showing also comparable stress exponents of about 2 and activation energies similar to that for molybdenum self-diffusion. The grain size exponent, however, was close to unity, which is in accordance with the assumed accommodation by dislocation movement. In the present material, the grain size exponent p is 4.4, which in part may stem from the $\beta\text{-Nb}_5\text{Si}_3$ networks forming during heat treatment. But even when $\beta\text{-Nb}_5\text{Si}_3$ is not present anymore after the additional HIP cycle, the grain size exponent falls to 3.1 which would only be expected for grain boundary diffusion accommodated grain boundary sliding, which in turn would implicate a lower activation energy. To better understand this, a larger range of investigated grain sizes would have been necessary. This is difficult to accomplish, as the starting grain size for PIM is already close to that of the HT1300-100 condition and coarsening at temperatures below $\beta\text{-Nb}_5\text{Si}_3$ formation would take very long as for HT1500-100 grain size not even doubled (see section 9.2).

Furthermore, it is often reported [211, p. 416, 216, 217] that grain boundary sliding necessitates grain boundary migration and subsequent coarsening. The grain sizes of PIM GA HT1300-100 were determined via EBSD after 100 % of true plastic deformation and are given in Table 7-5. No significant change in grain size of either phase could be found. No strain induced coarsening could be observed in a microstructure that seems stable at test temperatures.

Another well-established feature of grain boundary sliding, the clustering of phases during deformation [218, 219], however, was observed in EBSD sections prior and post creep (see Appendix Fig. 14-6).

Table 7-5: grain sizes of undeformed and deformed PIM GA HT1300-100 on a cross-section determined by EBSD

	undeformed	deformed
Nb_{ss} grain size / μm	4.9 ± 1.9	4.7 ± 1.8
$\alpha\text{-Nb}_5\text{Si}_3$ grain size / μm	4.6 ± 1.5	4.6 ± 1.3
$\gamma\text{-Nb}_5\text{Si}_3$ grain size / μm	4.2 ± 1.5	4.2 ± 1.6

8 Bending Tests

8.1 Fracture Toughness

Room temperature fracture toughness is a very important property even for materials designated for high-temperature application as it provides a measure of failure tolerance and makes components manageable. It is generally considered that a fracture toughness of 20 MPa·m^{0.5} is sufficient for structural components in aircraft engines [3, 85].

Fracture toughness values were determined for samples from gas-atomized powders in the AC as well as the HT1500-100 condition according to Eq. (4-6) (Table 8-1). The average values of all tested PM conditions (with five samples for each condition) lie in a narrow range between 7.7 and 8.7 MPa·m^{0.5}. The mean fracture toughness increases during the heat treatment for all conditions, but except for HIP CGA this change is insignificant due to scatter in the AC condition. ARC samples in comparison show a significantly higher toughness with 10 MPa·m^{0.5}.

Table 8-1: fracture toughness of GA material in the AC and HT1500-100 condition as well as ARC determined by the SEVNB-method

$K_{Ic} / \text{MPa}\cdot\text{m}^{0.5}$	HIP GA	HIP CGA	PIM GA	ARC
AC	8.3 ± 1.2	8.0 ± 0.1	7.7 ± 1.0	10.0 ± 0.7
HT1500-100	8.5 ± 0.3	8.7 ± 0.2	8.4 ± 0.1	–

The fracture toughness K_{Ic} is defined as the critical stress intensity in mode I loading where unstable crack propagation occurs. One pre-requisite is plane strain loading, meaning no strain component acting parallel to the crack tip, in this case parallel to B (compare section 4.3.2). The reason is that the plane stress loading condition facilitates plastification of the material in front of the crack tip and leads to an overestimation of K_{Ic} . An empirical condition to test for plane strain loading is given in ASTM E399 [220]:

$$B, a > 2.5 \left(\frac{K_{Ic}}{\sigma_{ys}} \right)^2 \quad (8-1)$$

Since K_{Ic} is needed in this equation, compliance can only be verified after the test itself. Hence, for proper choice of sample geometry, K_{Ic} should be estimated beforehand. From quasi-static compression tests at room temperature the 0.2 % offset yield stress is known to be larger than 1500 MPa for all tested conditions. With $K_{Ic} < 9 \text{ MPa}\cdot\text{m}^{0.5}$, the value for $2.5 \left(\frac{K_{Ic}}{\sigma_{ys}} \right)^2$ can be estimated to be below 0.09 mm which is by a factor of 100 smaller than the crack length a and by a factor of 300 smaller than the width B . Hence, the plane strain requirement is fulfilled and the measured values in Table 8-1 can be assumed to be valid K_{Ic} values. Fracture surfaces of HIP GA AC and HIP GA HT1500-100 can be seen in Fig. 8-1, showing only minimal signs of ductility. Even the solid solution fails by cleavage fracture.

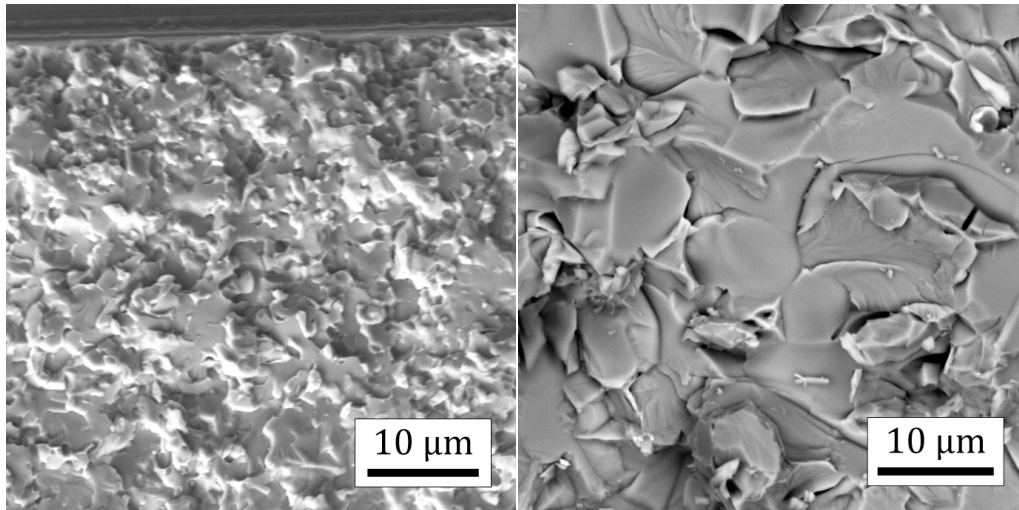


Fig. 8-1: SEM micrographs of fracture surfaces of HIP GA AC (left) and HIP GA HT1500-100 (right) showing mostly transgranular fracture with river patterns

8.1.1 Influence of Notch Root Diameter

For ceramics, the notch root diameter is often thought to have only minor influence on measured fracture toughness values [221]. Munz et al. [222] found decreasing fracture toughness in alumina down to 66 μm notch root diameter while Nishida et al. [223] reached a plateau (3.8 $\text{MPa}\cdot\text{m}^{0.5}$) below diameters of 20 – 40 μm (Fig. 8-2). Both found the fracture toughness to hardly exceed 5 $\text{MPa}\cdot\text{m}^{0.5}$ even for diameters of 400 μm .

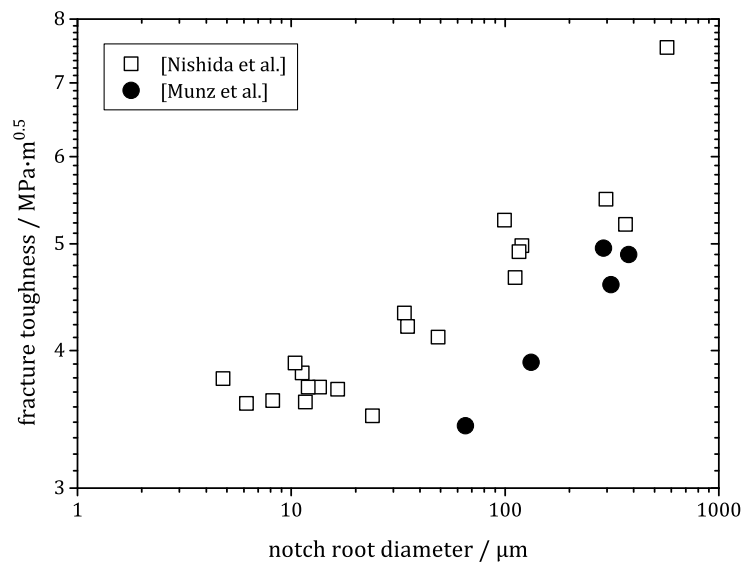


Fig. 8-2: influence of notch root diameter in SEVNB bend testing on fracture toughness of alumina; reproduced after [222, 223]

In order to easily estimate fracture toughness, many researchers do not implement proper fatigue crack initiation (as for single edge pre-cracked beams, SEPB) or, as done in this work, sharpening of the notch root (SEVNB), but only use the notch introduced by electro discharge machining, in the following referred to as SENB (single edge notched beam). This approach

may not yield the actual critical stress intensity and is thus usually designated K_q . To provide better comparability, HIP GA AC samples were also tested as SENB with a 1 mm EDM notch featuring a notch root diameter of 300 μm (see Fig. 14-1 in the Appendix). The resulting toughness K_q is $9.0 \pm 0.2 \text{ MPa}\cdot\text{m}^{0.5}$. This is only slightly higher than for the V-notched material and due to scatter not significant. A reason for the minor increase could be that fracture is not initiated in the same fracture plane over the whole thickness B of the sample and river patterns leading to a common fracture plane are visible. The strongest variation of toughness with increasing notch root radius is expected for HIP GA AC as it features the smallest grain size. For the other conditions a smaller deviation is expected. The high thermal gradient during EDM may also lead to fine cracks in the notch root yielding a toughness value much closer to K_{Ic} than expected. As can be seen in the following section, this indifference is not always the case and comparability is only given for properly determined K_{Ic} values.

8.1.2 Discussion of Fracture Toughness

As the pure intermetallic compounds $\alpha\text{-Nb}_5\text{Si}_3$ and Ti_5Si_3 ($\gamma\text{-Nb}_5\text{Si}_3$) provide a fracture toughness comparable to ceramics of only 3 [41] and 2 $\text{MPa}\cdot\text{m}^{0.5}$ [199], respectively, the main increase in toughness of the composites is considered to stem from ductile phase toughening. This can lead to crack bridging, plastic stretching, and interface debonding [224]. Accordingly, increasing volume fractions of solid solution with decreasing silicon content will lead to higher toughness values [41, 64, 74, 85, 225] (Fig. 8-3).

While pure niobium has a very high room temperature fracture toughness of 90-120 $\text{MPa}\cdot\text{m}^{0.5}$ [226], alloying considerably reduces it. Nekkanti and Dimiduk [41] produced niobium solid solution with 0.8 % silicon and found a toughness of 27 $\text{MPa}\cdot\text{m}^{0.5}$. A similarly detrimental effect of silicon in solid solution was also observed for molybdenum, decreasing toughness by factor of five for alloying with 0.5 % of silicon [227]. Murayama and Hanada [228] determined ASTM standard [220] compliant fracture toughness of Nb-0.7Si-3Al as 7.8 $\text{MPa}\cdot\text{m}^{0.5}$. Kong et al. [45] produced solid solution alloys (Nb-0/0.5Si-27.6Ti-12.9Cr-2.1Al-1.1Hf) much closer to the composition in this work (Nb-0.7Si-26.7Ti-8.2Al-5.7Cr-1.8Hf). While the silicon free solid solution still has a toughness of 20.3 $\text{MPa}\cdot\text{m}^{0.5}$, the addition of silicon leads to a steep reduction to 12.8 $\text{MPa}\cdot\text{m}^{0.5}$. The high chromium content led to the formation of minor amounts of NbCr_2 , and again only SENB samples were used. Aluminum [229] and chromium [85] are both known to have detrimental effects on the toughness, explaining, why the fracture toughness found by Murayama and Hanada [228] for the ternary alloy is quite low. The toughness decrease is based in parts on the formation of secondary phases (Nb_3Al and Nb_2Cr , respectively). Davidson et al. [85] attribute the decrease with added chromium to an increase in d-shell electron density. This is counterbalanced by the high amount of titanium solved in the multi component alloy. Toughness values below 10 $\text{MPa}\cdot\text{m}^{0.5}$ for binary Nb-Al and Nb-Cr alloys (around 15 % of Al or Cr) can be raised to 80 $\text{MPa}\cdot\text{m}^{0.5}$ when adding up to 40 % of titanium [85, 229]. Thus, a similar toughness to that found by Kong et al. can be expected for the solid solution phase in this work.

The toughness of the composite is expected to lie between those of intermetallic and solid solution while other factors such as crack bridging or ductile phase pullout may further increase it.

Oftentimes [74, 224, 230], the toughness increase by the ductile solid solution in a NbSi-composite is estimated with the following equation derived by Ashby [231]:

$$K_{Ic,c} = K_{Ic,m} + E_d \left(C V_f \frac{\sigma_{ys,d}}{E_d} a_0 \right)^{0.5} \quad (8-2)$$

$K_{Ic,c}, K_{Ic,m}$: fracture toughness of composite and matrix, respectively

E_d : elastic modulus of ductile phase

V_f : volume fraction of ductile phase

a_0 : diameter of ductile phase

If only crack bridging is assumed, the constant C is taken as 1.6. Taking rough but conservative estimates for E_d , V_f , $\sigma_{ys,d}$, and a_0 of 110 GPa, 0.46 (section 6.2), 350 MPa [230], and 8.9 μm (section 6.2), a composite toughness of 19 $\text{MPa}\cdot\text{m}^{0.5}$ is expected. Next to this model originally being constructed for an intermetallic matrix with a small phase fraction of spherical, ductile inclusions, it requires the solid solution to actually deform plastically at room temperature. While minor dimpling is visible on the fracture surface of heat-treated samples (Fig. 8-1, right), fracture is dominated by cleavage in both, the intermetallic phases and the solid solution.

Several groups have investigated binary NbSi alloys. Not only composition but also processing shows a large impact on toughness (Fig. 8-3). Arc-melted Nb-16Si displayed a mere fracture toughness of 5.4 $\text{MPa}\cdot\text{m}^{0.5}$ [224], while by directional solidification (DS) 7.8 $\text{MPa}\cdot\text{m}^{0.5}$ [74], and by extrusion and heat treatment 12.8 $\text{MPa}\cdot\text{m}^{0.5}$ [230] could be reached. For Nb-10Si, the same tendency was found with toughness rising from 8.9 to 20.6 $\text{MPa}\cdot\text{m}^{0.5}$ for the same processes, respectively. Specimens were cut for crack propagation being perpendicular to solidification and extrusion direction making the elongated solid solution grains more effective for toughening.

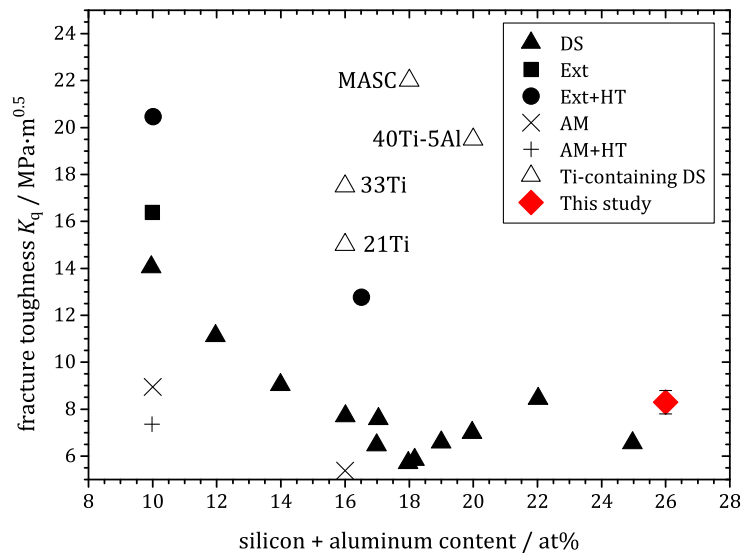


Fig. 8-3: fracture toughness K_q for binary niobium silicide composites as a function of silicon content for different processing conditions: directional solidification (DS), extrusion (Ext), and arc-melted (AM), partially heat treated (HT), reproduced after [74]; DS titanium-containing alloys [3] and average from the present work added

Titanium, as a major alloying element, can significantly increase the toughness also in the composite [3, 124], this effect was confirmed by Chan [232] by computational modeling; an increase was found from 6.5 to 15 and 17 MPa·m^{0.5} when adding 21 and 33 % of titanium to DS Nb-16Si, respectively (Fig. 8-3). For MA and hot-pressed Nb-16Si-20Ti, Wang et al. [124] measured 16.3 MPa·m^{0.5}. Bewlay et al. on the other hand obtained only 11.3 MPa·m^{0.5} also for DS Nb-16Si-27Ti [74], which hints at considerable scatter even for the same processing route.

For the complex alloys with five alloying elements and more, toughness values between 6 and 22 MPa·m^{0.5} were reached. A satisfactory toughness was achieved by Bewlay et al. [1] with the directionally solidified MASC alloy (Nb-16Si-25Ti-2Al-2Cr-8Hf) and Subramanian et al. [106] with a very similar (Nb-15Si-26Ti-2Al-2Cr-4Hf) extruded material, being 22 and 19.6 MPa·m^{0.5}, respectively. Those alloys have solid solution fractions of 54 and 65 %, respectively. A vanadium modified alloy with very similar Si+Al content (Nb-16Si-20Ti-3Al-3Cr-2Hf-2V) yields 14.7 MPa·m^{0.5} and was produced by arc-melting [30]. Jia et al. [31] cast Nb-16Si-22Ti-2Al-2Cr-2Hf and measured a similar value of 15.3 MPa·m^{0.5}. Those alloys often show R-curve behavior where crack propagation is stopped by crack bridging and ductile phase pullout. The crack initiation toughness usually is about 40 % smaller [1, 18]. On the other hand, extruded Nb-17.5Si-21.5Ti-2Al-9Cr-2Hf-1.2Sn could only reach 10.6 MPa·m^{0.5}. The higher silicon and chromium together with reduced titanium contents are detrimental. Beyond that, toughness values of the more complex alloys are scarce in literature as intellectual property interests of private companies prevent publication. The choice of 20 % silicon and 6 % aluminum for the alloy in this work (26 % Si+Al compared to 17 – 18 % for alloys reaching more than 19 MPa·m^{0.5}) reduced the solid solution fraction down to 46 % with the foreseeable effect on fracture toughness reaching only insufficient 8 – 9 MPa·m^{0.5}. But also interstitials such as oxygen have detrimental effect on toughness [77] (compare also section 9.1). Until toughness values of nickel-base superalloys are met, which typically reach values above 25 MPa·m^{0.5} [63, p. 464], an application of niobium-base alloys seems unlikely.

8.2 Ductile-to-Brittle Transition Temperature (DBTT)

As mentioned in section 7.1, for bcc metals the shear stress necessary for yielding τ_y is strongly temperature dependent due to the high Peierls barrier. The cleavage stress σ_c responsible for brittle fracture on the other hand is independent of temperature. This fact leads to the presence of a DBTT, as illustrated in Fig. 7-1, left, for some bcc metals. The DBTT is determined under tensile load, i.e. uniaxial tensile testing or often, due to constraints on material volume available, bending tests, as done in the present work. Charpy impact testing is used for DBTT under dynamic loading.

Based on the deflection measurement of the bending bars, fracture strains can be calculated in accordance to Eq. (4-9). It should be borne in mind, that this equation as well as the equation for the extreme fiber stress Eq. (4-8) is based on the elastic beam theory. Stresses and strains calculated beyond the yield point will deviate significantly from the actual local conditions. However, the strain will still grow more than proportionally, when the material yields, and the onset of plastic deformation can be determined. To obtain the true plastic strain corresponding to uniaxial loading, finite element calculations can be employed [233].

8.2.1 Fracture Strain

Fig. 8-4 shows the fracture strain obtained during bending for the AC condition. The onset of plastic deformation is assumed, if the fracture strain exceeds 0.2 % inspired by the 0.2 % offset yield strength $R_{p0.2}$. This is indicated by the dashed line. Tests were repeated at the point of transition; to guide the eye, the samples that show the highest ductility are connected. At a strain rate of 10^{-5} s^{-1} , HIP GA AC shows the lowest onset of plastic deformation at 750 °C. This is followed by PIM GA, HIP CGA, and ARC at 50 °C more, each.

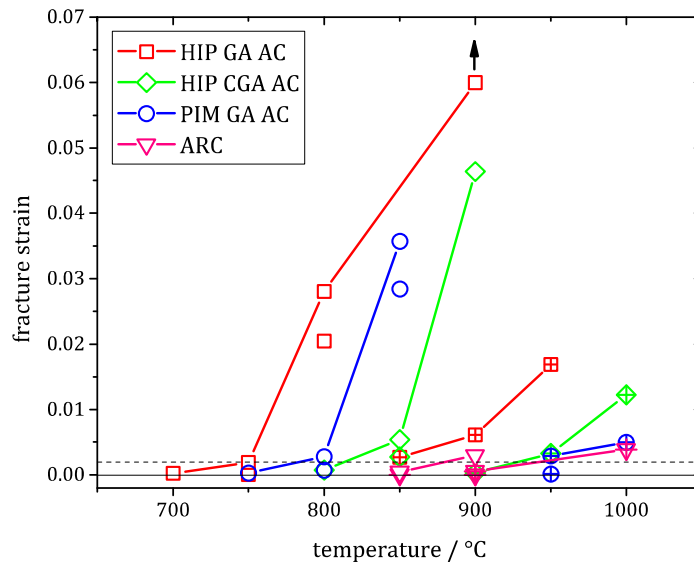


Fig. 8-4: fracture strain over temperature plotted for AC and ARC samples at strain rates of 10^{-5} s^{-1} (open symbols) and 10^{-3} s^{-1} (crossed symbols)

As described in the introduction to chapter 7, R_{eS} is strongly dependent on the strain rate. Hence, the DBTT, i.e. the onset of plastic deformation, where R_{eS} becomes smaller than the temperature-independent cleavage stress σ_c , is not a material constant, but will depend on the loading rate. As expected, an increase of deformation rate by two orders of magnitude (from 10^{-5} s^{-1} to 10^{-3} s^{-1}) leads to a strong increase of the plastic deformation onset by about 100 – 150 °C for all conditions equally.

The microstructure, represented by phase morphology, phase size, and porosity, will influence DBTT, as well [134, p. 2281, 176, 234]. PIM GA AC has a porosity of 1.8 %. If a pore is located in the volume of high tensile stresses, e.g. on the bottom side of the sample below the upper bearing (compare Fig. 4-6), fracture may be induced due to stress concentration around the pore. HIP CGA and ARC show large intermetallic regions, which will not deform plastically. If the fine-grained solid solution around it yields at a given stress, load transfer to the intermetallic particle will take place [196] leading to fracture of the intermetallic and subsequently of the whole sample (Fig. 8-5, left). The use of a different size fraction of GA powder, namely CGA, for HIP with otherwise identical processing leads to an increase in DBTT by around 100 °C.

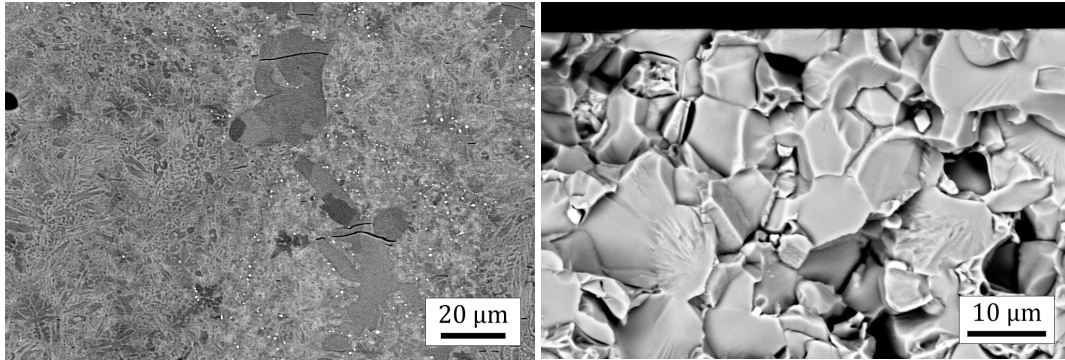


Fig. 8-5: backscatter electron micrographs of fractured three-point bend specimens, left: top view on the extreme tensile fiber of HIP CGA AC close to the fracture plane (out of frame) after testing at $850\text{ }^{\circ}\text{C} / 10^{-5}\text{ s}^{-1}$; tensile loading parallel to vertical figure edge; even outside the fracture plane, silicide particles show cracks perpendicular to tensile loading; right: fracture surface of PIM GA HT1500-100 after bending at $850\text{ }^{\circ}\text{C} / 10^{-5}\text{ s}^{-1}$, extreme tensile fiber at the top

The heat treatment with the greatest potential regarding creep strength is HT1500-100. Consequently, the influence of this heat treatment on the ductile-to-brittle transition temperature is evaluated as well.

The heat-treated HIP GA does not deform plastically until $900\text{ }^{\circ}\text{C}$ (Fig. 8-6). This is more than $100\text{ }^{\circ}\text{C}$ higher than in the AC condition. Partly, this may be explained by coarsening of the microstructure [134, p. 2281]. However, as phase sizes are comparable for HIP GA HT1500-100 and PIM GA HT1500-100, the same onset would be expected from PIM samples. During compression both show very good agreement in properties. PIM shows plasticity already at $850\text{ }^{\circ}\text{C}$.

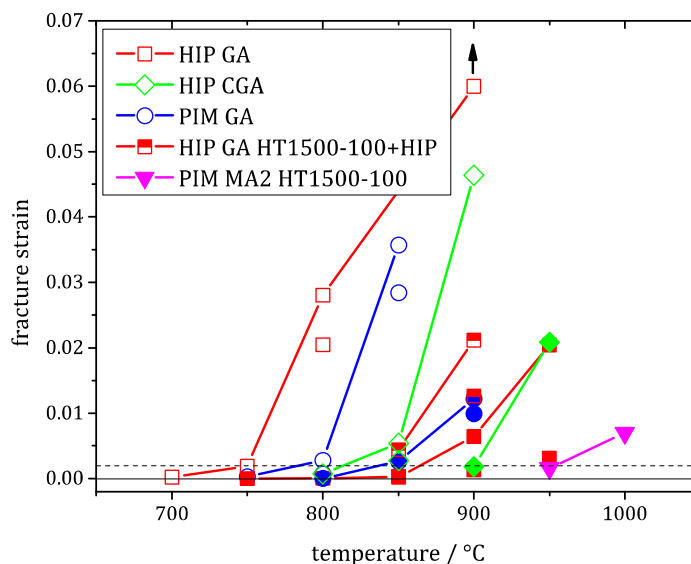


Fig. 8-6: fracture strain over temperature plotted for HIP GA, HIP CGA, and PIM GA in the AC (open symbols) and HT1500-100 (solid symbols) condition and additionally HIP GA HT1500-100+HIP at strain rates of 10^{-5} s^{-1}

There is a difference between both compaction methods, though. HIP develops additional porosity while being heat treated at 1500 °C. The likely explanation is called temperature-induced porosity (TIP) and was first described by Peebles [235], but also others [236][4], in titanium alloys produced from EIGA, PIGA, or PREP powder by HIP. The reason for TIP is found to be gas entrapment either in the powder itself during atomization (hollow spheres) or in the HIP can due to gas adhesion to the particles or improper evacuation. In any case, during HIP the gas as it was entrapped at normal pressure or below, will be compressed at, in this case, 150 MPa – or 1500 bar – leaving no noticeable porosity. When heat-treated, the material softens and the entrapped gas expands and coalesces, increasing the porosity. This can be seen e.g. on a micrograph of the fracture surface of HIP GA HT1500-100 loaded at 800 °C (Fig. 8-7, left), showing multiple pores in the fracture plane. The fracture inducing pore is visible at the extreme tensile fiber surface (top of the figure). Also, from a micrograph of the extreme tensile fiber, it becomes obvious that in every possible fracture plane there are surface pores that could induce premature fracture of the material.

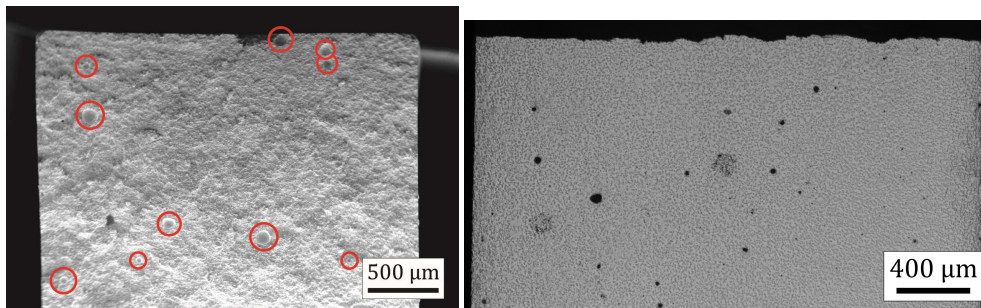


Fig. 8-7: left: secondary electron micrograph of HIP GA HT1500-100 tested at 800 °C; pores in the fracture plane are encircled in red, extreme tensile fiber at the top; right: topview optical micrograph of the extreme tensile fiber of the same sample, loading direction is vertical and fracture plane at the top.

In case of PIM, the brown part (injection-molded powder after debinding) is sintered under vacuum. This means that gas adsorbed at the powder particles' surface may very well leave the sample before porosity is closed. However, gas entrapped inside the particle may not be able to leave, limiting the minimum porosity achievable. This makes improper powder handling or evacuation prior to HIP more likely. As described in section 4.1.2, the powder was filled into the can and then evacuated overnight before crimping and welding. But the evacuation was done at room temperature. The problem may be averted by preheating the can during evacuation, to ensure that the powder is gas-free. This argument is backed by the porosity measurements of HIP GA and HIP CGA before and after heat treatment (Table 8-2). According to Wegmann et al. [4], the amount of atomization gas entrapped in the powder in form of hollow particles increases with increasing particle size. This would lead to a larger increase in porosity for HIP CGA ($d_p = 106 - 225 \mu m$) compared to HIP GA ($d_p < 25 \mu m$). However, the opposite is observed, indicating that it is in fact the surface gas causing the TIP, as the powder surface is about 13 times higher for the fine fraction than for the coarse fraction.

Table 8-2: porosity of samples produced from GA and CGA powder before and after heat treatment as determined by the Archimedes principle

porosity / vol%	HIP GA	PIM GA	HIP CGA
AC	1.0 ± 0.1	1.8 ± 0.1	0.6 ± 0.2
HT1500-100	1.7 ± 0.1	0.9 ± 0.2	0.3 ± 0.1

To verify that the pores are indeed responsible for the increased DBTT, bending bars from HIP GA – prior to grinding and polishing of the surfaces – were submitted to an additional HIP cycle with the same parameter set as for the compaction HIP cycle after being heat treated at 1500 °C for 100 h. Hence, those samples are called HIP GA HT1500-100+HIP. The surface layer was removed by grinding to ensure the removal of potentially open pores at the surfaces (see Fig. 14-4 in the Appendix), which cannot be closed by HIP. Sample thickness W was thus reduced to 3.6 mm. As expected, no pores are visible on the fracture plane of those bending bars. In Fig. 8-6 the reHIPed samples are represented by the half solid squares. Onset of ductility is lowered by about 50 °C to show good agreement with the strain values obtained for PIM GA HT1500-100. The removal of stress concentrations at the pores has a positive effect on DBTT. Similar to creep properties, there is essentially no difference between PIM and HIP, then. Coarsening effects due to the additional four hours at 1230 °C can be neglected as 100 h at 1300 °C showed hardly any coarsening in the much finer grained PIM GA AC.

PIM MA2 HT1500-100 was the only MA material tested in bending due to already poor performance in compression and limitations in the amount of available sample material. Considerable ductility is measured at 1000 °C and above (Fig. 8-6). This is 100 – 150 °C higher than for PIM GA material, a result of the continuous intermetallic matrix.

8.2.2 Yield / Cleavage Stress

Yield stresses for a strain rate of 10^{-5} s^{-1} are given in Fig. 8-8 for the AC and HT1500-100 conditions of HIP GA and PIM GA. Samples not reaching 0.2 % of plastic strain are marked with an “X” and fracture stress is given instead. For AC the difference in grain size between HIP GA and PIM GA is visible since at testing strain rates of 10^{-5} s^{-1} , creep is already non-negligible. This was also visible in sections 7.1.2 and 7.2.1. At 1000 °C, the maximum stresses for 10^{-5} s^{-1} are about 50 and 150 MPa for HIP GA AC and PIM GA AC, respectively, during creep. For a defect free HIP GA AC at 700 °C, however, 1250 MPa could be reached. PIM GA AC shows defect controlled behavior as some samples at 800 and 850 °C fracture in a brittle manner at stresses significantly lower than values reached at 750 °C. The same is true for the very weak HIP GA AC at 750 °C.

In the heat-treated HT1500-100 condition PIM GA and HIP GA with additional HIP cycle show very good conformity; both have low porosity and comparable grain size. Below 900 °C HIP GA shows low strength compared to all other conditions due to the TIP. From 900 °C onwards, ductility is sufficient to reduce the impact of the porosity. Fracture surfaces still show pores in the extreme tensile fiber as responsible feature to lead to eventual fracture.

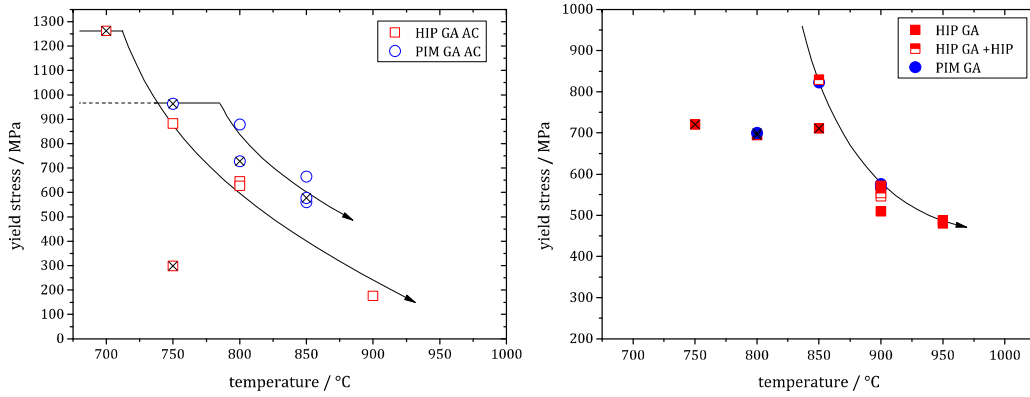


Fig. 8-8: yield stress over temperature plotted for HIP GA and PIM GA in the AC (left) and HT₁₅₀₀₋₁₀₀ (right) condition and additionally HIP GA HT₁₅₀₀₋₁₀₀+HIP (half filled symbols, right) at strain rates of 10^{-5} s^{-1} , note the different scales

8.2.3 Fracture Path

The fracture path changes with increasing temperature. At low temperatures fracture is controlled by cleavage of both, the intermetallic and the solid solution phase. With increasing temperature, the solid solution matrix becomes ductile and cleavage cracks of the intermetallic arrest in the solid solution or are bridged by it (Fig. 8-9, 850 °C). The fracture plane shows increased dimpling of the latter. Further increase in temperature weakens grain boundaries. Increasingly, cracks propagate along phase/grain boundaries and the fracture surface – next to transgranular cleavage of the intermetallics – shows intergranular fracture (Fig. 8-9, 900 and 950 °C). A tensile sample of HIP CGA HT₁₅₀₀₋₁₀₀ crept at 1100 °C and 150 MPa (the detailed results are not presented, because compaction to full density failed for those samples) exhibits only intergranular fracture of intermetallics and ductile dimple fracture of solid solution.

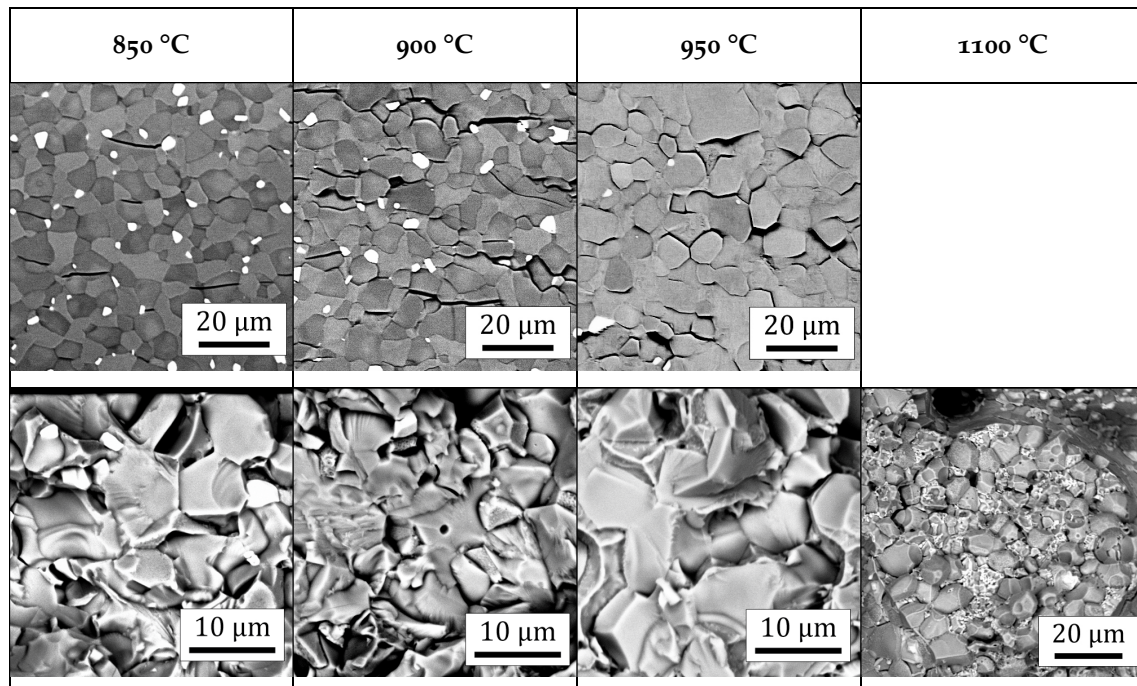


Fig. 8-9: top: extreme tensile fiber of HT₁₅₀₀₋₁₀₀ material close to the fracture plane for different deformation temperatures, loading direction vertical; bottom: fracture surface for the same samples

9 Final Discussion and Outlook

9.1 Ductility

Independent of loading mode and temperature, the investigated alloy shows extensive crack formation. At room temperature in compression, cracks will form mainly parallel to the loading direction, i.e. normal to tensile stresses. Cracks get trapped at the interface to the more ductile solid solution. When increasing the temperature, the solid solution becomes more ductile and the grain boundaries are weakened. Crack deflection at phase boundaries becomes more prominent. This behavior goes hand in hand with the onset of grain boundary sliding. E.g. PIM GA HT1500-100 deformed at 1000 °C with a strain rate of 10^{-3} s^{-1} , clearly shows void formation at triple junctions and phase boundaries. At this strain rate, accommodation processes cannot keep up with the overall deformation rate. This also manifests in the stress drop during compression testing of the coarse-grained, heat-treated material. In the AC material, diffusion paths are considerably shorter and the maximum stress level is maintained up to 20 % of plastic strain and more.

The ductility of the composite can be assumed to rely mainly on the ductility of the solid solution, as the intermetallics show no plastic deformation below 1300 °C [237]. A lack of ductility of the composite may hence be explained by two factors: insufficient amount of solid solution or insufficient ductility of the solid solution itself, e.g. by solid solution hardening through interstitials as well as substitutional atoms.

Except for titanium and hafnium, most other alloying elements have a strong negative impact on the ductile-to-brittle transition temperature of niobium (Fig. 9-1). Silicon and oxygen were previously shown to have detrimental impact on toughness and ductility [43-45, 46, p. 20]. While data on nitrogen and carbon impact is scarce, similar influence may be presumed. The undeformable intermetallic leads to strain localization in the solid solution, requiring an increased amount of ductility and, hence, causes a higher DBTT [196].

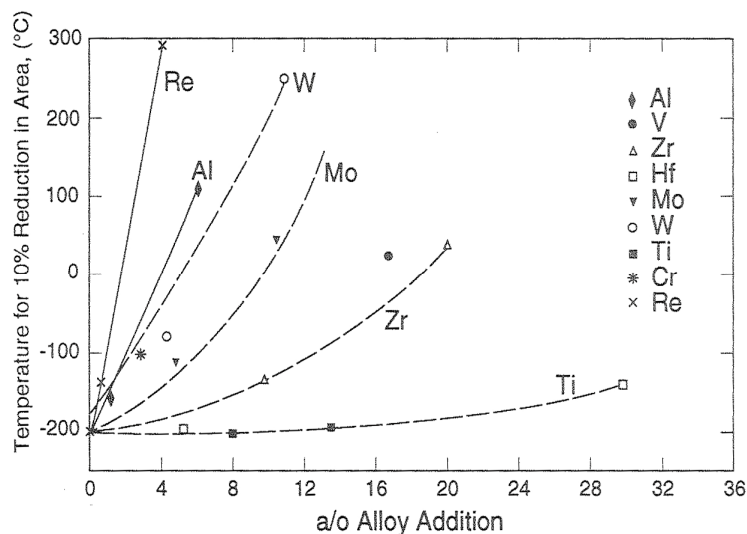


Fig. 9-1: influence of alloying elements on the DBTT of niobium [17]

A ductile solid solution matrix is better in providing ductility of the composite than ductile particles in an intermetallic matrix [238]. MA material shows significantly lower ductility at

room temperature, more pronounced damaging at high temperature, and a DBTT about 150 °C higher than for GA samples. The lower volume fraction of the solid solution phase plays a major role, as MA material features an intermetallic matrix. Additionally, higher overall contamination content of MA may also be representative of the contents in its solid solution, as not everything may be gettered by hafnium and titanium in the form of hafnium oxide, titanium nitride, and titanium carbide. Therefore, hardness of the solid solution is correlated with the composition determined via calibrated WDS in Fig. 9-2.

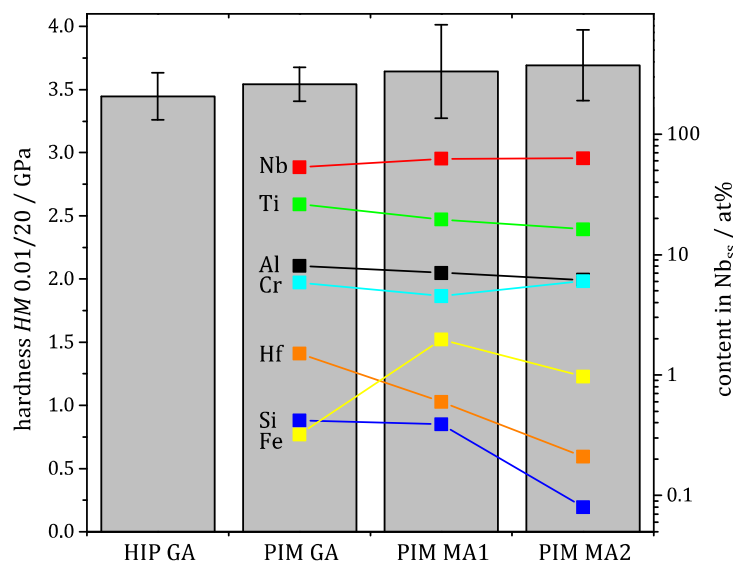


Fig. 9-2: nano-hardness HM and composition of Nb_{ss} from WDS measurements of different processing routes for the HT1500-100 condition, composition scale is logarithmic for emphasis on components with low contents

The main focus should lie on interstitial contents, i.e. carbon, nitrogen, and oxygen. Unfortunately, nitrogen K_{α} radiation coincides completely with titanium L_{α} radiation, and is hence not quantifiable. Adsorption of carbohydrates on polished surfaces is not avoidable and distorts small contents of oxygen and carbon. The interstitial contents obtained from WDS (Nb_{ss} phase) and hot carrier gas extraction (HCGE, composite) are given in Table 9-1. No correlation between overall interstitial contents and local interstitial contents in the solid solution phase can be found. This leads to the assumption, that contents of carbon and oxygen determined via WDS are dominated by surface adsorption and bulk solid solution contents of the material analyzed are actually much lower. This is backed by the calculations of Table 6-7 on page 77, suggesting, that most contaminations are gettered by hafnium and titanium to form hafnium oxide and titanium nitride/carbide, respectively. Typical interstitial concentrations of arc melted material are more than one order of magnitude lower [55, 66, 67, 107] than even those determined for GA material. Contaminations in directionally solidified material, which reaches the highest toughness values, are expected to undercut them due to zone refinement. Hence, even though most interstitials seem to be gettered by hafnium and titanium, concentrations in the solid solution may still be higher than for melt processed material, leading to the poor toughness of the present material. The hardness measurements show a slight tendency of higher hardness for MA material, which is far from being significant, though. This implies, that embrittlement by interstitials is unrelated to their overall content due to the good getter

behavior of titanium and hafnium. Regarding chemical composition of Nb_{ss}, as already shown in section 6.2.6, contaminations of MA powders shift solubilities of the other alloying elements significantly. Titanium content falls from 26 % for GA to 20 % for MA₁ and 16 % for MA₂. Hafnium solubility is decreased accordingly. Peculiar is the reduced amount of silicon in MA₂. While iron was determined previously in MA powder as a result of abrasion during milling (MA₂ shows lower iron content due to the use of hard metal balls; instead 2.43 and 0.52 % of tungsten and cobalt were measured, respectively), 0.32 % of iron were also verified in PIM GA solid solution. This may be abrasion from mixing and injection molding devices during PIM.

Table 9-1: contamination contents of carbon, nitrogen, and oxygen as determined by WDS on Nb_{ss} and by hot carrier gas extraction (HCGE) on the composite

contamination / wt%	PIM GA	PIM MA ₁	PIM MA ₂
carbon (WDS/HCGE)	0.34 ± 0.03 / 0.06 ± 0.00	0.20 ± 0.02 / 0.21 ± 0.02	0.26 ± 0.03 / 1.01 ± 0.02
nitrogen (WDS/HCGE)	0.00 / 0.04 ± 0.00	0.00 / 0.77 ± 0.00	0.00 / 0.01 ± 0.00
oxygen (WDS/HCGE)	0.53 ± 0.05 / 0.27 ± 0.00	0.40 ± 0.08 / 0.85 ± 0.00	0.50 ± 0.04 / 0.58 ± 0.01

As ductility is usually inversely proportional to hardness, it can be assumed, that ductility of the solid solution in MA material is not lower than for GA material, but that the amount of solid solution and the lack of its continuity are the reasons for increased amount of cracking during deformation, lack of ductility, and higher DBTT.

9.2 Strength

High-temperature creep strength achieved in this work is far away from the goal necessary for application in turbines and also from comparable alloys produced e.g. by directional solidification [98] or casting [106]. While the homogeneous microstructure of powder metallurgically produced material is desirable, the small equiaxed grains enable grain boundary sliding. As mentioned before, quasi-static compressive testing at elevated temperatures can also be considered a creep experiment. For a given strain rate, the flow stress will reach the same level that would be necessary in a creep experiment to yield the same steady-state strain rate. In the case of this material, as there exists a minimum strain rate at constant stress (instead of a steady-state regime), there exists also a maximum stress at constant strain rate. Hence, to increase the testing regime, in Fig. 9-3, creep data at 1000 °C is accompanied by quasi-static compressive data (open and solid symbols with dot in the middle) for the same testing temperature with the three tested strain rates 10^{-2} s^{-1} , 10^{-3} s^{-1} , and 10^{-4} s^{-1} . The strain rate sensitivity m introduced in section 7.1.2 is the inverse of the stress exponent n of section 7.2.1, as is obvious by comparing equations Eq. (7-1) and Eq. (7-2) for constant temperature. Extrapolating the power-laws for PIM GA AC of the quasi-static compression tests ($n = 5$) and the creep tests ($n = 2$), a transition from dislocation-based deformation to grain boundary

sliding for stresses below 230 MPa is apparent. In case of HIP GA AC, this transition is shifted to a higher stress (380 MPa) as the grain size is smaller for HIP than for PIM, and grain boundary sliding is activated also at higher strain rates. The compression test of HIP GA AC at a strain rate of 10^{-4} s^{-1} correlates well with the constant stress creep tests. For the HT₁₅₀₀₋₁₀₀ condition, the transition falls to 145 MPa.

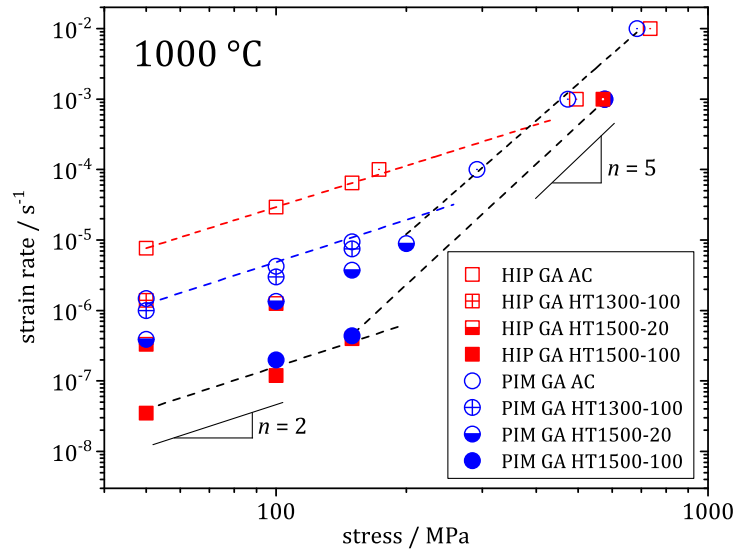


Fig. 9-3: Norton plot comprising compressive creep and quasi-static compressive (dotted symbols) deformation data for a testing temperature of 1000 °C for HIP and PIM samples in the AC and heat-treated conditions

It is established that dislocation-based creep deformation ($n = 3-5$) is mainly controlled by the sub-grain size d_{sg} of the dislocation structure forming during primary creep (Eq. (9-1)). This is, why dislocation creep shows little to no dependence on the grain size [185, p. 225]. Even though not being the dominating mechanism anymore, also for high stresses and strain rates – where the stress exponent is close to 5 – a small grain size dependence is observed due to grain boundary sliding still being active.

As the applied stress σ is reduced, the sub-grain size increases until it becomes larger than the grain size and no sub-grain structures are observed anymore ($d_{sg} \approx d_g$) [185, p. 225].

$$d_{sg} \sim \frac{Gb}{\sigma} \quad (9-1)$$

G : shear modulus

b : Burgers vector

This marks the transition from dislocation- to grain boundary sliding-based deformation. Depending on the grain size, a critical transition stress σ_{trans} can be defined:

$$\sigma_{trans} \sim \frac{Gb}{d_g} \quad (9-2)$$

Grain sizes were determined for PIM GA HT₁₃₀₀₋₁₀₀ and PIM GA HT₁₅₀₀₋₁₀₀ with an interpolated grain size for PIM GA HT₁₅₀₀₋₂₀. As dislocation-based deformation does not take

place in the silicides (at a test temperature of 1000 °C), the solid solution grain size will be used (Table 6-8). Quasi-static tests were not undertaken for PIM GA HT1500-20 but a transition stress of 190 MPa will be estimated based on Fig. 9-3. The inverse grain size plotted over the critical stress for grain boundary sliding indeed yields a fairly linear behavior. Extrapolation towards HIP GA AC gives a rough estimate of a solid solution grain size of 2.5 μm. This may not be too far off the actual value, even though extrapolation to that amount may be erroneous.

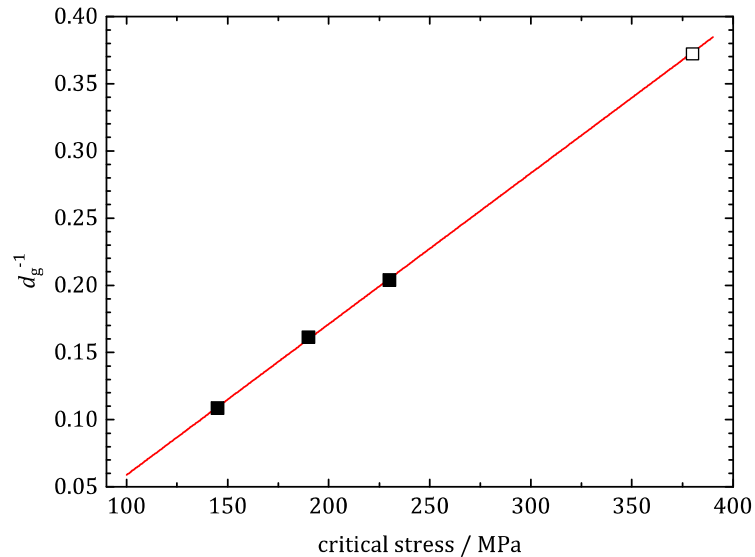


Fig. 9-4: inverse grain size over critical stress for grain boundary sliding, solid symbols represent measured data points, open symbol represents extrapolation

A high potential for increasing creep strength is, hence, to increase grain size to an extent that the transition stress is well below the application regime. It has also to be considered, that at higher temperatures, the transition stress will be higher. Grain growth generally follows the relation [134, p. 2475]

$$d_g - d_{g,0} = K \cdot t^{0.5} \quad (9-3)$$

$d_{g,0}$: initial grain size

K : constant

t : annealing time

Grain size data in this work is limited, but based on creep results, the initial grain size $d_{g,0}$ of PIM GA can be estimated to lie between 3.6 (HIP GA 1300-100) and 4.7 μm (PIM GA HT1300-100). For Fig. 9-5, a $d_{g,0}$ of 4.0 μm was assumed. The two additional data points at 1500 °C, 20 h and 100 h, yield a good regression with a K -value of 0.493. At 1300 °C, K is about 0.070. To reach a critical stress below 100 MPa, a grain size of about 20 μm would be necessary. Even at 1500 °C, the heat treatment duration would need to exceed 1000 h. Considering deformation under its own weight, probably also due to partial melting, the susceptibility of niobium alloys to oxygen pickup even from “inert” argon gas flow, and runtime costs, this seems unfeasible. The use of a reducing atmosphere such as hydrogen would lead to extensive embrittlement through the formation of niobium hydride [239]. At 1300 °C, the estimate would yield more than 50000 hours.

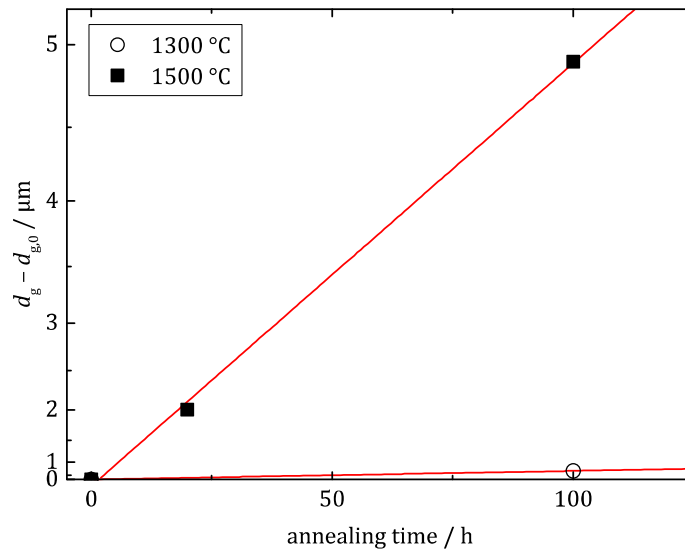


Fig. 9-5: reduced grain size of PIM GA for heat treatments at 1300 and 1500 °C, note the squared grain size scale

9.3 Outlook

The application of two net-shape capable powder compaction techniques – HIP and PIM – on the multi-component Nb-20Si-23Ti-6Al-3Cr-4Hf alloy was successfully piloted. In the course of the HYSOP project [35], even net-shaped turbine component demonstrators such as blades, vanes, and seal segments could be produced (see sections 3.2.3 and 3.2.4 on page 22). However, niobium is very reactive with a variety of interstitial elements, i.e. hydrogen, carbon, nitrogen, and oxygen, especially when processed as powder due to the increased surface area. The same applies to titanium, the main alloying element. Hence, extraordinary care has to be taken not to expose the powder to those species. This is not possible during mechanical alloying, especially since new powder surface is continually created. Gas-atomized powder, on the other hand, shows great potential. Still, interstitial contents are more than one order of magnitude higher than for melt metallurgy, thus inhibiting ductility. Powder handling has to be done under protective atmosphere at all times to keep contamination to a minimum. The biggest drawback, however, is what was thought to be an advantage: the homogeneous microstructure also resulted in a small grain size. This was coupled with the inability to coarsen the former in reasonable time to grain sizes, where grain boundary sliding can be sufficiently suppressed. This stems from the low melting point of the present alloy, which showed partial melting already at 1500 °C. A higher melting point and subsequently higher heat treatment temperatures may resolve this issue. The weak phase boundaries may also be addressed by alloy development to e.g. form grain boundary precipitates.

10 Summary

As nickel-base superalloys are limited in their application temperature by their melting point of about 1400 °C, new materials are sought after to open up operating temperatures beyond that. Due to their lower density and higher melting temperature, niobium silicide-based composites are potential candidates to replace them and had been proven to be promising by previous research. However, next to alloy development, the proper processing must also be established, as component manufacturing from nickel-base superalloys may not be readily transferable.

The goal of this work was to evaluate the feasibility and differences in ensuing properties of various powder metallurgical processing techniques that are capable of industrially manufacturing net-shape turbine components. A model alloy system similar to the well-established MASC-alloy (Nb-16Si-25Ti-2Al-2Cr-8Hf) developed by Bewlay et al. [1] was chosen, i.e. Nb-20Si-23Ti-6Al-3Cr-4Hf. Two routes for powder production were explored: mechanical alloying (MA) of elemental powders and electrode induction-melting gas atomization.

Optimum milling parameters for MA were determined to achieve a good balance of milling time, contamination level, and powder yield. Two possible ways were established to prevent cold-welding of the ductile powders to the milling equipment: reduction of processing temperature and the use of process control agents. Hence, two batches were produced for subsequent compaction, one with continuous cooling to -15 °C (MA₁), the other with continuous cooling at room temperature and the use of heptane as the process control agent (MA₂). By the use of proper balance of milling parameters, iron abrasion from milling balls, vial, and impeller could be minimized ($\approx 1\%$). Contamination levels with interstitials, i.e. carbon, nitrogen, and oxygen, were high in both cases, though: MA₁ showed high amounts of oxygen and nitrogen due to underpressure in the vial, MA₂ fair amounts of oxygen and high amounts of carbon due to cracking of the heptane.

Powder particles smaller than 25 μm were used for compaction via powder injection molding (PIM), larger particles were used for hot isostatic pressing (HIP).

Of the gas atomized powder, two size fractions, < 25 μm (GA) and the coarser 106 – 225 μm (CGA) were compacted via HIP, only the fine < 25 μm fraction could be consolidated by PIM.

HIP of MA powders was unsuccessful, as extensive cracking made the production of cuboid samples by EDM impossible. The closed can may have prevented gaseous species from escaping, leading to high internal stresses. Hence, this combination was abandoned early on, leaving HIP GA, HIP CGA, PIM GA, PIM MA₁, and PIM MA₂ for further analysis.

10.1 Microstructure

The microstructure of consolidated material mainly comprised the niobium solid solution, two modifications of Nb₅Si₃, i.e. α -Nb₅Si₃ and γ -Nb₅Si₃, and small amounts of hafnium oxide. Besides that, the nitrogen and carbon contamination of MA₁ and MA₂ were gettered by titanium and formed about 5 % of titanium nitride and titanium carbide in PIM MA₁ and PIM MA₂, respectively. HIP CGA samples showed larger grains of silicide phase as a result of the primary solidification of silicide during gas atomization.

Heat treatments between 1300 and 1500 °C for 20 and 100 hours were performed to evaluate the thermal stability of the phases and to coarsen the microstructure. While the amount of niobium solid solution stayed mainly constant during the heat treatments at 46 and 25 % for GA and MA material, respectively, strong variations in α -Nb₅Si₃ and γ -Nb₅Si₃ partitioning could be observed. This was mainly a result of varying hafnium and titanium solubilities in γ -Nb₅Si₃. By increasing heat treatment temperature, α -Nb₅Si₃ content is reduced from about 36 to 25 % in GA material and from 18 to 0 % for MA1 material. Contaminations of iron, carbon, and nitrogen lead to stabilization of γ -Nb₅Si₃. Compared to α -Nb₅Si₃, this silicide is reported to be detrimental to creep properties [2, 3]. Also, a higher CTE mismatch leads to cracking in heat-treated material, as was observed mainly for the high γ -Nb₅Si₃ containing MA alloys. Even though being interstitial elements, carbon, nitrogen, and oxygen contaminations led to considerable changes in phase chemistry, which is responsible for the unexpectedly low solid solution volume fraction of the MA material. For heat treatments at 1500 °C, local melting due to inhomogeneous oxygen distribution was observed in GA material, leading to the formation of network-like single grains of β -Nb₅Si₃. This limits the heat treatment regime available for coarsening. Initial grain sizes of HIP were around 2 μ m, those of PIM material around 4 μ m. During heat treatments they showed significant increase: after 100 hours at 1500 °C grain sizes of both compaction processes matched, but were still below 10 μ m.

10.2 Mechanical Properties

Very high compressive strength was obtained at room temperature for all conditions. However, MA material showed little to no ductility while GA reached about 3 % of plastic deformation, in both as-consolidated as well as heat-treated condition. At higher testing temperatures, MA gained ductility, while maintaining about 60 % higher strength. This was the result of a continuous intermetallic Nb₅Si₃ matrix also leading to significant damaging during deformation. Extensive cracking and shearing of the whole sample at a 45° angle to the compression direction deemed MA material insufficient.

Compressive creep experiments of GA material revealed grain boundary sliding, a deformation mechanism typically known from superplasticity, to be the dominant creep mechanism. With a stress exponent of two, an equiaxed, texture-free grain morphology could be retained up to very high compressive strains. This was the case for all conditions, as-consolidated with grain sizes below 3 μ m as well as heat-treated samples with grain sizes of about 9 μ m. The material showed stronger than usual dependence on the grain size, partly due to the grain boundary sliding mechanism, and partly due to the formation of β -Nb₅Si₃ during coarsening heat treatment and its transformation back to α -Nb₅Si₃ during deformation. As grain boundary sliding results in considerably higher creep rates than would be reached for dislocation-based deformation, further coarsening or strengthening of the grain boundaries is inevitable to make this powder metallurgical material usable in high-temperature applications. A coarsening to a sufficient grain size to prevent grain boundary sliding (\approx 20 μ m) would take about 1000 h at 1500 °C and even longer at lower temperatures. A strengthening of phase boundaries by fine precipitates may be possible by appropriate alloying. Overall, creep performance falls behind that of similar alloys that were produced by casting or directional solidification exhibiting a much coarser dendritic structure as well as current nickel-base superalloys.

Room temperature fracture toughness was determined by four-point bending of single edge V-notched beams. No significant differences between HIP and PIM of GA powder or heat treatment conditions were found yielding a fracture toughness between 7.7 and 8.7 MPa·m^{0.5}. This indifference can be attributed to a lack of ductility of the solid solution matrix at room temperature. Fracture surfaces showed only minor ductility and cleavage fracture was dominant for the intermetallic as well as the solid solution phase. This explains that toughness values of 15 – 20 MPa·m^{0.5} known for similar alloys could not be reached. Most likely the higher oxygen content even of GA material compared to melt processing leads to embrittlement of the solid solution. Even though most oxygen is gettered by hafnium, solubility for interstitials in niobium is high.

Using three-point bending, the onset of ductility under tensile loading was measured. The size of silicides and the amount of pores showed to have large effects on the ductile-to-brittle transition temperature (DBTT). Pore-free HIP GA (DBTT of 750 °C) and HIP CGA samples (DBTT of 850 °C) have a difference in DBTT of about 100 °C due to the larger silicide particles in the latter. The onset of local ductility leads to stress concentration and fracture in the silicide, and subsequent brittle global failure. The same is observed in arc-melted material. A similar but less pronounced effect results from residual porosity in PIM samples. The latter effect is reversed after a heat treatment (1500 °C / 100 h), as temperature-induced porosity (TIP [4]) appears in HIP while residual porosity of PIM is reduced. An additional HIP cycle of HIPed material after heat treatment closes the TIP again, leaving DBTT of HIP and PIM of the fine grained powder on the same level of about 850 °C. MA2 based compacts reveal a DBTT of at least 1000 °C due to their intermetallic matrix.

The fracture path is highly temperature dependent. At room temperature, cleavage fracture of all phases occurs with only minimal ductility in the solid solution phase. With increasing temperature, ductility of the solid solution increases. Crack arrest and crack deflection towards grain boundaries emerges. With further temperature increase, grain boundaries, especially between two silicides, are weakened and cracks propagate more and more along phase and grain boundaries. Above 1000 °C, transgranular cleavage fracture of silicides vanished – except for inhomogeneously large ones as in HIP CGA – in favor of intergranular fracture of silicides with ductile failure of the solid solution matrix.

Overall, room temperature behavior is dominated by an insufficient ductility of the solid solution, in case of MA, also by an insufficient amount of it. At high temperatures, the small grain size and weak grain boundaries lead to low strength and failure along those boundaries.

The use of net-shape capable powder metallurgical processes for a multi-component niobium silicide-based composite was in general successful. Several shortcomings have to be addressed, however, in the future. Mechanical alloying of the elements, which are highly sensitive to contamination, especially niobium and titanium, results in considerable pickup of interstitials, i.e. carbon, nitrogen, and oxygen. Because this strongly influences phase chemistry, the author advises not to employ mechanical alloying for this material system. Gas atomization shows a feasible way to produce powders of sufficient purity. However, powder handling has to be performed under protective atmosphere at all times to prevent temperature-induced porosity during heat treatment. The main problem, though, remains the small grain size, as it is detrimental to high-temperature strength.

11 References

- [1] B.P. Bewlay, M.R. Jackson, and H.A. Lipsitt, "The balance of mechanical and environmental properties of a multielement niobium-niobium silicide-based in situ composite", *Metall. Mater. Trans. A*, vol. **27**, no. 12, pp. 3801–3808, 1996.
- [2] B.P. Bewlay, C.L. Briant, E.T. Sylven, and M.R. Jackson, "The effects of substitutional additions on creep behavior of tetragonal and hexagonal Nb-silicides", *Mater. Res. Soc. Symp. Proc.*, vol. **753**, pp. BB5.24.1–6, 2003.
- [3] B.P. Bewlay, M.R. Jackson, and M.F.X. Gigliotti, "Niobium Silicide High Temperature In Situ Composites", in *Intermetallic Compounds - Principles and Practice*, vol. **3**, J. H. Westbrook and R. L. Fleischer, Eds. Chichester, UK: John Wiley & Sons, Ltd, 2002, pp. 541–560.
- [4] G. Wegmann, R. Gerling, and F.-P. Schimansky, "Temperature induced porosity in hot isostatically pressed gamma titanium aluminide alloy powders", *Acta Mater.*, vol. **51**, no. 3, pp. 741–752, 2003.
- [5] "About ACARE". [Online]. Available: <http://www.acare4europe.com/about-acare>. [Accessed: 30-Aug-2015].
- [6] "What is Horizon 2020? - Horizon 2020 - European Commission", *Horizon 2020*. [Online]. Available: <http://ec.europa.eu/programmes/horizon2020/en/what-horizon-2020>. [Accessed: 30-Aug-2015].
- [7] Boeing, "787 Propulsion System". [Online]. Available: http://www.boeing.com/commercial/aeromagazine/articles/2012_q3/2/. [Accessed: 27-Aug-2015].
- [8] W.J.G. Bräunling, *Flugzeugtriebwerke*. Berlin/Heidelberg: Springer-Verlag, 2009.
- [9] D.M. Dimiduk and J.H. Perepezko, "Mo-Si-B Alloys: Developing a Revolutionary Turbine-Engine Material", *MRS Bull.*, vol. **28**, no. 9, pp. 639–645, 2003.
- [10] P. Caron, "High σ' Solvus New Generation Nickel-Based Superalloys for Single Crystal Turbine Blade Applications", in *Superalloys 2000*, pp. 737–746, 2000.
- [11] A. Sato, H. Harada, A.-C. Yeh, K. Kawagishi, T. Kobayashi, Y. Koizumi, T. Yokokawa, and J.-X. Zhang, "A 5th generation SC superalloy with balanced high temperature properties and processability", in *Superalloys 2008*, pp. 131–138, 2008.
- [12] Y. Koizumi, T. Kobayashi, T. Yokokawa, J. Zhang, M. Osawa, H. Harada, Y. Aoki, and M. Arai, "Development of next-generation Ni-base single crystal superalloys", in *Superalloys 2004*, pp. 35–43, 2004.
- [13] D. Coutsouradis, A. Davin, and M. Lamberigts, "Cobalt-Based Superalloys for Applications in Gas-Turbines", *Mater. Sci. Eng.*, vol. **88**, pp. 11–19, 1987.
- [14] S.K. Makineni, A. Samanta, T. Rojhirunsakool, T. Alam, B. Nithin, A.K. Singh, R. Banerjee, and K. Chattopadhyay, "A new class of high strength high temperature Cobalt based γ - γ' Co-Mo-Al alloys stabilized with Ta addition", *Acta Mater.*, vol. **97**, pp. 29–40, 2015.
- [15] S. Neumeier, L.P. Freund, and M. Göken, "Novel wrought γ/γ' cobalt base superalloys with high strength and improved oxidation resistance", *Scr. Mater.*, vol. **109**, pp. 104–107, 2015.

- [16] M. Heilmaier, M. Krüger, H. Saage, J. Rösler, D. Mukherji, U. Glatzel, R. Völkl, R. Hüttner, G. Eggeler, C. Somsen, T. Depka, H.-J. Christ, B. Gorr, and S. Burk, "Metallic materials for structural applications beyond nickel-based superalloys", *JOM*, vol. **61**, no. 7, pp. 61–67, 2009.
- [17] E.N.C. Dalder, T. Grobstein, and C.S. Olsen, *Evolution of Refractory Metals and Alloys*. Warrendale, Pennsylvania, USA: Minerals, Metals & Materials Society, 1994.
- [18] M.R. Jackson, B.P. Bewlay, R.G. Rowe, D.W. Skelly, and H.A. Lipsitt, "High-temperature refractory metal-intermetallic composites", *JOM*, vol. **48**, no. 1, pp. 39–44, 1996.
- [19] P.R. Subramanian, M.G. Mendiratta, and D.M. Dimiduk, "The development of Nb-based advanced intermetallic alloys for structural applications", *JOM*, vol. **48**, no. 1, pp. 33–38, 1996.
- [20] P.R. Subramanian, M.G. Mendiratta, and D.M. Dimiduk, "Microstructures and Mechanical Behavior of Nb-Ti Base Beta + Silicide Alloys", *Mater. Res. Soc. Symp. Proc.*, vol. **322**, pp. 491–502, 1994.
- [21] R. Dicks, F. Wang, and X. Wu, "The manufacture of a niobium/niobium-silicide-based alloy using direct laser fabrication", *J. Mater. Process. Technol.*, vol. **209**, no. 4, pp. 1752–1757, 2009.
- [22] S. Mathieu, S. Knittel, P. Berthod, S. Mathieu, and M. Vilasi, "On the oxidation mechanism of niobium-base in situ composites", *Corros. Sci.*, vol. **60**, pp. 181–192, 2012.
- [23] P. Jéhanno, M. Heilmaier, H. Kestler, M. Boning, A. Venskutonis, B. Bewlay, and M. Jackson, "Assessment of a powder metallurgical processing route for refractory metal silicide alloys", *Metall. Mater. Trans. A*, vol. **36**, no. 3, pp. 515–523, 2005.
- [24] W. Ligang, J. Lina, C. Renjie, Z. Lijing, and Z. Hu, "Microstructure, Mechanical Properties and Oxidation Resistance of Nb-22Ti-14Si-2Hf-2Al-xCr Alloys", *Chin. J. Aeronaut.*, vol. **25**, no. 2, pp. 292–296, 2012.
- [25] W. Liu, Y.M. Fu, and J.B. Sha, "Microstructural Evolution and Mechanical Properties of a Multicomponent Nb-16Si-22Ti-2Al-2Hf-2Cr Alloy Prepared by Reactive Hot Press Sintering", *Metall. Mater. Trans. A*, vol. **44**, no. 5, pp. 2319–2330, 2012.
- [26] S. Zhang, X. Shi, and J. Sha, "Microstructural evolution and mechanical properties of as-cast and directionally-solidified Nb-15Si-22Ti-2Al-2Hf-2V-(2, 14) Cr alloys at room and high temperatures", *Intermetallics*, vol. **56**, pp. 15–23, 2015.
- [27] S.M. Zhang, J.R. Zhou, and J.B. Sha, "Effect of Fe additions on microstructure and mechanical properties of a multi-component Nb-16Si-22Ti-2Hf-2Al-2Cr alloy at room and high temperatures", *Intermetallics*, vol. **57**, pp. 146–155, 2015.
- [28] G.M. Cheng and L.L. He, "Microstructure evolution and room temperature deformation of a unidirectionally solidified Nb-22Ti-16Si-3Ta-2Hf-7Cr-3Al-0.2Ho (at.%) alloy", *Intermetallics*, vol. **19**, no. 2, pp. 196–201, 2011.
- [29] L. Su, L. Jia, J. Weng, Z. Hong, C. Zhou, and H. Zhang, "Improvement in the oxidation resistance of Nb-Ti-Si-Cr-Al-Hf alloys containing alloyed Ge and B", *Corros. Sci.*, vol. **88**, pp. 460–465, 2014.
- [30] Y. Kang, S. Qu, J. Song, Q. Huang, and Y. Han, "Microstructure and mechanical properties of Nb-Ti-Si-Al-Hf-xCr-yV multi-element in situ composite", *Mater. Sci. Eng. A*, vol. **534**, pp. 323–328, 2012.

- [31] L. Jia, J. Ge, J. Sha, and H. Zhang, "Effects of cooling rate and pouring temperature on microstructure and fracture toughness of the induction melted Nb-16Si-22Ti-2Hf-2Cr-2Al alloy", *Int. J. Mod. Phys. B*, vol. **24**, no. 15–16, pp. 2946–2951, 2010.
- [32] X. Li, H. Chen, J. Sha, and H. Zhang, "The effects of melting technologies on the microstructures and properties of Nb-16Si-22Ti-2Al-2Hf-17Cr alloy", *Mater. Sci. Eng. - Struct. Mater. Prop. Microstruct. Process.*, vol. **527**, no. 23, pp. 6140–6152, 2010.
- [33] K. Zelenitsas and P. Tsakirooulos, "Study of the role of Al and Cr additions in the microstructure of Nb-Ti-Si in situ composites", *Intermetallics*, vol. **13**, no. 10, pp. 1079–1095, 2005.
- [34] A. Lasalmonie, "Intermetallics: Why is it so difficult to introduce them in gas turbine engines?", *Intermetallics*, vol. **14**, no. 10–11, pp. 1123–1129, 2006.
- [35] S. Drawin, "Hybrid Silicide-Based Lightweight Components for Turbine and Energy Applications (HYSOP)", 266214.
- [36] L. Portebois, "Développement de matériaux réfractaires pour applications turbines aéronautiques: étude des effets microstructuraux sur le comportement en oxydation des alliages composites Nbss-Nb₅Si₃ et optimisation des solutions de protection associées", Doctoral Thesis, Université de Lorraine, France, 2014.
- [37] M.E. Schlesinger, H. Okamoto, A.B. Gokhale, and R. Abbaschian, "The Nb-Si (Niobium-Silicon) system", *J. Phase Equilibria*, vol. **14**, no. 4, pp. 502–509, 1993.
- [38] N. Sekido, Y. Kimura, S. Miura, F.-G. Wei, and Y. Mishima, "Fracture toughness and high temperature strength of unidirectionally solidified Nb-Si binary and Nb-Ti-Si ternary alloys", *J. Alloys Compd.*, vol. **425**, no. 1–2, pp. 223–229, 2006.
- [39] S. Miura, M. Aoki, Y. Saeki, K. Ohkubo, T. Mohri, and Y. Mishima, "Effects of Zr on the eutectoid decomposition behavior of Nb₃Si into (Nb)/Nb₅Si₃", *Metall. Mater. Trans. A*, vol. **36**, no. 3, pp. 489–496, 2005.
- [40] N. Sekido, Y. Kimura, F.-G. Wei, S. Miura, and Y. Mishima, "Effect of Lamellar Spacing on the Mechanical Properties of (Nb)/(Nb, Ti)₅Si₃ Two-Phase Alloys", *J. Jpn. Inst. Met.*, vol. **64**, no. 11, pp. 1056–1061, 2000.
- [41] R.M. Nekkanti and D.M. Dimiduk, "Ductile-Phase Toughening in Niobium-Niobium Silicide Powder Processed Composites", *Mater. Res. Soc. Symp. Proc.*, vol. **194**, 1990.
- [42] B. Predel, "Nb-Si (Niobium-Silicon)", in *Li-Mg – Nd-Zr*, vol. **H**, O. Madelung, Ed. Berlin/Heidelberg: Springer-Verlag, 1997, pp. 1–3.
- [43] E. Miura, K. Yoshimi, and S. Hanada, "Effect of Oxygen on Yield Stress and Slip Plane in Nb, Nb-Ta and Nb-Mo Single Crystals", *Mater. Trans. JIM*, vol. **40**, no. 5, pp. 365–368, 1999.
- [44] J.D. Rigney, P.M. Singh, and J.J. Lewandowski, "Effects of environmental exposure on ductile-phase toughening in niobium silicide-niobium composites", *Mater. Res. Soc. Symp. Proc.*, vol. **322**, 1993.
- [45] B. Kong, L. Jia, L. Su, K. Guan, J. Weng, and H. Zhang, "Effects of minor Si on microstructures and room temperature fracture toughness of niobium solid solution alloys", *Mater. Sci. Eng. A*, vol. **639**, pp. 114–121, 2015.
- [46] T.E. Tietz and J.W. Wilson, *Behavior and Properties of Refractory Metals*. Stanford, California, USA: Stanford University Press, 1965.

- [47] L. Zhang and J. Wu, "Thermal expansion and elastic moduli of the silicide based intermetallic alloys $Ti_5Si_3(X)$ and Nb_5Si_3 ", *Scr. Mater.*, vol. **38**, no. 2, pp. 307–313, 1997.
- [48] H. Schachner, E. Cerwenka, and H. Nowotny, "Neue Silizide vom M_5Si_3 -Typ mit D88-Struktur", *Monatshefte Für Chem.*, vol. **85**, no. 1, pp. 245–254, 1954.
- [49] W. Xu, J. Han, C. Wang, Y. Zhou, Y. Wang, Y. Kang, B. Wen, X. Liu, and Z.-K. Liu, "Temperature-dependent mechanical properties of α -/ β - Nb_5Si_3 phases from first-principles calculations", *Intermetallics*, vol. **46**, pp. 72–79, 2014.
- [50] Y.A. Kocherzhinsky, L.M. Yupko, and E.A. Shishkin, "The Nb-Si phase diagram", *Russ. Metall.*, vol. **1**, p. 184, 1980.
- [51] R.M. Waterstrat, K. Yvon, H.D. Flack, and E. Parthé, "Refinement of Nb_3Si and Nb_3As ", *Acta Crystallogr. B*, vol. **31**, no. 12, pp. 2765–2769, 1975.
- [52] M. Winter, "WebElements", *WebElements*, 2015. [Online]. Available: <http://www.webelements.com/niobium/physics.html>. [Accessed: 28-Jul-2015].
- [53] B.P. Bewlay, J.-C. Zhao, M.R. Jackson, and R.R. Bishop, "Determination of the Effect of Hf Additions on Phase Stability in Nb-Silicide Based In-Situ Composites", *Mater. Res. Soc. Symp. Proc.*, vol. **552**, pp. KK6.8.1–KK6.8.6, 1999.
- [54] B.P. Bewlay, M.R. Jackson, and H.A. Lipsitt, "The Nb-Ti-Si ternary phase diagram: Evaluation of liquid-solid phase equilibria in Nb- and Ti-rich alloys", *J. Phase Equilibria*, vol. **18**, no. 3, pp. 264–278, 1997.
- [55] J.-H. Kim, T. Tabaru, M. Sakamoto, and S. Hanada, "Mechanical properties and fracture behavior of an NbSS/ Nb_5Si_3 in-situ composite modified by Mo and Hf alloying", *Mater. Sci. Eng. A*, vol. **372**, no. 1–2, pp. 137–144, 2004.
- [56] I. Weiss, M. Thirukkonda, and R. Srinivasan, "Effect of Deformation Processing on Mechanical Properties of Nb-10 at/o Si In-Situ Composite", *Mater. Res. Soc. Symp. Proc.*, vol. **322**, pp. 377–386, 1994.
- [57] M. Bachmann, "Herstellung und Oxidation von Niobsilizid-Legierungen", Diplom Thesis, Technische Universität Darmstadt, 2012.
- [58] H. Nowotny, R. Kiefer, and F. Benesovsky, "Bericht für Pulvermetallurgie", vol. **5**, pp. 86–93, 1957.
- [59] J. Niebuhr, "Die niederen Oxide des Niobs", *J. Common Met.*, vol. **11**, no. 3, pp. 191–203, 1966.
- [60] A. Taylor and N. Doyle, "Solid-Solubility of Oxygen in Nb and Nb-Rich Nb-Hf Nb-Mo and Nb-W Alloys .1. The Nb-O System", *J. Common Met.*, vol. **13**, no. 3, pp. 313–330, 1967.
- [61] G.T.J. Mayo, W.H. Shepherd, and A.G. Thomas, "Oxidation behaviour of niobium-chromium alloys", *J. Common Met.*, vol. **2**, no. 2–4, pp. 223–232, 1960.
- [62] N.B. Pilling and R.E. Bedworth, "The Oxidation of Metals at High Temperatures", *J. Inst. Met.*, vol. **29**, pp. 529–591, 1923.
- [63] R. Bürgel, H.-J. Maier, and T. Niendorf, *Handbuch Hochtemperatur-Werkstofftechnik : Grundlagen, Werkstoffbeanspruchungen, Hochtemperaturlegierungen und -beschichtungen*, 4th ed. Wiesbaden: Vieweg+Teubner Verlag, 2011.
- [64] W.Y. Kim, H. Tanaka, A. Kasama, and S. Hanada, "Microstructure and room temperature fracture toughness of Nbss/ Nb_5Si_3 in situ composites", *Intermetallics*, vol. **9**, no. 9, pp. 827–834, 2001.

- [65] C.L. Ma, J.G. Li, Y. Tan, R. Tanaka, and S. Hanada, "Microstructure and mechanical properties of Nb/Nb₅Si₃ in situ composites in Nb-Mo-Si and Nb-W-Si systems", *Mater. Sci. Eng. A*, vol. **386**, no. 1–2, pp. 375–383, 2004.
- [66] J. Sha, H. Hirai, T. Tabaru, A. Kitahara, H. Ueno, and S. Hanada, "High-temperature strength and room-temperature toughness of Nb–W–Si–B alloys prepared by arc-melting", *Mater. Sci. Eng. A*, vol. **364**, no. 1–2, pp. 151–158, 2004.
- [67] J.-H. Kim, T. Tabaru, H. Hirai, A. Kitahara, and S. Hanada, "Tensile properties of a refractory metal base in situ composite consisting of an Nb solid solution and hexagonal Nb₅Si₃", *Scr. Mater.*, vol. **48**, no. 10, pp. 1439–1444, 2003.
- [68] R.M. Dasary and S.K. Varma, "Short-term oxidation response of Nb–15Re–15Si–10Cr–20Mo alloy", *J. Mater. Res. Technol.*, vol. **3**, no. 1, pp. 25–34, 2014.
- [69] M. del P. Moricca and S.K. Varma, "Isothermal oxidation behaviour of Nb-W-Cr Alloys", *Corros. Sci.*, vol. **52**, no. 9, pp. 2964–2972, 2010.
- [70] J.A. Ventura, B.I. Portillo, S.K. Varma, and R.N. Mahapatra, "Oxidation Behavior of Nb-20Mo-15Si-5B-20Cr and Nb-20Mo-15Si-5B-20Ti Alloys Up To 1300 °C", *ECS Trans.*, vol. **17**, no. 44, pp. 157–166, 2009.
- [71] B.I. Portillo and S.K. Varma, "Oxidation behavior of Nb–20Mo–15Si–5B–20Ti alloy in air from 700 to 1300 °C", *J. Alloys Compd.*, vol. **497**, no. 1–2, pp. 68–73, 2010.
- [72] K. Chattopadhyay, G. Balachandran, R. Mitra, and K.K. Ray, "Effect of Mo on microstructure and mechanical behaviour of as-cast Nbss–Nb₅Si₃ in situ composites", *Intermetallics*, vol. **14**, no. 12, pp. 1452–1460, 2006.
- [73] B. Xiong, C. Cai, and Z. Wang, "Microstructures and room temperature fracture toughness of Nb/Nb₅Si₃ composites alloyed with W, Mo and W–Mo fabricated by spark plasma sintering", *J. Alloys Compd.*, vol. **604**, pp. 211–216, 2014.
- [74] B.P. Bewlay, H.A. Lipsitt, M.R. Jackson, W.J. Reeder, and J.A. Sutliff, "Solidification processing of high temperature intermetallic eutectic-based alloys", *Mater. Sci. Eng. A*, vol. **192–193**, Part 2, pp. 534–543, 1995.
- [75] S. Knittel, S. Mathieu, L. Portebois, S. Drawin, and M. Vilasi, "Development of silicide coatings to ensure the protection of Nb and silicide composites against high temperature oxidation", *Surf. Coat. Technol.*, vol. **235**, pp. 401–406, 2013.
- [76] B.P. Bewlay, J.J. Lewandowski, and M.R. Jackson, "Refractory Metal-Intermetallic In-Situ Composites for Aircraft Engines", *JOM*, vol. **49**, no. 8, pp. 44–45, 1997.
- [77] B.P. Bewlay, M.R. Jackson, J.-C. Zhao, and P.R. Subramanian, "A review of very-high-temperature Nb-silicide-based composites", *Metall. Mater. Trans. A*, vol. **34**, no. 10, pp. 2043–2052, 2003.
- [78] K. Zelenitsas and P. Tsakirooulos, "Effect of Al, Cr and Ta additions on the oxidation behaviour of Nb-Ti-Si in situ composites at 800 °C", *Mater. Sci. Eng. A*, vol. **416**, no. 1–2, pp. 269–280, 2006.
- [79] M. Bulanova, I. Fartushna, and Materials Science International Team, "Nb-Si-Ti Ternary Phase Diagram Evaluation", MSI Materials Science International Services GmbH, Stuttgart, Phase Diagram Evaluation 10.23193.1.4, 2010.
- [80] S. Kashyap, C.S. Tiwary, and K. Chattopadhyay, "Microstructure and mechanical properties of oxidation resistant suction cast Nb-Si-Al alloy", *Mater. Sci. Eng. A*, vol. **559**, pp. 74–85, 2013.

- [81] D. Janda, H. Fietzek, M. Galetz, and M. Heilmaier, "The effect of micro-alloying with Zr and Nb on the oxidation behavior of Fe₃Al and FeAl alloys", *Intermetallics*, vol. **41**, pp. 51–57, 2013.
- [82] J.A. Nesbitt and C.E. Lowell, "Prediction of the High Temperature Oxidative Life of Intermetallics", *Mater. Res. Soc. Symp. Proc.*, vol. **288**, pp. 107–118, 1992.
- [83] T. Fujiwara, K. Yasuda, and H. Kodama, "High-Temperature Oxidation Behavior of Nb₃Al Based Alloys", *Mater. Res. Soc. Symp. Proc.*, vol. **288**, pp. 959–964, 1992.
- [84] W.-Y. Kim, I.-D. Yeo, M.-S. Kim, and S. Hanada, "Effect of Cr Addition on Microstructure and Mechanical Properties in Nb-Si-Mo Base Multiphase Alloys", *Mater. Trans.*, vol. **43**, no. 12, pp. 3254–3261, 2002.
- [85] D.L. Davidson, K.S. Chan, and D.L. Anton, "The effects on fracture toughness of ductile-phase composition and morphology in Nb-Cr-Ti and Nb-Si in situ composites", *Metall. Mater. Trans. A*, vol. **27**, no. 10, pp. 3007–3018, 1996.
- [86] J. Ventura and S.K. Varma, "The oxidation resistance of Nb-20Mo-15Si-5B-20Cr up to 1,300°C", *JOM*, vol. **61**, no. 7, pp. 72–75, 2009.
- [87] S.K. Varma, C. Parga, K. Amato, and J. Hernandez, "Microstructures and high temperature oxidation resistance of alloys from Nb–Cr–Si system", *J. Mater. Sci.*, vol. **45**, no. 14, pp. 3931–3937, 2010.
- [88] D. Alvarez and S.K. Varma, "Characterization of microstructures and oxidation behaviour of Nb–20Si–20Cr–5Al alloy", *Corros. Sci.*, vol. **53**, no. 6, pp. 2161–2167, 2011.
- [89] F. Gang and M. Heilmaier, "private communication".
- [90] M. del P. Moricca and S.K. Varma, "High temperature oxidation characteristics of Nb-10W-XCr alloys", *J. Alloys Compd.*, vol. **489**, no. 1, pp. 195–201, 2010.
- [91] B.P. Bewlay, J.A. Sutliff, and R.R. Bishop, "Evidence for the existence of Hf₅Si₃", *J. Phase Equilibria*, vol. **20**, no. 2, pp. 109–112, 1999.
- [92] S. Knittel, S. Mathieu, L. Portebois, and M. Vilasi, "Effect of tin addition on Nb–Si-based in situ composites. Part II: Oxidation behaviour", *Intermetallics*, vol. **47**, pp. 43–52, 2014.
- [93] S. Knittel, S. Mathieu, and M. Vilasi, "Effect of tin addition on Nb–Si-based in situ composites. Part I: Structural modifications", *Intermetallics*, vol. **47**, pp. 36–42, 2014.
- [94] S. Knittel, S. Mathieu, and M. Vilasi, "Tin addition to improve the oxidation behaviour of Nbss/Nb₅Si₃ based in-situ composite", *Adv. Mater. Res.*, vol. **278**, pp. 575–580, 2011.
- [95] Z. Li and P. Tsakiroopoulos, "Study of the effects of Ge addition on the microstructure of Nb-18Si in situ composites", *Intermetallics*, vol. **18**, no. 5, pp. 1072–1078, 2010.
- [96] Z. Li and P. Tsakiroopoulos, "The Effect of Ge and Ti Additions on the Microstructures and Properties of Nb-18Si Based Alloys", *Mater. Res. Soc. Symp. Proc.*, vol. **1295**, pp. 379–384, 2011.
- [97] Z. Li and P. Tsakiroopoulos, "The microstructures of Nb–18Si–5Ge–5Al and Nb–24Ti–18Si–5Ge–5Al in situ composites", *J. Alloys Compd.*, vol. **550**, pp. 553–560, 2013.
- [98] B.P. Bewlay, M.R. Jackson, J.-C. Zhao, P.R. Subramanian, M.G. Mendiratta, and J.J. Lewandowski, "Ultrahigh-Temperature Nb-Silicide-Based Composites", *MRS Bull.*, vol. **28**, no. 9, pp. 646–653, 2003.
- [99] R. Mitra, "Mechanical behaviour and oxidation resistance of structural silicides", *Int. Mater. Rev.*, vol. **51**, no. 1, pp. 13–64, 2006.

- [100] P. Tsakiroopoulos, "On the macrosegregation of silicon in niobium silicide based alloys", *Intermetallics*, vol. **55**, pp. 95–101, 2014.
- [101] Z. Li and P. Tsakiroopoulos, "Study of the effect of Cr and Ti additions in the microstructure of Nb–18Si–5Ge based in-situ composites", *Intermetallics*, vol. **26**, pp. 18–25, 2012.
- [102] Z. Li and P. Tsakiroopoulos, "Study of the effect of Ti and Ge in the microstructure of Nb–24Ti–18Si–5Ge in situ composite", *Intermetallics*, vol. **19**, no. 9, pp. 1291–1297, 2011.
- [103] I. Grammenos and P. Tsakiroopoulos, "Study of the role of Hf, Mo and W additions in the microstructure of Nb–20Si silicide based alloys", *Intermetallics*, vol. **19**, no. 10, pp. 1612–1621, 2011.
- [104] J. Geng, P. Tsakiroopoulos, and G. Shao, "Oxidation of Nb-Si-Cr-Al in situ composites with Mo, Ti and Hf additions", *Mater. Sci. Eng. A*, vol. **441**, no. 1–2, pp. 26–38, 2006.
- [105] S. Drawin, "Ultra high temperature materials for turbines (ULTMAT)", 502977.
- [106] P.R. Subramanian, M.G. Mendiratta, D.M. Dimiduk, and M.A. Stucke, "Advanced intermetallic alloys—beyond gamma titanium aluminides", *Mater. Sci. Eng. A*, vol. **239–240**, pp. 1–13, 1997.
- [107] M. Fujikura, A. Kasama, R. Tanaka, and S. Hanada, "Effect of alloy chemistry on the high temperature strengths and room temperature fracture toughness of advanced Nb-based alloys", *Mater. Trans.*, vol. **45**, no. 2, pp. 493–501, 2004.
- [108] W. Schatt, K.-P. Wieters, and B. Kieback, Eds., *Pulvermetallurgie*. Berlin/Heidelberg: Springer-Verlag, 2007.
- [109] R.M. German, *Powder metallurgy and particulate materials processing : the processes, materials, products, properties, and applications*. Metal Powder Industries Federation, 2005.
- [110] G.S. Upadhyaya, Ed., *Powder Metallurgy Technology and Equipment: Selected Topics*. Enfield, New Hampshire, USA: Trans Tech Publications Inc., 2012.
- [111] C.C. Wojcik, "Processing, Properties and Applications of High-Temperature Niobium Alloys", *Mater. Res. Soc. Symp. Proc.*, vol. **322**, pp. 519–530, 1993.
- [112] M. Krüger, "Pulvermetallurgische Herstellung und Charakterisierung von oxidationsbeständigen Molybdänbasislegierungen für Hochtemperaturanwendungen", Dissertation, Otto-von-Guericke Universität Magdeburg, Magdeburg, 2010.
- [113] P.S. Gilman and J.S. Benjamin, "Mechanical Alloying", *Annu. Rev. Mater. Sci.*, vol. **13**, no. 1, pp. 279–300, 1983.
- [114] E. Botcharova, M. Heilmaier, J. Freudenberger, G. Drew, D. Kudashov, U. Martin, and L. Schultz, "Supersaturated solid solution of niobium in copper by mechanical alloying", *J. Alloys Compd.*, vol. **351**, no. 1–2, pp. 119–125, 2003.
- [115] J.H. Schneibel, C.T. Liu, M.K. Miller, M.J. Mills, P. Sarosi, M. Heilmaier, and D. Sturm, "Ultrafine-grained nanocluster-strengthened alloys with unusually high creep strength", *Scr. Mater.*, vol. **61**, no. 8, pp. 793–796, 2009.
- [116] M.C. Brandes, L. Kovarik, M.K. Miller, G.S. Daehn, and M.J. Mills, "Creep behavior and deformation mechanisms in a nanocluster strengthened ferritic steel", *Acta Mater.*, vol. **60**, no. 4, pp. 1827–1839, 2012.
- [117] T. Hayashi, P.M. Sarosi, J.H. Schneibel, and M.J. Mills, "Creep response and deformation processes in nanocluster-strengthened ferritic steels", *Acta Mater.*, vol. **56**, no. 7, pp. 1407–1416, 2008.

- [118] R.K. Viswanadham, S.K. Mannan, and S. Kumar, "Mechanical alloying behavior in group V transition metal/silicon systems", *Scr. Metall.*, vol. **22**, no. 7, pp. 1011–1014, 1988.
- [119] C. Suryanarayana, "Mechanical alloying and milling", *Prog. Mater. Sci.*, vol. **46**, no. 1–2, pp. 1–184, 2001.
- [120] X.L. Wang, G.F. Wang, and K.F. Zhang, "Effect of mechanical alloying on microstructure and mechanical properties of hot-pressed Nb-16Si alloys", *Mater. Sci. Eng. A*, vol. **527**, no. 13–14, pp. 3253–3258, 2010.
- [121] M.N.R.V. Perdigão, J.R. Jordão, C.S. Kiminami, and W.J.F. Botta, "Phase transformation in Nb-16 at.% Si processed by high-energy ball milling", *J. Non-Cryst. Solids*, vol. **219**, pp. 170–175, 1997.
- [122] M.N.R.V. Perdigão, J.A.R. Jordão, C.S. Kiminami, and W.J. Botta, "Reactive Milling and Sintering of Nb-16at.% Si Mixtures", *Mater. Sci. Forum*, vol. **235–238**, pp. 151–156, 1997.
- [123] X.L. Wang and K.F. Zhang, "Mechanical alloying, microstructure and properties of Nb-16Si alloy", *J. Alloys Compd.*, vol. **490**, no. 1–2, pp. 677–683, 2010.
- [124] X.L. Wang, G. Wang, and K.F. Zhang, "Microstructure and room temperature mechanical properties of hot-pressed Nb-Si-Ti-Fe alloys", *J. Alloys Compd.*, vol. **502**, no. 2, pp. 310–318, 2010.
- [125] C.L. Ma, A. Kasama, H. Tanaka, Y. Tan, R. Tanaka, Y. Mishima, and S. Hanada, "Microstructures and Mechanical Properties of Nb/Nb-Silicide in-situ Composites Synthesized by Reactive Hot Pressing of Ball Milled Powders", *Mater. Trans. JIM*, vol. **41**, no. 3, pp. 444–451, 2000.
- [126] C.L. Ma, A. Kasama, Y. Tan, H. Tanaka, R. Tanaka, Y. Mishima, and S. Hanada, "Synthesis of Nb/Nb₅Si₃ in-situ Composites by Mechanical Milling and Reactive Spark Plasma Sintering", *Mater. Trans. JIM*, vol. **41**, no. 6, pp. 719–726, 2000.
- [127] F. Gang and M. Heilmaier, "Influence of Directional Solidification on the Creep Properties of a Binary NbSi Eutectic Alloy", *JOM*, vol. **66**, no. 9, pp. 1908–1913, 2014.
- [128] Y. Kimura, H. Yamaoka, N. Sekido, and Y. Mishima, "Processing, microstructure, and mechanical properties of (Nb)/Nb₅Si₃ two-phase alloys", *Metall. Mater. Trans. A*, vol. **36A**, no. 3, pp. 483–488, 2005.
- [129] J.L. Yu, Z.K. Li, K.F. Zhang, X. Zheng, J.J. Zhang, R. Bai, and W.S. Wang, "Mechanical properties of multiphase Nb-Si-Fe in situ composites", *Mater. Sci. Eng. A*, vol. **527**, no. 20, pp. 5230–5233, 2010.
- [130] J.L. Yu and K.F. Zhang, "Tensile properties of multiphase refractory Nb-16Si-2Fe in situ composite", *Scr. Mater.*, vol. **59**, no. 7, pp. 714–717, 2008.
- [131] J.L. Yu, K.F. Zhang, and G.F. Wang, "Superplasticity of multiphase fine-grained Nb-16Si-2Fe refractory alloy", *Intermetallics*, vol. **16**, no. 10, pp. 1167–1170, 2008.
- [132] J.L. Yu, K.F. Zhang, Z.K. Li, X. Zheng, G.F. Wang, and R. Bai, "Fracture toughness of a hot-extruded multiphase Nb-10Si-2Fe in situ composite", *Scr. Mater.*, vol. **61**, no. 6, pp. 620–623, 2009.
- [133] F. Gang, K. von Klinski-Wetzel, J.N. Wagner, and M. Heilmaier, "Influence of Vanadium on the Oxidation Resistance of the Intermetallic Phase Nb₅Si₃", *Oxid. Met.*, vol. **83**, no. 1–2, pp. 119–132, 2014.
- [134] R.W. Cahn and P. Haasen, *Physical Metallurgy*, 4th ed., vol. **3**, 3 vols. Amsterdam: Elsevier, 1996.

- [135] V. Seetharaman and M.R. Semiatin, "Powder Metallurgy", in *Intermetallic Compounds - Principles and Practice*, vol. 3, J. H. Westbrook and R. L. Fleischer, Eds. Chichester, UK: John Wiley & Sons, Ltd, 2002, pp. 641–662.
- [136] M. Omori, "Sintering, consolidation, reaction and crystal growth by the spark plasma system (SPS)", *Mater. Sci. Eng. A*, vol. 287, no. 2, pp. 183–188, 2000.
- [137] O. Guillon, J. Gonzalez-Julian, B. Dargatz, T. Kessel, G. Schierning, J. Raethel, and M. Herrmann, "Field-Assisted Sintering Technology/Spark Plasma Sintering: Mechanisms, Materials, and Technology Developments", *Adv. Eng. Mater.*, vol. 16, no. 7, pp. 830–849, 2014.
- [138] Y. Kubota, T. Nakamura, S. Tanaka, and K. Hayakawa, "Net Shape Forming of Thin Walled Cylindrical Can by DC Pulse Resistance Sintering Process of Titanium Powder Metal", *Steel Res. Int.*, vol. 81, no. 9, pp. 1336–1339, 2010.
- [139] T. Voisin, J.-P. Monchoux, L. Durand, N. Karnatak, M. Thomas, and A. Couret, "An Innovative Way to Produce γ -TiAl Blades: Spark Plasma Sintering", *Adv. Eng. Mater.*, vol. **online preview**, 2015.
- [140] M. Sannia, R. Orru, J.E. Garay, G. Cao, and Z.A. Munir, "Effect of phase transformation during high energy milling on field activated synthesis of dense MoSi₂", *Mater. Sci. Eng. A*, vol. 345, no. 1–2, pp. 270–277, 2003.
- [141] A. Yamauchi, K. Yoshimi, K. Kurokawa, and S. Hanada, "Synthesis of Mo-Si-B in situ composites by mechanical alloying", *J. Alloys Compd.*, vol. 434, pp. 420–423, 2007.
- [142] L. Zhang, K. Pan, J. Wang, and J. Lin, "Spark plasma sintering synthesis of intermetallic T₂ in the Mo-Si-B system", *Adv. Powder Technol.*, vol. 24, no. 6, pp. 913–920, 2013.
- [143] Z. Chen and Y. Yan, "Influence of sintering temperature on microstructures of Nb/Nb₅Si₃ in situ composites synthesized by spark plasma sintering", *J. Alloys Compd.*, vol. 413, no. 1–2, pp. 73–76, 2006.
- [144] W. Liu, Y. Fu, and J. Sha, "Microstructure and mechanical properties of Nb–Si alloys fabricated by spark plasma sintering", *Prog. Nat. Sci. Mater. Int.*, vol. 23, no. 1, pp. 55–63, 2013.
- [145] C. Broeckmann, "Hot isostatic pressing of near net shape components - process fundamentals and future challenges", *Powder Metall.*, vol. 55, no. 3, pp. 176–179, 2012.
- [146] Q.S. Wei, P.J. Xue, G.C. Liu, H. Lu, J. Huang, and Y.S. Shi, "Simulation and verification of near-net shaping a complex-shaped turbine disc by hot isostatic pressing process", *Int. J. Adv. Manuf. Technol.*, vol. 74, no. 9–12, pp. 1667–1677, 2014.
- [147] Y. Wu, P. Xue, Q. Wei, J. Huang, Y. Shi, and J. Liu, "An Integrated Forming Process for Manufacturing Ti6Al₄V Impeller with a Functional Coating Layer Using Hot Isostatic Pressing", *Mater. Manuf. Process.*, vol. 30, no. 6, pp. 756–765, 2015.
- [148] G. Petzow, *Metallographisches Ätzen*, 6th ed. Berlin, Stuttgart: Gebrüder Bornträger, 1988.
- [149] L. Spieß, G. Teichert, R. Schwarzer, H. Behnken, and C. Genzel, *Moderne Röntgenbeugung*. Wiesbaden: Vieweg+Teubner, 2009.
- [150] L. Lutterotti, M. Bortolotti, G. Ischia, I. Lonardelli, and H.-R. Wenk, "Rietveld texture analysis from diffraction images", *Z. Krist.*, pp. 125–130, 2007.
- [151] H.M. Rietveld, "A profile refinement method for nuclear and magnetic structures", *J. Appl. Crystallogr.*, vol. 2, no. 2, pp. 65–71, 1969.

- [152] Normenausschuß Materialprüfung, "Differenzthermoanalyse (DTA)", Standard DIN 51007, 1994.
- [153] H. Kuhn, *ASM Handbook: Volume 8: Mechanical Testing and Evaluation*, 10 edition. Materials Park, Ohio: ASM International, 2000.
- [154] Normenausschuß Materialprüfung, "Instrumentierte Eindringprüfung zur Bestimmung der Härte und anderer Werkstoffparameter", Standard DIN EN ISO 14577-1, 2002.
- [155] M. Krueger, S. Franz, H. Saage, M. Heilmaier, J.H. Schneibel, P. Jéhanno, M. Boening, and H. Kestler, "Mechanically alloyed Mo-Si-B alloys with a continuous alpha-Mo matrix and improved mechanical properties", *Intermetallics*, vol. **16**, no. 7, pp. 933–941, 2008.
- [156] "ICDD PDF-2 Database", 2015. [Online]. Available: <http://www.icdd.com/products/pdf2.htm>.
- [157] Y.M. Savitskiy, V.V. Baron, and K.N. Ivanova, "Investigation into recrystallization of niobium and its alloys", *Inzhenerno-Fiz. Zhurnal*, vol. **1**, no. 11, pp. 38–45, 1958.
- [158] R. Srinivasan, G.B. Viswanathan, V.I. Levit, and H.L. Fraser, "Orientation effect on recovery and recrystallization of cold rolled niobium single crystals", *Mater. Sci. Eng. A*, vol. **507**, no. 1–2, pp. 179–189, 2009.
- [159] C. Suryanarayana, W.K. Wang, H. Iwasaki, and T. Masumoto, "High-pressure synthesis of A_{15} Nb₃Si phase from amorphous Nb-Si alloys", *Solid State Commun.*, vol. **34**, no. 11, pp. 861–863, 1980.
- [160] J. Kajuch, J.W. Short, C. Liu, and J.J. Lewandowski, "On the Kinetics of Nb₅Si₃ Compound Formation", *Mater. Res. Soc. Symp. Proc.*, vol. **288**, pp. 853–859, 1993.
- [161] Materials Science International Team, MSIT® and O. Fabrichnaya, "Iron – Oxygen – Silicon", in *Iron Systems, Part 5*, vol. **11D5**, G. Effenberg and S. Ilyenko, Eds. Berlin/Heidelberg: Springer-Verlag, 2009, pp. 385–439.
- [162] P. Franke, D. Neuschütz, and Scientific Group Thermodata Europe (SGTE), "Nb-O", in *Binary Systems. Part 4: Binary Systems from Mn-Mo to Y-Zr*, vol. **19B4**, P. Franke and D. Neuschütz, Eds. Berlin/Heidelberg: Springer-Verlag, 2006, pp. 1–2.
- [163] G.F.V. Voort, *Metallography, Principles and Practice*. ASM International, 1984.
- [164] J.-C. Zhao, L.A. Peluso, M.R. Jackson, and L. Tan, "Phase diagram of the Nb-Al-Si ternary system", *J. Alloys Compd.*, vol. **360**, no. 1–2, pp. 183–188, 2003.
- [165] J.H. Schneibel and C.J. Rawn, "Thermal expansion anisotropy of ternary titanium silicides based on Ti₅Si₃", *Acta Mater.*, vol. **52**, no. 13, pp. 3843–3848, 2004.
- [166] T. Nakashima and Y. Umakoshi, "Anisotropy of electrical resistivity and thermal expansion of single-crystal Ti₅Si₃", *Philos. Mag. Lett.*, vol. **66**, no. 6, pp. 317–321, 1992.
- [167] G.A. Henshall, M.J. Strum, B.P. Bewlay, and J.A. Sutliff, "Ductile-phase toughening in V-V₃Si in situ composites", *Metall. Mater. Trans. A*, vol. **28**, no. 12, pp. 2555–2564, 1997.
- [168] E.O. Hall, "The Deformation and Ageing of Mild Steel: III Discussion of Results", *Proc. Phys. Soc. Sect. B*, vol. **64**, no. 9, p. 747, 1951.
- [169] N. Petch, "The Cleavage Strength of Polycrystals", *J. Iron Steel Inst.*, vol. **174**, no. 1, pp. 25–28, 1953.
- [170] C.A. Schuh and T.G. Nieh, "Hardness and Abrasion Resistance of Nanocrystalline Nickel Alloys Near the Hall-Petch Breakdown Regime", *Mater. Res. Soc. Symp. Proc.*, vol. **740**, pp. 11.8.1–6, 2002.

- [171] D. Padhi and J.J. Lewandowski, "Effects of test temperature and grain size on the charpy impact toughness and dynamic toughness (KID) of polycrystalline niobium", *Metall. Mater. Trans. A*, vol. **34**, no. 4, pp. 967–978, 2003.
- [172] A. Seeger, "Dislocation relaxation and alloy softening of bcc alloys", *Philos. Mag. Lett.*, vol. **90**, no. 10, pp. 699–706, 2010.
- [173] R. Gröger and V. Vitek, "Temperature and strain rate dependent flow criterion for bcc transition metals based on atomistic analysis of dislocation glide", *Int. J. Mater. Res.*, vol. **100**, no. 3, pp. 315–321, 2009.
- [174] A. Seeger and W. Wasserbäch, "Anomalous Slip – A Feature of High-Purity Body-Centred Cubic Metals", *Phys. Status Solidi A*, vol. **189**, no. 1, pp. 27–50, 2002.
- [175] G. Gottstein, *Physikalische Grundlagen der Materialkunde*, 3rd ed. Berlin/Heidelberg: Springer-Verlag, 2007.
- [176] J. Rösler, H. Harders, and M. Bäker, *Mechanisches Verhalten der Werkstoffe*, 3rd ed. Wiesbaden: B.G. Teubner Verlag, 2008.
- [177] H.J. Frost and M.F. Ashby, *Deformation-mechanism maps: the plasticity and creep of metals and ceramics*. Pergamon Press, 1982.
- [178] C.L. Ma, J.G. Li, Y. Tan, R. Tanaka, and S. Hanada, "Effect of B addition on the microstructures and mechanical properties of Nb–16Si–10Mo–15W alloy", *Mater. Sci. Eng. A*, vol. **384**, no. 1–2, pp. 377–384, 2004.
- [179] M. Wenderoth, S. Vorberg, B. Fischer, Y. Yamabe-Mitarai, H. Harada, U. Glatzel, and R. Völkl, "Influence of Nb, Ta and Ti on microstructure and high-temperature strength of precipitation-hardened Pt-base alloys", *Mater. Sci. Eng. A*, vol. **483–484**, pp. 509–511, 2008.
- [180] C.D. Allan, "Plasticity of nickel base single crystal superalloys", Dissertation, MIT, Cambridge, MA, 1995.
- [181] R.D. Schmidt-Whitley, "On the role of grain size in superplastic deformation", *Scr. Metall.*, vol. **8**, no. 1, pp. 49–54, 1974.
- [182] M.E. Kassner, *Fundamentals of Creep in Metals and Alloys*, 2nd ed. Amsterdam: Elsevier, 2009.
- [183] J. Wolfenstine, G. González-Doncel, and O.D. Sherby, "Deformation behaviour under constant structure of creep-resistant Al-Fe alloys", *J. Mater. Sci. Lett.*, vol. **9**, no. 4, pp. 410–413, 1990.
- [184] C. Barrett and W. Nix, "A Model for Steady State Creep Based on Motion of Jogged Screw Dislocations", *Acta Metall.*, vol. **13**, no. 12, pp. 1247–1258, 1965.
- [185] B. Ilschner, *Hochtemperatur-Plastizität*. Berlin/Heidelberg: Springer-Verlag, 1973.
- [186] H. Mughrabi, Ed., *Plastic deformation and fracture of materials*, vol. **6**. Weinheim New York Basel Cambridge: VCH, 1993.
- [187] U.F. Kocks, C.N. Tomé, H.-R. Wenk, A.D. Rollet, and S.I. Wright, "Typical Textures in Metals", in *Texture and Anisotropy: Preferred Orientations in Polycrystals and Their Effect on Materials Properties*, Cambridge, UK: Cambridge University Press, 1998, pp. 178–239.
- [188] W. Pichl, "Slip Geometry and Plastic Anisotropy of Body-Centered Cubic Metals", *Phys. Status Solidi A*, vol. **189**, no. 1, pp. 5–25, 2002.

- [189] B. Vishwanadh, K.V. Mani Krishna, A.K. Revelly, I. Samjdar, R. Tewari, and G.K. Dey, "Textural and microstructural evolutions during deformation and annealing of Nb-1% Zr-0.1% C (wt%) alloy", *Mater. Sci. Eng. A*, vol. **585**, pp. 343-355, 2013.
- [190] D. Raabe and K. Lücke, "Rolling and Annealing Textures of BCC Metals", *Mater. Sci. Forum*, vol. **157-162**, pp. 597-610, 1994.
- [191] H.F.G. Abreu, S.S.M. Tavares, S.S. Carvalho, T.H.T. Eduardo, A.D.S. Bruno, and M.H. Prado da Silva, "Texture and Microstructure of Cold Rolled and Recrystallized Pure Niobium", *Mater. Sci. Forum*, vol. **539-543**, pp. 3436-3441, 2007.
- [192] F.R.N. Nabarro, in *Report of a Conference on the Strength of Solids*, London: Physical Society, 1948, p. 75.
- [193] C. Herring, "Diffusional viscosity of a polycrystalline solid", *J. Appl. Phys.*, vol. **21**, no. 5, p. 437, 1950.
- [194] R.L. Coble, "A model for boundary diffusion controlled creep in polycrystalline materials", *J. Appl. Phys.*, vol. **34**, no. 6, p. 1679, 1963.
- [195] O.A. Ruano and O.D. Sherby, "Low stress creep of fine-grained materials at intermediate temperatures: Diffusional creep or grain boundary sliding?", *Mater. Sci. Eng.*, vol. **56**, no. 2, pp. 167-175, 1982.
- [196] A.P. Alur, N. Chollacoop, and K.S. Kumar, "High-temperature compression behavior of Mo-Si-B alloys", *Acta Mater.*, vol. **52**, no. 19, pp. 5571-5587, 2004.
- [197] P.R. Subramanian, T.A. Parthasarathy, M.G. Mendiratta, and D.M. Dimiduk, "Compressive creep behavior of Nb₅Si₃", *Scr. Metall. Mater.*, vol. **32**, no. 8, pp. 1227-1232, 1995.
- [198] B.P. Bewlay, C.L. Briant, E.T. Sylven, M.R. Jackson, and G. Xiao, "Creep Studies of Monolithic Phases in Nb-Silicide Based In-Situ Composites", *Mater. Res. Soc. Symp. Proc.*, vol. **646**, pp. N2.6.1-6, 2000.
- [199] R. Rosenkranz, G. Frommeyer, and W. Smarsly, "Microstructures and Properties of High Melting-Point Intermetallic Ti₅Si₃ and Ti₅Si₂ Compounds", *Mater. Sci. Eng. A*, vol. **152**, no. 1-2, pp. 288-294, 1992.
- [200] B.P. Bewlay, C.L. Briant, A.W. Davis, and M.R. Jackson, "The Effect of Silicide Volume Fraction on the Creep Behavior of Nb-Silicide Based In-Situ Composites", *Mater. Res. Soc. Symp. Proc.*, vol. **646**, pp. N2.7.1-6, 2001.
- [201] B.P. Bewlay, P.W. Whiting, A.W. Davis, and C.L. Briant, "Creep Mechanisms in Niobium-Silicide Based In-Situ Composites", *Mater. Res. Soc. Symp. Proc.*, vol. **552**, p. KK6.11.1, 1999.
- [202] R.E. Einziger, J.N. Mundy, and H.A. Hoff, "Niobium self-diffusion", *Phys. Rev. B*, vol. **17**, no. 2, pp. 440-448, 1978.
- [203] D. Ablitsee, "Diffusion of niobium, iron, cobalt, nickel and copper in niobium", *Philos. Mag.*, vol. **35**, no. 5, pp. 1239-1256, 1977.
- [204] T.S. Lundy, F.R. Winslow, R.E. Pawel, and C.J. Mchargue, "Diffusion of Nb-95 and Ta-182 in Niobium (columbium)", *Trans. Metall. Soc. AIME*, vol. **233**, no. 8, pp. 1533-1539, 1965.
- [205] R. Resnick and L. Castleman, "The Self-Diffusion of Columbium", *Trans. Am. Inst. Min. Metall. Eng.*, vol. **218**, no. 2, pp. 307-310, 1960.

- [206] J. Pelleg, "Diffusion of ^{44}Ti into niobium single crystals", *Philos. Mag.*, vol. **21**, no. 172, pp. 735–742, 1970.
- [207] S. Prasad and A. Paul, "Growth mechanism of phases by interdiffusion and diffusion of species in the niobium–silicon system", *Acta Mater.*, vol. **59**, no. 4, pp. 1577–1585, 2011.
- [208] C. Milanese, V. Buscaglia, F. Maglia, and U. Anselmi-Tamburini, "Reactive growth of niobium silicides in bulk diffusion couples", *Acta Mater.*, vol. **51**, no. 16, pp. 4837–4846, 2003.
- [209] E. Fitzer and F.K. Schmidt, "Die Diffusion von Silizium in Nb_5Si_3 ", *Monatshefte Für Chem. Chem. Mon.*, vol. **102**, no. 5, pp. 1608–1625, 1971.
- [210] R.W. Cahn and P. Haasen, *Physical Metallurgy*, 4th ed., vol. **1**, 3 vols. Amsterdam: Elsevier, 1996.
- [211] A.K. Mukherjee, "Superplasticity in Metals, Ceramics and Intermetallics", in *Materials Science and Technology*, Weinheim: Wiley-VCH Verlag, 2006.
- [212] B.P. Kashyap, A. Arieli, and A.K. Mukherjee, "Microstructural aspects of superplasticity", *J. Mater. Sci.*, vol. **20**, no. 8, pp. 2661–2686, 1985.
- [213] J.H. Schneibel and P.M. Hazzledine, "The role of Coble creep and interface control in superplastic Sn-Pb alloys", *J. Mater. Sci.*, vol. **18**, no. 2, pp. 562–570, 1983.
- [214] P. Jéhanno, M. Heilmaier, H. Saage, M. Böning, H. Kestler, J. Freudenberger, and S. Drawin, "Assessment of the high temperature deformation behavior of molybdenum silicide alloys", *Mater. Sci. Eng. A*, vol. **463**, no. 1–2, pp. 216–223, 2007.
- [215] P. Jéhanno, M. Heilmaier, H. Saage, H. Heyse, M. Boening, H. Kestler, and J.H. Schneibel, "Superplasticity of a multiphase refractory Mo-Si-B alloy", *Scr. Mater.*, vol. **55**, no. 6, pp. 525–528, 2006.
- [216] A.K. Ghosh and C.H. Hamilton, "Mechanical behavior and hardening characteristics of a superplastic Ti-6Al-4V alloy", *Metall. Trans. A*, vol. **10**, no. 6, pp. 699–706, 1979.
- [217] B.H. Prada, J. Mukhopadhyay, and A.K. Mukherjee, "Effect of Strain and Temperature in a Superplastic Ni-Modified Ti-6Al-4V Alloy", *Mater. Trans. JIM*, vol. **31**, no. 3, pp. 200–206, 1990.
- [218] W. Hotz, E. Ruedl, and P. Schiller, "Observation of processes of superplasticity with the scanning electron microscope", *J. Mater. Sci.*, vol. **10**, no. 11, pp. 2003–2006, 1975.
- [219] G.L. Dunlop and D.M.R. Taplin, "A metallographic study of superplasticity in a micrograin aluminium bronze", *J. Mater. Sci.*, vol. **7**, no. 3, pp. 316–324, 1972.
- [220] "Standard Test Method for Linear-Elastic Plane-Strain Fracture Toughness K_{Ic} of Metallic Materials", ASTM, E399, 2013.
- [221] H. Vehoff, "Fracture and Toughness of Intermetallics", *Mater. Res. Soc. Symp. Proc.*, vol. **288**, pp. 71–82, 1992.
- [222] D. Munz, R.T. Bubsey, and J.L. Shannon, "Fracture Toughness Determination of Al_2O_3 Using Four-Point-Bend Specimens with Straight-Through and Chevron Notches", *J. Am. Ceram. Soc.*, vol. **63**, no. 5–6, pp. 300–305, 1980.
- [223] T. Nishida, Y. Hanaki, and G. Pezzotti, "Effect of Notch-Root Radius on the Fracture Toughness of a Fine-Grained Alumina", *J. Am. Ceram. Soc.*, vol. **77**, no. 2, pp. 606–608, 1994.

- [224] M.G. Mendiratta, J.J. Lewandowski, and D.M. Dimiduk, "Strength and ductile-phase toughening in the two-phase Nb/Nb₅Si₃ alloys", *Metall. Trans. A*, vol. **22**, no. 7, pp. 1573–1583, 1991.
- [225] W.-Y. Kim, H. Tanaka, and S. Hanada, "Microstructure and high temperature strength at 1773 K of Nbss/Nb₅Si₃ composites alloyed with molybdenum", *Intermetallics*, vol. **10**, no. 6, pp. 625–634, 2002.
- [226] *CES EduPack 2015*. Cambridge, UK: Granta Design Limited, 2015.
- [227] D. Sturm, M. Heilmaier, J.H. Schneibel, P. Jéhanno, B. Skrotzki, and H. Saage, "The influence of silicon on the strength and fracture toughness of molybdenum", *Mater. Sci. Eng. A*, vol. **463**, no. 1–2, pp. 107–114, 2007.
- [228] Y. Murayama and S. Hanada, "High temperature strength, fracture toughness and oxidation resistance of Nb-Si-Al-Ti multiphase alloys", *Sci. Technol. Adv. Mater.*, vol. **3**, no. 2, pp. 145–156, 2002.
- [229] J. Dipasquale, D. Gahutu, D. Konitzer, and W. Soboyejo, "Fatigue Crack Growth In Niobium Aluminide Intermetallics", *Mater. Res. Soc. Symp. Proc.*, vol. **364**, 1994.
- [230] M.G. Mendiratta and D.M. Dimiduk, "Strength and toughness of a Nb/Nb₅Si₃ composite", *Metall. Trans. A*, vol. **24**, no. 2, pp. 501–504, 1993.
- [231] M. Ashby, F. Blunt, and M. Bannister, "Flow Characteristics of Highly Constrained Metal Wires", *Acta Metall.*, vol. **37**, no. 7, pp. 1847–1857, 1989.
- [232] K.S. Chan, "Alloying effects on fracture mechanisms in Nb-based intermetallic in-situ composites", *Mater. Sci. Eng. A*, vol. **329–331**, pp. 513–522, 2002.
- [233] B.X. Xu, Z.F. Yue, and G. Eggeler, "A numerical procedure for retrieving material creep properties from bending creep tests", *Acta Mater.*, vol. **55**, no. 18, pp. 6275–6283, 2007.
- [234] S.R. Srinivasan, R.B. Schwarz, and J.D. Embury, "Ductile-to-Brittle Transition in MoSi₂", *Mater. Res. Soc. Symp. Proc.*, vol. **288**, pp. 1099–1104, 1992.
- [235] R.E. Peebles, "Titanium powder metallurgy forging", U.S. Air Force Technical Report, AFML-TR-71-148, 1971.
- [236] D. Eylon, S.W. Schwenker, and F.H. Froes, "Thermally induced porosity in Ti-6Al-4V prealloyed powder compacts", *Metall. Trans. A*, vol. **16**, no. 8, pp. 1526–1531, 1985.
- [237] Y. Umakoshi, T. Nakashima, T. Nakano, and E. Yanagisawa, "Plastic Behavior and Deformation Structure of Silicide Single Crystals with Transition Metals at High Temperatures", *Mater. Res. Soc. Symp. Proc.*, vol. **322**, pp. 9–20, 1993.
- [238] R. Raj and L. Thompson, "Design of the Microstructural Scale for Optimum Toughening in Metallic Composites", *Acta Metall. Mater.*, vol. **42**, no. 12, pp. 4135–4142, 1994.
- [239] S. Semboshi, T.J. Konno, N. Masahashi, and S. Hanada, "Fracture behavior of niobium by hydrogenation and its application for fine powder fabrication", *Metall. Mater. Trans. A*, vol. **37**, no. 4, pp. 1301–1309, 2006.
- [240] National Institute of Standards and Technology, "Chemistry WebBook", 2015. [Online]. Available: <http://webbook.nist.gov/chemistry/form-ser.html>.

12 List of Figures

Fig. 1-1: schematic of modern aircraft engine General Electrics GENx-1B [7]; blue indicates cold air (before entering the combustion chamber), yellow the combustion chamber, and red air leaving the combustion chamber through the turbine.....	1
Fig. 1-2: core power versus turbine inlet temperature, blue points show specific engines; the inset shows a turbine blade coated with TBC, modified after [9].....	2
Fig. 1-3: development of creep strength and consequently operating temperature over time [12]3	
Fig. 2-1: binary phase diagram of the Nb-Si system [42]	5
Fig. 2-2: proposed ternary phase diagram Nb-Si-Ti up to 37.5 % of silicon [54].....	9
Fig. 2-3: isothermal section at 1000 °C of the ternary Nb-Si-Ti system modified after [79] with the three phase field typically researched highlighted in red	9
Fig. 2-4: sample of Nb-18Si-24Ti-5Al after oxidation at 800 °C for 100 h [78].....	10
Fig. 2-5: isothermal section at 1500 °C of the ternary Nb-Si-Hf system [53]	11
Fig. 2-6: typical microstructure of a directionally solidified multi-component alloy (Nb-16Si-19Ti-2Al-13Cr-4Hf-4B, transverse section) [77].....	12
Fig. 2-7: data of normalized mass gain over isothermal oxidation time for different arc-melted niobium silicide-based composites at 800 °C; dash-dotted line: Bachmann [57], dashed lines: Zelenitsas and Tsakiroopoulos [78], dotted lines: Geng et al. [104], solid lines: Knittel et al. [92] (copper crucible induction melted).....	13
Fig. 2-8: data of normalized mass gain over isothermal oxidation time for different niobium silicide-based composites at 1200 °C; solid lines: data produced within the HYSOP project for arc-melted material and samples produced via hot isostatic pressing of gas-atomized powder, dashed lines: Knittel et al. [92] (copper crucible induction melted)	13
Fig. 2-9: creep data as minimum creep rate over applied constant stress for different niobium silicide-based composites as well as CMSX-4 (second generation single crystal nickel-base superalloy) and Cb-753 (commercial niobium-base alloy, Nb-5V-1.25Zr) at 1200 °C; solid lines: data produced during the ULTMAT project [105], dashed line: Bewlay et al. [1], dotted lines: Subramanian et al. [106], dash-dotted line: Fujikura et al. [107]	14
Fig. 3-1: trial to drop cast Nb-20Si-23Ti-6Al-3Cr-4Hf into a cylindrical copper mould by arc-melting; only few drops reached the bottom of the mold; using the same technique, drop casting of molybdenum silicides with an even higher melting point was possible.....	15
Fig. 3-2: schematic of the VIGA (left), EIGA (middle), and PIGA (right) processes.....	17
Fig. 3-3: schematic of ball-powder-ball collision early during MA showing layered structure of elements by cold-welding and breaking, after [113]	18
Fig. 3-4: schematic of ball motion in the vial of a planetary ball mill [119].....	19
Fig. 3-5: schematic of the spark plasma sintering process, a modification of hot pressing	22

Fig. 3-6: double vane segment (left) and turbine blade geometries (middle and right) produced by HIPing of a gas-atomized Nb-20Si-23Ti-6Al-3Cr-4Hf powder, HIP can was produced by SLM, courtesy of The University of Birmingham, Interdisciplinary Research Centre in Materials Processing, Birmingham, UK	23
Fig. 3-7: schematic of powder injection molding process	24
Fig. 3-8: seal segment of a turbine produced via PIM from gas-atomized Nb-20Si-23Ti-6Al-3Cr-4Hf powder	24
Fig. 3-9: schematic of the direct laser fabrication process	25
Fig. 4-1: picture of attritor setup (left), schematic section of the double walled design	27
Fig. 4-2: temperature profile of thermal debinding and sintering for the PIM process and pressure and temperature profile for the HIP cycle	28
Fig. 4-3: indexed EBSD diffraction pattern for a bcc-metal	31
Fig. 4-4: schematic of strain measurement in compression; sample in red, SiC compression punches in blue, TZM load discs in black, and Al ₂ O ₃ strain gage rods in grey	34
Fig. 4-5: schematic (left) and photograph (right) of 4-point-bending of V-notched samples.	35
Fig. 4-6: sample and loading geometry for DBTT testing (left), distribution of the bending torque along the bottom edge (right)	36
Fig. 5-1: powder particle size in relation to milling time and vial temperature	39
Fig. 5-2: backscatter electron micrographs of milled powder for process 2 (top) and process 3 (bottom); all with same magnification, net milling time as indicated	40
Fig. 5-3: calculated phase diagram of Nb-Hf by PANDAT	41
Fig. 5-4: calculated phase diagram of Nb-Ti by PANDAT	42
Fig. 5-5: TGA-MS measurement of MA powder with heptane additton	43
Fig. 5-6: cp-measurement of MA ₁ powder; dashed lines indicate holding temperatures for subsequent XRD measurements	44
Fig. 5-7: XRD-patterns for differently heat-treated MA ₁ powders.....	45
Fig. 5-8: intensity ratios of niobium solid solution and silicide phases in differently heat-treated MA ₁ powders; calculated lattice constant of niobium solid solution aNb _{ss} shown in black	46
Fig. 5-9: DSC/DTA measurement of MA ₁ powder compared to literature data by Ma et al. [125] and Kajuch et al. [160].....	47
Fig. 5-10: left: weight distribution in the size classes of gas-atomized powder for the three batches produced; right: backscatter electron micrograph of < 25 μm gas-atomized powder; silicides in dark gray and solid solution in bright grey	48
Fig. 5-11: XRD pattern of gas-atomized powder showing the presence of Nb _{ss} , β-Nb ₅ Si ₃ and γ-Nb ₅ Si ₃	48

Fig. 6-1: photographs of cracked HIP MA material after EDM trials; partially still encased by the iron HIP can; can diameter 30 mm.....	49
Fig. 6-2: phase diagram calculation using PANDAT of the Nb-xSi-23Ti-6Al-3Cr-4Hf ($0 < x < 30$) isopleth, solid red line indicates the nominal composition used, dashed lines indicate Nb _{ss} and α -Nb ₅ Si ₃ two-phase field boundary temperatures	50
Fig. 6-3: XRD pattern of as-consolidated samples	51
Fig. 6-4: backscatter electron micrograph of HIP CGA AC; inset with higher magnification showing dendritic structures of the solidification; Nb _{ss} , α -Nb ₅ Si ₃ , γ -Nb ₅ Si ₃ , and HfO ₂ in light grey, dark grey, medium grey, and white, respectively	52
Fig. 6-5: backscatter electron micrograph of HIP GA AC showing HfO ₂ lining of the former powder particles; Nb _{ss} , α -Nb ₅ Si ₃ , γ -Nb ₅ Si ₃ , and HfO ₂ in light grey, dark grey, medium grey, and white, respectively	52
Fig. 6-6: backscatter electron micrograph of ARC showing large blocky primary silicide dendrites; inset with higher magnification showing interdendritic eutectic microstructure; Nb _{ss} , α -Nb ₅ Si ₃ , γ -Nb ₅ Si ₃ , and HfO ₂ in light grey, dark grey, medium grey, and white, respectively	53
Fig. 6-7: backscatter electron micrograph of PIM GA AC showing an equiaxed microstructure after sintering at 1500 °C for 3 h; Nb _{ss} , α -Nb ₅ Si ₃ , γ -Nb ₅ Si ₃ , and HfO ₂ in light grey, dark grey, medium grey, and white, respectively	53
Fig. 6-8: backscatter electron micrograph of PIM MA ₁ AC; Nb _{ss} , γ -Nb ₅ Si ₃ , HfO ₂ , and titanium nitride in light grey, dark grey, white, and black, respectively	54
Fig. 6-9: backscatter electron micrograph of PIM MA ₂ AC; Nb _{ss} , γ -Nb ₅ Si ₃ , HfO ₂ , and titanium carbide in light grey, dark grey, white, and black, respectively	54
Fig. 6-10: XRD pattern for HIP GA AC and heat-treated conditions.....	55
Fig. 6-11: XRD pattern for PIM MA ₁ AC and heat-treated conditions.....	55
Fig. 6-12: backscatter electron micrographs of AC and heat-treated conditions for HIP GA, HIP CGA, PIM GA, PIM MA ₁ , PIM MA ₂ ; Nb _{ss} in light grey, α -Nb ₅ Si ₃ in dark grey, γ -Nb ₅ Si ₃ in medium grey, HfO ₂ in white, and titanium nitride and titanium carbide in black for PIM MA ₁ and PIM MA ₂ , respectively; for HT ₁₃₀₀₋₁₀₀ of GA material, γ -Nb ₅ Si ₃ is brighter than Nb _{ss}	56
Fig. 6-13: indexed electron backscatter diffraction pattern of β -Nb ₅ Si ₃ with the relevant bands marked in red.....	57
Fig. 6-14: left: EBSD phase map of HIP GA HT ₁₅₀₀₋₁₀₀ , Nb _{ss} in red, α -Nb ₅ Si ₃ in blue, β -Nb ₅ Si ₃ in light blue, γ -Nb ₅ Si ₃ in green, image width 320 μ m; right: detail of left, HfO ₂ (not indexed) manually recolored in black from image quality data, image width 80 μ m.....	58
Fig. 6-15: EBSD orientation map of β -Nb ₅ Si ₃ (left) and Nb _{ss} (middle), same field of view as the left part of Fig. 6-14, with IPF coloring legend (right).....	58

Fig. 6-16: backscatter electron micrograph of PIM GA HT1500 showing high hafnium oxide content close to the surface lying on the boat with resulting β -Nb ₅ Si ₃ formation (right) and only select spots of β -Nb ₅ Si ₃ in the bulk (left).....	59
Fig. 6-17: brightness histogram for PIM GA AC (left) showing insufficient separation of the brightness ranges of the three main phases, hafnium oxide to the right is separable; brightness histogram for PIM MA ₁ AC (right) shows four separable phases with acceptable overlap of the brightness ranges of Nb _{ss} and silicides	61
Fig. 6-18: phase fractions determined by brightness threshold on BSE micrographs for PIM MA ₁	61
Fig. 6-19: optical micrograph of PIM GA HT1400-20 after polishing and etching. A typical grid used for counting is overlaid	62
Fig. 6-20: phase fractions determined by grid counting for PIM GA.....	62
Fig. 6-21: partial of a phase map of HIP GA HT1300-100 (Nb _{ss} : red, α -Nb ₅ Si ₃ : blue, γ -Nb ₅ Si ₃ : green) showing obviously wrong phase identifications mainly in the γ -Nb ₅ Si ₃ phase and influences from cleanups: raw (left), standard cleanup procedure consisting of three steps: grain dilation, neighbor CI correlation, and neighbor phase correlation (middle), one-step cleanup with grain dilation only (right); image width is 15 μ m, each.....	63
Fig. 6-22: indexed EBSD pattern of Nb _{ss} , α -Nb ₅ Si ₃ , β -Nb ₅ Si ₃ , and γ -Nb ₅ Si ₃ (from left to right)....	63
Fig. 6-23: phase fractions obtained by the RIR method for HIP GA; I _a I _c ratios were calibrated on the EBSD measurement of the heat treatment HT1300-100.....	67
Fig. 6-24: phase fractions obtained by the RIR method for PIM GA; I _a I _c ratios were calibrated on the EBSD measurement of the heat treatment HT1300-100.....	68
Fig. 6-25: phase fractions obtained by the RIR method for PIM MA ₁ ; I _a I _c ratios were calibrated on the threshold analysis fractions for heat treatment HT1300-100.	68
Fig. 6-26: phase fractions calculated by the expanded lever rule for HIP GA for the AC and different heat treatment conditions.....	71
Fig. 6-27: phase fractions calculated by the expanded lever rule for PIM GA for different heat treatment conditions	71
Fig. 6-28: phase fractions calculated by the expanded lever rule for PIM MA ₁ for the AC and different heat treatment conditions.....	72
Fig. 6-29: overall chemical composition of HIP GA, PIM GA, and PIM MA ₁ as determined by EDS in the AC condition; dashed lines indicate nominal composition	72
Fig. 6-30: chemical composition of Nb _{ss} in HIP GA (squares), PIM GA (circles), and PIM MA ₁ (hexagons) as determined by EDS over heat treatment; dashed lines indicate PANDAT calculations	73
Fig. 6-31: chemical composition of α -Nb ₅ Si ₃ in HIP GA (squares), PIM GA (circles), and PIM MA ₁ (hexagons) over heat treatment; dashed lines indicate PANDAT calculations..	74

Fig. 6-32: chemical composition of γ -Nb ₅ Si ₃ in HIP GA (squares), PIM GA (circles), and PIM MA ₁ (hexagons) over heat treatment; dashed lines indicate PANDAT calculations..	74
Fig. 6-33: phase fractions determined by all introduced methods for HIP GA; additionally, the EBSD data was extended by a HT ₁₅₀₀₋₁₀₀ measurement, which was put in at HT ₁₅₀₀₋₂₀	75
Fig. 6-34: phase fractions determined by all introduced methods for PIM GA; additionally the EBSD data was extended by a HT ₁₅₀₀₋₁₀₀ measurement, which was put in at HT ₁₅₀₀₋₂₀	76
Fig. 6-35: phase fractions determined by all introduced methods for PIM MA ₁	76
Fig. 6-36: calculated phase diagram of Nb-20Si-23Ti-6Al-3Cr-4Hf for increasing iron content; the red dashed line indicates the iron content determined by EDS.....	78
Fig. 6-37: plot of the EBSD grain size over the phase size from the linear intersect method (LIM), solid symbols are data points, the open symbol is an interpolation	81
Fig. 7-1: left: yield stress and cleavage stress in case of brittle fracture for some bcc metals and nickel, modified after [175, p. 230]; right: Mohr circle for a three-dimensional stress state, including the temperature dependent shear stress for yielding τ_y and the temperature independent cleavage stress σ_c , based on [176, p. 196].....	83
Fig. 7-2: deformation mechanism map for pure niobium (grain size 100 μm) showing lines of constant strain rate over normalized shear stress and homologous temperature; heavy lines separate regimes of different dominant deformation mechanisms [177].....	84
Fig. 7-3: stress-strain curves for consolidated material at room temperature (RT) with a strain rate of 10^{-3} s^{-1}	85
Fig. 7-4: stress-strain curves for consolidated material at 1000 °C with a strain rate of 10^{-3} s^{-1}	85
Fig. 7-5: backscatter electron micrographs of PIM GA HT ₁₅₀₀₋₁₀₀ after deformation at room temperature until fracture (left) after deformation at 1000 °C to 20 % true plastic strain (middle) and PIM MA ₁ HT ₁₅₀₀₋₁₀₀ after deformation at 1000 °C to 20 % true plastic strain; strain rate of 10^{-3} s^{-1} ; loading direction parallel to vertical edge	86
Fig. 7-6: maximum strength over temperature for a strain rate of 10^{-3} s^{-1} ; literature data by Wenderoth et al. [179], Allan [180], Bewlay et al. [1, 98], and Jéhanno et al. [23].....	87
Fig. 7-7: maximum strength over strain rate for a testing temperature of 1000 °C	88
Fig. 7-8: typical creep curve of the analyzed material, in this case HIP GA HT ₁₅₀₀₋₁₀₀ tested at 1100 °C and 100 MPa	90
Fig. 7-9: TEM micrographs of HIP GA HT ₁₅₀₀₋₁₀₀ after plastic deformation of 15 % showing the presence of phase boundary cracks.....	90
Fig. 7-10: plot of minimum strain rate over applied true stress at testing temperature of 1000 °C for material produced by HIP or PIM from gas-atomized powders in the AC and heat treated conditions; the dashed line indicates the creep goal for 1200 °C and stresses of 150 MPa	91

- Fig. 7-11: plot of minimum strain rate over applied true stress at testing temperature of 1100 °C for material produced by HIP or PIM from gas-atomized powders in the AC and heat treated conditions 91
- Fig. 7-12: schematic of deformation for an originally cubic grain with edge length a (left) to a uniaxially compressed cuboid grain of the same volume (right) 92
- Fig. 7-13: standard triangle of a cubic crystal, colored according to the maximum Schmid-factor available in any of the bcc slip systems (blue); dotted lines connect an arbitrary crystal orientation with the respective active slip plane normal (red); heavy arrows indicate rotation of the compression direction towards symmetry lines, 111, or 100, depending on the initial orientation; dashed lines connect slip plane normals under multiple slip condition 93
- Fig. 7-14: EBSD mapping of the cross-section of the deformed PIM GA HT1300-100, the coloring indicates the crystallographic orientation of the lattice parallel to the deformation direction, i.e. parallel to the vertical figure edge; image width is 320 μm 94
- Fig. 7-15: TEM micrographs of solid solution grains showing dislocations 95
- Fig. 7-16: strain rate of HIP GA HT1500-100 during temperature jump test; temperature in red, reference strain rate at 1000 °C in black (also dashed lines), strain rate for deviating temperatures in blue 96
- Fig. 7-17: temperature dependence of strain rate for select sample conditions to determine activation energy for creep 96
- Fig. 7-18: double logarithmic plot of creep rate over grain size for PIM GA; grain sizes of 4.7, 6.0, and 8.9 μm correspond to the heat treatments HT1300-100, HT1500-20, and HT1500-100, respectively 98
- Fig. 7-19: EBSD phase mapping of the cross-section of the deformed HIP GA HT1500-100, Nb_{ss} in red, $\alpha\text{-Nb}_5\text{Si}_3$ in blue, $\gamma\text{-Nb}_5\text{Si}_3$ in green, high angle grain boundaries in black, low angle grain boundaries in grey; black boxes highlight fine grained $\alpha\text{-Nb}_5\text{Si}_3$ regions after deformation; image width 320 μm 99
- Fig. 8-1: SEM micrographs of fracture surfaces of HIP GA AC (left) and HIP GA HT1500-100 (right) showing mostly transgranular fracture with river patterns 104
- Fig. 8-2: influence of notch root diameter in SEVNB bend testing on fracture toughness of alumina; reproduced after [222, 223] 104
- Fig. 8-3: fracture toughness K_{Ic} for binary niobium silicide composites as a function of silicon content for different processing conditions: directional solidification (DS), extrusion (Ext), and arc-melted (AM), partially heat treated (HT), reproduced after [74]; DS titanium-containing alloys [3] and average from the present work added 106
- Fig. 8-4: fracture strain over temperature plotted for AC and ARC samples at strain rates of 10^{-5} s^{-1} (open symbols) and 10^{-3} s^{-1} (crossed symbols) 108
- Fig. 8-5: backscatter electron micrographs of fractured three-point bend specimens, left: top view on the extreme tensile fiber of HIP CGA AC close to the fracture plane (out of frame) after testing at 850 °C / 10^{-5} s^{-1} ; tensile loading parallel to vertical figure edge; even outside

the fracture plane, silicide particles show cracks perpendicular to tensile loading; right: fracture surface of PIM GA HT1500-100 after bending at 850 °C / 10^{-5} s^{-1} , extreme tensile fiber at the top	109
Fig. 8-6: fracture strain over temperature plotted for HIP GA, HIP CGA, and PIM GA in the AC (open symbols) and HT1500-100 (solid symbols) condition and additionally HIP GA HT1500-100+HIP at strain rates of 10^{-5} s^{-1}	109
Fig. 8-7: left: secondary electron micrograph of HIP GA HT1500-100 tested at 800 °C; pores in the fracture plane are encircled in red, extreme tensile fiber at the top; right: topview optical micrograph of the extreme tensile fiber of the same sample, loading direction is vertical and fracture plane at the top.....	110
Fig. 8-8: yield stress over temperature plotted for HIP GA and PIM GA in the AC (left) and HT1500-100 (right) condition and additionally HIP GA HT1500-100+HIP (half filled symbols, right) at strain rates of 10^{-5} s^{-1} , note the different scales.....	112
Fig. 8-9: top: extreme tensile fiber of HT1500-100 material close to the fracture plane for different deformation temperatures, loading direction vertical; bottom: fracture surface for the same samples	112
Fig. 9-1: influence of alloying elements on the DBTT of niobium [17]	113
Fig. 9-2: nano-hardness HM and composition of Nb_{ss} from WDS measurements of different processing routes for the HT1500-100 condition, composition scale is logarithmic for emphasis on components with low contents.....	114
Fig. 9-3: Norton plot comprising compressive creep and quasi-static compressive (dotted symbols) deformation data for a testing temperature of 1000 °C for HIP and PIM samples in the AC and heat-treated conditions	116
Fig. 9-4: inverse grain size over critical stress for grain boundary sliding, solid symbols represent measured data points, open symbol represents extrapolation.....	117
Fig. 9-5: reduced grain size of PIM GA for heat treatments at 1300 and 1500 °C, note the squared grain size scale	118
Fig. 14-1: Exemplary micrographs of notched samples: EDM notch with polished V-notch (left) and EDM notch (right).....	147
Fig. 14-2: Mass spectrum for heptane [240].....	147
Fig. 14-3: XRD pattern for PIM GA AC and heat-treated conditions.....	148
Fig. 14-4: backscatter electron micrograph of HIP GA HT1500-100 after an additional HIP cycle at 1230 °C for 4 h.....	148
Fig. 14-5: XRD pattern for $\text{Nb-36.5Si-13Ti-1Al-4Hf}$ ($\alpha\text{-Nb}_5\text{Si}_3$) and $\text{Nb-36Si-23.5Ti-2.5Al-0.5Cr-7.5Hf}$ ($\gamma\text{-Nb}_5\text{Si}_3$) showing only the intended monolithic intermetallic with only minimal solid solution in $\gamma\text{-Nb}_5\text{Si}_3$	149
Fig. 14-6: EBSD phase map of PIM GA HT1300-100 before (left) and after (right) deformation to $\epsilon_t = 1$, Nb_{ss} in red, $\alpha\text{-Nb}_5\text{Si}_3$ in blue, $\gamma\text{-Nb}_5\text{Si}_3$ in green; low angle grain boundaries ($2 - 15^\circ$) in grey, high angle grain boundaries ($> 15^\circ$) in black; image width 80 μm , each.....	149

Fig. 14-7: stress-strain curves in compression of PIM GA repeated with three identically prepared samples 153

13 List of Tables

Table 1-1: refractory elements and their basic properties [17]	3
Table 2-1: properties of phases in the Nb-Si system, niobium atoms in green and silicon atoms in blue	6
Table 5-1: investigated milling parameters, each cycle comprising 1 min net milling time (top), powder yield and contamination level after given net milling time (bottom).....	40
Table 5-2: typical contents of gaseous impurities in milled and elemental powders; * is taken from the certificate of analysis from the supplier Alfa Aesar	42
Table 5-3: calculated lattice constants for niobium solid solution in milled and heat-treated MA1 and AC	45
Table 6-1: processing routes for compact material explored in this work	49
Table 6-2: heat treatments investigated	50
Table 6-3: area fraction of HfO ₂ as determined from backscatter electron micrographs in %.....	60
Table 6-4: phase fractions of HIP and PIM after HT ₁₃₀₀₋₁₀₀ determined by EBSD	64
Table 6-5: diffraction plane of highest intensity, diffraction angle of this peak in the database and as determined in this work, and corresponding PDF entry from the ICDD database.	66
Table 6-6: inverse pole figures for the three main phases of HIP GA HT ₁₃₀₀₋₁₀₀ (left) and PIM GA HT ₁₃₀₀₋₁₀₀ (right); colors indicate multiples of the uniform distribution (MUD)	67
Table 6-7: oxygen, nitrogen, and carbon contents determined by hot carrier gas extraction and resulting, calculated amounts of hafnium oxide, titanium nitride, and titanium carbide, respectively; measured contents from threshold analysis presented previously (section 6.2.1) in paranthesis.....	77
Table 6-8: phase and grain sizes of undeformed HIP GA and PIM GA for different heat treatment conditions on a cross-section determined by the linear intersect method (top) and EBSD (bottom).....	80
Table 7-1: strength values obtained for bulk material in the AC condition, 0.2 % offset yield strength and maximum stress in parantheses, both in MPa	87
Table 7-2: phase sizes of deformed and undeformed PIM GA HT ₁₃₀₀₋₁₀₀ on a cross-section determined by the linear intersect method.....	92
Table 7-3: inverse pole figures for the three main phases of undeformed and deformed PIM GA HT ₁₃₀₀₋₁₀₀ ; colors indicate multiples of the uniform distribution (MUD).....	95
Table 7-4: minimum creep rates obtained for monolithic silicides α -Nb ₅ Si ₃ and γ -Nb ₅ Si ₃ at 200 MPa in s ⁻¹	100
Table 7-5: grain sizes of undeformed and deformed PIM GA HT ₁₃₀₀₋₀₀ on a cross-section determined by EBSD	102

Table 8-1: fracture toughness of GA material in the AC and HT₁₅₀₀₋₁₀₀ condition as well as ARC determined by the SEVNB-method..... 103

Table 8-2: porosity of samples produced from GA and CGA powder before and after heat treatment as determined by the Archimedes principle..... 111

Table 9-1: contamination contents of carbon, nitrogen, and oxygen as determined by WDS on Nb_{ss} and by hot carrier gas extraction (HCGE) on the composite 115

Table 14-1: composition of phases in HIP GA for various conditions as determined by EDS... 150

Table 14-2: composition of phases in PIM GA for various conditions as determined by EDS... 151

Table 14-3: composition of phases in PIM MA₁ for various conditions as determined by EDS 152

14 Appendix

14.1 Figures

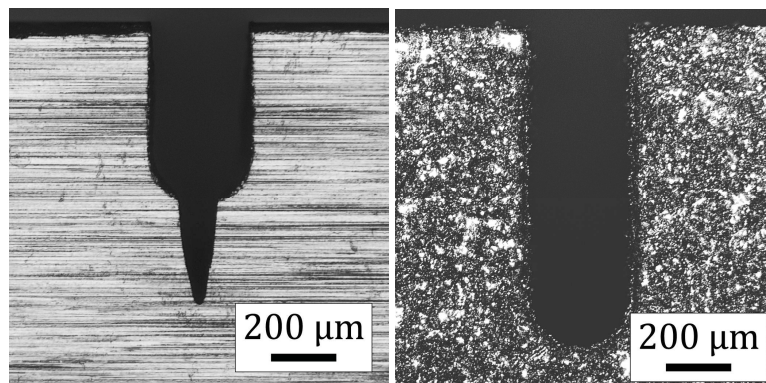


Fig. 14-1: Exemplary micrographs of notched samples: EDM notch with polished V-notch (left) and EDM notch (right)

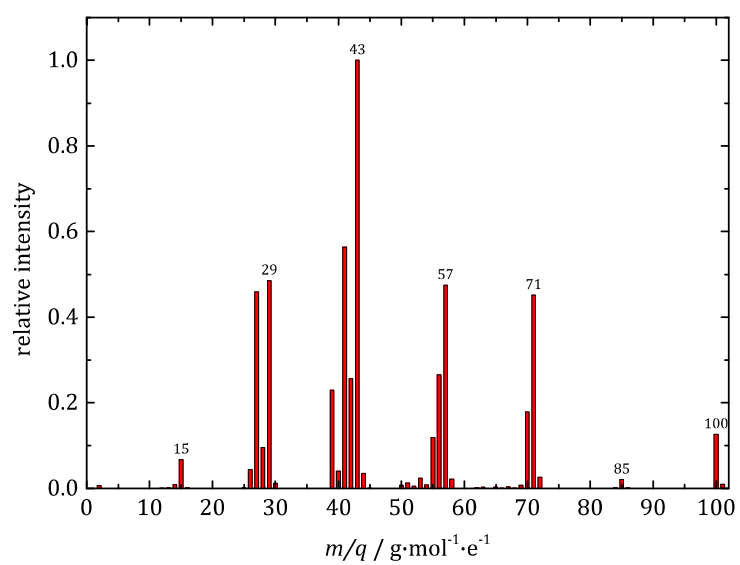


Fig. 14-2: Mass spectrum for heptane [240]

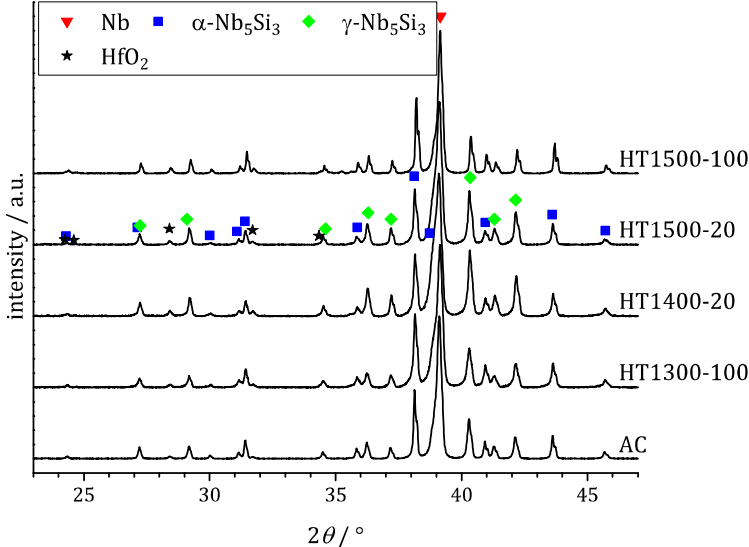


Fig. 14-3: XRD pattern for PIM GA AC and heat-treated conditions

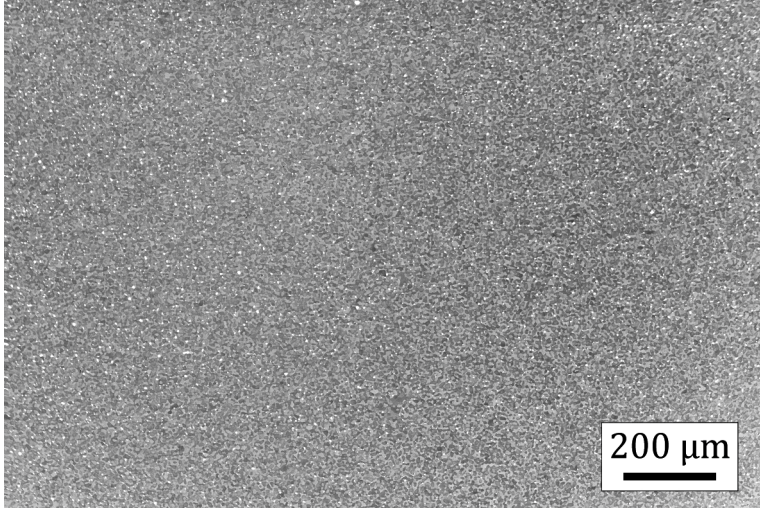


Fig. 14-4: backscatter electron micrograph of HIP GA HT1500-100 after an additional HIP cycle at 1230 $^\circ\text{C}$ for 4 h

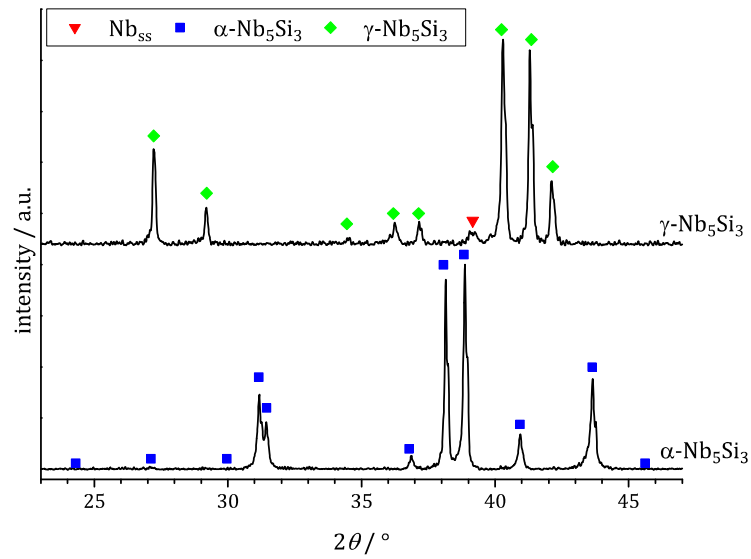


Fig. 14-5: XRD pattern for Nb-36.5Si-13Ti-1Al-4Hf (α -Nb₅Si₃) and Nb-36Si-23.5Ti-2.5Al-0.5Cr-7.5Hf (γ -Nb₅Si₃) showing only the intended monolithic intermetallic with only minimal solid solution in γ -Nb₅Si₃

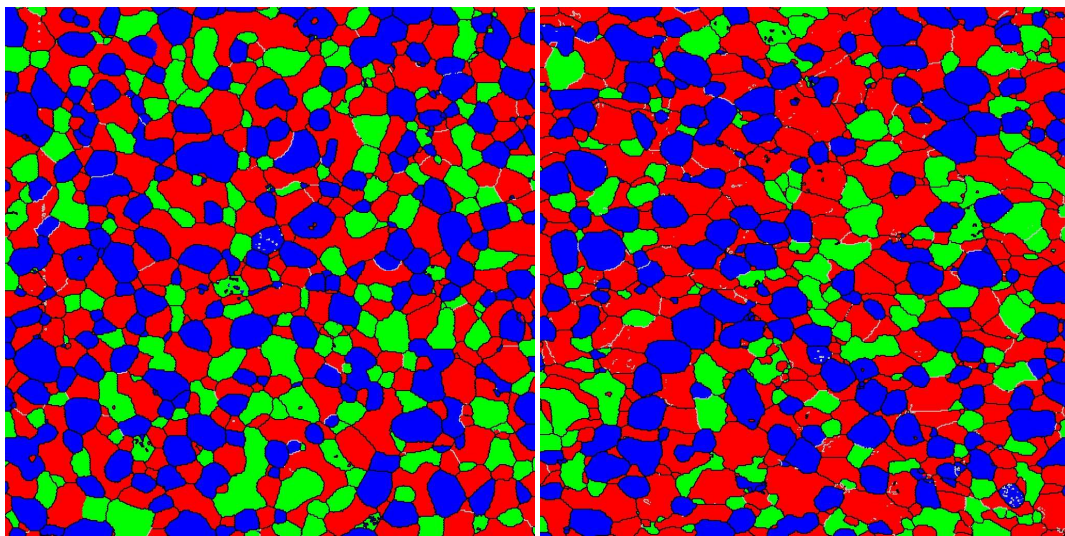


Fig. 14-6: EBSD phase map of PIM GA HT₁₃₀₀₋₁₀₀ before (left) and after (right) deformation to $\epsilon_t = 1$, Nb_{ss} in red, α -Nb₅Si₃ in blue, γ -Nb₅Si₃ in green; low angle grain boundaries ($2 - 15^\circ$) in grey, high angle grain boundaries ($> 15^\circ$) in black; image width 80 μm , each

14.2 Tables

Table 14-1: composition of phases in HIP GA for various conditions as determined by EDS

phase	condition	Nb	Si	Ti	Al	Cr	Hf
Nb _{ss}	HT1300-100	55.9 ± 0.5	0.3 ± 0.1	27.7 ± 0.2	8.3 ± 0.2	6.0 ± 0.1	1.7 ± 0.1
	HT1400-20	56.2 ± 0.2	0.8 ± 0.6	27.3 ± 0.4	8.3 ± 0.1	5.8 ± 0.1	1.8 ± 0.1
	HT1500-20	57.0 ± 0.9	1.2 ± 1.3	26.5 ± 0.3	7.9 ± 0.2	5.5 ± 0.2	1.9 ± 0.2
α-Nb ₅ Si ₃	HT1300-100	42.4 ± 0.3	35.0 ± 0.4	16.5 ± 0.2	2.1 ± 0.1	0.2 ± 0.0	3.8 ± 0.1
	HT1400-20	42.8 ± 0.4	34.5 ± 0.6	16.4 ± 0.4	2.2 ± 0.1	0.3 ± 0.1	3.9 ± 0.2
	HT1500-20	43.3 ± 0.4	34.5 ± 0.8	16.1 ± 0.3	2.0 ± 0.1	0.3 ± 0.1	3.7 ± 0.1
γ-Nb ₅ Si ₃	HT1300-100	26.6 ± 0.6	33.9 ± 0.5	26.0 ± 0.3	4.2 ± 0.1	0.7 ± 0.1	8.7 ± 0.2
	HT1400-20	29.1 ± 0.5	33.1 ± 0.8	25.4 ± 0.4	4.0 ± 0.1	0.7 ± 0.1	7.8 ± 0.1
	HT1500-20	30.5 ± 0.5	33.9 ± 0.6	24.1 ± 0.1	3.5 ± 0.1	0.7 ± 0.1	7.2 ± 0.1
overall	HT1300-100	45.9 ± 0.0	19.3 ± 0.0	22.9 ± 0.0	5.2 ± 0.0	2.7 ± 0.0	4.0 ± 0.0
	HT1400-20	45.8 ± 0.2	19.7 ± 0.2	22.8 ± 0.0	5.1 ± 0.1	2.7 ± 0.1	4.0 ± 0.1
	HT1500-20	45.9 ± 0.2	19.5 ± 0.3	22.8 ± 0.1	5.1 ± 0.0	2.7 ± 0.1	3.9 ± 0.1

Table 14-2: composition of phases in PIM GA for various conditions as determined by EDS

phase	condition	Nb	Si	Ti	Al	Cr	Hf
Nb _{ss}	AC	57.3 ± 0.1	0.6 ± 0.1	26.4 ± 0.1	8.2 ± 0.1	5.7 ± 0.1	1.8 ± 0.1
	HT1300-100	56.0 ± 0.4	1.5 ± 0.9	27.0 ± 0.2	8.2 ± 0.2	5.7 ± 0.1	1.6 ± 0.1
	HT1400-20	56.8 ± 0.2	0.3 ± 0.1	26.9 ± 0.2	8.4 ± 0.0	5.9 ± 0.1	1.8 ± 0.0
	HT1500-20	57.6 ± 0.2	0.3 ± 0.1	26.4 ± 0.2	8.2 ± 0.1	5.7 ± 0.1	1.8 ± 0.1
α-Nb ₅ Si ₃	AC	43.1 ± 0.1	34.7 ± 0.3	16.0 ± 0.3	2.1 ± 0.1	0.3 ± 0.1	3.8 ± 0.1
	HT1300-100	43.0 ± 0.3	35.0 ± 0.3	16.0 ± 0.2	2.0 ± 0.0	0.3 ± 0.0	3.8 ± 0.1
	HT1400-20	43.2 ± 0.4	34.9 ± 0.2	16.0 ± 0.2	2.1 ± 0.1	0.3 ± 0.1	3.6 ± 0.2
	HT1500-20	43.0 ± 0.1	35.0 ± 0.2	16.0 ± 0.3	2.0 ± 0.0	0.3 ± 0.1	3.8 ± 0.1
γ-Nb ₅ Si ₃	AC	31.2 ± 1.5	33.8 ± 1.0	23.6 ± 0.3	3.8 ± 0.2	0.8 ± 0.1	6.8 ± 0.8
	HT1300-100	27.4 ± 0.9	33.8 ± 0.8	25.0 ± 0.3	4.3 ± 0.1	0.7 ± 0.1	8.9 ± 0.6
	HT1400-20	30.3 ± 1.0	33.5 ± 0.8	24.5 ± 0.3	3.9 ± 0.1	0.8 ± 0.1	7.1 ± 0.2
	HT1500-20	30.5 ± 0.4	34.2 ± 0.3	23.9 ± 0.1	3.7 ± 0.0	0.8 ± 0.0	7.0 ± 0.4
overall	AC	46.1 ± 0.1	19.6 ± 0.2	22.4 ± 0.2	5.2 ± 0.1	2.7 ± 0.1	4.0 ± 0.1
	HT1300-100	46.0 ± 0.3	19.7 ± 0.2	22.6 ± 0.1	5.1 ± 0.1	2.7 ± 0.0	4.0 ± 0.0
	HT1400-20	46.1 ± 0.1	19.4 ± 0.1	22.7 ± 0.1	5.1 ± 0.0	2.7 ± 0.1	4.1 ± 0.1
	HT1500-20	45.9 ± 0.2	19.6 ± 0.4	22.6 ± 0.3	5.3 ± 0.0	2.7 ± 0.1	4.0 ± 0.2

Table 14-3: composition of phases in PIM MA1 for various conditions as determined by EDS

phase	condition	Nb	Si	Ti	Al	Cr	Hf	Fe
Nb _{ss}	AC	65.0 ± 0.3	0.4 ± 0.1	19.1 ± 0.2	7.5 ± 0.1	5.2 ± 0.1	0.8 ± 0.1	1.9 ± 0.1
	HT1300-100	65.9 ± 0.3	0.3 ± 0.1	20.2 ± 0.2	7.1 ± 0.1	4.5 ± 0.1	1.0 ± 0.1	0.9 ± 0.3
	HT1400-20	65.3 ± 0.4	0.3 ± 0.1	20.1 ± 0.1	7.1 ± 0.2	4.5 ± 0.3	1.0 ± 0.2	1.6 ± 0.3
	HT1500-20	66.1 ± 0.4	0.3 ± 0.1	19.1 ± 0.2	7.2 ± 0.3	4.9 ± 0.2	0.7 ± 0.2	1.7 ± 0.3
γ-Nb ₅ Si ₃	AC	37.5 ± 0.4	32.4 ± 0.4	20.0 ± 0.2	4.3 ± 0.0	0.8 ± 0.0	4.3 ± 0.5	0.7 ± 0.3
	HT1300-100	36.7 ± 2.0	31.8 ± 1.6	21.2 ± 1.9	4.6 ± 0.4	0.8 ± 0.2	4.3 ± 0.6	0.6 ± 0.2
	HT1400-20	36.9 ± 0.7	32.2 ± 0.4	20.5 ± 0.2	4.4 ± 0.1	0.8 ± 0.1	4.2 ± 0.5	0.9 ± 0.1
	HT1500-20	38.4 ± 2.5	31.4 ± 2.7	20.2 ± 0.3	4.5 ± 0.3	0.9 ± 0.3	3.9 ± 0.3	0.8 ± 0.2
TiN	AC	10.0 ± 2.3	4.5 ± 2.8	81.5 ± 5.4	0.8 ± 0.4	0.2 ± 0.1	2.7 ± 0.3	0.2 ± 0.1
	HT1300-100	7.0 ± 1.7	1.4 ± 1.8	88.0 ± 3.8	0.6 ± 0.3	0.2 ± 0.2	2.7 ± 0.1	0.2 ± 0.1
	HT1400-20	7.1 ± 1.4	0.8 ± 0.5	88.1 ± 2.3	0.4 ± 0.2	0.2 ± 0.2	3.1 ± 0.5	0.3 ± 0.2
	HT1500-20	8.4 ± 1.7	2.6 ± 2.3	85.1 ± 4.2	0.6 ± 0.3	0.2 ± 0.2	3.0 ± 0.4	0.2 ± 0.2
overall	AC	45.3 ± 0.2	21.1 ± 0.3	21.5 ± 0.2	4.8 ± 0.1	2.0 ± 0.1	4.0 ± 0.1	1.3 ± 0.1
	HT1300-100	44.8 ± 0.3	21.1 ± 0.5	22.0 ± 0.1	4.8 ± 0.1	2.0 ± 0.1	4.1 ± 0.1	1.3 ± 0.0
	HT1400-20	45.3 ± 0.0	21.1 ± 0.1	21.8 ± 0.1	4.8 ± 0.1	1.8 ± 0.0	4.0 ± 0.1	1.4 ± 0.0
	HT1500-20	45.2 ± 0.3	21.2 ± 0.2	21.7 ± 0.2	4.7 ± 0.1	1.9 ± 0.1	4.0 ± 0.1	1.2 ± 0.1

14.3 Reproducibility

While at low temperatures, defects may determine mechanical properties, at high temperatures reproducibility is very good. Fig. 14-7 shows three tests of the same condition of PIM GA samples at 1000 °C and a strain rate of 10^{-3} s^{-1} . Maximum stress is at $534 \pm 3 \text{ MPa}$ attesting excellent repeatability of mechanical properties.

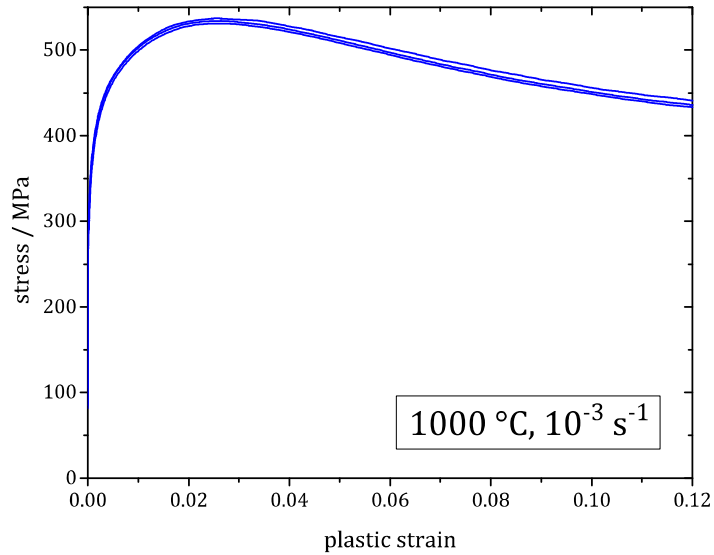


Fig. 14-7: stress-strain curves in compression of PIM GA repeated with three identically prepared samples

15 Prior Publications on Parts of this Work

C. Seemüller, T. Hartwig, M. Mulser, N. Adkins, M. Wickins, and M. Heilmaier, "Influence of Powder Metallurgical Processing Routes on Phase Formations in a Multicomponent NbSi-Alloy," *JOM*, vol. 66, no. 9, pp. 1900–1907, 2014.

C. Seemüller, M. Heilmaier, T. Hartwig, M. Mulser, N. Adkins, and M. Wickins, "Influence of microstructure and processing on mechanical properties of advanced Nb-silicide alloys," *Mater. Res. Soc. Symp. Proc.*, vol. 1516, pp. 317–322, 2013.

M. Mulser, T. Hartwig, C. Seemüller, M. Heilmaier, N. Adkins, and M. Wickins, "Influence of the processing technique on the properties of Nb-Si intermetallic composites for high-temperature applications processed by MIM and HIP," *Advances in Powder Metallurgy & Particulate Materials*, part 4, pp. 8-16, 2014

M. Mulser, T. Hartwig, C. Seemüller, M. Heilmaier, N. Adkins, and M. Wickins, "Nb-Si intermetallic composites for high-temperature applications produced by MIM," *Proceedings of Euro PM2013 Congress & Exhibition (Gothenburg, Sweden)*, vol. 1, pp. 259-264, EPMA Shrewsbury, UK, 2013